ulm university universität
uulm

Aircraft-to-Aircraft Communications: Channel Modeling and Data Link Design

DISSERTATION

zur Erlangung des akademischen Grads eines

DOKTOR-INGENIEURS

(Dr.-Ing.)

der Fakultät für Ingenieurwissenschaften,
Informatik und Psychologie der Universität Ulm

von

Miguel Ángel Bellido Manganell
aus Granada (Spanien)

Gutachter:	Prof. Dr.-Ing. Robert Fischer
	Univ.-Prof. Dipl.-Ing. Dr.techn. Gerald Matz
Amtierender Dekan:	Prof. Dr. Matthias Tichy

Ulm, 04. April 2025

Acknowledgements

Sir Isaac Newton once wrote: “If I have seen further, it is by standing on the shoulders of giants.” In the same way, this thesis could never have been completed without the support of many giants.

My deepest thanks go to my life partner, Rosa. She is my rock. She has been there for me in good times and bad, always supporting me and managing to keep me motivated despite the difficulties. I owe her a lot of what I have achieved so far. Now she has blessed me with Gabriel, who has given me the final push I needed to finish.

Without my parents and my sister, I would not be the person I am today. My parents raised me and gave me the environment to grow and fulfil my potential. My father instilled inventiveness and ingenuity in me through his many creations, unwittingly guiding me towards engineering and research. His international recognition has shown me that hard work and perseverance are key elements of success. And this is beautifully complemented by the endless love of my mother, who also strives in every conversation to teach me the emotional intelligence needed to enjoy life, not just live it. These tributes would be incomplete without mentioning my boxing partner, my sister. She has never ceased to show me affection, even when I have often failed to show it back as I should, and to remind me how proud she is of me.

I would like to express my sincere thanks to Prof. Dr.-Ing. Robert Fischer for supervising this thesis and for his availability, helpful discussions and feedback. In addition, I cannot imagine working at DLR without the close cooperation with Michael Walter, whom I would like to thank very much for the work we have done together and for his support. Many other colleagues have contributed in one way or another to this thesis. I would like to thank Michael Schnell, Alexandra Filip, Lukas Schalk, Daniel Mielke, Dennis Becker, Ayten Gürbüz, Oliver Heirich, Thomas Gräupl, Nils Mäurer, and Nicolas Schneckenburger, as well as my department heads, Stephan Sand and Uwe-Carsten Fiebig, and institute head Florian David for their support. I would also like to thank all those involved in the A2A measurement campaign and Rohde & Schwarz GmbH & Co. KG for providing the A2A measurement data.

Abstract

Aircraft-to-aircraft (A2A) communications are poised to play a crucial role in the future of air traffic. The saturation of airspace in many parts of the world is leading to the need for air traffic management systems that can operate as autonomously as possible. This autonomy can only be achieved if aircraft are able to make decisions without involving the already overburdened air traffic controllers. To do this, aircraft must be able to communicate directly with each other in order to be fully aware of the air traffic around them, resolve conflicts, and coordinate trajectories directly with each other. A2A communications are also gaining a lot of attention in other areas, such as the military, where new air combat systems require reliable communications between a large number of flying vehicles. The stringent requirements set for the new A2A communication systems imply the need for an optimal design of the data links. This is only possible if the characteristics of the radio propagation channel are known accurately and if realistic models are available to reproduce the channel faithfully. Both aspects have not been thoroughly investigated in the literature and prevent the optimal design and testing of new A2A communication systems.

In this thesis we embark on a comprehensive study of A2A channels, analyzing a wealth of channel measurements and deriving numerous statistics of the different channel components for various configurations. These configurations encompass multiple ground surfaces, including forest, fields, and lakes, different geometries between aircraft and the Earth's surface, and diverse antenna configurations. Analyzing the measured amplitude of the channel components in the different scenarios allows us to provide very valuable statistics not yet measured in A2A channels in such detail. In our quest for an accurate model and for a deeper understanding of the scattering components, we develop and validate a novel theoretical technique to characterize the scattering components with a particular emphasis on their delay/Doppler distribution, an aspect that has been largely disregarded in the literature. Building upon this foundation, a geometry-based stochastic A2A channel model is proposed. This model not only merges the information acquired from the measurements and the novel technique to characterize the scattering components, but also offers a significant advancement in

the field by providing a practical tool for simulating the propagation channels in any arbitrary A2A scenario. Its practicability is demonstrated by applying it to the design of the A2A extension of the L-band Digital Aeronautical Communications System (LDACS). By using the developed channel model, we are able to determine the optimal design of the physical layer through computer simulations. Among others, we investigate the performance of orthogonal frequency-division multiplexing (OFDM) and of different forward error correction schemes, including low-density parity-check (LDPC) and polar codes used in 5G communications, in A2A scenarios.

Contents

Chapter 1

Introduction

Air transport is seen as a key enabler of economic growth and development. According to [Ind19], 35% of world trade by value was carried by aircraft and around 4.3 billion passengers used air transport in 2018. Until the COVID-19 pandemic, its importance grew steadily over the years, with reports predicting a 53% increase in the number of flights in Europe between 2017 and 2040 in the most-likely scenario [STA18]. The COVID-19 pandemic inflicted a severe blow to aviation, practically putting on halt most non-critical air transport for years. However, the relaxation of the global restrictions imposed to prevent the spread of the COVID-19 virus led air traffic to experience a strong year-on-year growth after the initial crash, with the year 2024 seen by the International Civil Aviation Organization (ICAO) as a milestone when pre-pandemic air traffic levels are finally surpassed [Int24]. In fact, recent reports forecast a 3.3% average annual increase in the number of air passengers between 2019 and 2040 [Int22].

The steady air traffic growth entails a significant challenge to the air traffic management (ATM), which must enable and sustain such traffic growth while further guaranteeing safety and the allocation of cost-effective, environmentally-friendly flight routes. This is critical, given that even with the current air traffic levels, the air-ground voice and data communications needed for ATM, e.g., between pilots and air traffic controllers, are suffering from the saturation of the VHF band in some regions of the world such as central Europe [Int18a; EUR21]. Moreover, with geopolitical conflicts constraining the usable airspace, ATM becomes even more challenging in the regions where the air traffic is redirected to because of the high, unplanned load. An ATM capable of meeting these challenges is to be achieved through the deployment of a set of communication data links providing high-throughput low-latency data communications to the aircraft and enabling the new services and operational concepts defined by the Federal Aviation Administration (FAA) and Eurocontrol in [ER07] for a more efficient and secure ATM. This set of communication data links, commonly named

the Future Communications Infrastructure (FCI), shall jointly support the exchange of air traffic service (ATS) and airline operational control (AOC) data between the aircraft and other entities within the Aeronautical Telecommunication Network (ATN), such as air traffic controllers, throughout all phases of flight. The aircraft shall be able to achieve ATN connectivity via either deployed ground stations (GSs) or satellites. Having both options is preferred such that single points of failure are avoided. In continental airspace, terrestrial communication systems are the preferred option for ATM communications, with satellite-based systems being employed primarily as a contingency measure in the event of unavailability of the former. However, the air-ground communications system currently used for ATM communications in continental airspace, the VHF data link (VDL) mode 2 (VDL-m2), is suffering from the increasing saturation of the VHF band in some parts of the world [Int18a; EUR21]. This has led to the development of a new and more capable air-ground communications system, the L-band Digital Aeronautical Communications System (LDACS), which is currently undergoing the standardization process of the ICAO and shall be able to sustain the air traffic growth even in the most challenging regions. In regions where no ground infrastructure can be deployed, such as oceanic, remote, and polar (ORP) regions, satellite links represent the only capable option currently available for data communications.

In addition to air-ground communications, some of the new services and operational concepts defined for the modernization of the ATM rely on the availability of a direct aircraft-to-aircraft (A2A) communications data link [ER07]. Unfortunately, no system currently available is capable of supporting the desired communication performance requirements. Even though direct A2A voice communications are possible on the VHF common traffic advisory frequency (CTAF), no data communications are supported. Other standardized system supporting A2A communications and operating in the VHF band is the VDL mode 4 (VDL-m4) [Int04], which supports addressed and broadcast data communications not only between aircraft, but also between airport vehicles and ground stations. Unfortunately, it has only been implemented in Europe on a regional basis [WM15] and, in addition, Airbus reported on-board co-site interference issues with other VHF radios and recommended the use of an alternative system operating in the aeronautical L-band [PW03], i.e., in the 960–1164 MHz band. In this frequency band, several systems currently support A2A data communications. The traffic alert and collision avoidance system (TCAS) uses the 1030 MHz and 1090 MHz frequencies to transmit interrogation squitters and replies, respectively, for collision avoidance with other aircraft. In addition, the 1090 extended squitter (1090ES) [RTC09] allows equipped aircraft and airport vehicles to broadcast their automatic dependent surveillance – broadcast (ADS–B) positional information at 1090 MHz. Moreover, the

universal access transceiver (UAT) [Int09] supports the transmission of ADS–B reports and related surveillance services at 978 MHz. Unfortunately, none of these systems is expected to support all services defined in [ER07] under the minimum performance requirements. While 1090ES and UAT systems support broadcast transmissions of ADS–B reports, which are the basis of most A2A services defined in [ER07], UAT is only operated in the US at altitudes below 18 000 feet and 1090ES was not expected to meet the minimum required update rate of ADS–B by as early as 2020, according to [WM15]. In addition, the shared usage of the 1090 MHz frequency for the transmission of ADS–B reports and of interrogation replies from both TCAS and secondary surveillance radar systems is expected to lead to a significant degradation of the performance of these systems in airspaces with a high traffic density due to the contention-based multiple access scheme [WM15]. Consequently, a new A2A data link capable of supporting the new services and operational concepts for the modernization of the ATM is required. This is proposed to be achieved by further developing LDACS, originally an air-ground (A/G) communications system, to also support direct A2A communications via the so-called LDACS A2A data link. LDACS A2A will not only support the applications requiring direct A2A communications, but it will also be able to effectively extend the LDACS A/G coverage, currently limited to continental airspace, towards ORP regions where ground infrastructure cannot be deployed. In this thesis, we address the challenges related to the development of an A2A data link and propose a design for LDACS A2A.

The propagation channel can be considered the basic building block in the design of communication systems. Only an extensive knowledge of the channel allows an optimal and reliable design of the data link, more specifically of the physical layer on which the communications system is built. However, a literature review revealed a significant research gap on the A2A propagation channel. The few A2A channel measurements did not shed much light on the channel statistics and generally only focused on very specific scenarios, which could hardly be considered as the most challenging ones. The few models proposed have been mainly theoretical and ignore many of the peculiarities of the aeronautical channel, not being able to represent it faithfully. Therefore, this thesis focuses on investigating the A2A propagation channel. First, A2A channel measurements are analyzed thoroughly to extract the channel characteristics in different scenarios and considering numerous geometries and antenna positions, allowing us to parameterize the different channel effects and to represent them accurately. Having observed in the measurements the peculiar distribution of the channel scattering components over the delay/Doppler frequency plane, a theoretical geometry-based technique to recreate the scattering components is developed and later validated with

A2A measurements in several scenarios. Then, we propose an A2A geometry-based stochastic channel model by combining the statistics of the A2A channel measured in the first step with the theoretical, geometry-based characterization of the channel proposed and validated in the second step.

The proposed A2A geometry-based stochastic channel model is used to design the physical layer of LDACS A2A. For this, we firstly collect the communication performance requirements for LDACS A2A and the boundary conditions that it must fulfill, including its backwards compatibility with the current LDACS specification. Then, different alternatives for the design of the physical layer of LDACS A2A are investigated and its optimal design is determined through simulations using the proposed A2A channel model. Among others, we assess the performance of cyclic prefix (CP)-orthogonal frequency-division multiplexing (OFDM) and different forward error correction (FEC) coding schemes, including low-density parity-check (LDPC) and polar codes used in 5G communications, in A2A channels.

The contributions of this thesis are structured thematically in different chapters. In Chapter 2, the past and future air traffic is analyzed using both radar-correlated data and simulated future air traffic based on forecasts. This is followed by a comprehensive review on the systems currently used for ATM communications and on the ones planned to be used in the future, including the main challenges and how they are being addressed. Chapter 3 is dedicated to the A2A propagation channel. First, the fundamentals of the propagation channel are summarized and the relevant literature is outlined. Second, given the observed lack of in-depth analyses on the A2A channel in the literature, the A2A channel is analyzed thoroughly using available channel measurements. Then, a novel technique to model the channel scattering is developed and verified with measurements in multiple scenarios. The chapter concludes with the proposal and verification of a general geometry-based stochastic A2A channel model that can be used for the optimal design of new A2A radio links. Chapter 4 addresses the design of the LDACS A2A data link. The performance requirements and the boundary conditions for the operation of the LDACS A2A are initially discussed. Then, after investigating multiple options for the design of the LDACS A2A considering the characteristics of the L-band and using the A2A channel model presented in Chapter 3, an optimum physical-layer design for LDACS A2A is proposed. The conclusions of this thesis are presented in Chapter 5, together with an outline of future areas of research.

Chapter 2

Current Status in Aeronautical Communications

This chapter discusses the aeronautical communication systems currently in use, or planned, for aviation, as well as the air traffic experienced in the past and expected for the future. Past and future air traffic is analyzed on the basis of historical radar-correlated data and simulated future air traffic based on growth forecasts. This is complemented by a discussion of the communication systems currently used in aviation for ATM communications, including those still in the process of deployment or standardization.

2.1 Air Traffic

It is well known that the air traffic is growing all over the world and that, even after massive disruptions such as the one caused by the COVID-19 pandemic, the air traffic recovers very quickly and reaches pre-disruption values promptly. However, it is worth asking exactly what figures we are talking about and how many aircraft can be expected per day in each region. This air traffic information is essential for sizing the systems used for ATM. For example, for the design of an A2A communications system, it is critical to know how many aircraft can be found within the communications range of a single aircraft. Therefore, we analyze various databases to quantify the air traffic, both experienced in the past and expected for the future. We additionally distinguish between the continental airspace and the oceanic one, focusing on Europe to characterize the former and on the North Atlantic Corridor (NAC) for the latter. Some of the contents of this section are published by the author in [BMS19].

2.1.1 European Continental Airspace

First, we use radar-correlated flight data[1] containing the position of the aircraft flying over Germany during a day (July 30, 2015). As depicted in Fig. 2.1, the number of flights fluctuates over the day, reaching a peak of 567 aircraft active simultaneously. Few or no aircraft operate at night due to night flight restrictions.

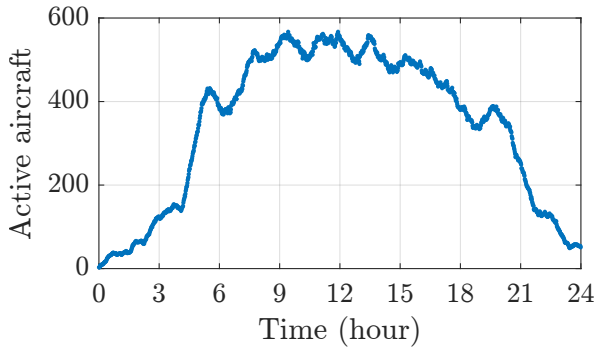

Figure 2.1. Number of active aircraft within Germany according to the 2015 radar-correlated flight data.

Over the entire day, we compute the highest number of active aircraft within a certain range from any other aircraft. Given that the communications range desired for an A2A data link depends on the application, four communication ranges usually discussed in the literature are considered: 90, 120, 150, and 200 nautical miles (nmi). The results can be seen in Fig. 2.2. As expected, the number of *reachable* aircraft increases with the considered range, saturating at the peak of 567 aircraft active simultaneously over Germany that day. In any case, the results show that an aircraft might have several hundred other aircraft within communications range, which will have to be taken into account in the design of the A2A data link, especially for the medium access control (MAC) protocol.

Given that the main objective of developing a new A2A data link is to sustain the continuous air traffic growth, it is essential to analyze the air traffic that the A2A data link will have to support in the future. Thus, we use the FACTS2 simulator described in [Grä16], which reproduces the future European air traffic by using Poisson processes to model the probability distribution of flights between airports and by adjusting the models based on real flight plans and on the predicted air traffic growth. The FACTS2 simulator is used to generate a realization of the European air traffic on a busy summer

[1]Data were provided by the German air navigation service provider, the Deutsche Flugsicherung (DFS).

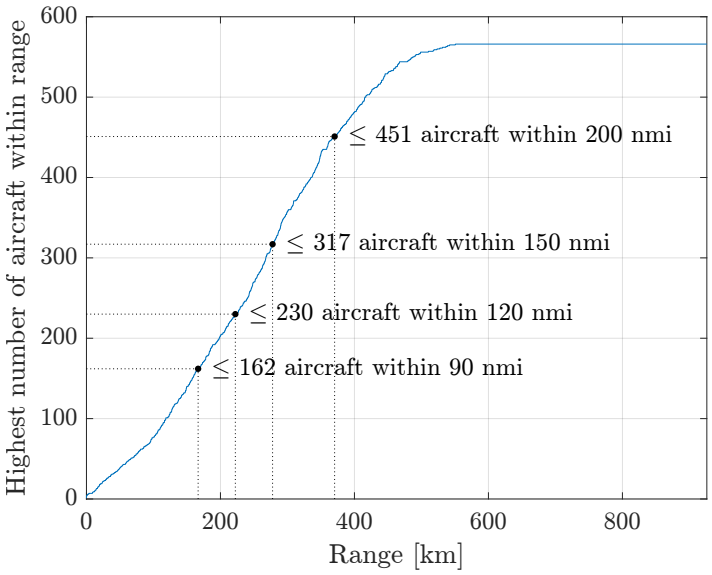

Figure 2.2. Highest number of aircraft within a certain range in the 2015 radar-correlated flight data (Germany).

day of 2035[2], with up to almost 49 000 flights taking place during the day [Grä17a]. The number of active aircraft, shown in Fig. 2.3, fluctuates strongly and reaches a maximum of 8161 active aircraft shortly after 14:00.

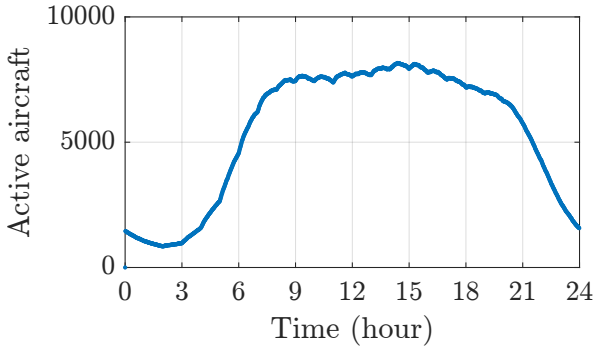

Figure 2.3. Number of active aircraft in the realization of air traffic for one summer day in 2035 using the FACTS2 simulator. Adapted from [BMS19]. © 2019 IEEE.

The number of aircraft that can be reached by another aircraft increases almost linearly with the assumed communications range, as shown in the results for this scenario in Fig. 2.4. In this case, we also show the number of aircraft within a range of 500 nmi, i.e., 4342 aircraft. This value is important, as 500 nmi is a good approximation to the radio line-of-sight (LoS) distance between two aircraft flying at a high altitude, i.e., the distance from which the radio waves are blocked by the Earth because of its curvature.

[2]The scenario A of the FACTS2 simulator is considered, as it was shown to reproduce the actual air traffic growth much more accurately than the other scenarios [Grä17b].

Thus, the results show that, even if we design the system to support the 1604 aircraft that can be found within a communications range of 200 nmi, one also has to account for the 2738 aircraft that are within radio LoS but beyond the communications range of the system, in order to avoid harmful interference between the aircraft.

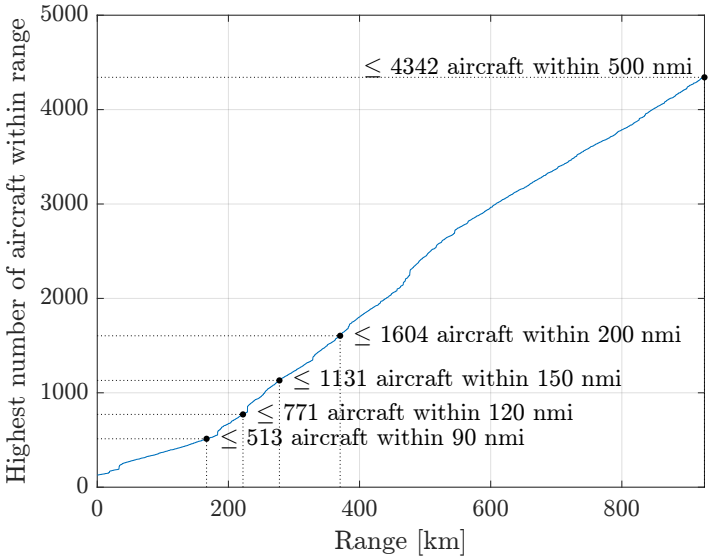

Figure 2.4. Highest number of aircraft within a certain range in the flight data recreated for 2035 by the FACTS2 simulator.

To help visualizing the results, Fig. 2.5 depicts a snapshot of the aircraft positions at the time instant when the maximum number of aircraft were found within a range of 120 nmi from another aircraft. One can see that the air traffic is distributed very heterogeneously over Europe, with a very dense air traffic in the central part of Europe (around the Netherlands and the west of Germany) and a very sparse one in other parts of the continent.

2.1.2 Oceanic Airspace: North Atlantic Corridor

For the oceanic airspace, the focus is set on the North Atlantic region, where aircraft fly between Europe and North America around the clock. Establishing an ad hoc network between the aircraft in the North Atlantic region is one of the main use cases for the A2A data link. Such a network would allow aircraft to operate autonomously and to communicate with any other aircraft of the network, even if it is beyond its direct communications range, by using intermediate aircraft as relays. Of course, the aircraft in the aeronautical network that also have a direct communication link with the ground infrastructure can act as gateways to relay messages between the ground infrastructure and the aeronautical network, making all aircraft within the network also reachable by

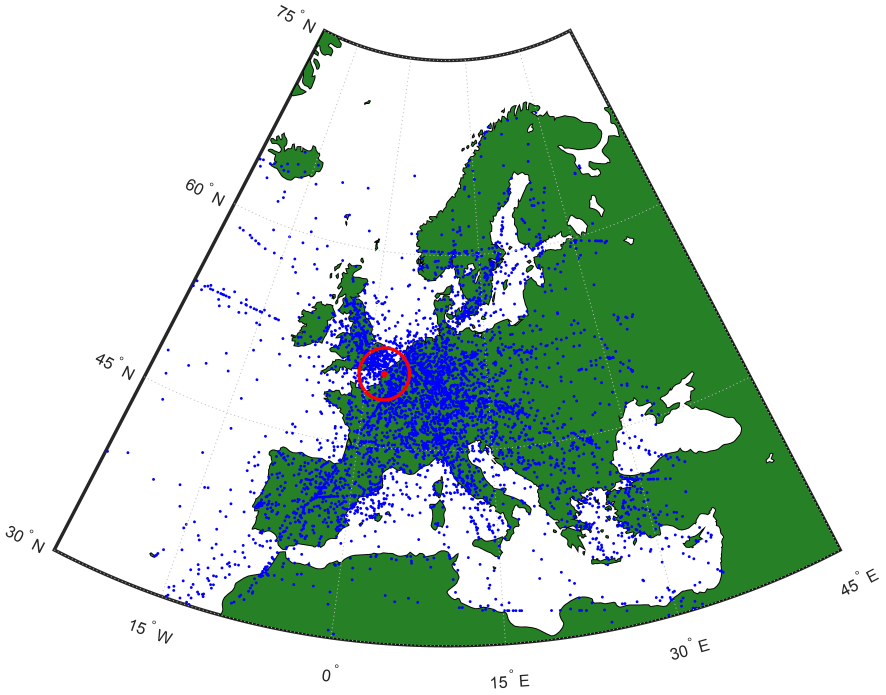

Figure 2.5. Snapshot of the aircraft positions (blue dots) at the time instant of the FACTS2 simulation when the maximum number of aircraft were observed within a radius of 120 nmi. The red dot represents the central aircraft seeing the maximum number of aircraft, i.e., 771, within the 120 nmi radius depicted with the red circle. From [BMS19].

the ground ATM entities, e.g., the air traffic controllers. An analysis of the air traffic in the North Atlantic region was conducted in [Med+08]. The authors analyzed the airline flight schedule database from the International Air Transport Association (IATA). The number of aircraft present in the North Atlantic region over the course of a day is shown in Fig. 2.6. One can see the cyclic behaviour of the air traffic in the North Atlantic region, with two segments corresponding to the westbound and eastbound flights. There are significantly fewer aircraft than in the continental airspace, ranging from around 45 aircraft to a peak of 280.

More recent analyses were conducted to assess the minimum communications range that would be required in the North Atlantic region to enable air-ground connectivity through A2A hops. The authors in [MHL23] investigated the relation between the communications range and multiple factors related to it, including the ground connectivity through A2A hops, the number of hops to the ground, and the ratio of aircraft equipped with the A2A data link. Given that this is a multi-variable problem, and that a higher communications range leads to a higher aircraft connectivity and fewer required hops, no conclusive range is given. However, they indicate that at least 225 km

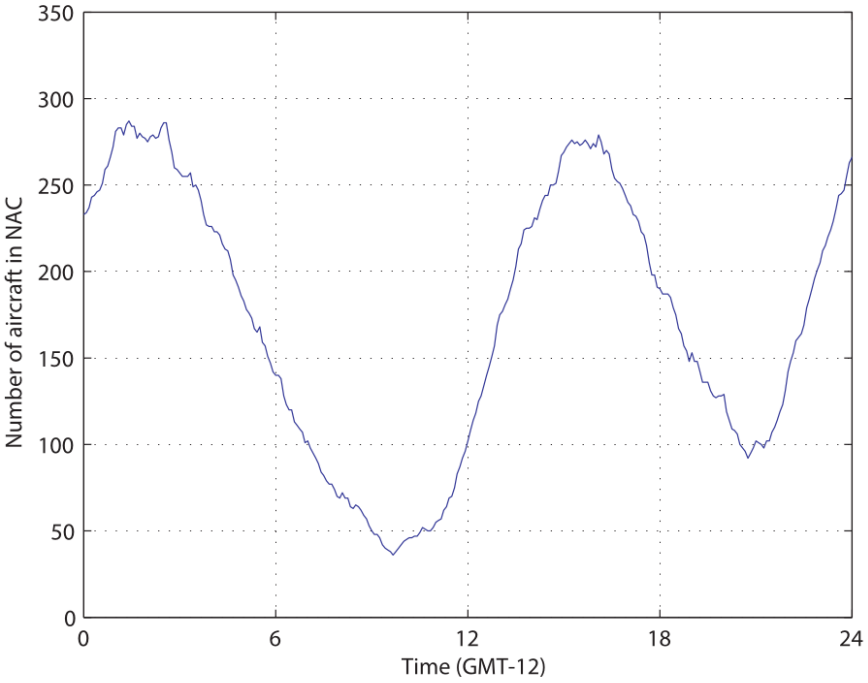

Figure 2.6. Number of aircraft in the North Atlantic region during a day. From [Med+08].

(121.49 nmi) or 300 km (161.99 nmi) would be required to achieve an aircraft connectivity of 80% or 90%, respectively, in the North Atlantic region. Achieving a higher connectivity might be inefficient, as for example increasing it up to 95% would require a range of over 400 km (215.98 nmi). It is to be noted that, as the air traffic grows, the number of aircraft in the ORP regions will increase, which will lead to a higher connectivity. The authors in [HMG22] indicate that a range of over 135 nmi is required for sufficient coverage and for avoiding high data rate peaks.

2.2 Aeronautical Communication Systems

Once analyzed the past and future air traffic, we dive into the communication systems that enable it. There are numerous communication, navigation, and surveillance (CNS) systems used in aviation, but we focus on those with communication capabilities. One can distinguish between satellite-based, also commonly denoted as space-based, and terrestrial systems. The latter have been the preferred choice for ATM communications when available, i.e., in continental airspace, and the use of satellite-based systems has been mainly limited to ORP regions, i.e., regions without ground infrastructure. For the purposes of this work, the terrestrial links are additionally divided into air-ground

and air-air links. Some of the contents of this section have been published by the author in [BM18; BMGS19; BM+22].

2.2.1 Satellite-Based Links

Two main types of satellite constellations are used or envisaged for ATM: geostationary and low earth orbit (LEO).

Inmarsat is the main geostationary constellation providing voice and data communications for ATM purposes. The great advantage of geostationary satellite-based links over terrestrial links or lower-orbit satellite-based links is their high altitude, which allows them to provide a vast coverage using few satellites and to support communications in regions without ground infrastructure. The altitude, however, also leads to a very high minimum communications delay caused alone by the propagation. At an orbit of roughly 35 786 km, a one-way communication between an aircraft and the ground through one of these satellites would present a minimum delay of 0.24 s. Another disadvantage is the huge effort needed to put the satellite into orbit, which makes building the constellation significantly more expensive than building ground stations or using LEO satellites, as well as more difficult to replace in case a satellite malfunctions. For these reasons, the use of satellite-based data links has been mainly limited to ORP regions where no terrestrial deployments are possible, such as in the NAC.

At a much lower altitude, the **LEO constellation** of satellites operated by **Iridium** also provides services for the ATM with its 66 satellites currently active at an orbit of roughly 780 km above the Earth's surface. In order to cover regions as vast as the ones covered by the geostationary constellations, significantly more satellites are required. However, these satellites are significantly smaller, less expensive and easier to put in orbit compared to the geostationary ones. Their low altitude yields a minimum one-way propagation delay roughly 50 times lower than the one for geostationary satellites, e.g., 5.2 ms for the Iridium satellites compared to 0.24 s for the geostationary ones. This makes LEO constellations a better option to support the stringent quality-of-service (QoS) requirements of many delay-critical applications. Of course, the processing delay increases the real latency by at least some tens of milliseconds, but that would still be significantly lower than the physical propagation delay of the geostationary networks, which are on top also affected by the processing delay.

LEO satellites have gained significant attention in the last years with the deployment of massive constellations of satellites by companies like Starlink and OneWeb, with the former planning to deploy 42 000 satellites to cover the entire Earth's surface. Such massive constellations promise to support stable communications with a low delay and very high data throughput thanks to the massive number of satellites,

their low altitude, e.g., 550 km for most Starlink satellites, and the use of modern communication techniques, such as multiple-input/multiple-output (MIMO). As an example, Starlink claims upload and download speeds of 2–25 Mbps and 5–220 Mbps, respectively, depending on the service plan. These networks already support communications for aircraft, but so far are mainly limited to non-critical communications, such as passenger entertainment services. Using them for ATM communications would be very advantageous in regions without ground infrastructure, but it must be clarified yet whether they can support the much stricter requirements, e.g., availability, required for ATM compared to the current mainstream use. As an example, Starlink claims an availability of at least 99%, while safety-critical ATM communications require at least 99.999%. It is also unclear if such networks can cope well with aircraft maneuvers affecting the communications link. For example, we show in Section 3.2 that the banking of the aircraft leads to a significant decrease in the signal power because of the reduction of the antenna gain, the cross-polarization losses, and the blockage caused by the aircraft fuselage. The lower distances considered for terrestrial networks generally lead to a larger margin in the link power budget, and thus to less disturbances caused by the banking turns, but the use of smart antennas by the LEO satellites and their large numbers might tip the balance in their favour.

2.2.2 Air-Ground Links

Historically, ATM communications were supported by air-ground analog links, including **HF voice communications** still used in some ORP regions thanks to the long range achievable through tropospheric ducting. Following the worldwide trend, analog communications were slowly replaced by more modern digital communications to efficiently support the transmission of data and to achieve a higher degree of automation in ATM. The first significant step was the development of the family of VDL systems. **VDL mode 0/A** was the first link of this family, providing air-ground data communication capabilities at a comparatively low rate. It was quickly updated to the more capable **VDL-m2**, which employs differential 8-ary phase-shift keying (PSK) modulation with a rate of 31.5 kbps [Int01]. The user data throughput lies significantly below this value in practice, as the overhead data for synchronization and redundancy also need to be considered. Also, this could only be reached if a perfect channel access is achieved. However, this is not the case as the contention-based carrier-sense multiple access (CSMA) technique employed by VDL-m2 to share the channel between multiple users reduces the achievable data rate considerably, saturating at approximately 40% channel utilization [Roy15]. VDL-m2 is deployed widely and used in many regions of the world. In some regions, the modest data rate of VDL-m2 proved insufficient to

fulfill the ATM requirements as the air traffic increased, which was compensated by using more frequency channels with 25 kHz bandwidth each. This solution is, however, leading to the saturation of the VHF band in some regions of the world, especially in central Europe [Int18a; EUR21]. An initial screening of the FAA and Eurocontrol concluded that no system operating at the time (2007) could satisfy all ATM requirements [EUR07], which triggered worldwide research into the modernization of the ATM infrastructure including the introduction of new operational concepts and services as well as the development of new CNS technologies to support them. The communication systems shall act complementary to each other in order to support ATM communications throughout all phases of flight, as well as to add a certain degree of redundancy to increase availability. Together, these systems conform the so-called FCI.

One piece of the FCI is the **aeronautical mobile airport communications system (AeroMACS)** [RTC14], which supports data communications in the airport and terminal maneuvering area. Thus, it enables ATS and AOC communications between the aircraft and the ground entities, e.g., the control tower, required prior to departure and after landing. It is based on the IEEE 802.16 WiMAX technology and operates in the aviation C-band from 5091 MHz to 5150 MHz [Kam18]. A well-established system and part of the ICAO's Global Air Navigation Plan (GANP) [Int19], AeroMACS is already deployed in more than 40 airports worldwide and is also commonly used to connect the airport infrastructure.

The communications system currently supporting ATS and AOC air-ground communications in continental airspace is VDL-m2. However, because of the saturation of the VHF band used by VDL-m2 and its inability to further support the air traffic growth in some parts of the world, the World Radiocommunication Conference (WRC) allocated the frequencies 960–1164 MHz in the L-band for the operation of aeronautical mobile (route) service (AM(R)S) systems [Int07]. Following this allocation, **LDACS** was developed as the air-ground segment of the FCI to provide air-ground ATS and AOC communications with a much higher data rate than the currently available alternative, VDL-m2. Thus, LDACS is expected to be able to support all applications currently supported by VDL-m2, in addition to new applications and operational concepts required for the ATM modernization. LDACS was designed to circumvent the main shortcomings of VDL-m2, which are known to be its low user data rate and its lack of QoS support and data traffic prioritization. We compare the main specifications of LDACS and VDL-m2 in Table 2.1. The operation of LDACS in the aeronautical L-band allows it to use a much higher bandwidth of roughly 500 kHz per channel compared to the 25 kHz used by VDL-m2. Moreover, LDACS uses a contention-free channel access scheme. First, LDACS follows a cellular deployment with different GSs deployed to

Table 2.1. Comparison between LDACS and VDL-m2 technologies. Adapted from [BM+22]. © 2022 IEEE.

	LDACS [Grä+19]	**VDL-m2** [Int01]
Frequency band	960–1164 MHz	117.975–137 MHz
Channel bandwidth	495.05 kHz (FL) + 495.05 kHz (RL)	25 kHz
Channel access	Contention-free	Contention-based CSMA
Maximum data throughput	2818.7 kbps	$<$ 31.5 kbps
QoS with traffic prioritization	Yes	No
Operation	Full duplex	Half duplex
Status	In standardization [Int18b]	Operational

cover different air volumes, called cells. Each cell employs a pair of frequency channels; one for ground-to-air communications, i.e., forward link (FL), and one for air-to-ground communications, i.e., reverse link (RL). This way, LDACS moves from the half-duplex operation of VDL-m2 to a frequency-division full-duplex operation, enabling the controlling GS and the controlled airborne stations (ASs) to transmit simultaneously. The use of a much higher bandwidth with full-duplex operation and the modern OFDM technology allow LDACS to achieve user data rates from 610.4 kbps up to 2818.7 kbps (for a pair of FL and RL channels), adapting to the channel conditions, while VDL-m2 reaches in reality less than 31.5 kbps as discussed before. Given that VDL-m2 employs no data prioritization mechanism, higher volume AOC data traffic, i.e., the low-priority business communications of the airliners, can starve out safety-related, high-priority ATS data traffic. This was addressed by LDACS by implementing different QoS levels and data prioritization mechanisms, which effectively prioritize ATS over AOC data traffic. All these characteristics, including the full-duplex operation and the data prioritization, reduce the communications latency significantly.

The main disadvantage of LDACS compared to VDL-m2 is its current status. While VDL-m2 is widely deployed, LDACS is being currently standardized by the ICAO. In order to test and measure the in-flight LDACS capabilities under real operating conditions, the author conducted in 2019 the first worldwide LDACS flight campaign. The results of the campaign were published in [BM+22]. The flight experiments were conducted using an LDACS AS installed in a Dassault Falcon 20E aircraft and four

LDACS GSs deployed in different locations in the south of Germany (see Fig. 2.7). Two GSs were fully operational and communicated with the AS bidirectionally using the full LDACS capabilities. The other two GSs were only capable of transmitting but enabled the AS to estimate its position using the LDACS signals from the four GSs. Among others, the measurements showed that LDACS can effectively prioritize ATS over AOC data traffic. High-priority messages transmitted in the RL, i.e., from the aircraft, experienced an end-to-end delay lower than 80 ms and 240 ms in 50% and 95% of the cases, respectively. This can be seen in Fig. 2.8, where we show the end-to-end message latency during one of the experiments. The measured latency is significantly lower than the latency that could be achieved using geostationary satellite communications, given that the propagation delay alone is already 240 ms, with the processing delay increasing the total latency of the geostationary link significantly above that. The measured latency is, however, comparable to the nominal advertised by Starlink, i.e., < 99 ms in the *mobile* service plan, which makes clear that LEO satellite networks represent a strong competitor to terrestrial communications such as the ones offered by LDACS. Importantly for this work, the LDACS campaign also showed the critical role of the ground reflection in the performance of the system, as multiple link outages were experienced as the AS approached or flew away from the GS. These link outages were highly correlated with signal power drops, which were presumably caused by the ground reflection [BM+22].

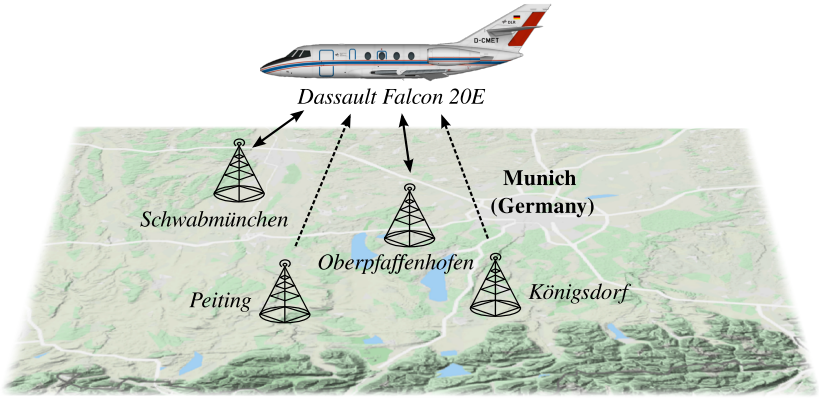

Figure 2.7. LDACS flight trials using four LDACS ground stations deployed in southern Germany and one LDACS airborne station carried by a Dassault Falcon 20E aircraft. From [BM+22].

The main challenge slowing down the standardization of LDACS is its operation in the aeronautical L-band. LDACS can only operate in this band if it does not cause any harmful interference in the operation of the legacy systems operating there, especially to the aeronautical radio navigation services (ARNSs) [Int07]. This is very challenging,

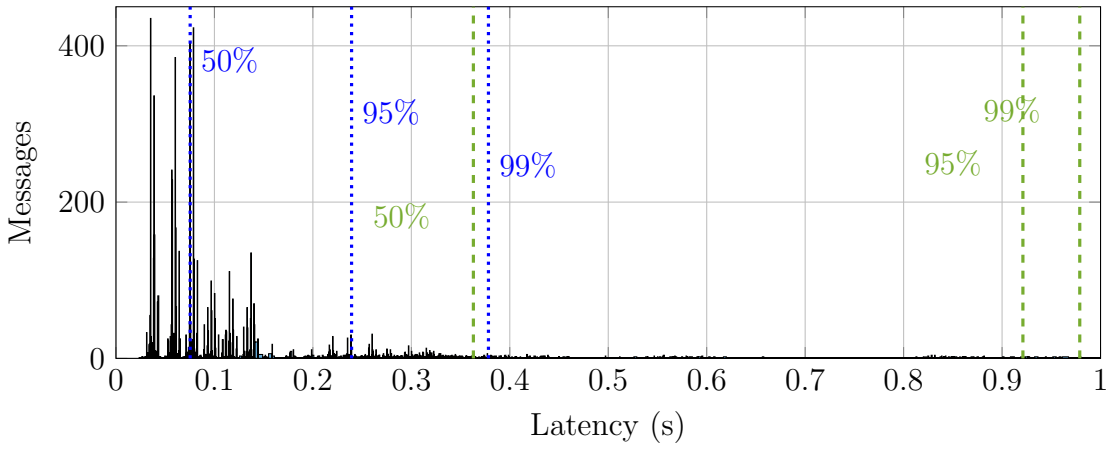

Figure 2.8. Histogram of the latency of 7837 application messages transmitted by the LDACS AS in flight in one of the scenarios analyzed in [BM+22]. The lines depict the 50th, 95th, and 99th latency percentiles of the small ATS messages of 290±10 bytes (blue dotted lines, 85.2% of the messages) and of the big AOC messages of 1800±10 bytes (green dashed lines, 13.6% of the messages). From [BM+22].

as the L-band is populated by numerous systems, some of which operate throughout the band. Thus, compatibility criteria must be defined for each one of these systems, which require to conduct compatibility analysis and measurements to identify under which conditions the operation of LDACS does not disturb the operation of the other system. The systems operating within the aeronautical L-band (960–1164 MHz), or adjacent to it, are shown in Fig. 2.9. At frequencies immediately below the L-band we find commercial mobile technologies. On the upper side of the L-band starts the operation of the global navigation satellite system (GNSS) systems. One of the systems using most of the aeronautical L-band is the distance measuring equipment (DME), used by the aircraft to estimate its slant range to a ground station. The DME airborne station, or interrogator, sends an interrogation at a certain frequency channel, which is replied to by the DME ground station, or transponder, at a frequency 63 MHz apart. The slant range is estimated by measuring the delay between the interrogation and the reply. The DME frequency channels have a bandwidth of roughly 1 MHz and are located at a 1-MHz grid spanning most of the L-band and even going beyond 1164 MHz to share some frequencies with the GNSS systems. DME is mainly used by civil aviation, but there is an equivalent system used by the military and named the tactical air navigation system (TACAN). We do not make any distinction between DME and TACAN hereinafter and refer to both as DME. One can see in Fig. 2.9 that practically the entire frequency range allocated for LDACS, i.e., 964–1010 MHz for the RL and 1110–1156 MHz for the FL, overlaps with the spectrum used by DME. Thus, the design

of LDACS and the main efforts for its development have been focused on guaranteeing spectral compatibility with DME. Among others, the LDACS channel bandwidth of roughly 500 kHz is intended to enable an in-lay operation between the DME frequencies. Moreover, a methodology was proposed in [MBMG18] to conduct a DME-compliant LDACS frequency planning, which we extended later in [BMS21]. Comparatively, DME uses the allocated spectrum very inefficiently, as pulses are transmitted very sporadically and the duty cycle is very low. This can be seen in Fig. 2.10, which depicts a spectrogram measured at the aircraft during the flight campaign [BM+22]. The continuous transmissions from the LDACS GSs can be seen at 992.5, 994, 1000, and 1001.5 MHz. The pulsed transmissions from DME transponders can be seen at 993, 997, and 999 MHz. Although it becomes clear that DME uses the spectrum inefficiently, this can be understood given that making an efficient use of the spectrum became a priority long after DME was developed.

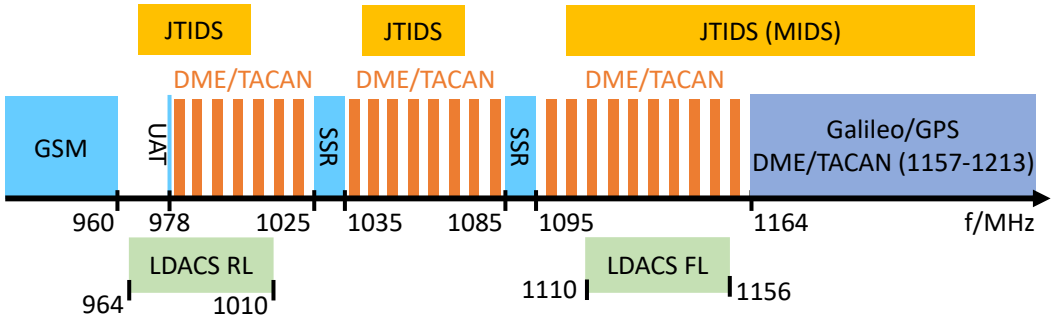

Figure 2.9. Systems operating in the aeronautical L-band.

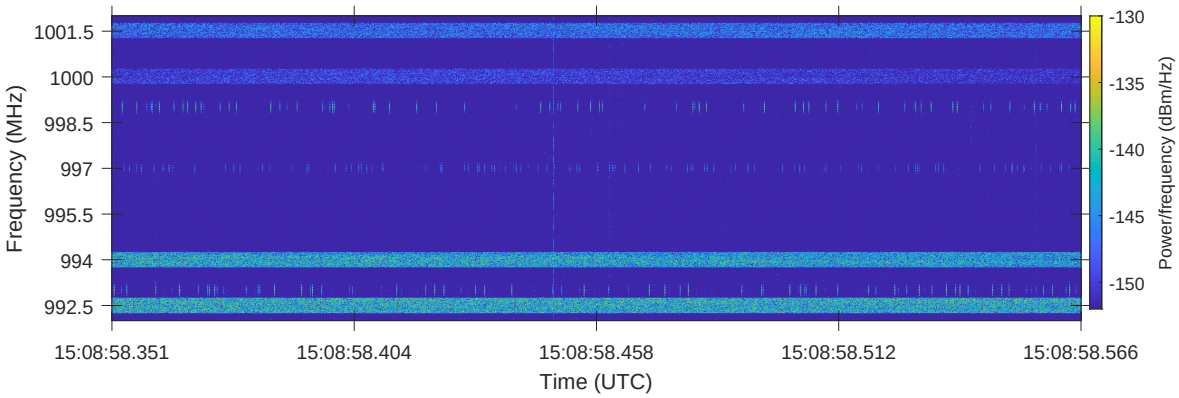

Figure 2.10. Spectrogram measured by the LDACS AS on 2 April 2019 in the experimental FL band used in the campaign. From [BM+22].

2.2.3 Air-Air Links

The focus is placed now on the direct A2A radio communication links used in aviation. These systems can operate in an ad hoc manner and are commonly used not only for A2A communications but also for air-ground and even ground-ground communications.

Direct A2A communications are possible on the VHF **CTAF**, but these transmissions are limited to voice analog communications and no data exchange is supported. Another standardized system supporting A2A communications and operating in the VHF band is **VDL-m4** [Int04]. It supports the exchange of addressed and broadcast data not only between aircraft but also between airport vehicles and fixed stations. Unfortunately, VDL-m4 has only been implemented in Europe on a regional basis [WM15] and, in addition, Airbus reported on-board co-site interference issues with other VHF radios and recommended the use of the L-band for any new A2A link [PW03].

In the L-band, several systems already support A2A communications, but they are mainly used for surveillance purposes because of their limited capabilities. **TCAS** uses the frequencies 1030 MHz and 1090 MHz to transmit interrogations and replies, respectively, for collision avoidance with other aircraft. In addition, the **1090ES** [RTC09] allows equipped aircraft and airport vehicles to transmit ADS–B messages, containing identification and positional information for situational awareness, using the 1090 MHz frequency. **UAT** [Int09] is also used to transmit ADS–B messages to enhance situational awareness, but it is only operated in the US at altitudes below 18 000 feet.

There is another system operating in the L-band and capable of supporting A2A data and voice communications. It is the **Link 16**, implemented via **joint tactical information distribution system (JTIDS)** or **multifunctional information distribution system (MIDS)**, a classified system used by the military to support ad hoc communications. Given that it is a military system, it would not be usable for the civil aviation and therefore we do not discuss its capabilities here. However, although it is a classified system, some of its characteristics can be found in [BMGS19], where we conducted an impact assessment of LDACS on JTIDS by building baseband models of both systems using publicly available information.

The extensive ATM modernization being carried out under SESAR [Ses] and NextGen [Nex] frameworks includes a series of services and operational concepts that require the availability of an A2A data link. This A2A data link shall be able to support the services defined in [ER07], which involve addressed, multicast, and broadcast data and voice communications. Unfortunately, none of the above-mentioned A2A systems are expected to support all services defined in [ER07] under the minimum performance requirements, given that they are mainly designed for surveillance and their actual data communication capabilities are too limited. In fact, a report from the NASA

[WM15] already identified that the 1090 MHz frequency was reaching saturation and that 1090ES was not expected to meet the minimum required update rate of ADS–B by as early as 2020. The congestion of the 1090 MHz frequency would not only affect the ADS–B performance, but other systems such as TCAS and the secondary surveillance radar (SSR) might experience a significant degradation of their performance in airspaces with a high traffic density [WM15]. Although the COVID-19 pandemic alleviated this congestion, the rapid air traffic growth experienced since then might have only postponed the saturation of the 1090 MHz frequency for some years. Consequently, a new data link capable of supporting A2A data and voice communications for the services defined in [ER07] is expected to be required in the near-to-mid future.

The new A2A data link should operate in the aeronautical L-band within 960–1164 MHz. The VHF band is already congested and the interference issues from VDL-m4 led Airbus to recommend the use of the L-band instead [PW03]. A higher frequency band, such as the C-band, would prevent the A2A link from reaching the long communication ranges required in the oceanic airspace because of the larger propagation path losses compared to the L-band. Introducing a new system in the L-band is challenging because of the operation of DME. The long standardization process of LDACS as the new system being introduced in the L-band shows how difficult this is. Thus, instead of starting from scratch with a new A2A system, it has been decided to develop the new A2A data link as an extension of the current LDACS A/G specification, and consequently has been named **LDACS A2A**.

The main objective of LDACS A2A is to enable the services and operational concepts defined for the ATM modernization by supporting efficient broadcasting of surveillance information, such as positional information, trajectory, and identification, as well as point-to-point A2A communications. In addition, LDACS A2A will be used to extend the coverage of LDACS to regions without ground infrastructure. This way, the same applications and services supported by LDACS in the continental airspace will still be supported when the aircraft enter ORP domains and loss connection with any ground infrastructure. For this, the A2A link will be used to create an ad hoc network, which will connect to the LDACS A/G network using intermediate aircraft to relay messages within and between the networks. This will enable end-to-end communications between any station within the LDACS network, even if they are not within direct communications range.

The initial steps in the design of the LDACS A2A revealed a lack of information about the A2A propagation channel in the literature, preventing a realistic and optimal design of the physical layer of the LDACS A2A link. In order to fill the gap found in the literature and to shed some light on the characteristics of the A2A channel, as

well as to enable the design of the LDACS A2A link, the A2A propagation channel is investigated in the next chapter.

Chapter 3

A2A Propagation Channel

This chapter delves into the intricacies of the radio A2A propagation channel. Section 3.1 explores its fundamental characteristics and the primary effects that shape its behaviour, also discussing the previous work on this topic and the novelty of the contributions of this thesis. In Section 3.2, A2A channel measurements are analyzed to estimate the most relevant statistics of the channel components. Section 3.3 presents a novel theoretical model to compute any mobile-to-mobile (M2M) channel analytically. The model is then validated with measurements in multiple A2A scenarios. Finally, an A2A geometry-based stochastic channel model (GBSCM) is proposed in Section 3.4. The A2A GBSCM combines the geometry-based characterization of the channel proposed and validated in Section 3.3, with the stochastic properties of its main components derived in Section 3.2.

3.1 Channel Fundamentals

3.1.1 Overview

Radio communication plays a major role in modern telecommunications, enabling wireless connectivity for a myriad of uses ranging from cellular networks to vehicular CNS applications. At the heart of wireless communications lies the radio propagation channel, a dynamic medium through which electromagnetic waves propagate from transmitter to receiver. In reality, the electromagnetic field generated by the transmitter antenna propagates in all possible directions of space following the Maxwell equations[1].

[1]For simplicity, we do not discuss the complex behaviour of the electromagnetic field in the near field of the antenna, but focus on its much simpler plane-wave interpretation in the far field, which allows us to visualize the electromagnetic waves as rays.

While propagating through the channel, the radiated signal[2] is reflected, scattered, and/or diffracted by the objects (or particles) found in its propagation. As a consequence, the radiated signal propagates to the receiver following multiple propagation paths and the signal picked up by the receiver antenna is actually composed of multiple versions of the transmitted signal, each of which has traveled a different path and has been affected by the channel differently. Terming this effect as multi-path propagation, the different versions of the transmitted signal are called multi-path components (MPCs). Because of its relevance, one of these components stands out above the others: the LoS component. It propagates directly from transmitter to receiver through the shortest propagation path, i.e., the LoS path. This will not always be the *geometrically* shortest path, i.e., a straight line between the stations, given that the signals propagate in a bent path when the propagation medium presents a changing refractive index, e.g., in the troposphere. Although one usually uses the same parametrization for the LoS component and for the remaining MPCs, it is common in the literature not to term the LoS component as an MPC, and so we do hereinafter.

The MPCs are affected by many propagation effects.

When a signal hits a *smooth* surface, a part of it is reflected and other part enters the surface and experiences refraction, i.e., a change in its direction. These phenomena are described by the Snell's law. Focusing on the reflection, the Snell's law states that the angle of incidence, defining it as the angle between the impinging signal and the normal of the surface, equals the angle of reflection, defined as the angle between the reflected signal and the normal of the surface. Although we do not dive into the refraction in this work, it is worth mentioning that it causes the radio signals to not propagate in straight paths through the atmosphere, given that subtle changes in the media lead to the signal slightly changing its direction.

When the radio signal hits a *rough* surface, it is scattered in multiple directions. The *smoothness* or *roughness* of a surface is relative to the wavelength of the radio signal and its grazing angle, complementary of the incidence angle, compared to the surface irregularities. These relations are accounted for in the Rayleigh roughness criterion, which provides a useful indication of the roughness, or smoothness, of a surface. In reality, reflection and scattering are not exclusive, and the same surface reflects and scatters the impinging wave in different proportions. Generally, a surface is rougher for radio signals with lower frequencies (higher wavelengths) and lower grazing angles. As the frequency increases, reflection becomes more relevant at the expense of a less significant scattering, and vice versa. Some surfaces are more prone to either reflection

[2] As common in the field, we instinctively refer to the electromagnetic wave carrying the information as radio signal, or signal.

or scattering because of their shape. For example, a 1 GHz wave will be mainly reflected off a lake surface, i.e., calm water, but mostly scattered off vegetation, e.g., grass.

Another phenomenon affecting the radio signals propagating through the wireless channel is the diffraction. It occurs when the radio signal encounters an obstacle or aperture and is bent around its edges to reach the space behind it. Diffraction is considered to happen when the size of the obstacle or aperture is comparable to the wavelength of the signal.

When propagating through the channel, each MPC might be affected by multiple of these phenomena. Using the A2A channel as an example, the radio signal transmitted by an aircraft might be reflected off the Earth's surface, e.g., a lake, then be scattered by the vegetation covering a mountainside before finally reaching the receiver aircraft, where it can also be affected by diffraction caused by parts of its fuselage before reaching the receiver antenna. These so-called multi-bounce reflections are more common in other environments, such as the urban one, than in the A2A scenario. Thus, in this work, we focus on single-bounce reflections. To simplify our terminology, any object interacting with the MPCs, e.g., by causing a reflection, scattering, diffraction, etc, and thus composing the channel, is called an interacting object (IO).

After going through the channel and being affected by all these phenomena, the radio signal reaching the receiver can be significantly different to the one sent. To characterize these changes, we parameterize the MPCs using some well-known parameters: delay τ, complex amplitude α, and Doppler frequency shift f_d.

The delay τ of each MPC represents the time it takes from the transmission of the signal to the reception of the MPC. It is directly proportional to the distance covered by the MPC, i.e., the length of its propagation path. The relation between the delay and the distance is given by the speed of the electromagnetic wave in the medium. In the A2A channel, the medium between the aircraft is the air of the troposphere, and we can approximate the speed of the radio signal in this medium to its well-known speed in the vacuum, denoted as c_0. The LoS component, if present, has the lowest delay. Thus, it is common to define the delay of the MPCs relative to the LoS delay. To avoid ambiguities, we term this as the excess delay of the MPC.

The complex amplitude α of an MPC characterizes its amplitude and phase, both changing as the component propagates through the channel. Usually, the amplitude and phase of the MPC are relative to their values at transmission. Thus, α is generally used to model the attenuation and phase shift experienced by the MPC, as we do hereinafter. The signal's amplitude decreases according to the free-space path loss (FSPL) and its phase fluctuates depending on the distance traveled and the radio signal frequency. Both are additionally affected by the interaction of the signal with

an IO, following any of the phenomena discussed above. In the case of a reflection, the complex amplitude of the MPC changes according to the complex reflection coefficient of the IO. This coefficient depends on the electromagnetic properties of the object, its roughness, and the angle of incidence of the impinging wave.

The Doppler frequency shift f_d of the MPC represents its frequency shift, caused by the Doppler effect, with respect to the carrier frequency f_c. The Doppler frequency shift is intrinsically related to the rate of change of the delay over time and can actually be formally expressed as

$$f_\mathrm{d} = -\frac{\partial \tau}{\partial t} f_\mathrm{c} \tag{3.1}$$

for narrowband signals. The rate of change of the delay can also be expressed in terms of the velocity vectors of the transmitter, receiver, and the objects reflecting or scattering the wave. Thus, it is common to see closed-form expressions for the Doppler frequency for the most common cases, e.g., a two-dimensional scenario with a fixed station and a mobile one. We dive into the Doppler frequency in Section 3.3 and provide closed-form expressions of the Doppler frequency for the MPCs in a three-dimensional scenario with mobile stations.

3.1.2 System Representation of the Channel

The channel can be described as a linear system with an input (transmitted signal), an output (received signal), and a series of linear operations (the propagation channel). A channel remaining constant over time can be seen as a linear time-invariant (LTI) system. This does not happen in reality, as any movement of the transmitter, receiver, or IOs, or even a change in the electromagnetic properties of the IOs, will lead to an alteration of the channel. A time-variant channel is then described as a linear time-variant (LTV) system.

The most commonly used function to describe the channel is its weight function $h(t, \tau)$, defined from the input-output relationship of the system as

$$r_\mathrm{rx}(t) = \int_{-\infty}^{\infty} s_\mathrm{tx}(t-\tau) h(t,\tau)\, \mathrm{d}\tau\,, \tag{3.2}$$

where $s_\mathrm{tx}(t)$ represents the transmitted signal and $r_\mathrm{rx}(t)$ the received signal. In other words, the received signal is a convolution of the transmitted signal with the channel weight function, and the channel can then be seen as a linear filter. The channel can also be represented, or modeled, as the tapped delay line shown in Fig. 3.1. The output signal is composed of a sum of $L \to \infty$ delayed versions of the input signal, each version being affected by different channel coefficients. The general model shown in Fig. 3.1

is useful to later understand the consequences of the different assumptions made to simplify the channel model.

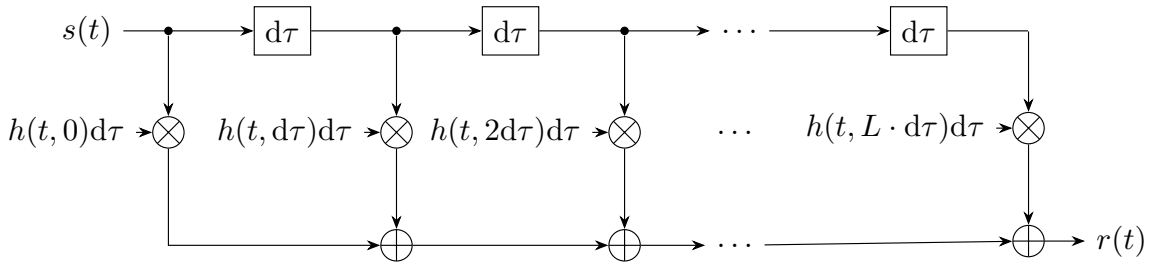

Figure 3.1. Tapped-delay-line representation of a time-variant channel in the equivalent complex baseband.

Importantly, the weight function (WF) depends on two variables: time t and delay τ. This already indicates that three other functions can be obtained from $h(t,\tau)$ as Fourier pairs. The first related function is the time-variant transfer function (TF) $H(t,f)$, obtained as the Fourier transform of $h(t,\tau)$ in the delay direction, i.e.,

$$H(t,f) = \int_{-\infty}^{\infty} h(t,\tau)\mathrm{e}^{-\mathrm{j}2\pi f\tau}\,\mathrm{d}\tau\,. \tag{3.3}$$

Another function that will be used often in this work is the Doppler-variant weight function given by

$$s(f_\mathrm{d},\tau) = \int_{-\infty}^{\infty} h(t,\tau)\mathrm{e}^{-\mathrm{j}2\pi f_\mathrm{d}t}\,\mathrm{d}t\,, \tag{3.4}$$

i.e., the Fourier transform of $h(t,\tau)$ in the time direction. This function is also commonly known as the delay/Doppler-spread function or spreading function, as it describes how the channel is spread over the Doppler/delay plane. We will see many examples of this function later in this chapter.

The remaining function is the Doppler-variant transfer function $T(f_\mathrm{d},f)$ and can be obtained as the Doppler transform of $s(f_\mathrm{d},\tau)$ with respect to τ, i.e.,

$$T(f_\mathrm{d},f) = \int_{-\infty}^{\infty} s(f_\mathrm{d},\tau)\mathrm{e}^{-\mathrm{j}2\pi f\tau}\,\mathrm{d}\tau\,. \tag{3.5}$$

Stochastic System Functions

In reality, the channel changes continuously and in different ways. These variations can be characterized statistically, giving rise to stochastic descriptions of the channel.

Delay-Doppler Probability Density Function. One could represent the stochastic system using the multidimensional probability density function (pdf) of the weight function. In this work, we focus on the time-variant joint delay Doppler pdf $p(t, \tau, f_\mathrm{d})$ and propose in Section 3.3 a methodology to compute analytically $p(t, \tau, f_\mathrm{d})$, as well as the marginal delay-dependent Doppler pdf $p(t, f_\mathrm{d}|\tau)$, and then validate it with measurements in multiple scenarios.

Autocorrelation Functions. In practice, most authors ignore the joint pdf because of its theoretical complexity and impossibility to measure it directly. Thus, the most commonly used statistical descriptions of the channel are based on the (ensemble) autocorrelation of the four system functions introduced before, i.e.,

$$r_\mathrm{hh}(t, t', \tau, \tau') = \mathbb{E}\{h^*(t, \tau)h(t', \tau')\}\,, \tag{3.6}$$

$$r_\mathrm{HH}(t, t', f, f') = \mathbb{E}\{H^*(t, f)H(t', f')\}\,, \tag{3.7}$$

$$r_\mathrm{ss}(f_\mathrm{d}, f_\mathrm{d}', \tau, \tau') = \mathbb{E}\{s^*(f_\mathrm{d}, \tau)s(f_\mathrm{d}', \tau')\}\,, \text{and} \tag{3.8}$$

$$r_\mathrm{TT}(f_\mathrm{d}, f_\mathrm{d}', f, f') = \mathbb{E}\{T^*(f_\mathrm{d}, f)T(f_\mathrm{d}', f')\}\,, \tag{3.9}$$

with $\mathbb{E}\{\cdot\}$ being the expectation operator, $(\cdot)^*$ the complex conjugate, and the autocorrelation function being defined as in [Pät02; Bel63].

If some assumptions are made, these four-dimensional functions can be simplified to two dimensions. The most common assumptions are the wide-sense stationary (WSS) and uncorrelated scattering (US) assumptions, which combined yield the popular wide-sense stationary uncorrelated scattering (WSSUS) model introduced by Bello in [Bel63].

Wide-Sense Stationary (WSS). The first assumption is to consider that the statistical properties of the channel do not change over time. A strict stationarity is, however, not required to simplify the channel description, but it suffices with assuming that the channel is WSS. Mathematically, the WSS assumption implies that the mean remains constant over time and that the autocorrelation functions do not depend on the absolute time but on the time difference, allowing us to simplify the autocorrelation functions to $r_\mathrm{hh}(t, t', \tau, \tau') = r_\mathrm{hh}(\Delta t, \tau, \tau')$ and $r_\mathrm{HH}(t, t', f, f') = r_\mathrm{HH}(\Delta t, f, f')$, where $\Delta t = t' - t$. It can be shown that the WSS assumption also implies that the MPCs with different frequency Doppler shifts experience uncorrelated fading [Mol11], such that $r_\mathrm{TT}(f_\mathrm{d}, f_\mathrm{d}', f, f') = \delta(f_\mathrm{d}' - f_\mathrm{d})P_\mathrm{TT}(f_\mathrm{d}, f, f')$ and the equivalent relation can be derived for $r_\mathrm{ss}(f_\mathrm{d}, f_\mathrm{d}', \tau, \tau')$. It is important to understand that the statistics of the channel do change with time in reality. One can, however, consider the channel to be WSS within short-enough observation windows, which was termed quasi-WSS by Bello in [Bel63]. The channel can generally be considered WSS if the stations move a short

distance compared to the signal wavelength, e.g., in the dimension of a few tens of the wavelength according to [PB82]. A similar criterion is applied in Section 3.2 to delimit the observation window used to obtain the channel statistics from the measurements.

Uncorrelated Scattering (US). In this case, we assume that the scattering components with different delays are statistically uncorrelated. In practice, this assumption allows us to simplify the autocorrelation functions as $r_{\mathrm{hh}}(t,t',\tau,\tau') = \delta(\tau'-\tau)P_{\mathrm{hh}}(t,t',\tau)$ and equivalently for $r_{\mathrm{ss}}(f_{\mathrm{d}},f'_{\mathrm{d}},\tau,\tau')$. In addition, the US assumption leads to the autocorrelation not depending on the absolute frequencies, but only on the frequency difference, i.e., $r_{\mathrm{HH}}(t,t',f,f') = r_{\mathrm{HH}}(t,t',\Delta f)$, where $\Delta f = f' - f$.

Wide-Sense Stationary Uncorrelated Scatterers (WSSUS). Both assumptions are usually combined to create the well-known WSSUS model[3], where the autocorrelation functions become dependent of only two variables. Given that the WSSUS model has been very widely used over decades, each one of the resulting simplified functions has acquired a characteristic name. These are

$$r_{\mathrm{hh}}(t,t',\tau,\tau') = \delta(\tau'-\tau)P_{\mathrm{hh}}(\Delta t,\tau)\,, \tag{3.10}$$

with $P_{\mathrm{hh}}(\Delta t,\tau)$ as the delay cross power spectral density,

$$r_{\mathrm{TT}}(f_{\mathrm{d}},f'_{\mathrm{d}},f,f') = \delta(f'_{\mathrm{d}}-f_{\mathrm{d}})P_{\mathrm{TT}}(f_{\mathrm{d}},\Delta f)\,, \tag{3.11}$$

where $P_{\mathrm{TT}}(f_{\mathrm{d}},\Delta f)$ is the Doppler cross power spectral density,

$$r_{\mathrm{HH}}(t,t',f,f') = r_{\mathrm{HH}}(\Delta t,\Delta f)\,, \tag{3.12}$$

with $r_{\mathrm{HH}}(\Delta t,\Delta f)$ called the time-frequency correlation function, and

$$r_{\mathrm{ss}}(f_{\mathrm{d}},f'_{\mathrm{d}},\tau,\tau') = \delta(f'_{\mathrm{d}}-f_{\mathrm{d}})\delta(\tau'-\tau)P_{\mathrm{s}}(f_{\mathrm{d}},\tau)\,, \tag{3.13}$$

with $P_{\mathrm{s}}(f_{\mathrm{d}},\tau)$ as the well-known scattering function.

Simplified Representations

Given that the autocorrelation functions in the WSSUS model still depend on two variables, simpler representations depending on only one variable are commonly used.

[3]The WSSUS assumption is commonly denoted as the WSSUS model given that its main application is channel modeling.

Power Delay Profile. First, the scattering function $P_{\mathrm{s}}(f_{\mathrm{d}}, \tau)$ is integrated over the Doppler shift f_{d} to obtain the delay power spectral density, usually known as the power delay profile (PDP) $P_{\mathrm{h}}(\tau)$. Another common way to obtain it is from the WF, i.e.,

$$P_{\mathrm{h}}(\tau) = \lim_{T\to\infty} \frac{1}{2T} \int_{-T}^{T} |h(t,\tau)|^2 \, \mathrm{d}t \,, \tag{3.14}$$

although one must carefully choose the observation window to guarantee the quasi-stationarity of the channel. The cost of having a simpler representation is losing the information on the Doppler shifts of the different MPCs.

Doppler Power Spectral Density. The Doppler shift information is however represented in a compact manner by the Doppler power spectral density $P_{\mathrm{T}}(f_{\mathrm{d}})$, which is obtained by integrating the scattering function $P_{\mathrm{s}}(f_{\mathrm{d}}, \tau)$ over the delay τ.

Mean Delay and Delay Spread. A very common way to summarize the channel characteristics is through its mean delay μ_τ and its root mean square (RMS) delay spread σ_τ. These are respectively obtained from the PDP as its normalized first-order moment, i.e.,

$$\mu_\tau = \frac{\int_{-\infty}^{\infty} P_{\mathrm{h}}(\tau)\tau \, \mathrm{d}\tau}{P_{\mathrm{m}}} \,, \tag{3.15}$$

and as its normalized second-order central moment, i.e.,

$$\sigma_\tau = \sqrt{\frac{\int_{-\infty}^{\infty} P_{\mathrm{h}}(\tau)\tau^2 \, \mathrm{d}\tau}{P_{\mathrm{m}}} - \mu_\tau^2} \,, \tag{3.16}$$

where the total power P_{m} is given by

$$P_{\mathrm{m}} = \int_{-\infty}^{\infty} P_{\mathrm{h}}(\tau) \, \mathrm{d}\tau \,. \tag{3.17}$$

Obviously, the mean delay and RMS delay spread do not provide a complete understanding of the channel. However, they are some of the most common parameters to describe a channel because of their simplicity and their direct application to the design of communication systems.

Mean Doppler and Doppler Spread. We can obtain the equivalent information of the Doppler shift from the Doppler power spectral density $P_{\mathrm{T}}(f_{\mathrm{d}})$. The mean Doppler shift $\mu_{f_{\mathrm{d}}}$ is obtained as its normalized first-order moment, i.e.,

$$\mu_{f_{\mathrm{d}}} = \frac{\int_{-\infty}^{\infty} P_{\mathrm{T}}(f_{\mathrm{d}}) f_{\mathrm{d}} \, \mathrm{d}f_{\mathrm{d}}}{P_{\mathrm{m}}} \,, \tag{3.18}$$

and the RMS Doppler spread σ_{f_d} as its normalized second-order central moment, i.e.,

$$\sigma_{f_\mathrm{d}} = \sqrt{\frac{\int_{-\infty}^{\infty} P_\mathrm{T}(f_\mathrm{d}) {f_\mathrm{d}}^2 \,\mathrm{d}f_\mathrm{d}}{P_\mathrm{m}} - \mu_{f_\mathrm{d}}^2}\,, \tag{3.19}$$

where the total power P_m can also be obtained as

$$P_\mathrm{m} = \int_{-\infty}^{\infty} P_\mathrm{T}(f_\mathrm{d})\,\mathrm{d}f_\mathrm{d}\,. \tag{3.20}$$

Frequency Correlation Function and Coherence Bandwidth. The frequency correlation function can be obtained from the time-frequency correlation function $r_\mathrm{HH}(\Delta t, \Delta f)$ by setting $\Delta t = 0$, i.e., $r_\mathrm{HH}(0, \Delta f)$, and gives an idea of how long, in frequency, the channel remains quasi-stable. A widely used parameter is the coherence bandwidth B_coh, defined as the 3-dB bandwidth of the function, i.e., B_coh such that

$$|r_\mathrm{HH}(0, B_\mathrm{coh})| = \frac{1}{2}\,|r_\mathrm{HH}(0,0)|\,. \tag{3.21}$$

Given that the frequency correlation function can also be obtained as the Fourier transform of the PDP, the coherence bandwidth and the delay spread are considered to be reciprocally proportional. A very common approximation used to derive one from the other is through the uncertainty relationship [Fle96]

$$B_\mathrm{coh} \gtrsim \frac{1}{2\pi\sigma_\tau}\,, \tag{3.22}$$

but it is important to notice that this does not allow us to obtain one from the other and it shall only be used as a very rough, preliminary approximation.

Time Correlation Function and Coherence Time. The time correlation function can be obtained from the time-frequency correlation function $r_\mathrm{HH}(\Delta t, \Delta f)$ by setting $\Delta f = 0$, i.e., $r_\mathrm{HH}(\Delta t, 0)$, and gives an idea of how long, in time, the channel remains quasi-stable. A widely used parameter is the coherence time T_coh, defined as the 3-dB bandwidth of the function, i.e., T_coh such that

$$|r_\mathrm{HH}(T_\mathrm{coh}, 0)| = \frac{1}{2}|r_\mathrm{HH}(0,0)|\,. \tag{3.23}$$

Given that the time correlation function can also be obtained as the inverse Fourier transform of the Doppler power spectral density, the coherence time and the Doppler spread are considered to be reciprocally proportional. There are many approximations found in the literature. A very popular approximation commonly used in modern digital communications is [Rap01]

$$T_\mathrm{coh} \approx \frac{1}{f_\mathrm{m}}\sqrt{\frac{9}{16\pi}}\,, \tag{3.24}$$

where f_{m} is the maximum Doppler shift. However, it is again important to understand that this is just an approximation and that the exact value of T_{coh} can only be found via the time correlation function.

3.1.3 Channel Modeling

Designing a wireless communication system requires an accurate knowledge of the propagation channel. Given that it is unfeasible to conduct a measurement campaign every time a new configuration is to be tested, channel models are developed to enable theory-based and simulation-based designs as well as performance analyses. Channel models are usually divided into three categories: purely deterministic, purely stochastic, and geometry-based stochastic.

Deterministic Channel Models

This type of channel models accounts for the specific environment, including buildings, vehicles, or any type of IO, around the transmitter and receiver to compute the channel response. Depending on their complexity, multiple propagation mechanisms, such as reflection, scattering, or diffraction, are considered to obtain the channel MPCs and their characteristics. Ray tracing is probably the most popular technique to compute channel models deterministically. Ray tracers approximate the electromagnetic waves as rays and estimate the effect of the different channel propagation phenomena on the rays reaching the receiver, to later obtain the channel response as a compound of the rays. In a deterministic channel model, the tapped-delay-line model of the channel shown in Fig. 3.1 would have a fixed number of delay lines and the line coefficients would be deterministically computed from the geometry between the stations and the environment, as well as its electromagnetic properties. The delays and coefficients would then be adjusted over time to account for the change in the geometry. One can already grasp the major disadvantage of using such channel models: there is a non-negligible trade-off between the accuracy to represent the channel and the complexity required in the model. In the extreme case, the model should account for all the IOs of the channel and characterize their interactions with the impinging waves to compute all resulting rays, which becomes computationally unfeasible for most channels. On the other hand, deterministic channel models can provide a rough estimate of the channel response in scenarios where no channel measurements are yet available, or impossible to take. In addition, the seemingly unstoppable increase in computational capacity is enabling the use of increasingly complex channel models that account for more phenomena, and thus recreate the channel more faithfully. The environment is

also becoming progressively easier to reproduce in a semi-automatic manner, as more modern systems require to fetch information about the environment to understand it in order to operate, e.g., vision-based autonomous driving. As the computational capacity grows further and the environment is more faithfully reproducible, we expect the deterministic channel models to rapidly gain more popularity. A clear example of this is the development of the GPU-accelerated open-source library Sionna ray tracer (RT) [Hoy+23]. In Section 3.3, we propose a novel methodology to model the channel deterministically, making special emphasis on the scattering components of the channel, which are usually either ignored or only modeled in a stochastic manner.

Stochastic Channel Models

Complementary in concept to the deterministic channel models, the stochastic channel models ignore the actual environment around the stations and use statistical distributions to model the MPCs. These statistical distributions are based on measurements conducted in one or multiple locations. Once the measurements are conducted and the distributions are obtained, they are assumed to be the same for other scenarios that are considered to be similar, e.g., urban ones, not taking into account the specifics of the different scenarios. For example, driving around the city with a car might yield a channel with a LoS component whose fading can be approximated to a statistical distribution, and several more MPCs at different delays whose spectra and fading occurrences can be recreated using other distributions. Once defined, stochastic channel models are extremely simple to use, given that their characteristics are fixed and they can be easily implemented for computer simulations. Considering the tapped-delay-line model of the channel shown in Fig. 3.1, a stochastic channel model would be generally implemented with a fixed number of delay taps and the line coefficients would simply follow the stochastic distribution modeling each tap. Going back to our example of the stochastic channel model created from the measurements of a car driving around a city, one can directly notice that the model would only be valid for that specific drive in that specific city, and assuming that no IO moves or changes its characteristics. Even in that case, the actual statistics of the MPCs are time-variant, as they change as the car drives around the city. Using a time-invariant model would only allow to use an average of the otherwise time-variant statistics. This was not too problematic for the radio systems using a comparatively narrow bandwidth, as most MPCs fell into few delay taps and the subtle variations in their statistics would be mitigated by the many different contributions affecting each tap. However, as the bandwidth of the systems have increased over time, the channel models have had to be valid for the wider bandwidth, and the time-variant characteristics of the channel have become more rel-

evant and important to be accurately modeled. Recreating the variation over time of the channel characteristics becomes too complex if the environment is not taken into account, which is where the GBSCMs come into play.

Geometry-Based Stochastic Channel Models

GBSCMs can be seen as a combination of deterministic and stochastic channel models, as they parameterize some characteristics of the channel based on the actual geometry, i.e., in a deterministic manner, and other parts of it following stochastic distributions. For example, a GBSCM can use the geometry to identify the IOs that will cause the main MPCs, then obtain deterministically the characteristics of those MPCs, such as their delay, Doppler shift, and attenuation coefficient, and then use stochastic distributions to recreate their fading characteristics, i.e., their complex amplitude. MPCs that are difficult to resolve, e.g., with similar Doppler shifts and delays, will generally be grouped into clusters, making it easier to implement them. The main advantage of GBSCMs is the ability to recreate the variation over time of the channel, i.e., its non-stationarity, by updating the geometry-dependent parameters as the geometry between the stations and the environment evolves. This is achieved at the cost of a higher computational complexity compared to stochastic channel models. However, it is not so computationally challenging as deterministic channel models given that the non-resolvable channel characteristics are simply recreated using stochastic distributions. As the computational capacity increases, one can expect that more parts of the GBSCMs will be modeled deterministically, but still some non-resolvable parts of it will benefit from a stochastic representation. Going back to the tapped-delay-line model of the channel shown in Fig. 3.1, a GBSCM would generally have a number of delay taps driven by the main clusters of MPCs observed in the geometry, and the line coefficients would have a deterministic component, for example accounting for the FSPL and the reflection coefficients, and a stochastic component, recreating the overall fast fading statistics expected for that cluster. In Section 3.2, we analyze the A2A channel measurements to obtain the statistics of the different components of the channel, e.g., the LoS, specular reflection (SR), and scattering components, which we identify by considering the underlying geometry. Knowing the statistics of the channel components and which parts of the environment causes them allows us to propose an A2A GBSCM in Section 3.4, that we later use in Chapter 4 to design the physical layer of an A2A communications system.

3.1.4 Previous Work and Main Contributions of This Chapter

In general, research on the propagation channel has moved from the omnipresent pure stochastic modeling of the channel to the incorporation of deterministic components into it. Since Bello introduced the WSSUS model in [Bel63], traditional narrowband fixed-to-mobile channels were generally assumed to behave like WSSUS systems and were often characterized by purely stochastic models like in [Cla68]. For uniformly distributed scatterers around the transmitter and considering a stationary receiver, Clarke derived in [Cla68] the well-known Jakes power spectral density [Jak94].

For M2M channels, where transmitter and receiver are mobile, the authors in [AH86] derived the Doppler spectral density by assuming that the scattering around the transmitter and receiver is uncorrelated, leading to a convolution of two Jakes spectra. Additional M2M channel models were proposed in [VF97; PSP05; TM03; Zaj+09] for various 2D and 3D scenarios, as well as for MIMO scenarios in [Pät+05; AK02; PHY08; ZS08; ZS09]. Nonetheless, the problem for most M2M channels is that the WSSUS assumption is violated due to the movement of the transmitter and receiver. This has been observed in different M2M channels, including vehicle-to-vehicle (V2V) [Pai+08; Ber12] and A2A [Wal+19] channels. The non-stationarity in channel modeling has been addressed in multiple ways. In [Mat05], Matz generalized Bello's model to provide a non-WSSUS description of the channel consisting of four-dimensional channel correlation functions. More recently, the authors in [Ge+22] addressed the non-stationarity of the channel by defining, among others, the probabilistic presence and movement of clusters of scatterers.

The electromagnetic spectrum is a limited resource of great value. New radio systems are trying to squeeze the most out of it, using parts of the spectrum that were not technically usable before, increasing the spectral bandwidth as much as possible, and imposing ever more stringent performance requirements, e.g., throughput and latency. This, coupled with the desire to connect all devices together, e.g., aircraft, drones, cars, pedestrians, etc., has made it necessary to study the propagation channel in depth in all possible M2M scenarios of interest. The contributions to this field are thus practically inexhaustible, including theoretical considerations, measurements, modeling, and validation. Therefore, we restrict our analysis to the A2A aeronautical channel, a comparatively niche field with significantly less contributions given the difficulty to actually measure the channel and its main applicability to safety-of-life services and ATM, both applications being of less economic interest compared to the highly profitable mobile communications, e.g., 4G/5G. Understanding the A2A propagation channel is, however, crucial for the development of new A2A communication and surveillance systems that shall guarantee a safe operation in all domains of the airspace and enable the new

ATM services and operational concepts required to sustain the continuous air traffic growth. Of course, research on the A2A propagation channel is also applicable in the military field, where aircraft, drones, and other aerial vehicles are proving to play a key role in dominating the battlefield.

Höher and Haas proposed first in [HH99] and later in [Haa02] a theoretical WSSUS stochastic model for the aeronautical channel mainly focused on air-ground. The model was extended to also account for the A2A case by using the air-ground en-route model and simply considering a higher relative aircraft speed (higher Doppler shift) and a higher maximum delay. Thus, the same characteristics defined for the air-ground scenario were applied to the A2A case, like for example the limitation of the scattering components to a very narrow angle of arrival and, thus, to a very narrow range of Doppler shifts. As we will show later in the analysis of the A2A measurements in Section 3.2, this limitation does not hold true for the A2A channel, which presents scattering components throughout the entire range of possible Doppler shifts.

Given the difficulty and expensiveness of measuring the A2A channel, very few measurements have been reported publicly. In [Tak+14], the authors summarize the main findings of a wideband A2A channel measurement campaign conducted in the S-band at 2.3 GHz between small manned aircraft at low altitude (roughly between 200 m and 1000 m above ground). The flights were conducted over the Hawaiian island Oahu and included flights over different terrains, including urban, suburban, pineapples fields, mountains, and over the sea. The results shown in [Tak+14] are mainly limited to some measured PDPs with no in-depth statistical analysis of the main channel components. It was highlighted that a strong SR component could be observed over sea but not in the other scenarios, where mainly diffuse scattering components could be observed. Another wideband A2A channel measurement campaign was reported in [Ono+17] by some of the authors from [Tak+14]. This time, the A2A channel was measured in the C-band at 5.11 GHz using two fixed-wings small unmanned aircraft. The flights were conducted near the city of Sakaide, Japan, and comprised segments flying at low altitude (between 100 m and 700 m above ground) over hilly regions and over calm sea. In both scenarios, the authors observed that the measured A2A channel at 5 GHz was mainly composed of the LoS and SR components, including some weaker, diffuse components when flying above the hilly area. However, the results shown in [Ono+17] are limited to the PDP measured in each scenario, with a power range of 20 dB that might have masked weaker components. Walter et al. conducted wideband A2A channel measurements in the VHF/UHF band at 250 MHz between two manned aircraft using multiple antenna configurations and testing different geometries, including different altitudes (mainly 600 m, 1600 m, and 2600 m above ground) and distances

between the aircraft [Wal+10]. The flights were conducted near Munich, Germany, and included many flights over lakes, forests, fields, and some sub-urban regions, as well as within the Alps mountain range. The statistical analysis of the measurements published in [WS11a] focused on analyzing the properties of the LoS and SR component, although the relatively strong scattering components were also highlighted in some scenarios. The analysis, however, was restricted to a single antenna configuration and a single aircraft altitude. To the best of our knowledge, no other wideband A2A channel measurements, or an analysis thereof, have been reported publicly. The presence of significant scattering components at low aircraft altitudes reported in [Wal+10; WS11a] led the author to investigate a theoretical way to model it. Based on their work in [WSF14a] and [WSF14b] for V2V and A2A channels, respectively, Walter et al. proposed in [Wal+20] a general way of theoretically deriving the delay-dependent and joint delay Doppler pdfs of M2M channels. The approach is based on defining an infinite, arbitrarily-oriented scattering plane where all effective scatterers are located. Using a prolate spheroidal coordinate system to profit from the common ellipsoid-based description of the channel, and the theory of algebraic curves to solve ambiguities, the authors obtained closed-form expressions for the delay-dependent and joint delay Doppler pdf in M2M channels. The potential of such an approach was shown with measurement data in V2V [WFZ14; WZS15; Som+19] and A2A [Wal16; WS11b] scenarios. However, both the technique and its validation had two major constraints: the scatterers could only be assumed to be distributed over a single plane, which must also be infinite. This prevents the technique to be applicable to more complex M2M scenarios where the scatterers or reflectors are present over multiple surfaces, which might also be limited in space. It also prevented the technique from being validated in diverse M2M scenarios, as only few of them could be realistically recreated with a single infinite plane.

In this thesis, we fill the gaps found in the study of the A2A propagation channel. First, we thoroughly analyze in Section 3.2 the A2A channel measurements initially presented in [Wal+10], obtaining the fading statistics of the main channel components when different antenna configurations, i.e., using either bottom or top aircraft antennas, and geometries, i.e., different aircraft altitudes and distances, are considered. This analysis is not limited to the LoS and SR components, but also considers the diffuse scattering components usually ignored in the literature. Second, we propose in Section 3.3 a geometry-based, deterministic technique to obtain the delay-dependent and joint delay Doppler pdfs of a M2M channel, of course being it also applicable to the A2A case. The main aim of the proposed technique is recreating the delay/Doppler distribution of the scattering components, but it also accounts for the LoS and SR

components. Our technique finds its roots in the work proposed by Walter et al. in [Wal+20]. However, we avoid the two main constraints of the technique proposed in [Wal+20] by extending the analytical framework to 1) enable the use of any number of arbitrarily-oriented planes and to 2) allow the planes to be either infinite or finite, i.e., limited in space. This enables us to obtain the channel between two mobile stations by firstly recreating the environment around them using infinite and finite planes, and by secondly using the proposed analytical model to calculate the time-variant channel. Our approach, applicable to any M2M scenario, is validated with measurements in multiple A2A, drone-to-drone (D2D), ship-to-ship (S2S), and V2V[4] scenarios. Given that this work focuses on the A2A channel, we present in Section 3.3 the general channel modeling technique, applicable to any M2M channel, but only its validation with A2A measurements. Its verification with S2S, D2D, and V2V measurements can be found in [BMW24]. Finally, we propose in Section 3.4 an A2A GBSCM, where the geometry-based characterization of the channel proposed and validated in Section 3.3 is combined with the stochastic properties of the channel components derived in Section 3.2.

3.2 Analysis of A2A Channel Measurements

In this section, an A2A channel measurement campaign is described and its measurements analyzed to obtain the fading statistics of the main A2A channel components. These statistics are used in Section 3.4 to define a geometry-based stochastic channel model. Most of the content of this section was published by the author in [BMFW22].

3.2.1 A2A Flight Campaign

The A2A channel measurements were taken during a flight campaign [Wal+10] in southern Germany in 2009 using the Cessna Grand Caravan C-208B (D-FDLR) and the Dornier Do-228101 (D-CODE) aircraft shown in Fig. 3.2. The channel was measured using a Medav RUSK channel sounder [Unt+16]. Table 3.1 shows the main parameters of the channel measurements. The Medav RUSK channel sounder measured the TF of the channel every $\Delta t = 2.048\,\text{ms}$ using a carrier frequency $f_\text{c} = 250\,\text{MHz}$ with a bandwidth $B_\text{s} = 20\,\text{MHz}$, leading to a delay resolution $\Delta\tau = 50\,\text{ns}$. Accurate time and frequency synchronization was achieved through pre- and post-calibration, as well as by using GNSS receivers and atomic clocks. The Cessna aircraft carrying the transmitter (TX) followed the Dornier aircraft carrying the receiver (RX). One

[4]We use the term V2V to refer to car-to-car (C2C) as it is the most common terminology found in the literature.

(a) Cessna (transmitter). (b) Dornier (receiver).

Figure 3.2. Aircraft and positions of the antennas. Adapted from [BMFW22]. © 2022 IEEE.

Table 3.1. Parameters of the A2A channel measurements [Wal+10].

Carrier frequency	250 MHz
Bandwidth	20 MHz
Measurement time grid	2.048 ms
Signal period	25.6 µs
Delay resolution	50 ns
Max. Doppler frequency	±244 Hz
Airborne antennas	UHF blade antennas (*Cooper 21-30-18*)
Polarization	vertical
Transmit power	42.15 dBm EIRP

can see in Fig. 3.2 that each aircraft had a bottom antenna facing downwards ('D' antenna) and a top antenna facing upwards ('U' antenna). The propagation channel was measured in different flights using the four possible single-input/single-output (SISO) antenna configurations, i.e., down-to-down, down-to-up, up-to-down, and up-to-up, where 'down' refers to the bottom antenna and 'up' refers to the top antenna. The antennas of the Cessna were installed behind its wings, roughly at the middle of its fuselage, whereas the top antenna of the Dornier was mounted between the cockpit and the wings, practically between both propellers, and its bottom antenna was installed near its tail.

A total of 17 flights were conducted. In addition to using different SISO antenna configurations, two different routes were flown at multiple flight levels, i.e., nominally 600 m, 1600 m, and 2600 m above ground level. More information on the flights can be found in Appendix A. The accurate timestamps of the channel sounding data allow us to map the time-variant TX and RX positions and velocity vectors to the channel measurement data. As an example, Fig. 3.3 shows the flight tracks and the altitude of

the first two flights, which covered the two different routes considered in the campaign. One can see that the aircraft flew over multiple terrains, including fields, lakes and forests. The aircraft also flew close to mountains and through valleys.

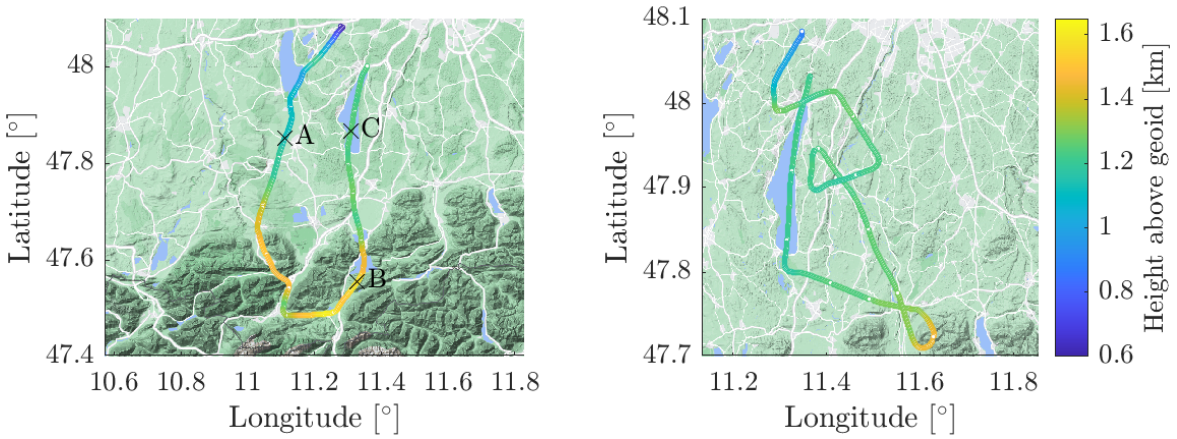

(a) First flight (route 1).

(b) Second flight (route 2).

Figure 3.3. Tracks of the first two flights covering the two different flight routes.

3.2.2 Channel Measurements

The channel sounder measured the TF of the channel, $H(m \cdot \Delta t, n \cdot \Delta f)$, every 2.048 ms, with m being the time index, $n = 0, 1, ..., N-1$ the frequency bin index with $N = 513$, and $\Delta f = \frac{1}{25.6\,\mu s}$ the frequency resolution. The WF of the channel is obtained as

$$h(m,k) = \frac{1}{N} \sum_{n} H(m,n) \mathrm{e}^{\mathrm{j}\frac{2\pi}{N}nk}, \tag{3.25}$$

where $k = 0, 1, ..., K-1$, with $K = N$, denotes the delay bin index. Using the TF or the WF, one can obtain other representations of the channel as discussed in Section 3.1. Figure 3.4 depicts the time-variant WF measured during a part of the first flight.

Main Channel Components

One can distinguish three main channel components in Fig. 3.4: the LoS component, the ground-reflected SR component, and the scattering components. First, one can recognize the LoS component as the one with the lowest delay, i.e., between 4 µs and 5 µs, and presenting the highest power and stability. Next, the SR component from the Earth's surface appears roughly 1.5 µs after the LoS component at an absolute delay between 5 µs and 7 µs, approximately. Contrary to the LoS component, the SR component is not always stable as it depends on the terrain causing the reflection. The

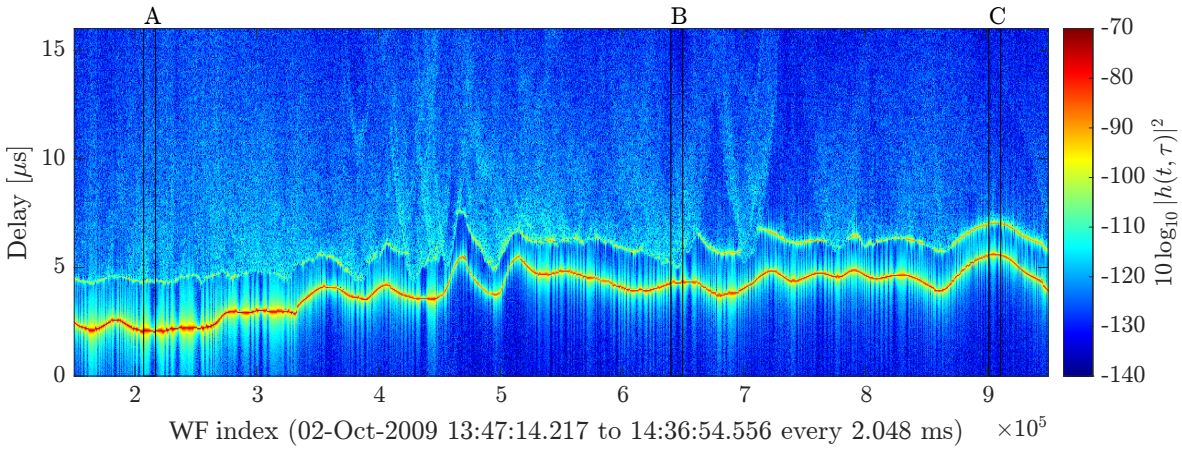

Figure 3.4. Weight function (squared magnitude) measured during the first flight.

diffuse scattering components also present significantly different power depending on the scattering surface and decrease as the delay increases. This can be clearly seen in Fig. 3.4 if we focus on the three regions, i.e., A, B, and C, where the aircraft flew over the field (A), the forest (B), and the lake (C) marked on Fig. 3.3a.

Figure 3.5 shows the time-variant squared WF and its resulting squared spreading function (SF) measured around point A, where the aircraft flew above a field. Again, one can see the LoS component with the lowest delay and stronger than the other components, followed by the SR and scattering components. Both, the LoS and SR components, present a Doppler frequency shift close to 0 Hz. This is understandable given the geometry and velocity vectors of the aircraft, i.e., the aircraft fly in the same direction, at the same speed, and maintaining the same altitude above the ground, yielding practically no change in delay for either the LoS or the SR component, and consequently no Doppler frequency shift. The SR component can be relatively strong but is in general very unstable. The scattering components are significantly weaker than the LoS and SR components, but they are spread in the Doppler direction as the delay increases, forming a parabolic shape. As we will later show in Section 3.3, the limiting frequencies of this parabolic shape can be computed analytically.

The channel changes significantly when the aircraft fly over a forest, marked with the point B. The time-variant WF and its resulting SF are shown in Fig. 3.6. In this case, the SR component vanishes and the scattering components become significantly stronger compared to the flight over the field.

The SR component becomes very strong and stable when flying over water. This can be seen in the time-variant squared WF and its resulting squared SF, shown in Fig. 3.7, measured when flying over the lake marked as the point C. Although in this example the LoS component is still stronger than the SR component, the latter became as strong

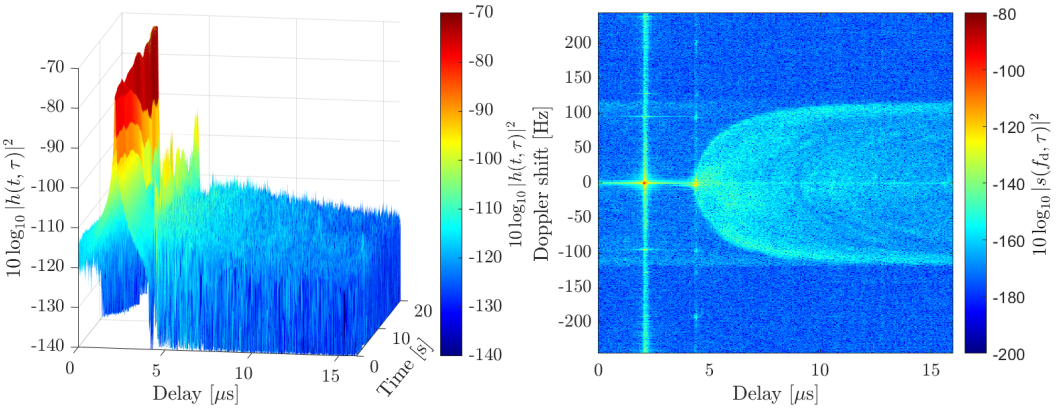

(a) WF over field. (b) SF over field.

Figure 3.5. WF and SF (squared magnitude) measured when flying over a field, i.e., point A marked in Fig. 3.3a and Fig. 3.4, during the first flight.

as the LoS component, or even stronger, during other parts of the flight where other geometries were experienced. The scattering components seem significantly weaker when flying over the lake, compared to the forest scenario. However, although this is true for higher delays, Fig. 3.7b shows that there are strong MPCs arriving just after the SR component at the limiting Doppler frequencies. We believe these MPCs to be caused by the presence of waves on the lake surface in the flight direction, and this assumption will be later consolidated in Section 3.3 when we model the lake scenario.

There are also multiple artifacts present in the measurements that can be mentioned for completeness. First, one can see some channel components before the LoS component, i.e., before 5 µs in Fig. 3.7b, at the limiting Doppler frequencies (±120 Hz). These components can be neglected as they are actually artifacts caused by the periodic correlation of the channel sounding signal during the channel measurements. In addition, the LoS and SR components should have a discrete delay and Doppler frequency shift, and thus should theoretically appear as a Dirac delta centered at its delay in the WF, or equivalently as a discrete point in the SF. However, these components appear in the measurements, e.g., in Fig. 3.7b, as sinc functions centered at the nominal delay and Doppler shift, and stretching in the delay and Doppler directions. As we demonstrate in Appendix B, this effect is caused by the time- and bandwidth-limited sampling of the channel and can be recreated analytically. Finally, although less visible and in general negligible, one can also see some weaker components with the same delay of the LoS component but at higher positive and negative Doppler shifts, e.g., they can be seen with a Doppler shift of roughly ±100 Hz in Fig. 3.7b. These are caused by the propellers of the aircraft as we discuss and verify later in Section 3.2.4.

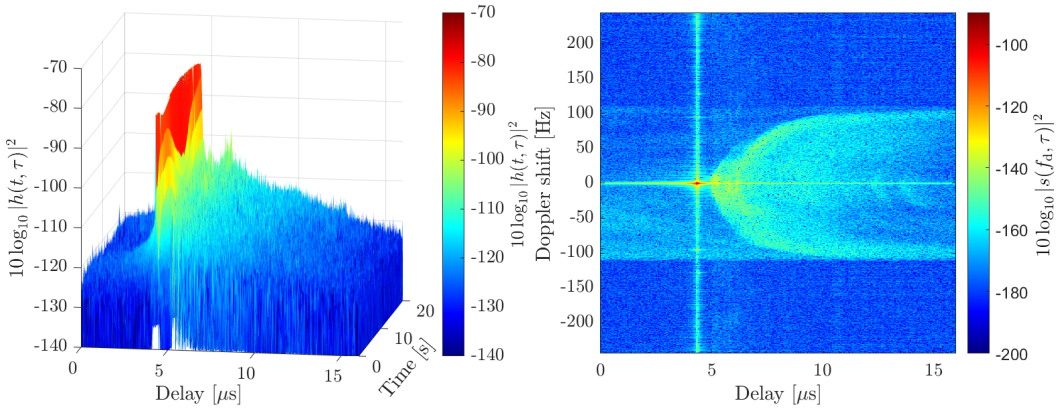

(a) WF over forest.

(b) SF over forest.

Figure 3.6. WF and SF (squared magnitude) measured when flying over a forest, i.e., point B marked in Fig. 3.3a and Fig. 3.4, during the first flight.

Banking

The measurements show that the channel components can be significantly affected by the banking maneuvers of the aircraft, as the fuselage of the aircraft might block the signal. This effect can be clearly seen in Fig. 3.8a, which shows the flight track during a segment of the flight and the measured LoS component power relative to the theoretical FSPL. Figure 3.8b also shows the effect of the banking by depicting the histogram of the LoS component power relative to FSPL for different roll angles of the TX. Note that only the roll angle of the TX is considered since the attitude information of the RX was not recorded. However, with the TX roll angle, one can already approximately delimit the parts of the flight when banking maneuvers were conducted. The results show that, for low roll angles, e.g., $< 3°$, the normalized LoS component power generally has a value of around 3 dB. For high roll angles, e.g., $> 10°$, the power of the LoS component decreases significantly, in some cases down to -15 dB.

3.2.3 Methodology to Analyze the Measurements

Scenarios of Interest

The channel measurements are used to extract useful statistics of the main channel components. However, the measurements show that these components depend strongly on the geometry and the terrain below the aircraft. Thus, we do not consider all measurements jointly for the analysis, but split the flights into multiple scenarios of interest and analyze the different channel components separately in the different scenarios. In addition, we only consider the flight segments with no significant flight maneuvers, such as

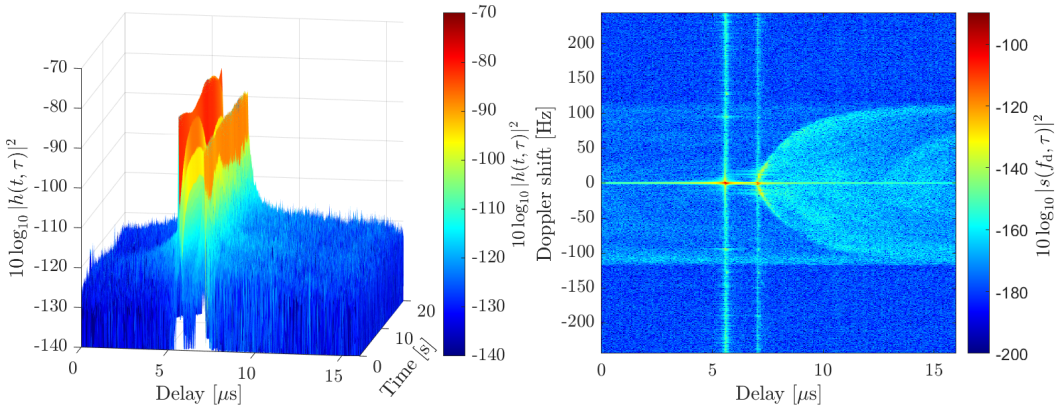

(a) WF over lake. (b) SF over lake.

Figure 3.7. WF and SF (squared magnitude) measured when flying over a lake, i.e., point C marked in Fig. 3.3a and Fig. 3.4, during the first flight.

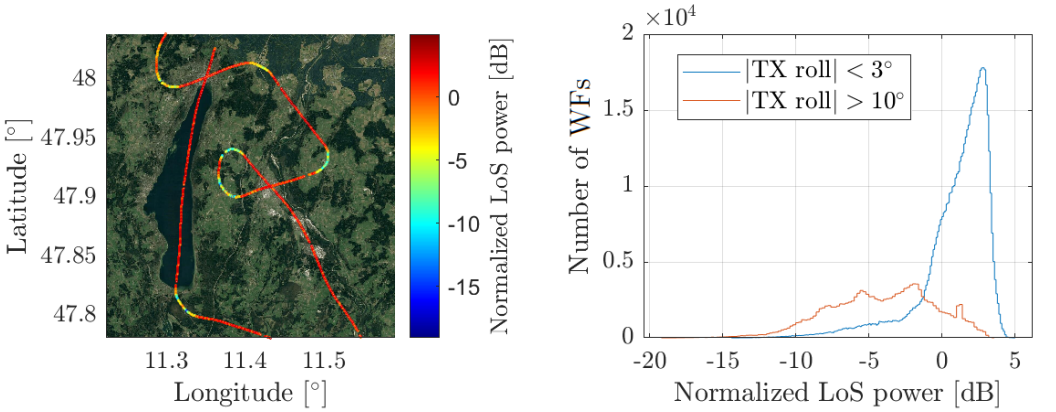

(a) Normalized power on the map. (b) Histogram depending on roll angle.

Figure 3.8. Power of the LoS component normalized to the FSPL for a part of a flight.

banking turns or steep variations in the aircraft altitude. This is due to the significant power loss observed during such maneuvers, as shown in Fig. 3.8, which would make the analysis too dependent on the specific maneuver and its duration. The different scenarios considered for the analysis of the channel components are described in detail in Appendix A. In all scenarios, both aircraft tried to maintain a constant altitude and distance between them. However, the aircraft had to do short-term flight track corrections, e.g., slight changes in the altitude, which were in general unavoidable and can be expected in a normal flight. These corrections were generally less significant the higher the aircraft flew. The considered scenarios allow us to isolate the impact that either the aircraft altitude or the antenna position had on the channel components, as the same antenna configuration was used at multiple altitudes, and different antenna

configurations were tested at the same altitude. Each scenario is named such that it is easy to identify its main parameters, e.g., LOS-U-D-1600-600 means that the scenario is used to analyze the LoS component, that TX uses the top antenna facing upwards ('U') and RX uses the bottom antenna facing downwards ('D'), and that TX and RX fly at 1600 m and 600 m above ground level, respectively.

Tracking of the Channel Components

In order to analyze the channel components separately for each measured WF, one must first estimate their delay accurately in each WF. For this, a simple algorithm to detect and track the LoS and SR components is developed. Our algorithm exploits the fact that, in all considered scenarios, both components are sufficiently separated from each other in delay and present a power significantly higher than other MPCs, being also the LoS component generally stronger than the SR component.

Given its stability and high power, the LoS component can be easily detected following a simple maxima search. In some isolated cases, the SR component becomes more powerful than the LoS component, and in such cases the maxima search might not deliver correct results. To avoid this, we delimit the maxima search to a delay window of $\Delta\tau_{\mathrm{w}} = 1\,\mu\mathrm{s}$ around the GNSS-derived LoS delay $\tau_{\mathrm{los}}^{\mathrm{gnss}}$. Prior to conducting the maxima search within the delay window, each WF is upsampled to enhance the resolution of the delay estimation. This way, the delay of the LoS component of the m-th WF can be accurately estimated as

$$\tau_{\mathrm{los}}(m) = \underset{k_{\mathrm{u}} \in \left[\left\lfloor \left(\tau_{\mathrm{los}}^{\mathrm{gnss}}(m) - \frac{\Delta\tau_{\mathrm{w}}}{2}\right)\frac{r_{\mathrm{u}}}{\Delta\tau}\right\rfloor, \left\lceil \left(\tau_{\mathrm{los}}^{\mathrm{gnss}}(m) + \frac{\Delta\tau_{\mathrm{w}}}{2}\right)\frac{r_{\mathrm{u}}}{\Delta\tau}\right\rceil\right]}{\arg\max} \left|h_{\mathrm{u}}(m, k_{\mathrm{u}})\right|, \tag{3.26}$$

where $h_{\mathrm{u}}(m, k_{\mathrm{u}})$ is obtained by upsampling $h(m, k)$ in the delay domain with $k_{\mathrm{u}} = 0, 1, ..., K \cdot r_{\mathrm{u}} - 1$ as the upsampled delay bin index and $r_{\mathrm{u}} = 10$ the upsampling rate. The upsampling is done via a Fourier transform, the appending of zeros, and an inverse Fourier transform. The accurate estimation of the LoS delay in each WF achieved by the algorithm can be seen in the example shown in Fig. 3.9. We have verified that the LoS component is also tracked accurately in the other considered scenarios.

The SR component search is significantly more complex given its lack of short-term stability in some scenarios. Thus, we develop the more complex SR delay search algorithm outlined in Algorithm 1. Also, the explanation of the algorithm is illustrated with the example shown in Fig. 3.9, where the estimated SR delay and the intermediate steps can be seen for a part of the first flight. First, a block-wise search of the most prominent SR components is conducted. For this, instead of looking for the SR component in each WF, as done for the LoS component, the WFs are grouped in

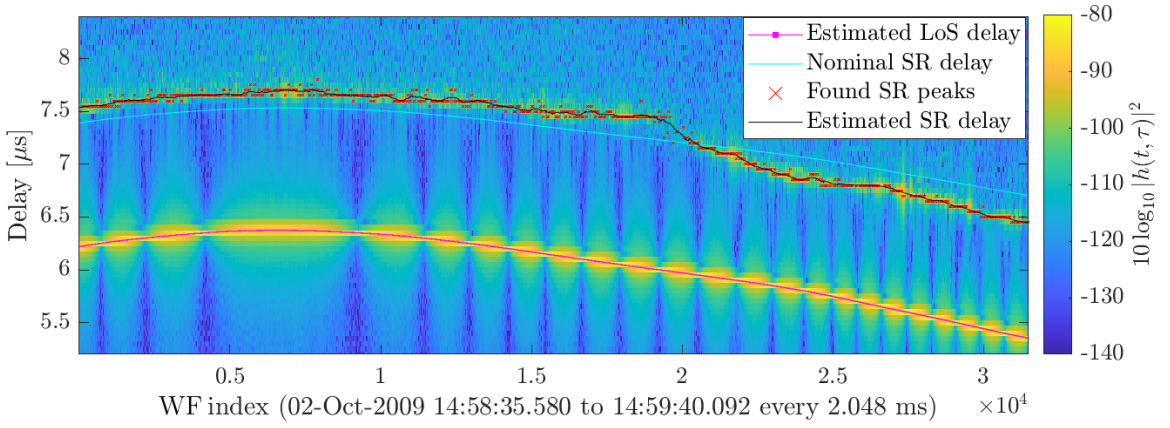

Figure 3.9. Time-variant WF (squared magnitude) in a flight segment where the aircraft flew over a field. One can see the accurate tracking of the LoS and SR components in each WF. In the lake scenario, where the SR component is strong and stable, the algorithm tracks the LoS and SR components perfectly.

blocks of 48 consecutive WFs. Within each block, with a duration of 0.098 s, the SR delay can be considered to remain constant. Then, we obtain the average PDP of each block and look for the two most prominent peaks in the PDP[5]. One of the peaks is identified as the SR component if its delay is at least 0.5 µs higher than the average τ_{los} of this block (obtained in the previous LoS component search using (3.26)), and it does not deviate more than 2 µs from the nominal SR component delay $\tau_{\text{sr}}^{\text{geo}}$ derived from the geometry. The latter is obtained by using the GNSS-derived aircraft positions and the nominal height above ground in each flight (Table A.1). In Fig. 3.9, one can see that a prominent SR component was found in many blocks, but in others it could not be detected given that the aircraft were flying over a field and the SR component was vanishing intermittently. Once the SR delay is found accurately in the sparsely distributed blocks, one can profit from the knowledge of the nominal SR component delay $\tau_{\text{sr}}^{\text{geo}}$ to fill the gaps between the blocks with prominent SR components. More specifically, we compute the deviation ϵ_τ between the actual delay of the prominent SR components and the nominal delay. Then, for each WF, we obtain the mean deviation $\overline{\epsilon_\tau}$ of the nearby blocks found within a time window centered at the WF. This window must be increased in length until at least 10 blocks are contained in it. Finally, the SR delay of each WF is approximated by using the mean deviation as a bias correction with respect to the nominal SR delay obtain from the geometry. One can see in Fig. 3.9 that the estimated SR delay is very accurate, even in the regions where the SR component almost vanishes below the scattering components. The example shown in

[5]We use the *findpeaks* MATLAB function requiring a peak prominence of at least 10 dB.

Fig. 3.9 only covers a flight over a field, which is comparatively more challenging than flying over water in terms of tracking the SR component. In the scenarios where the aircraft fly over water, the SR component is very strong and stable, yielding a practically perfect estimation of the SR delay through the proposed algorithm. Note that more complex algorithms are feasible, but this algorithm already yields very accurate results in all tested scenarios despite its low computational complexity. Also, considering only blocks of the WFs would allow us to track both components more easily, as the short-term fluctuations would be averaged out. However, we opt for this approach in order to track the LoS and SR components in each WF separately, which allows us to later analyze the statistics of both components in much more detail compared to a block-wise estimation.

Algorithm 1 Find delay of SR component, $\tau_{\mathrm{sr}}(m)$, in each WF $h(m,k)$

Block-wise search of prominent SR components

Group the N_{WFs} WFs into N_{blocks} blocks of $L_{\mathrm{block}} = 48$ consecutive WFs each.

for n_{b}-th block **do** ▷ Index of blocks: $n_{\mathrm{b}} = 0, 1, ..., N_{\mathrm{blocks}} - 1$

  Compute PDP of the block, i.e., $P_{\mathrm{h},n_{\mathrm{b}}}(k)$.

  Look for a prominent SR peak: at least 10 dB prominence and fulfilling $\tau - \overline{\tau_{\mathrm{los}}}(n_{\mathrm{b}}) > 0.5\,\mu\mathrm{s}$ and $|\tau - \tau_{\mathrm{sr}}^{\mathrm{geo}}(n_{\mathrm{b}})| \leq 2\,\mu\mathrm{s}$.
  → If found, this is the delay $\tau_{\mathrm{sr}}(n_{\mathrm{b}}) = \tau$ of the SR peak of this block.

  If the SR peak is found, compute the deviation between the SR delay and the nominal one from the geometry: $\epsilon_\tau(n_{\mathrm{b}}) = \tau_{\mathrm{sr}}(n_{\mathrm{b}}) - \tau_{\mathrm{sr}}^{\mathrm{geo}}(n_{\mathrm{b}})$.

end for

Estimation of SR delay for each WF

for m-th WF **do** ▷ Index of WFs: $m = 0, 1, ..., N_{\mathrm{WFs}} - 1$

  Obtain mean deviation $\overline{\epsilon_\tau}(m) = \frac{1}{K_{\mathrm{b}}} \sum_{k_{\mathrm{b}}:|t_{\mathrm{WF}}(m) - t_{\mathrm{block}}(k_{\mathrm{b}})| \leq T_{\mathrm{w}}/2} \epsilon_\tau(k_{\mathrm{b}})$
  → Starting from $T_{\mathrm{w}} = T_{\mathrm{w},0} = 1\,\mu\mathrm{s}$, increase $T_{\mathrm{w}} = T_{\mathrm{w}} + T_{\mathrm{w},0}$ until $K_{\mathrm{b}} \geq 10$.

  Estimate SR delay $\tau_{\mathrm{sr}}(m) = \tau_{\mathrm{sr}}^{\mathrm{geo}}(m) + \overline{\epsilon_\tau}(m)$.

end for

Measuring the Power of the LoS and SR Components

In order to obtain the fading statistics of the LoS and SR channel components, we now measure their power in each WF. Given that the channel is measured with a finite bandwidth, the components do not appear in a single delay bin but spread among consecutive delay bins following a $f_{\mathrm{s}}(k) = \mathrm{sinc}\left(k - B_{\mathrm{s}}\tau\right) / \mathrm{sinc}\left(\frac{1}{K}\left(k - B_{\mathrm{s}}\tau\right)\right)$ pattern, where τ is the delay of the component, B_{s} the measurement bandwidth, and K the number of delay taps per WF. We demonstrate this effect analytically in Appendix B

and obtain closed-form expressions for it. The effect can also be observed clearly in the LoS component depicted in Fig. 3.9. The delay width of the component fluctuates as the aircraft move and $f_{\mathrm{s}}(k)$ becomes wider or narrower depending on the difference between the sampling instant and the actual LoS component delay. Therefore, the power of each component is obtained by applying a delay window centered at the delay measured for each component in each WF, i.e.,

$$P_{\mathrm{mpc}}(m) = \sum_{k'=k_{\mathrm{mpc}}-\frac{K_{\mathrm{w}}-1}{2}}^{k_{\mathrm{mpc}}+\frac{K_{\mathrm{w}}-1}{2}} |h(m,k')|^2 \,, \tag{3.27}$$

where K_{w} is the number of delay bins of the delay window and k_{mpc} is the delay bin where the component was detected by our tracking algorithm. Using (3.27), one can compute the power of the LoS and SR components as P_{los} and P_{sr}, respectively. Of course, K_{w} must be sufficient to accurately measure the power of each component without being affected by the time- and bandwidth-limited sampling of the channel, but at the same time not too large as other MPCs might also be erroneously included in the measurement. In practice, increasing K_{w} reduces the delay resolution of the measurements. Depending on the component and the scenario of interest, one may employ a different K_{w}. This way, a small K_{w} is used for the LoS component, which can be tracked very accurately, and for the SR component in the scenarios where it is strong and stable, e.g., over water. A larger K_{w} is employed for the SR component when its tracking presents a lower accuracy, such as over fields. The employed K_{w} value is provided explicitly when presenting the different results. Also, it is important to understand that the channel sounder was calibrated before the measurements. Thus, the power measured for each component can be seen as the attenuation suffered by that component because of its propagation through the channel. This is valid for the power, or attenuation, of all components shown throughout this section.

Computing the Slow Fading of the LoS and SR Components

The slow fading is obtained by comparing the received power of each component, i.e, P_{los} and P_{sr}, with the power expected in theory if only the FSPL between both aircraft is taken into account, which can be obtained as

$$\alpha_{\mathrm{p}}(m) = \left(\frac{\mathrm{c}_0}{4\pi f_{\mathrm{c}} d(m)}\right)^2 , \tag{3.28}$$

where $d(m)$ is the distance traveled by the component at the time index m, i.e., $d_{\mathrm{los}}(m)$ and $d_{\mathrm{sr}}(m)$ for the LoS and SR components, respectively. These distances are derived from the delay estimated by the tracking algorithm for each component.

Of course, the power of a component is also affected by the gain of the transmitting and receiving antennas, which changes with the geometry between the aircraft, as well as between them and the ground in the case of the SR component. According to the laboratory measurements conducted by the manufacturer, the antennas are omnidirectional in the azimuth plane and present a maximum gain of approximately 4 dBi. The main radiation lobe spans approximately elevations from 5 to 40 degrees, decreasing rapidly for higher elevation angles and presenting multiple side-lobes. Unfortunately, the radiation pattern was only measured in the laboratory and not mounted on the aircraft, and thus it is expected to diverge, although not too significantly, from the one experienced during the flight.

Computing the Fast Fading of the LoS and SR Components

In order to characterize the fast fading of each component, we first compensate the slow fading of each component by applying a moving average filter as in [Ber+15]. In other words, the measured power of each component is normalized to its slow fading, such that the underlying fast fading can be characterized. For this, one must assume the channel to be stationary during the filter's length of M_w samples. A common approach is to consider the channel to be stationary at least between tenfold to hundredfold of the signal wavelength with respect to the aircraft velocity. Following this approach, we choose M_w such that a distance of 70λ is covered by the aircraft. Thus, M_w changes according to the slowly-changing aircraft speed. Similar analyses consider larger distances with respect to the wavelength, e.g., over 100λ in [Ber+15] and 170λ in [WRJ19], being our analysis more conservative in terms of the assumed stationarity. The mean power of each component within the averaging window is estimated as

$$P_\mathrm{LS}(m) = \frac{1}{M_\mathrm{w}} \sum_{m'=m-M_\mathrm{w}/2}^{m+M_\mathrm{w}/2-1} P(m') \tag{3.29}$$

and its amplitude without slow fading effects as

$$|h'(m)| = \sqrt{\frac{P(m)}{P_\mathrm{LS}(m)}}\,. \tag{3.30}$$

Note that P_LS is computed using only the component under test, i.e., either the LoS or the SR component, while other works use the average of all components jointly, e.g., [Ber+15]. We choose this normalization because the aim is to analyze each component independently of the others.

The distribution of the measured fast fading of the LoS and SR components can be compared with multiple theoretical distributions usually considered in the literature.

For simplicity and easier reproducibility of our results, the maximum likelihood estimate for each theoretical distribution is obtained by using the inbuilt MATLAB *mle* function[6]. In order to decide which distribution fits the fading envelope more accurately, we use the commonly employed (see [WRJ19; Ber+15]) Kolmogorov–Smirnov (KS) test with the goodness-of-fit (GoF) indicator [MJ51] obtained as

$$\mathrm{GoF} = \sup_{z}\{|F_Z(z) - F_0(z)|\}\,, \tag{3.31}$$

where $\sup\{\cdot\}$ is the supremum, $F_Z(z)$ is the cumulative distribution function (cdf) of the measured data, and $F_0(z)$ is the cdf of the fitted distribution. A lower GoF value indicates a better fit. The results of this comparison, together with the parameters of the best-fitting distribution, will be discussed in Section 3.2.4.

Computing the Power of the Scattering Components

A separate section is devoted to the scattering components, given that they cannot be tracked or measured the same way the LoS and SR components are. Tracking or measuring the scattering components is very challenging, as they appear just after the SR component, which in many scenarios is much stronger. Also, because of the spread in delay and Doppler of the main channel components, shown in Appendix B, the SR component generally conceals the scattering components presenting a similar delay, which in turn are usually the most powerful ones. We explore two different ways to measure them: one for the forest scenario and one for the lake scenario. The field scenario is not considered because it was not possible to identify when the SR component was present together with the scattering components.

The forest scenario is the simplest one in terms of measuring the power of the scattering components, since virtually no SR component is present. Thus, one can measure the power of the scattering components by using a delay window as done for the LoS and SR components. However, in this case, the delay window starts slightly before the SR delay, in order to also include the ramp-up part caused by the time- and bandwidth-limited sampling of the channel. The power of the scattering components is then obtained as

$$P_{\mathrm{scatt}}(m) = \sum_{k'=k_{\mathrm{sr}}-K_{\mathrm{w,bef}}}^{k_{\mathrm{sr}}+K_{\mathrm{w,aft}}} |h(m,k')|^2\,, \tag{3.32}$$

where $K_{\mathrm{w,bef}} = 1$ and $K_{\mathrm{w,aft}} = 18$ for a 1-μs measuring delay window. Note that the SR delay k_{sr} has been determined manually for each WF in the forest scenario instead of by

[6]The MATLAB *mle* function finds the maximum likelihood estimate of the distribution under test by minimizing a negative log-likelihood function built as the negative logarithm of the product of the probabilities of the observations given the parameters of the distribution.

using the algorithm proposed for the LoS and SR components, because the scattering components could not be tracked faithfully.

In the lake scenario, the SR component is always present (see Fig. 3.7a), so the technique used for the forest scenario would not be valid. One could think of measuring their power immediately after the SR component, i.e., from the next delay bin, but that is not possible given the spread of the SR component in delay (see Appendix B). There is, however, a way to measure the power of the scattering components. Paying attention to the SF shown in Fig. 3.7b, one can see that the strongest scattering components can be separated from the SR component in the Doppler domain. Thus, one can measure the scattering components in a delay/Doppler region that excludes the SR component. This is done by first obtaining the SF in blocks of 1 second. Then, the delay and Doppler shift of the SR component is estimated through a peak search in the delay/Doppler plane. The delay/Doppler window to measure the scattering components is 1 µs long in delay and starts from one delay bin (50 ns) after the SR delay. To exclude the SR component in the Doppler domain, only the values that are at least 5.5 Hz[7] away from the SR Doppler shift are considered. The SF within the delay/Doppler window is then used to obtain the power of the scattering components. Note that the way we obtained the power of the scattering components in the forest scenario allowed us to measure it for each WF, while in the lake scenario we have to obtain the SF by using blocks of WFs spanning 1 second. As a result, fewer (but more solid) estimations of the power of the scattering components are available in the lake scenario compared to the forest scenario.

The obtained power of the scattering components P_{scatt} is then used to estimate the radar cross section (RCS) σ_{RCS} based on the bistatic radar equation [Sko08; FD20]

$$\frac{P_{\text{r}}}{P_{\text{t}}} = G_{\text{t}} G_{\text{r}} \frac{{c_0}^2}{f_c^2 (4\pi)^3 (d_{\text{t,sc}} d_{\text{sc,r}})^2} \sigma_{\text{RCS}} \,, \tag{3.33}$$

where P_{r} and P_{t} are the received and transmitted power, respectively, whose relation $P_{\text{r}}/P_{\text{t}}$ is obtained when measuring the scattering components power in the calibrated channel measurements. The actual transmit and receive antennas gains, G_{t} and G_{r} respectively, can be roughly estimated from the geometry taking into account the antenna radiation pattern provided by the antenna manufacturer. The distance from the transmitter to the scattering point $d_{\text{t,sc}}$ and from it to the receiver $d_{\text{sc,r}}$ can also be obtained from the geometry. In reality, these geometry-dependent parameters change for the different scatterers contributing to the scattering components. However, the most powerful scattering components are present in the area near the SR point and the geometry is practically identical for all of them, yielding roughly the same geometry-dependent

[7]This value has been obtained experimentally based on our observations.

parameters. Thus, we approximate the above-mentioned geometry-dependent parameters, such as G_t, G_r, $d_\mathrm{t,sc}$, and $d_\mathrm{sc,r}$, to the ones obtained at the SR point. This way, using the measured scattering components power $P_\mathrm{scatt} = P_\mathrm{r}/P_\mathrm{t}$ and deriving G_t, G_r, $d_\mathrm{t,sc}$, and $d_\mathrm{sc,r}$ from the geometry, one can estimate σ_RCS using (3.33). Of course, these parameters depend on the geometry and, thus, might change from measurement to measurement, e.g., between consecutive WFs. Note that we measure the RCS of the ground as a specific target and not as a surface. This is done on purpose as it will later help us to define the A2A channel model in Section 3.4.

Removing the LoS and SR Components. Before measuring the power of the scattering components, we have to suppress the LoS and SR components from the data. Despite the LoS component presenting a much lower delay than the scattering components, the spread in delay caused by the time- and bandwidth-limited sampling of the channel (see Appendix B) leads to having to remove it, as much as possible, to have a realistic measure of the power of the scattering components. Of course, the same applies to the SR component in the lake scenario, where it is beneficial to remove it in order to mitigate its impact on the nearby scattering components. No SR component is present in the forest scenario and, thus, it is not removed. Suppressing MPCs is a common technique employed by tracking algorithms, such as the well-known SAGE algorithm [Fle+99], to find other MPCs hidden below the stronger ones, which are tracked and suppressed first. We use the same approach, which consists of firstly finding the delay of the LoS and SR components, already done in a previous step (see Fig. 3.9), and secondly using the model recreating the spreading of each component in delay, given by (B.5), to subtract the LoS and SR components from the weight function. An example of the result is shown in Fig. 3.10, where the average PDP measured within 1 second when flying over a lake is shown. One can see that the suppression of both components is not perfect but their peaks are suppressed by approximately 20 dB and, more importantly, their sidelobes are brought effectively under the noise floor, making sure that they do not affect the measurement of the scattering components.

3.2.4 Fading Analysis of the LoS and SR Components

The fading statistics of the LoS and SR channel components are analyzed in this section. We distinguish between the large-scale (slow) fading and the small-scale (fast) fading. The slow fading is mainly caused by the change in the geometry between the transmitter and the receiver, as well as with the ground surface for the SR component. The change in the geometry can lead to different antenna gains, to possible blockages of the components by obstacles, and to a variation of the reflection coefficient. As it

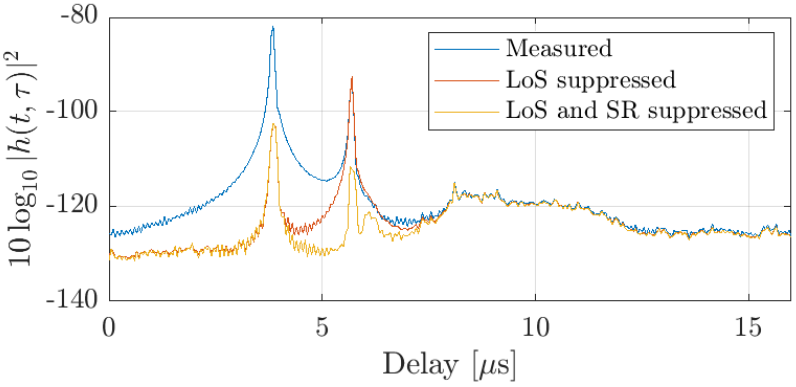

Figure 3.10. Average PDP measured in the lake scenario, during 1 second, with and without suppressing the LoS and SR components.

will be shown, these changes are generally slow and can be roughly estimated if the actual geometry is taken into account, for example by computing the expected FSPL affecting each component. By contrast, the small-scale fading is caused by a compound of many rapidly-changing effects. Among others, one can highlight the presence of non-resolvable MPCs near the antennas, e.g., caused by the propellers or by the aircraft fuselage, or near the SR reflection point, as well as the short-term fluctuations of the aircraft, e.g., vibrations. Since the many effects contributing to the fast fading cannot be resolved or realistically modeled separately, statistical distributions with scenario-dependent parameters are generally used to model them as a whole.

Power of the LoS Component

Once the LoS component is tracked as described before, its power is measured by using a delay window of 0.25 µs. The LoS component power for some chosen scenarios is depicted in Fig. 3.11. The results for the remaining scenarios can be found in Appendix A (Fig. A.2 and Fig. A.3). Note that the channel sounding devices were calibrated before and after the measurements, such that the transmit power used for the measurements does not play a role in the results shown here. Thus, the resulting power can be understood as the attenuation suffered by the signal component when propagated through the channel. In the scenarios shown in Fig. 3.11, both aircraft fly at the same altitude (600 m above ground) and use different antenna configurations. First, one can see that the LoS component remains very stable throughout all flight segments, with no sharp changes in its power like the ones observed during the banking maneuvers in Fig. 3.8. Second, a very significant ripple in the LoS component power can be observed when the top antenna of the Dornier (receiver) is used (Fig. 3.11b). This ripple has been observed in all measurements where the top antenna of the Dornier

is employed and is not present when its bottom antenna is used. In order to identify the cause of the ripple, Fig. 3.12 shows one SF measured in each scenario. The results for the remaining scenarios can be found in Appendix A (in Fig. A.5). One can clearly see that, in the scenarios where the top antenna of the Dornier is employed, there are additional components with the same delay as the LoS component but with a Doppler shift of approximately ±120 Hz.

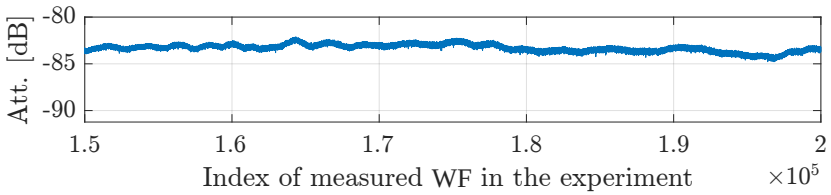

(a) LOS-D-D-600-600 scenario.

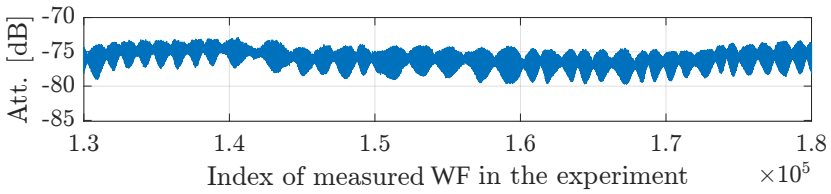

(b) LOS-D-U-600-600 scenario.

Figure 3.11. Measured LoS component attenuation (or relative power) in two scenarios with both aircraft at 600 m above ground.

This can be explained by the propellers employed by the Dornier, which are located very close to its top antenna, as shown in Fig. 3.2, and whose rotation might lead to a modulation of the wave reflected off them. In fact, the Dornier employs five propeller blades and flies at 1400–1420 revolutions per minute (rpm), whereas the Cessna employs three propeller blades and flies at 1700–1800 rpm. This leads to modulation frequencies of roughly ±118 Hz and ±88 Hz caused by the propellers of the Dornier and Cessna, respectively[8]. Thus, one can conclude that the ripple in the LoS component power is caused by the propellers of the Dornier when its top antenna is employed. Although the components caused by the propeller of the Cessna can also be seen slightly in Fig. 3.12 at around ±90 Hz, they are not as strong as the ones caused by the Dornier because of the larger distance between the antennas and propeller of the Cessna. Interestingly, one can also see additional components at ±120 Hz Doppler shifts with the SR delay, which are caused by the reflection of the SR component off the propellers of the Dornier.

Consequently, when measuring the power of the LoS component, we also account for the effect of the propellers. They appear at practically the same delay as the

[8]The modulation frequency is obtained by multiplying the number of propeller blades by the revolutions per second of the propeller.

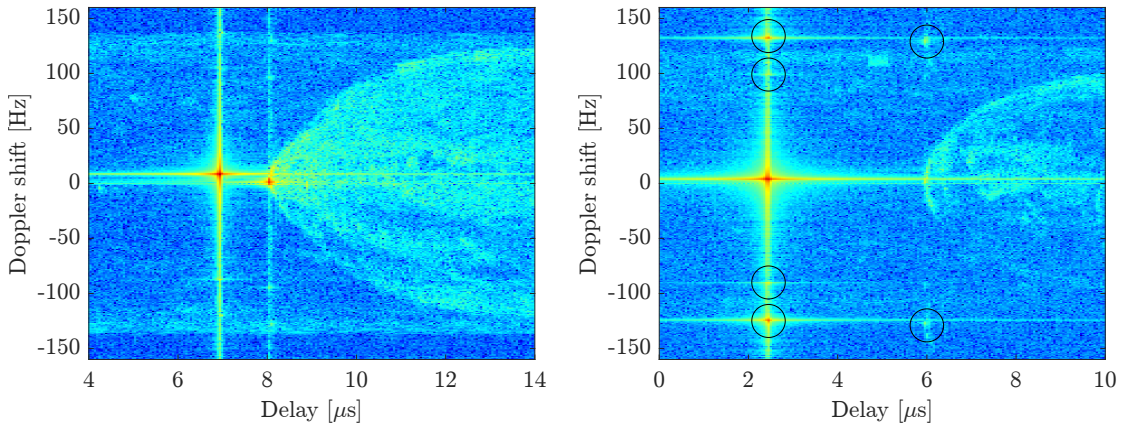

(a) LOS-D-D-600-600 scenario. (b) LOS-D-U-600-600 scenario.

Figure 3.12. Measured SF (1 second) in different scenarios of interest with the aircraft at the same altitude. One can see the significant MPCs at the LoS delay with ±120 Hz Doppler shifts caused by the propeller blades of the Dornier (receiver) when its top antenna is used (Fig. 3.12b). The MPCs caused by the propellers of the Cessna are weaker but also visible at ±90 Hz Doppler shifts. These components are highlighted with black circles for clarity.

LoS component and they could only be separated from the LoS component in the Doppler domain, which would require a block-wise analysis where valuable statistics of the short-term fading of the LoS component would be lost because of the implicit block averaging. Thus, we decide not to separate them from the LoS component and consider it as an intrinsic effect contributing to its fast fading statistics. This will allow the reader to use the fast fading statistics, e.g., the Rician K-factor, of the measured scenario that best matches its own scenario to model, e.g., with or without propellers near the antenna. The same applies to the SR component.

In order to compare the LoS component power between the different scenarios, we compute the LoS component power relative to the theoretical FSPL, which can be obtained using (3.28). Figure 3.13 shows the estimated pdf[9] of the measured LoS component power relative to the FSPL power in the different scenarios of interest.

LoS component for multiple antenna configurations with the aircraft at the same altitude. Let us first analyze the results shown in Fig. 3.13a, where both aircraft fly at the same altitude and the bottom antennas are used. In these scenarios, the relative LoS component power is stable between 2 dB and 4 dB at the three considered

[9]The graphical representation of the pdfs is obtained as an estimation of the pdfs based on a normal kernel function by using the in-built *ksdensity* function of MATLAB.

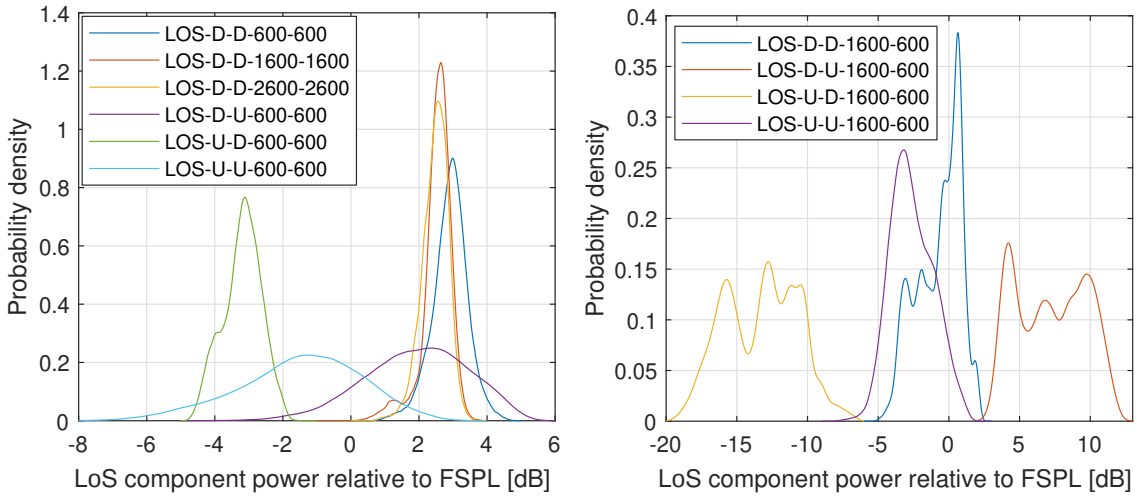

(a) Aircraft at the same altitude.

(b) Aircraft at different altitudes.

Figure 3.13. Estimated pdf of the LoS component power relative to the FSPL in different scenarios of interest. Adapted from [BMFW22]. © 2022 IEEE.

flight levels. This is to be expected, given that the bottom antennas are used and generally nothing obstructs the direct path between them. In addition, the antenna elevation is low and a slight joint antenna gain (> 0 dBi) is expected. The results change significantly when other antenna configurations are employed. Using an up-to-down antenna configuration (LOS-U-D-600-600 in Fig. 3.13a) yields a significantly lower relative power. This might be caused by the fact that the aircraft do not fly strictly parallel to the ground but raising their noses slightly, i.e., 3.7° on average as measured at the Cessna in this scenario. Therefore, a part of the Cessna fuselage, mainly its cockpit, obstructs the LoS path and leads to a higher attenuation compared to the other scenarios. Using the top antenna of the Dornier for reception results in greater variations in the LoS component power, which is now between -6 dB and 5 dB. This wider range is caused by the ripple already observed in Fig. 3.11, which we concluded to be caused by the propellers of the Dornier being close to its antenna. Because of the slight aircraft pitch-up, the down-to-up configuration yields a higher average power compared to the up-to-up case, while the width of their pdfs is similar.

LoS component for multiple antenna configurations with the aircraft at different altitudes. Fig. 3.13b shows the results for the four antenna configurations when the aircraft flew at 1600 m and 600 m above ground, respectively. One can see that the relative power changes now significantly compared to when the aircraft fly at the same altitude. The down-to-up antenna configuration yields now the highest relative power, which is to be expected given that the geometry in this scenario maximizes the

antenna gain. The opposite case is observed in the up-to-down antenna configuration, where both aircraft obstruct the direct LoS path. The down-to-down and up-to-up configurations yield a more moderate LoS component power, but still cover a wide power range because of the presence of multiple peaks in the pdfs. In general, we observe that the pdfs shown in Fig. 3.13b are significantly wider than those shown in Fig. 3.13a. This is explained by the fact that the angle between both aircraft changed significantly during each flight, which led to fluctuations in the antenna gain and, consequently, to multiple peaks in the power pdf. This was verified by estimating, for each WF used to measure the power of the component, the elevation angle of the antennas at the time of measuring the WF. Then, the relation between the transmit antenna elevation angle and the power of the component is depicted, for two scenarios, in the histograms shown in Fig. 3.14. Figure 3.14a shows this relation in the LOS-D-U-1600-600 scenario and demonstrates that the antenna elevation angle changed during the flight, which led to fluctuations in the power. The results for the LOS-U-D-1600-600 scenario are shown in Fig. 3.14b. In this case, the top antenna is used for transmission and the geometry leads to the LoS path being blocked by the fuselage of the aircraft, yielding a much lower LoS component power. Note that negative angles are used to indicate that the transmit antenna is pointing up instead of down. Of course, a lower negative angle represents a more obstructed LoS path, which leads to a lower relative power as shown in Fig. 3.14b.

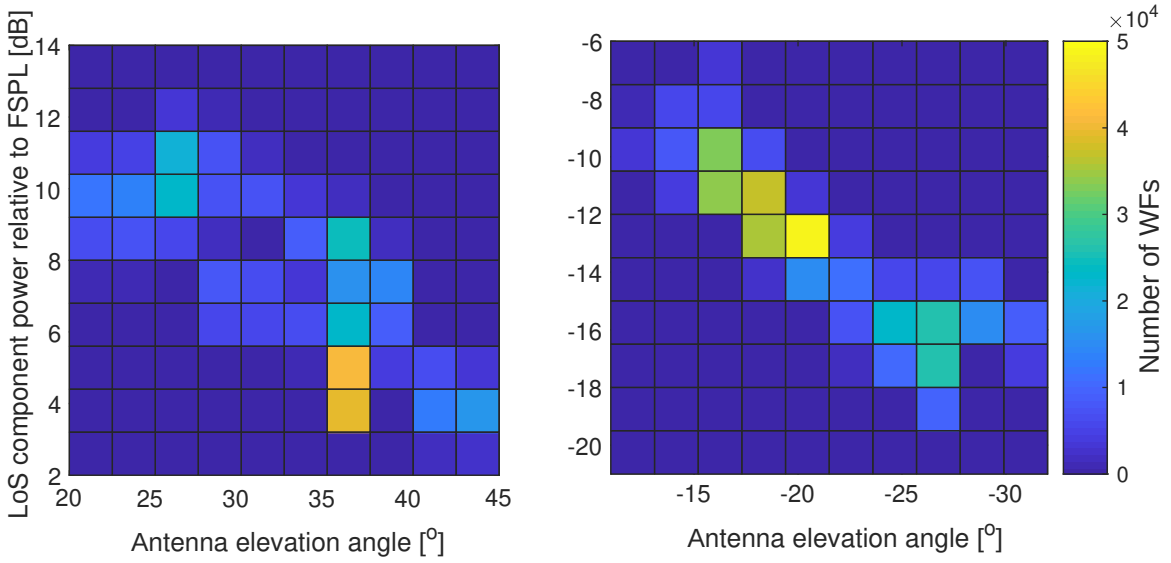

(a) LOS-D-U-1600-600 scenario.

(b) LOS-U-D-1600-600 scenario.

Figure 3.14. Histogram of the LoS component power relative to the FSPL for different TX antenna elevation angles. Adapted from [BMFW22]. © 2022 IEEE.

Power of the SR Component over Lakes

The power of the SR component is measured when flying over multiple lakes. Figure 3.15 shows the obtained results for two scenarios where the aircraft flew at 600 m above the lake surface with different antenna configurations. The results for the remaining scenarios can be found in Appendix A (Fig. A.4). As already observed in the LoS component, the power of the SR component presents a significant ripple only when the top antenna of the Dornier is employed. This is shown clearly in Fig. 3.15b. Again, this ripple is caused by the propellers of the Dornier. Actually, one can also observe in Fig. 3.12b the components caused by the propellers at roughly ±118 Hz with the same delay of the SR component. When the bottom antenna of the Dornier is employed, the SR component power is quite stable and does not fluctuate significantly.

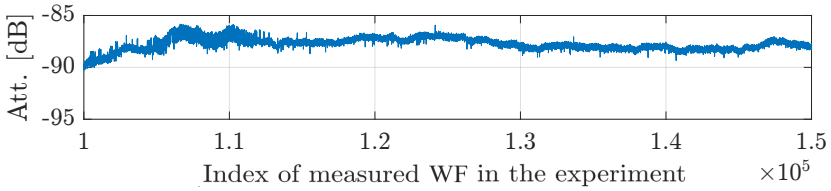

(a) SR-D-D-600-600 scenario.

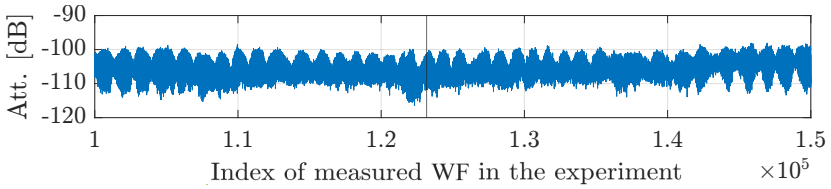

(b) SR-D-U-600-600 scenario.

Figure 3.15. Measured SR component attenuation (or relative power) in multiple scenarios with both aircraft at 600 m above ground.

Figure 3.16 shows the pdf of the SR component power relative to the FSPL for multiple antenna configurations with both aircraft flying at the same altitude. One can notice the very strong and stable SR component when the bottom antennas are employed and the aircraft fly at a low altitude, i.e., at 600 m. However, the SR component power decreases significantly when flying at a higher altitude, i.e., at 1600 m. Again, this is caused by the change in the antenna elevation angle, which leads to a decrease in the antenna gain affecting the SR component. This can be seen in Fig. 3.17. The SR component power at 600 m (Fig. 3.17a) is reduced as the antenna elevation angle increases and leaves the main antenna radiation lobe. At 1600 m (Fig. 3.17b), the elevation angle was significantly higher, i.e., between 60 and 65 degrees, leading to lower antenna gains and, consequently, to the lower power shown in Fig. 3.16. Of course, the reflection coefficient of the water surface is also affected by the geometry

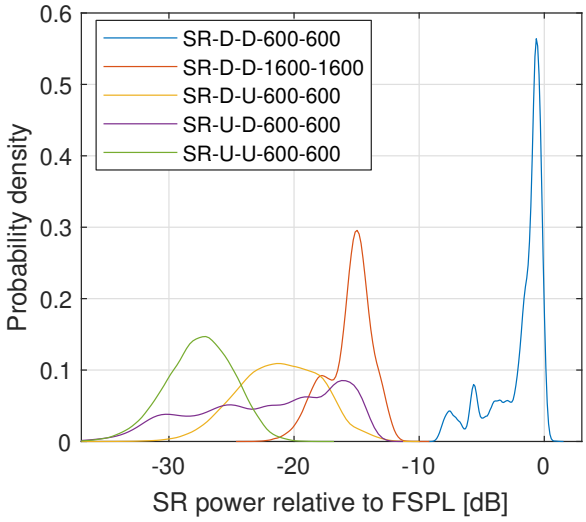

Figure 3.16. Estimated pdf of the SR component power relative to the FSPL in different scenarios of interest. Adapted from [BMFW22]. © 2022 IEEE.

and might have led to additional fluctuations in the SR component power. In the other scenarios, where at least one top antenna is employed, the SR component is mostly blocked by the aircraft fuselage and presents a much lower power. The SR component is attenuated the most in the up-to-up antenna configuration.

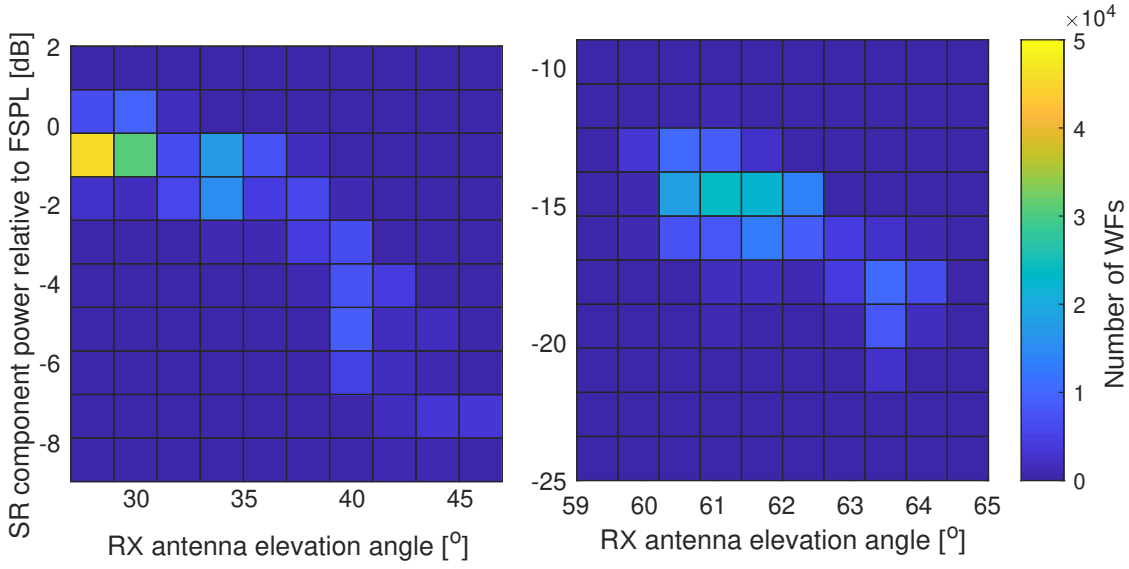

(a) SR-D-D-600-600 scenario.

(b) SR-D-D-1600-1600 scenario.

Figure 3.17. Histogram of the SR component power relative to the FSPL for different RX antenna elevation angles. One can see in Fig. 3.17a that the SR component power decreases significantly as the antenna elevation angle increases. Adapted from [BMFW22]. © 2022 IEEE.

Small-Scale Fading

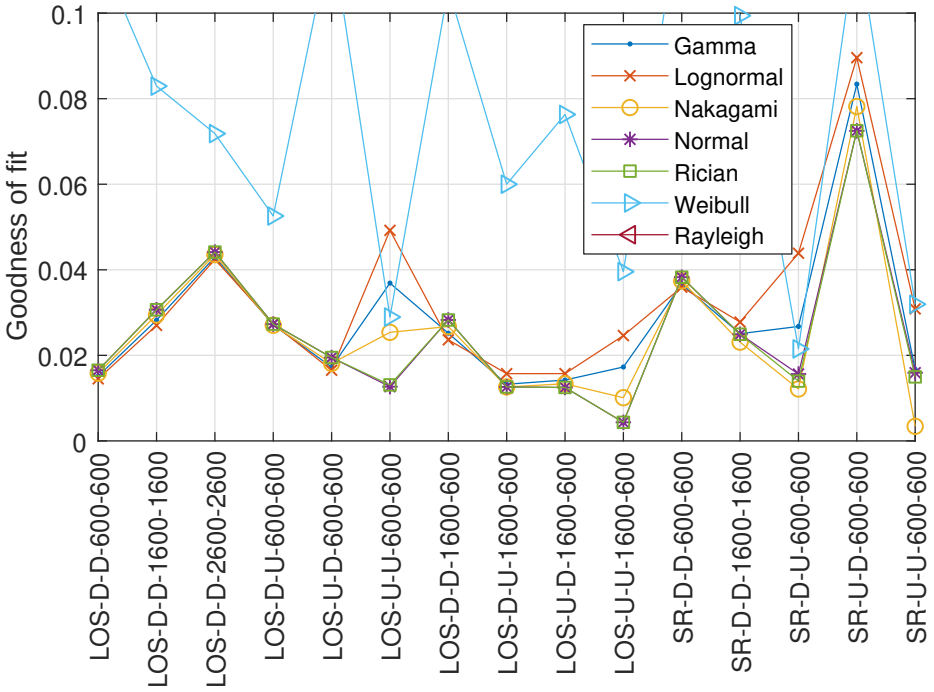

Figure 3.18. Small-scale fading analysis. GoF values for different fitted distributions in the scenarios of interest for the LoS and SR components. The Rayleigh distribution provides the worst fit and its GoF lies above the depicted limits. Adapted from [BMFW22]. © 2022 IEEE.

Once the amplitude of the LoS and SR components without large-scale fading is computed following (3.30), we obtain the best fit that multiple well-known distributions can provide in the different scenarios. In order to identify which distribution provides the best fit in each scenario, the GoF indicator is obtained using (3.31). The results can be seen in Fig. 3.18 for the LoS and SR components in the different scenarios of interest. In general, with the exception of the Weibull and Rayleigh distributions, all considered distributions are capable of achieving a similarly good fit for the LoS component's envelope. However, when the up-to-up antenna configuration is used, the normal and Rician distributions provide a better fit than the others. The envelope of the SR component can also be realistically modeled using some of these distributions, as they provide a reasonably good fit in most scenarios. However, one can see that the best fits are achieved by the Rician and Nakagami distributions. In general, a strong SR component is better represented by a Rician distribution, e.g., when bottom antennas are employed, and a weak SR component is better modeled with a Nakagami distribution, e.g., in the up-to-up configuration. It is to be noted that the fit for the SR component in the SR-U-D-600-600 scenario is significantly worse than the fit achieved

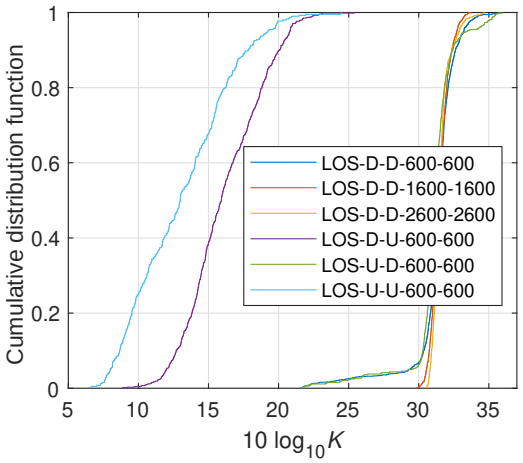

(a) LoS component at same altitude.

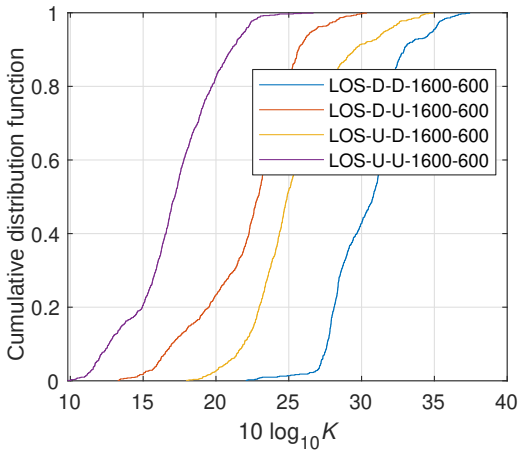

(b) LoS component at different altitude.

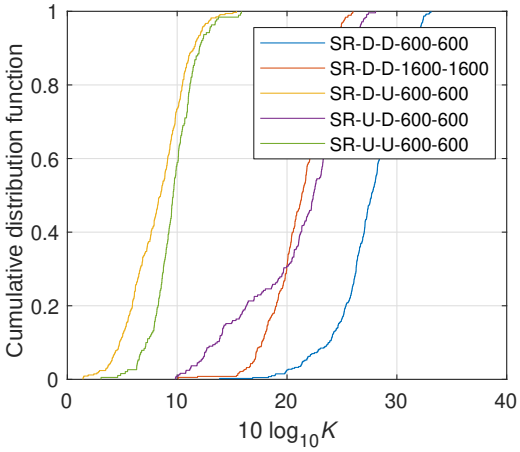

(c) SR component over lake.

Figure 3.19. Cumulative distribution function of the estimated Rician K-factor in each scenario with TX and RX at the same altitude (Fig. 3.19a and Fig. 3.19c) and at different altitudes (Fig. 3.19b). Adapted from [BMFW22]. © 2022 IEEE.

in the other scenarios. We believe this to be caused by short-term flight maneuvers not sufficiently compensated when removing the large-scale fading.

Given that the Rician distribution has shown to provide a good fit for the LoS and SR components in all scenarios, we estimate the Rician K-factor using the method of moments [GME99; Abd+01], as commonly done in the literature, e.g., see [Unt+21; WRJ19]. More information on the Rician distribution and on the Rician K-factor can be found in Appendix A. As explained in Section 3.2.3, we use a sliding window of variable length to estimate the characteristics of the fast fading, such that the channel can be considered stationary within the window. Thus, multiple estimations of the Rician K-factor are obtained in each scenario. Figure 3.19 shows the cdf of

Table 3.2. Nakagami distribution parameters fitted to the SR component [BMFW22].

Scenario	$\hat{\mu}$	Var$\{\mu\}$	$\hat{\omega}$	Var$\{\omega\}$	GoF
SR-D-D-600-600	209.24	0.39	1.000	2e-8	0.037
SR-D-D-1600-1600	54.15	0.03	1.000	9e-8	0.023
SR-D-U-600-600	3.55	1e-4	0.993	1.5e-6	0.012
SR-U-D-600-600	31.92	1.5e-2	0.997	2.4e-7	0.078
SR-U-U-600-600	5.07	4.7e-4	0.995	1.9e-6	0.003

the estimated Rician K-factor for both components in the different scenarios. As expected, the LoS and SR components are best modeled using a high K-factor when the components are received with a high power and they are not disturbed by parts of the aircraft fuselage, such as the propellers of the Dornier. For example, one can see in Fig. 3.19a that using the bottom antennas of the Dornier leads to a very high and almost constant K-factor for the LoS component. By contrast, if the top antenna of the Dornier is used, the K-factor decreases significantly because the propellers of the Dornier cause the aforementioned ripple in the LoS component. A perfect example for this is the LOS-D-U-1600-600 scenario shown in Fig. 3.19b, where the highest relative power was measured (see Fig. 3.13b) but the top antenna leads to a low K-factor, compared to the one obtained whenever the bottom antenna of the Dornier is employed. A similar effect is observed for the SR component in Fig. 3.19c. The highest K-factor for the SR component is obtained when the SR component is strongest and the bottom antennas are used, i.e., in the SR-D-D-600-600 scenario. As the power of the SR component decreases, e.g., because of the geometry and the antenna gain, the K-factor is also reduced. As observed for the LoS component, the minimum K-factor for the SR component is again obtained when the top antenna of the Dornier is employed and the component is affected by its propellers. In these cases, Fig. 3.18 shows that a Nakagami distribution yields a better fit. For the sake of completeness, Table 3.2 lists the parameters of the Nakagami distribution fitted to the envelope of the SR component. More information on the Nakagami distribution and its parameters can be found in Appendix A. As expected, the variance of the shape parameter μ of the Nakagami distribution is lowest in the scenarios where the top antenna of the Dornier is employed. It is to be noted that, although the Nakagami distribution yields a slightly better fit than the Rician distribution for the SR component in some scenarios, the difference is marginal and it would still make sense to model the SR component using a Rician distribution, as the scenarios can be entirely parameterized with the K-factor and its implementation is generally faster.

3.2.5 Power and Radar Cross Section of the Scattering Components

The measured relative power and σ_{RCS} of the scattering components for the forest and lake scenarios are presented in this section. Only the scenarios where the aircraft flew 600 m above ground using bottom antennas are considered, since in these scenarios the noise floor was still significantly below the scattering components (at least 15–20 dB). Considering higher altitudes or the use of top antennas would yield less accurate results, as the scattering components are weaker and closer to the noise floor. Multiple flight segments of 20 seconds each are considered for each measurement. These are shown in Appendix A (Fig. A.6) for completeness and comprise four segments for the forest scenario and seven for the lake scenario.

The results for the forest scenario are shown in Fig. 3.20 as histograms. The measured relative power of the scattering components as well as the estimated RCS present a shape similar to a normal distribution in the logarithmic domain. Note that, although P_{scatt} and σ_{RCS} are proportional to each other according to (3.33), the proportionality factor depends on geometry-dependent factors, e.g., the antenna gain, and thus might change from measurement to measurement, i.e., between consecutive WFs. One can model $10\log_{10}\sigma_{\mathrm{RCS}}$ with a normal distribution $\mathcal{N}(\mu = 43.8, \sigma^2 = 8.36)$, whose parameters are obtained as the maximum likelihood estimate using

$$\mu = \frac{1}{L_{\mathrm{RCS}}} \sum_{i=0}^{L_{\mathrm{RCS}}-1} 10\log_{10}\sigma_{\mathrm{RCS},i} \tag{3.34}$$

for the mean and

$$\sigma^2 = \frac{1}{L_{\mathrm{RCS}}} \sum_{i=0}^{L_{\mathrm{RCS}}-1} \left(10\log_{10}\sigma_{\mathrm{RCS},i} - \mu\right)^2 \tag{3.35}$$

for the variance, being L_{RCS} the number of estimations of σ_{RCS}. Note that σ_{RCS} is given in square meters but we spare the logarithm units notation for simplicity. The variance estimator (3.35) is biased but allows to obtain the normal distribution that is *most likely* to match the measured data. For the sake of completeness, and to demonstrate the small difference between the two, we also indicate in the caption of each figure the variance obtained using the unbiased estimator

$$\sigma^2_{\mathrm{ub}} = \frac{1}{L_{\mathrm{RCS}}-1} \sum_{i=0}^{L_{\mathrm{RCS}}-1} \left(10\log_{10}\sigma_{\mathrm{RCS},i} - \mu\right)^2 . \tag{3.36}$$

The lake scenario is more difficult to analyze, given that the need to get the Doppler information via the SF leads to fewer measurements per segment. Analyzing the segments comprising the lake scenario in blocks of 1 second yields the results shown

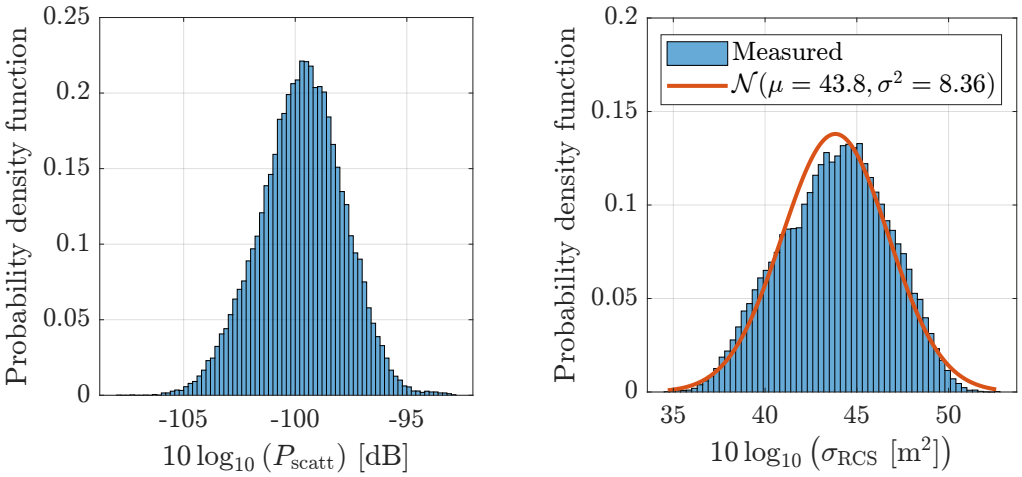

(a) Relative power.

(b) Estimated RCS.

Figure 3.20. Histogram of the relative power, or attenuation, of the scattering components and of the RCS measured in the forest scenario. A normal distribution $\mathcal{N}(\mu = 43.8, \sigma^2 = 8.36)$ can be used to model $10\log_{10}\sigma_{\text{RCS}}$. The unbiased estimator (3.36) also yields a variance of 8.36 dB. Note that σ_{RCS} is given in square meters and P_{scatt} is a relative power or attenuation as defined in (3.32).

in Fig. 3.21. The histogram of the power of the scattering components (Fig. 3.21a) suggests that two different distributions might be present in the data. Looking into the results more specifically, it becomes clear that three flight segments present significantly weaker scattering components than the other four segments. Within each segment, however, no strong divergences in the power of the scattering components are observed. After visually verifying this difference in power between segments in the SF of each segment, we reach the conclusion that the state of the lake surface, e.g., either calmer or rougher, affected significantly the RCS of the water surface and the power of the scattering components. To visualize this, we show in Fig. 3.22 the SF of one segment of each subset. One can see that the main scattering components, arriving after the SR delay, are much stronger in Fig. 3.22b than in Fig. 3.22a, where in turn are only present at negative Doppler shifts.

Figure 3.21b shows the histograms of $10\log_{10}(\sigma_{\text{RCS}})$ for both subsets separately, as well as their maximum likelihood estimate fit with a normal distribution. Assuming that the reason for the significant difference in power was caused by the state of the lake surface, one could use the subset with lower σ_{RCS}, i.e., following $\mathcal{N}(\mu = 38.8, \sigma^2 = 0.67)$, to obtain the scattering components for calmer lakes, and the subset with higher σ_{RCS}, i.e., following $\mathcal{N}(\mu = 43.7, \sigma^2 = 2.05)$, to recreate rougher lake conditions. Nonetheless, this should be confirmed by future research.

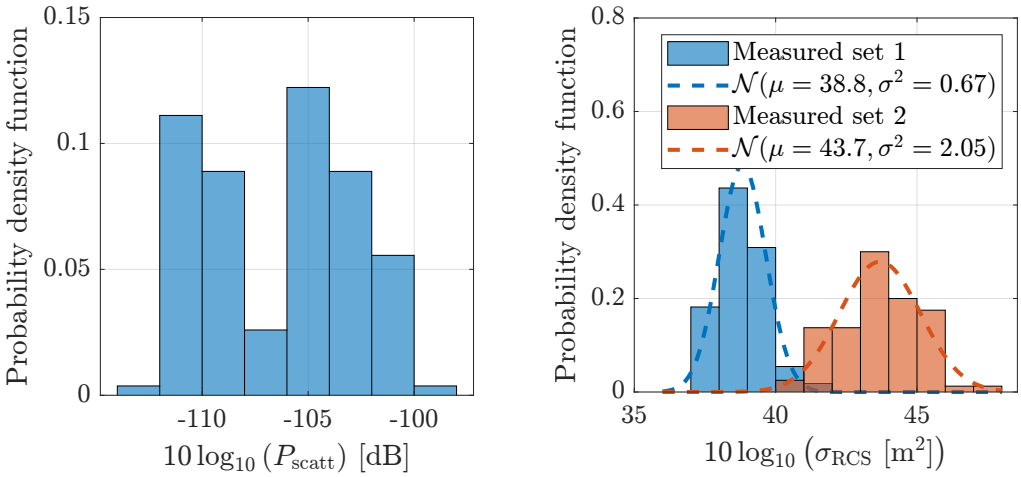

(a) Relative power. (b) Estimated RCS.

Figure 3.21. Histogram of the relative power, or attenuation, of the scattering components and of the RCS measured in the lake scenario. A normal distribution can be used to model $10\log_{10}\sigma_{\text{RCS}}$. The parameters of the distribution depend on the calmness or roughness of the water surface. The unbiased estimator (3.36) yields a variance of 0.69 dB for the first set and 2.07 dB for the second one. Note that σ_{RCS} is given in square meters and P_{scatt} is a relative power or attenuation as defined in (3.32).

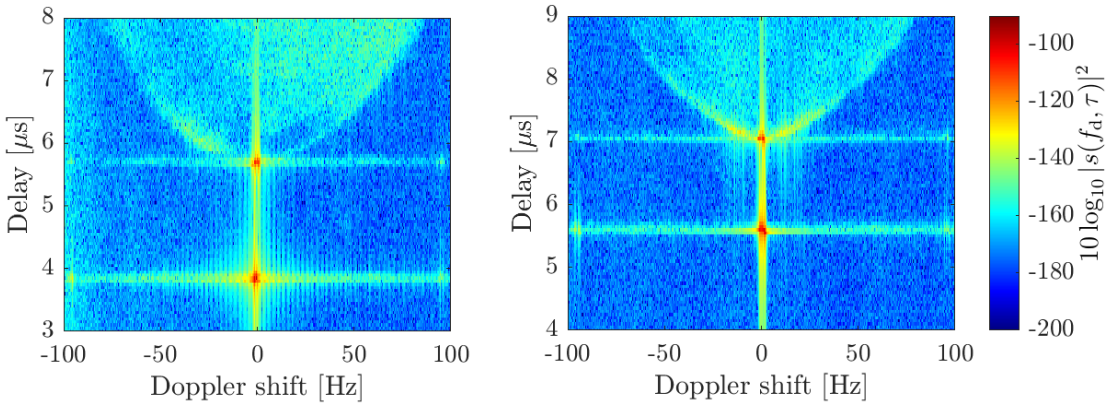

(a) From subset with lower RCS. (b) From subset with higher RCS.

Figure 3.22. Measured SF in two of the seven segments used to measure the power of the scattering components and the RCS of a lake. Each segment corresponds to one subset of segments presented separately in Fig. 3.21b.

3.3 Delay-Doppler Probability Density Function

The LoS and SR components can now be fully characterized through geometrical considerations, which provide the delay and Doppler shift of both components, and using

the fading statistics derived from the measurements. The scattering components can also be characterized in terms of power and RCS thanks to the analysis conducted in Section 3.2. However, the measurements showed that they present a unique distribution in the delay and Doppler domains (see Figs. 3.5–3.7) that has not been characterized so far. This distribution is of special interest for designing datalinks based on multi-carrier waveforms, since the distribution of the channel components over the delay/Doppler plane plays a crucial role. Thus, the focus is placed now on modeling the peculiar delay and Doppler frequency distribution of the scattering components accurately. For this, we propose in this section a novel methodology to recreate analytically the scattering components in any arbitrary M2M channel and then verify it in multiple A2A scenarios by comparing its results with measurements. A particularity of the proposed approach is that it allows to obtain the time-variant joint delay-Doppler pdf of the channel without having to rely on the autocorrelation functions under the WSSUS assumption. The contents of this section have been published by the author in [BMW24].

3.3.1 Methodology

The proposed methodology comprises two main steps. First, the environment around the transmitter and receiver is recreated using planes. Second, assuming that the scatterers causing the scattering components are distributed uniformly over the planes, the scattering components of the channel are characterized semi-analytically. A time-variant representation of the channel can be accomplished by re-obtaining the channel as the stations move through the environment and the geometry with the surrounding planes changes. In previous works, the concept of using a single plane to obtain the scattering components was applied to V2V [WSF14a] and A2A [WSF14b] channels, and later extended to any M2M channel in [Wal+20], where the authors proposed a general way of analytically deriving the delay-dependent and joint delay Doppler pdfs in such channels. However, the technique proposed in [Wal+20] has two key limitations. First, only a single plane can be used to recreate the environment. Second, the plane has to be infinite in space. Although the technique could still be applied realistically to some scenarios, for example for aircraft flying at a high altitude above a relatively flat field, it could not be used to reproduce more complex M2M scenarios where the scatterers are distributed over multiple surfaces, which additionally might be limited in space. Thus, we adapt and extend the analytical technique proposed in [Wal+20] to 1) enable the use of *any* number of arbitrarily-oriented planes containing the scatterers, and to 2) allow the planes to be either *infinite* or *finite*, i.e., limited in space. This allows us to reproduce any 3D M2M environment much more accurately and, thus, to obtain an accurate estimate of the time-variant propagation channel between two mobile stations.

In order to verify our theoretical model, we apply our channel modeling technique to multiple M2M scenarios of interest where channel measurements are available. These include A2A, D2D, V2V, and S2S scenarios. In this thesis, the focus is placed on the analysis and verification of the model in the A2A scenarios. However, in order to strengthen our mainly theoretical approach and to demonstrate its applicability to any M2M scenario, the verification of our model in D2D, V2V, and S2S scenarios can be found in our publication in [BMW24].

Defining Planes and Exploiting the Advantages of Each Coordinate System

Two local coordinate systems, shown in Fig. 3.23, are used: a local Cartesian coordinate system (CCS) and a local prolate spheroidal coordinate system (PSCS). The local CCS is mainly used to define the planes, while the local PSCS allows us to obtain closed-form expressions. Both coordinate systems are local as they are solely defined by the position of the TX and RX and thus move together with them.

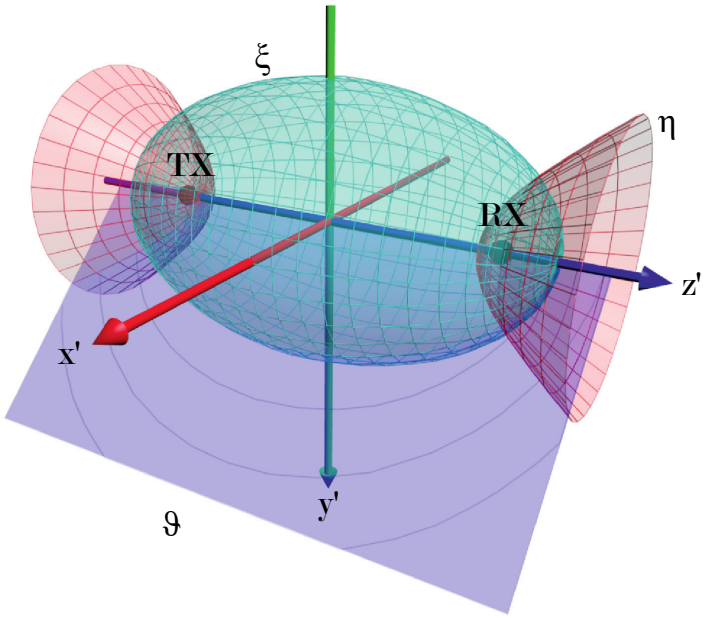

Figure 3.23. Two coordinate systems are used: a local Cartesian system and a local prolate spheroidal system. The prolate spheroidal coordinate system is defined by an ellipsoid (constant ξ), hyperboloids (constant η), and a half-plane (constant ϑ). The transmitter (TX) and receiver (RX) are the foci of the ellipsoid and hyperboloids. From [Wal+20].

The v-th plane reproducing the environment is defined in the local CCS relative to the position of both stations as [Wal+20]

$$A_v x' + B_v y' + C_v z' = \frac{d_{\text{los}}}{2} D_v \,, \tag{3.37}$$

where d_{los} is the LoS distance between the stations. Of course, the planes can be defined initially in any arbitrary coordinate system more suitable to the specific environment. They just need to be converted afterwards to our local CCS to calculate the channel. This enables recreating any new M2M scenario with low effort, as only the new planes defining the new environment have to be defined and later transformed to the local CCS, but from that point on the applied methodology is the same. For instance, the A2A scenarios considered in Section 3.3.2 to validate our model are recreated with planes defined using topographical data. In addition, the navigation data, i.e., the positions and velocity vectors of the aircraft, from the A2A measurement campaign are derived from the GNSS. Thus, for convenience, we use the Earth-centered, Earth-fixed (ECEF) coordinate system to reproduce the A2A scenarios, which are later simply transformed to the local CCS in order to run our channel modeling technique. The definition of the A2A scenarios is discussed in more detail in Section 3.3.2.

The description in Cartesian coordinates is convenient for defining the planes, but it turns out to be non-tractable to determine the channel, since in this coordinate system the symmetries of the geometric setup are not exploited. Thus, we use the more advantageous PSCS. In this particular coordinate system, the orthogonal surfaces are ellipsoids (with constant ξ), hyperboloids (with constant η), and a half-plane (with constant ϑ). The TX and RX are the foci of the ellipsoid and hyperboloids. The PSCS is very advantageous to characterize the multi-path in the channel. For example, any point of an ellipsoid, with TX and RX as foci, presents the same delay in the TX-point-RX path. This is very helpful to obtain closed-form expressions for the scattering components, as it entails that any scatterer located in the ellipsoid presents the same single-bounce scattering delay. The coordinate transformation between the local CCS and the PSCS is given by [Fla57] as

$$\begin{aligned} x' &= \frac{d_{\text{los}}}{2}\sqrt{(\xi^2-1)(1-\eta^2)}\cos\vartheta\,, \\ y' &= \frac{d_{\text{los}}}{2}\sqrt{(\xi^2-1)(1-\eta^2)}\sin\vartheta\,, \\ z' &= \frac{d_{\text{los}}}{2}\xi\eta\,, \end{aligned} \tag{3.38}$$

where $\xi \in [1,\infty)$, $\eta \in [-1,1]$, and $\vartheta \in [0,2\pi)$. The coordinate ξ has a direct physical meaning, since it represents the distance (or delay) normalized to the one of the LoS. The total distance $d_{\text{sc}}(t,\xi)$ from the transmitter via a scatterer to the receiver in prolate spheroidal coordinates (PSCs) is defined as $d_{\text{sc}}(t,\xi) = d_{\text{t,sc}}(t,\xi,\eta) + d_{\text{sc,r}}(t,\xi,\eta) = \xi d_{\text{los}}$. Consequently, the total distance $d_{\text{sc}}(t,\xi)$ – or total reflection delay $\tau_{\text{sc}} = d_{\text{sc}}(t,\xi)/\text{c}_0$ –

of a scattered signal *only* depends on the ξ-coordinate in the PSCS. One can represent the v-th plane from (3.37) in the PSCS as

$$A_v \frac{d_{\text{los}}}{2}\sqrt{(\xi^2-1)-(1-\eta^2)}\cos\vartheta \tag{3.39}$$
$$+ B_v \frac{d_{\text{los}}}{2}\sqrt{(\xi^2-1)-(1-\eta^2)}\sin\vartheta + C_v \frac{d_{\text{los}}}{2}\xi\eta = \frac{d_{\text{los}}}{2} D_v \,.$$

Using the PSCS, one can now obtain the Doppler frequency of a component scattered off any arbitrary point. The Doppler frequency can be seen as the spatial derivative of the total distance $d_{\text{sc}}(t,\xi)$ times the velocity vectors $\mathbf{v'}_{\text{t}}(t) = [v_{\text{t}x'}, v_{\text{t}y'}, v_{\text{t}z'}]^{\text{T}}$ and $\mathbf{v'}_{\text{r}}(t) = [v_{\text{r}x'}, v_{\text{r}y'}, v_{\text{r}z'}]^{\text{T}}$ of the transmitter and receiver, respectively. Note that the components of $\mathbf{v'}_{\text{t}}(t)$ and $\mathbf{v'}_{\text{r}}(t)$ are also time variant. However, we drop the time parameter to simplify the notation. The Doppler frequency in PSCs is given by [WSF15]

$$f_{\text{d}}(t;\xi,\eta,\vartheta) = \frac{f_{\text{c}}}{\text{c}_0}\Bigg(\tag{3.40}$$
$$\frac{\sqrt{(\xi^2-1)(1-\eta^2)}}{\xi+\eta}\left(v_{\text{t}x'}\cos\vartheta + v_{\text{t}y'}\sin\vartheta\right) + \frac{\xi\eta+1}{\xi+\eta}v_{\text{t}z'}$$
$$+ \frac{\sqrt{(\xi^2-1)(1-\eta^2)}}{\xi-\eta}\left(v_{\text{r}x'}\cos\vartheta + v_{\text{r}y'}\sin\vartheta\right) + \frac{\xi\eta-1}{\xi-\eta}v_{\text{r}z'}\Bigg) \,.$$

Thus, we have a full 3D Doppler frequency description in PSCs, where the normalized delay ξ is included in the description. Now, a delay-dependent realization of the Doppler frequency can be easily obtained by fixing $\xi = \xi^*$.

Computing the Delay-Doppler PDFs of the Scattering Components

Our way of computing the pdf of the scattering components is based on the methodology proposed by Walter et al. in [Wal+20], where they propose to use one infinite plane, or scattering plane, to obtain the delay-dependent Doppler pdf and the joint delay Doppler pdf of the scattering components. For each delay, that is described by one ellipsoid in the PSCS, one determines the ellipse $q(\eta,\vartheta) = 0$ intersecting the scattering plane, and then the density of scatterers, either along the intersecting ellipse for the delay-dependent Doppler pdf, or circumscribed by it for the joint delay Doppler pdf. Then, the spatial distribution of the scatterers is transformed to obtain their Doppler frequency, leading to the computation of the pdfs. The transformation from the spatial domain to the frequency domain leads to ambiguities, which are solved by using the algebraic curve theory. An important assumption here is that all scatterers are identical and uniformly distributed over the scattering plane. In addition, the plane must be infinite such that the ellipse is complete and it can be resolved analytically. As discussed, these limitations prevent the approach presented in [Wal+20] to be applied to

scenarios where an arbitrary number of finite or infinite planes are needed to recreate the environment faithfully.

In this work, the methodology proposed in [Wal+20] is generalized by modifying and extending it to account for any arbitrary number of planes, which can now be either finite or infinite. Using more than one plane leads to the challenge that the planes might block each other entirely or partially. In other words, not all points of a plane might contribute to the scattering components of the channel, as either the transmitter-to-scatterer path or the scatterer-to-receiver path might be blocked by another plane. A similar problem is faced when considering finite planes. The analytical expressions developed in [Wal+20] assume an infinite plane where all points of the plane contribute to the scattering components equally. This allows for the analytical computation of the intersection ellipses, as well as the computation and normalization of the delay-dependent and joint delay Doppler pdfs of the channel. Nonetheless, in the case of a finite plane, some intersection ellipses (determined analytically assuming an infinite plane) may not contribute entirely to the scattering components, as some parts of them might fall outside the limits of the actual finite plane. In any case, it is to be noted that only single-bounce scattering is considered.

The generalized methodology to compute the delay/Doppler pdfs entails relating the physical distribution of the scatterers with their Doppler frequency. The density of scatterers along each intersection ellipse $q_\xi(\eta, \vartheta) = 0$ is considered to be uniform and given by

$$p(t, q_\xi(\eta, \vartheta) = 0; s|\xi) = 1/L_\mathrm{T}\,, \tag{3.41}$$

where

$$L_\mathrm{T} = \sum_{v=1}^{V} L_v^\star = \sum_{v=1}^{V} r_{\mathrm{l},v} L_v \tag{3.42}$$

is the accumulated effective length of all intersection ellipses with a delay ξ, L_v is the theoretical maximum length of the ellipse with the v-th plane, and $r_{\mathrm{l},v} \in [0, 1]$ models the ratio of the intersection ellipse with the v-th plane that actually contributes to the scattering components. Thus, $L_v^\star = r_{\mathrm{l},v} L_v$ is the effective length of each intersection ellipse with the v-th plane. Note that L_v can be obtained analytically for each plane separately. However, as we discuss later, this is not required as we take advantage of L_T being a normalization factor.

The delay-dependent Doppler pdf is then given by

$$\begin{aligned} p(t, f_\mathrm{d}|\xi) &= p(t, q_\xi(\eta, \vartheta) = 0; s|\xi) \left| \frac{\mathrm{d}s}{\mathrm{d}f_\mathrm{d}} \right| \\ &= \frac{1}{L_\mathrm{T}} \sum_{v=1}^{V} m_{1,v}\,, \end{aligned} \tag{3.43}$$

where $m_{1,v}$ represents the contribution of each plane, depends on the parametrization that can be used for the plane depending on the geometry, i.e., either $q_\xi(\eta) = 0$ or $q_\xi(\vartheta) = 0$, and is given by

$$m_{1,v} = \begin{cases} \sum_{j=1}^{|\mathcal{H}|} a_{v,j}\delta_{v,j}\left|\frac{\partial\eta^\star_{v,j}}{\partial f_\mathrm{d}}\right|, & \text{if } A_v \neq 0 \text{ or } B_v \neq 0 \\ g_v \sum_{i=1}^{2} \delta_{v,i}\left|\frac{\partial\vartheta_{v,i}}{\partial f_\mathrm{d}}\right|, & \text{otherwise} \end{cases}, \tag{3.44}$$

where

$$a_{v,j} = \tfrac{d_\mathrm{los}}{2}\sqrt{\frac{(\xi^2-1)\left((A_v^2+B_v^2)\left(\xi^2-\eta^{\star 2}_{v,j}\right)-(D_v^2-\xi^2C_v^2)\right)-\left(D_v-C_v\xi\eta^\star_{v,j}\right)^2}{(\xi^2-1)\left(1-\eta^{\star 2}_{v,j}\right)(A_v^2+B_v^2)-(D_v-C_v\xi\eta^\star_{v,j})^2}}, \tag{3.45}$$

$$g_v = \frac{d_\mathrm{los}}{2}\sqrt{(\xi^2-1)\left(1-\left(\tfrac{D_v}{C_v\xi}\right)^2\right)}, \tag{3.46}$$

$$\left|\frac{\partial\vartheta_{v,i}}{\partial f_\mathrm{d}}\right| = \frac{1}{|f_{\mathrm{lim}_v}|\sqrt{1-\left(\frac{f_\mathrm{d}-f_{\mathrm{o}v}}{f_{\mathrm{lim}_v}}\right)^2}}, \tag{3.47}$$

and

$$\delta_{v,u} = \delta^\mathrm{in}_{v,u}\delta^\mathrm{TX}_{v,u}\delta^\mathrm{RX}_{v,u} \in \{0,1\} \tag{3.48}$$

models whether a specific point on a plane, defined by its $(\eta^\star_{v,u=j},\xi)$ – or $(\vartheta_{v,u=i},\xi)$ – coordinates, contributes to the scattering components. First, $\delta^\mathrm{in}_{v,u} \in \{0,1\}$ denotes if a point is actually located within the v-th plane. This allows us to consider finite planes while exploiting the analytical expressions valid for infinite planes. Second, $\delta^\mathrm{TX}_{v,u} \in \{0,1\}$ and $\delta^\mathrm{RX}_{v,u} \in \{0,1\}$ model if a possible scatterer from the v-th plane is blocked by any other planes either in the transmitter-to-scatterer path or in the scatterer-to-receiver path, respectively[10]. To obtain the function $\eta(f_\mathrm{d})$, one must inverse the $f_\mathrm{d}(\eta)$ function, given in [Wal+20] as

$$\begin{aligned} f_\mathrm{d}(\eta) = \frac{1}{(A^2+B^2)(\xi^2-\eta^2)}\Bigg(& (D-C\xi\eta)\left(A\left(v_{\mathrm{r}x'}(\xi+\eta)+v_{\mathrm{t}x'}(\xi-\eta)\right)\right. \\ & \left.+B\left(v_{\mathrm{r}y'}(\xi+\eta)+v_{\mathrm{t}y'}(\xi-\eta)\right)\right)+\left(A^2+B^2\right)\left(v_{\mathrm{r}z'}(\xi\eta-1)(\xi+\eta)+v_{\mathrm{t}z'}(\xi\eta+1)(\xi-\eta)\right) \\ & \pm\sqrt{\left((\xi^2-1)(1-\eta^2)(A^2+B^2)-(D-C\xi\eta)^2\right)}\times \\ & \sqrt{\left(B\left(v_{\mathrm{r}x'}(\xi+\eta)+v_{\mathrm{t}x'}(\xi-\eta)\right)-A\left(v_{\mathrm{r}y'}(\xi+\eta)+v_{\mathrm{t}y'}(\xi-\eta)\right)\right)^2}\Bigg)\frac{f_\mathrm{c}}{\mathrm{c}_0}. \end{aligned} \tag{3.49}$$

[10]Modeling each path as a geometrical line, one can easily assess if the path is blocked by checking if the (finite) line intersects with any other plane (within its boundaries).

Then, $\eta(f_\mathrm{d})$ can be obtained as

$$\eta : \Big\{ \Big(f_\mathrm{d} \frac{\mathrm{c}_0}{f_\mathrm{c}} \left(A^2+B^2\right)\left(\xi^2-\eta^2\right) - (D-C\xi\eta)\left(A\left(v_{\mathrm{r}x'}\left(\xi+\eta\right)+v_{\mathrm{t}x'}\left(\xi-\eta\right)\right)\right.$$
$$\left.+B\left(v_{\mathrm{r}y'}\left(\xi+\eta\right)+v_{\mathrm{t}y'}\left(\xi-\eta\right)\right)\right) - \left(A^2+B^2\right)\left(v_{\mathrm{r}z'}\left(\xi\eta-1\right)\left(\xi+\eta\right)+v_{\mathrm{t}z'}\left(\xi\eta+1\right)\left(\xi-\eta\right)\right)\Big)^2$$
$$-\Big(\left(\xi^2-1\right)\left(1-\eta^2\right)\left(A^2+B^2\right) - \left(D-C\xi\eta\right)^2 \Big)$$
$$\cdot\Big(B\left(v_{\mathrm{r}x'}\left(\xi+\eta\right)+v_{\mathrm{t}x'}\left(\xi-\eta\right)\right) - A\left(v_{\mathrm{r}y'}\left(\xi+\eta\right)+v_{\mathrm{t}y'}\left(\xi-\eta\right)\right)\Big)^2 = 0 \Big\}, \tag{3.50}$$

where the square root from (3.49) is conveniently removed by isolating it on one side of the equation and squaring both sides. Since a four-degree polynomial is obtained, there are four different solutions to (3.50), which we denote $\eta_j(f_\mathrm{d})$ for $j = 1, 2, 3, 4$. These functions can be now derived with respect to f_d to compute $\frac{\partial \eta_j}{\partial f_\mathrm{d}}$, also required in (3.44). We do not provide explicitly the closed-form solutions of $\eta_j(f_\mathrm{d})$ and $\frac{\partial \eta_j}{\partial f_\mathrm{d}}(f_\mathrm{d})$ here, as they are extremely long and can be easily obtained. Furthermore, they are available in Code Ocean as the supplementary material of [Wal+20].

Note that each value of f_d leads to four values of η. Some of them might be, however, not valid. We denote the valid ones as $\eta^\star(f_\mathrm{d})$ with $|\mathcal{H}| \leq 4$ representing the number of valid solutions. A valid $\eta^\star(f_\mathrm{d})$ must be real, fulfill the theoretical limits of η, i.e., $\eta_\mathrm{min} \leq \eta \leq \eta_\mathrm{max}$, and must map back to the right f_d, i.e., to the one originally investigated. The limits of η, i.e., η_min and η_max, can be obtained as [Wal+20]

$$\eta_{\mathrm{min,max}_v}(\xi) = \frac{1}{A_v^2\xi^2 + B_v^2\xi^2 + C_v^2\xi^2 - A_v^2 - B_v^2} \Bigg(D_v C_v \tag{3.51}$$
$$\pm\sqrt{D_v^2 C_v^2 \xi^2 - (A_v^2\xi^2 + B_v^2\xi^2 + C_v^2\xi^2 - A_v^2 - B_v^2)(A_v^2 + B_v^2 + D_v^2 - A_v^2\xi^2 - B_v^2\xi^2)} \Bigg).$$

When $A_v = 0$ and $B_v = 0$, the intersection ellipse with the v-th plane becomes a circle composed of two symmetric branches, which are denoted as $i = \{1, 2\}$ in (3.44). In this case, the offset frequency for the v-th plane is given by [Wal+20]

$$f_{\mathrm{o}_v}(t,\xi) = \frac{f_\mathrm{c}}{\mathrm{c}_0} \left(\frac{\frac{D_v}{C_v}+1}{\xi + \frac{D_v}{C_v\xi}} v_{\mathrm{t}z'} + \frac{\frac{D_v}{C_v}-1}{\xi - \frac{D_v}{C_v\xi}} v_{\mathrm{r}z'} \right), \tag{3.52}$$

and the limiting frequencies for the v-th plane by [Wal+20]

$$f_{\mathrm{lim}_v}(t,\xi) = \pm\frac{f_\mathrm{c}}{\mathrm{c}_0} \sqrt{(\xi^2-1)\left(1-\left(\frac{D_v}{C_v\xi}\right)^2\right)} \times \tag{3.53}$$
$$\sqrt{\left(\frac{v_{\mathrm{t}x'}}{\xi+\frac{D_v}{C_v\xi}} + \frac{v_{\mathrm{r}x'}}{\xi-\frac{D_v}{C_v\xi}}\right)^2 + \left(\frac{v_{\mathrm{t}y'}}{\xi+\frac{D_v}{C_v\xi}} + \frac{v_{\mathrm{r}y'}}{\xi-\frac{D_v}{C_v\xi}}\right)^2}.$$

The limiting frequencies $f_{\lim}$ denote the poles of the delay/Doppler pdf, i.e., the delay-dependent frequencies for which the density of scatterers tends to infinite. These are, however, referred to as limiting frequencies as they define, for some geometries, the boundaries of the delay/Doppler region with scattering components. These boundaries can be clearly seen for example in Fig. 3.22b. We maintain the *limiting* frequency nomenclature to be consistent with the literature.

The joint delay Doppler pdf is computed as

$$p(t, \xi, f_{\mathrm{d}}) = \frac{1}{\mathcal{Y}_{\mathrm{T}}} \sum_{v=1}^{V} m_{2,v} \,, \tag{3.54}$$

where $m_{2,v}$ is weighted by the path loss and is obtained as

$$m_{2,v} = \begin{cases} \sum\limits_{j=1}^{|\mathcal{H}|} b_{v,j} \delta_{v,j} \left| \frac{\partial \eta^{\star}_{v,j}}{\partial f_{\mathrm{d}}} \right|, & \text{if } A_v \neq 0 \text{ or } B_v \neq 0 \\ \frac{d_{\mathrm{los}}^2 \left(\xi - \frac{D_v^2}{C_v^2 \xi^3} \right)}{4 \left(\xi^2 - \left(\frac{D_v}{C_v \xi} \right)^2 \right)^2} \sum\limits_{i=1}^{2} \delta_{v,i} \left| \frac{\partial \vartheta_{v,i}}{\partial f_{\mathrm{d}}} \right|, & \text{otherwise} \end{cases} , \tag{3.55}$$

and

$$b_{v,j} = \frac{d_{\mathrm{los}}^2 \sqrt{A_v^2 + B_v^2 + C_v^2} \left(\xi^2 - \left(\eta^{\star}_{v,j} \right)^2 \right)^{-1}}{4 \sqrt{(\xi^2 - 1) \left(1 - \left(\eta^{\star}_{v,j} \right)^2 \right) (A_v^2 + B_v^2) - \left(D_v - C_v \xi \eta^{\star}_{v,j} \right)^2}} \,. \tag{3.56}$$

The accumulated effective weighted area within all intersection ellipses is given by

$$\mathcal{Y}_{\mathrm{T}} = \sum^{v} \mathcal{Y}^{\star}_{v} = \sum^{v} r_{\mathcal{Y},v} \mathcal{Y}_{1,v} \,, \tag{3.57}$$

where $\mathcal{Y}_{1,v}$ is the maximum area of the v-th intersection ellipse, and could be obtained theoretically as in [Wal+20], and $r_{\mathcal{Y},v} \in [0, 1]$ denotes the ratio of the area of the v-th intersection ellipse that actually contributes to the scattering components. Thus, $\mathcal{Y}^{\star}_{v} = r_{\mathcal{Y},v} \mathcal{Y}_{1,v}$ represents the effective weighted area within the intersection ellipse.

A fully analytical computation of L_{T} and $\mathcal{Y}_{\mathrm{T}}$ is not trivial, as one has to determine the ratios $r_{\mathrm{l},v}$ and $r_{\mathcal{Y},v}$ for each plane. This is very complex to do analytically as these ratios depend on the amount of shadowing caused by other planes and on the actual bounds of the finite planes. However, we can avoid their analytical computation by exploiting the fact that L_{T} and $\mathcal{Y}_{\mathrm{T}}$ are actually the normalization factors that guarantee that the delay-dependent and joint delay Doppler pdfs, respectively, integrate to 1. Then, one can simply estimate L_{T} and $\mathcal{Y}_{\mathrm{T}}$ as the factors normalizing (3.43) and (3.54), respectively, taking into account the sampling interval used for ξ and f_{d}.

Algorithm 2 shows the steps to compute the delay-dependent and joint delay Doppler pdfs efficiently. Note that, depending on the parametrization that can be

used for each plane, the computation of the pdfs is based either on η (if $A_v \neq 0$ or $B_v \neq 0$) or on ϑ (otherwise). For simplicity, Algorithm 2 only shows the computation for the η-based parametrization, as it is the most common case. However, the same steps are followed for the ϑ-based parametrization, but using the expressions for ϑ instead of those for η, e.g., in (3.44). Note that a more efficient implementation of Algorithm 2 is possible by defining f_d as an array and performing array operations.

Algorithm 2 Compute the delay-dependent and joint delay Doppler pdfs

1: Define positions and velocity vectors of the stations
2: Define planes, i.e., (A_v, B_v, C_v, D_v) for $v = 0, 1, ..., V-1$, including the boundaries of the finite planes
3: Define vectors of ξ and f_d to be investigated
4: **for** ξ **do**
5: **for** f_d **do**
6: **for** v-th plane **do**
7: Obtain $\eta_{v,j}(f_\mathrm{d})$ for $j = 1, 2, 3, 4$ using (3.50)
8: Keep only unambiguous values $\eta^\star_{v,j}$, i.e., real, fulfilling $\eta_{\min_v} \leq \eta_{v,j} \leq \eta_{\max_v}$, and mapping back to the investigated f_d
9: Compute $\left|\frac{\partial \eta^\star_{v,j}}{\partial f_\mathrm{d}}(f_\mathrm{d})\right|$
10: Compute $\delta^{\mathrm{in}}_{v,j}$ by evaluating if each scatterer is actually within the plane ($\delta^{\mathrm{in}}_{v,j} = 1$) or not ($\delta^{\mathrm{in}}_{v,j} = 0$)
11: Compute $\delta^{\mathrm{TX}}_{v,j}$ and $\delta^{\mathrm{RX}}_{v,j}$ by checking if each scatterer is blocked by other planes in the TX-to-scatterer or scatterer-to-RX paths, respectively
12: Obtain $m_{1,v}$ using (3.44) and $m_{2,v}$ using (3.55)
13: **end for**
14: **end for**
15: **end for**
16: Compute the delay-dependent and joint delay Doppler pdfs using (3.43) and (3.54), respectively

Once the joint delay/Doppler pdf of the channel is computed, one can use it to estimate the squared delay/Doppler-spread function of the channel. Both results provide the distribution of the components in delay and Doppler domains. However, while the pdf is normalized to 1, the squared delay/Doppler-spread function presents the channel power (or attenuation). According to [WSD17], the squared delay/Doppler-spread function is proportional to the joint delay Doppler pdf. Thus, we can estimate the latter by scaling the joint delay Doppler pdf by a certain factor. We approximate this scaling factor by using the radar equation (3.33) to account for the path loss and the

radar cross section experienced by the scattering components. While most parameters of (3.33) are derived from the geometry of each scenario, we approximate σ_{RCS} to the one measured in Section 3.2. A theoretical derivation of σ_{RCS} for each scenario is complex and considered out of the scope of this work, as our main aim is recreating the delay and Doppler distribution of the scattering components.

The delay-dependent and joint delay Doppler pdfs are obtained for instantaneous positions and velocity vectors of the stations. Thus, the channel is determined for a specific instant. Changing the positions of the stations according to their velocity vectors leads to a new snapshot of the channel. This allows us to see how the channel evolves as the stations move and the geometry between them and the environment varies, as shown later in Section 3.3.2.

The obtained delay/Doppler pdfs can be used to derive numerous properties of the channel, such as the mean delay and mean Doppler, as well as their spreads. In addition, these properties can be derived for specific channel delays, i.e., delay-dependent, for specific Doppler frequencies, i.e., Doppler-dependent, or for the entire channel. Thanks to the time-variant description of the pdfs, these properties can also be computed for different time instants in order to assess how they evolve over time as the stations move. This enables a very detailed description of the channel, which can be useful when designing wireless links. For example, the delay-dependent Doppler mean and spread can be used for the design of an equalizer where the different delay taps are updated at different speeds. Given that the computation of the mean and standard deviation, i.e., spread, of a variable from its pdf is straightforward, these relations are not discussed here but several examples are provided in Section 3.3.2.

LoS and SR Components

This section aims at recreating the scattering components faithfully. However, in order to verify our technique with the measurements, one also has to reproduce the LoS and SR components using the presented framework. If no plane blocks the direct path between the stations, the LoS component travels a path of length d_{los} and is received after a delay $\tau_{\mathrm{los}} = d_{\mathrm{los}}/\mathrm{c}_0$ with a Doppler shift $f_{\mathrm{d_{los}}}$ and with an amplitude α_{los} mainly driven by the FSPL.

Each plane may cause a specular reflection of the transmitted wave. The relative delay of the SR component off the v-th plane can be obtained as

$$\xi_{\mathrm{sr}_v} = \sqrt{\frac{A_v^2 + B_v^2 + D_v^2}{A_v^2 + B_v^2 + C_v^2}}\,, \tag{3.58}$$

leading to an absolute delay $\tau_{\mathrm{sr}_v} = d_{\mathrm{los}}\xi_{\mathrm{sr}_v}/\mathrm{c}_0$. However, the SR component off the v-th plane is only received if certain conditions are met: $\xi_{\mathrm{sr}_v} \geq 1$, the point of reflection is

within the actual plane boundaries, and neither the reflector-to-receiver path nor the transmitter-to-reflector path is blocked by another plane. The SR component off the v-th plane would be received with a Doppler frequency shift $f_{\mathrm{d}_{\mathrm{sr},v}}$ and with an amplitude α_{sr_v}. Among others, the attenuation is driven by the FSPL over the traveled distance and by the reflection loss. The reflection coefficient can be obtained as [Int90]

$$\alpha_{\mathrm{r}_v} = \frac{\sin(\theta_v) - X}{\sin(\theta_v) + X}\,, \tag{3.59}$$

where $X = X_{\mathrm{h}} = \sqrt{e_{\mathrm{g}_v} - \cos^2(\theta_v)}$ for horizontal polarization and $X = X_{\mathrm{v}} = \frac{X_{\mathrm{h}}}{e_{\mathrm{g}_v}}$ for vertical polarization. One can derive the angle θ_v between the v-th plane and the reflected signal from the geometry. The complex relative permittivity e_{g_v} is given by the ITU Recommendation P.527-6 [Int21] for different frequencies and types of surfaces.

Each LoS or SR component has a deterministic delay and Doppler shift that only depend on the geometry between the stations and the planes. Thus, the LoS and SR components should be represented in the weight function as Dirac deltas centered at their delays. Equivalently, they should appear as discrete points in the delay/Doppler-spread function. However, as observed in the channel measurements in Section 3.2.2, the LoS and SR component are centered at the expected delay and Doppler shift but are spread in the delay and Doppler directions. As shown in Appendix B, this spreading is caused by the time- and bandwidth-limited sampling of the channel. In order to account for this effect and to be able to compare our results with the measurements, (B.10) is used to model the LoS and SR components.

3.3.2 Verification

In order to verify our technique to model the scattering components of the channel, we recreate multiple M2M scenarios where channel measurements are available. These include A2A, D2D, V2V, and S2S scenarios. This section focuses on the validation of the model in the A2A scenarios since it is the aim of this work. However, the verification of our technique in the other scenarios can be found in [BMW24].

The A2A channel measurements used to verify our approach were already described in Section 3.2 and the main parameters of the measurements were shown in Table 3.1. The accurate timestamps of the channel sounding data are used to map the time-variant aircraft positions and velocity vectors to the channel measurements. This allows us to recreate the same scenarios that were flown in the measurement campaign and to compare the results of our approach with the measurements.

As discussed in Section 3.3.1, one can initially define the environment using any arbitrary coordinate system. For the definition of the A2A scenarios, we consider

the ECEF coordinate system. This is very useful as the GNSS-derived positions and velocity vectors of the aircraft can be easily converted to this coordinate system, as well as the topographical data used to define the scenarios. The scenarios defined in the ECEF coordinate system are then transformed to the local coordinate system defined in Section 3.3.1 (see Fig. 3.23) in order to apply our channel modeling technique.

Aircraft-to-Aircraft (A2A) Scenarios

Three A2A scenarios are considered: i) flying over a field, ii) through a valley, and iii) over a lake. Figure 3.24 shows the aircraft positions in the three scenarios, as well as the flight route of that part of the A2A measurement campaign. In all cases, both aircraft flew at an altitude of approximately 600 m above the ground and tried to keep a constant speed in order to maintain a LoS distance between them of approximately $d_{\text{los}} = 1.5\,\text{km}$. As described in Section 3.2, the Cessna aircraft carrying the transmitter followed the Dornier aircraft carrying the receiver. Both aircraft employed the bottom antennas for the measurements in these scenarios.

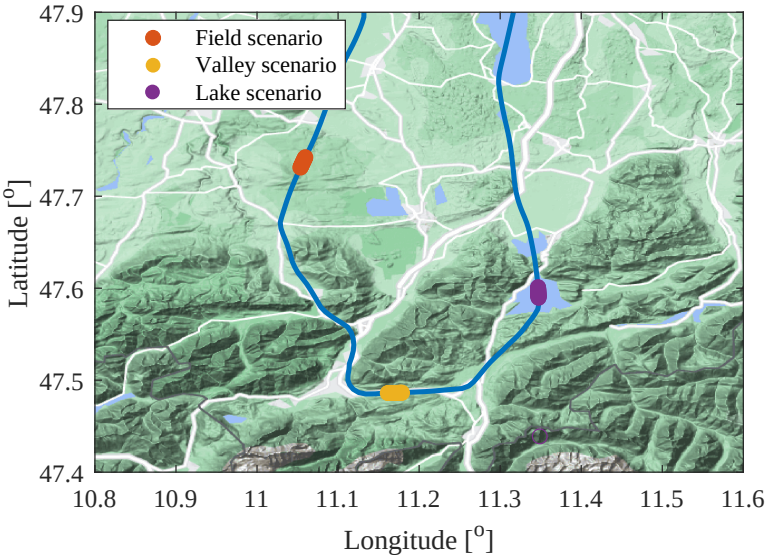

Figure 3.24. Flight route of the A2A channel measurement campaign in southern Germany. The three A2A scenarios of interest are highlighted. From [BMW24].

Field: In the field scenario, the aircraft flew over a field with a small hill nearby. As explained in Section 3.3.1, one can recreate the scenario by employing finite and infinite planes. In this case, one infinite plane is used to model the ground, i.e., the field, and 14 finite planes to model the nearby hill. The algorithm to build each scenario is outlined in Algorithm 3. To be able to accurately define the planes, one can employ topographical data available for the region. For simplicity, we use the

topographical data provided by Google Earth. The data are sampled such that each scattering surface, e.g., the field or a hillside, is well represented by a set of data triplets (latitude, longitude, and elevation). Then, the plane for each scattering surface is computed by finding the best-fitting plane for the set of data triplets representing the scattering surface. Of course, an infinite plane only needs three data triplets, i.e., three points in space, to reproduce it, but using more points leads to a better estimation of the plane. In the case of finite planes, which are all planes except the ground plane in this scenario, the set of data triplets must also enclose the surface. Figure 3.25a depicts the resulting model of the field scenario. Of course, the process of modeling the environment can be fully automatized, as only the positions of the aircraft and the topographical data are required. Nevertheless, as automatizing the process is not the focus of this work, we employ the tools provided by the Google Earth application to identify which mountainsides might contribute to the scattering components, taking into account the area of operation of the aircraft, and to manually sample the environment around them. Which surfaces are sampled to define planes is a decision taken based on the apparent importance of the surface, i.e., on its visibility by the stations and its area. Smaller surfaces can be neglected or merged into bigger ones. A higher accuracy can be reached if more, smaller surfaces are sampled, at the cost of a more time-consuming scenario definition and a higher computational effort.

Algorithm 3 Build an arbitrary M2M scenario based on planes.

1: Sample topography, e.g., using Google Earth, to obtain a set of data triplets (latitude, longitude, and elevation) for each surface, e.g., a mountainside.
   Note that for finite planes, the set of data triplets must also enclose the surface.
2: **for** v-th surface (set of data triplets) **do**
3: Compute the plane parameters (A_v, B_v, C_v, D_v) of the best-fitting plane.
4: **end for**

Valley: For the valley scenario, the valley within the German Alps mountain range system, shown in Fig. 3.24, is considered. Given that the aircraft flew at a low altitude, the mountainsides were located on both sides of the aircraft and a very rich scattering was expected. Following the same procedure presented for the field scenario, the topographical data provided by Google Earth are used to define a set of 38 finite planes modeling the mountains that form the valley, as well as one infinite plane to model the ground under the aircraft. Figure 3.25b depicts the resulting model.

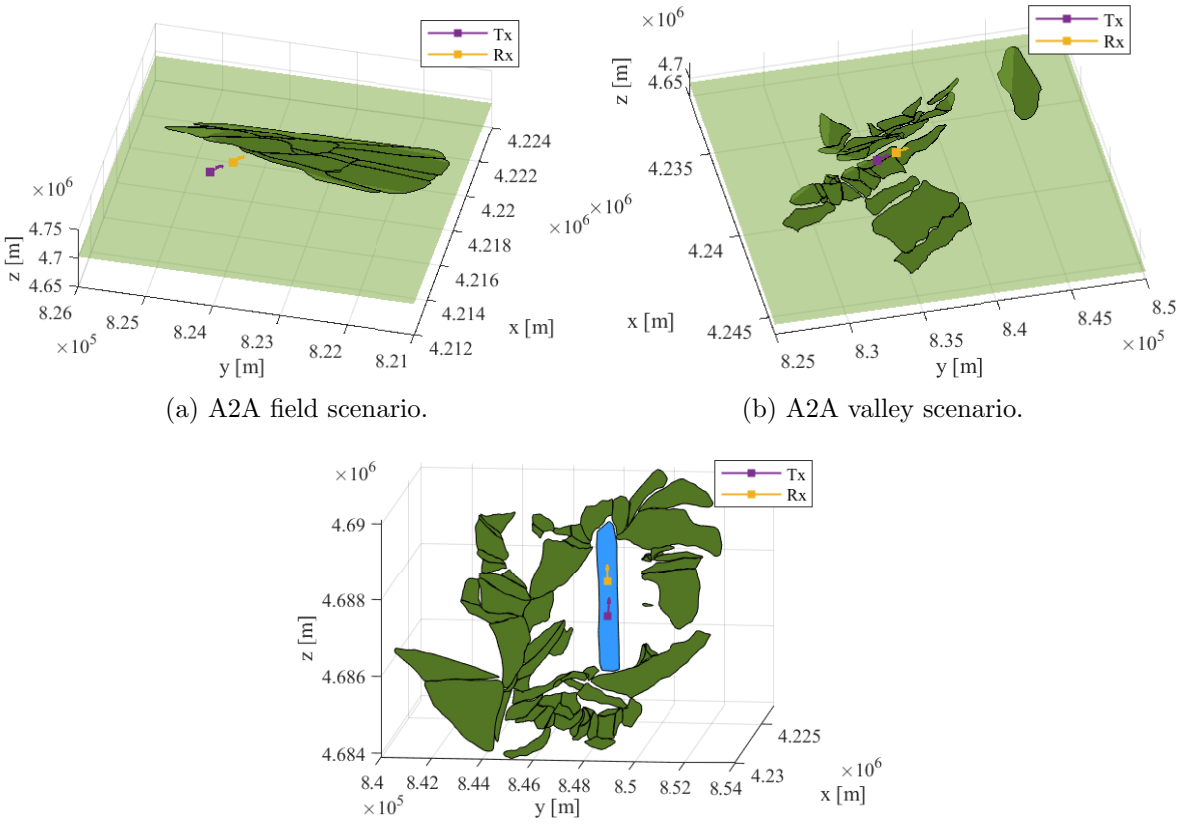

(a) A2A field scenario.

(b) A2A valley scenario.

(c) A2A lake scenario.

Figure 3.25. Models of the A2A scenarios in ECEF coordinates. The topographical data are sampled and used to calculate the best-fitting infinite and finite planes modeling the topography. The planes are shown together with the instantaneous aircraft positions and velocity vectors in the middle of each scenario. One can see the multiple finite planes (dark green) modeling the hills or mountains. An infinite plane (light green) models the ground in Fig. 3.25a and Fig. 3.25b. The lake is modeled in Fig. 3.25c using a narrow finite plane (blue) and no ground plane is considered. Note that the ECEF, or geocentric, coordinate system defines the center of the Earth as its origin and the Z-axis as the line between the North and South Poles, and thus z does not represent the height above the ground (except on the North Pole). From [BMW24].

Lake: In this scenario, both aircraft fly over a lake. As shown in Fig. 3.24, the lake is surrounded by mountains, as it is also located within the Alps mountain range system. In this case, 71 finite planes are defined to model the mountains and the ground around the lake, as shown in Fig. 3.25c. Interestingly, the reflection off a completely calm lake should theoretically only be specular and present no scattering. However, the lake surface was not calm during the measurements as there were waves caused by the wind. After investigating this case, we learnt that a more realistic way to model the

lake in these conditions is to use a narrow plane under the aircraft, stretching in the direction of the water waves, i.e., in the direction of the wind, as depicted in Fig. 3.25c.

Results and Comparison with Measurements

The scattering modeling technique is applied to each defined scenario to compute the *estimated* time-variant squared delay/Doppler-spread function of the channel as described in Section 3.3.1. Separately, the channel measurements are used to obtain the *measured* time-variant squared delay/Doppler-spread function of the channel. Both results are then compared to verify our technique, making emphasis on the scattering components as their modeling is the main objective of the proposed methodology.

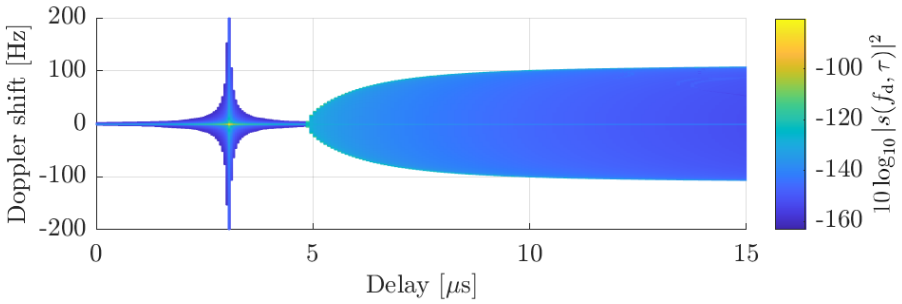

(a) Results of our model.

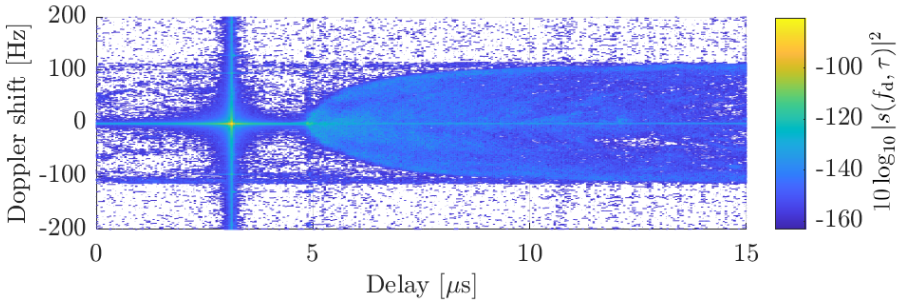

(b) Measurements.

Figure 3.26. Channel obtained using a) the proposed channel modeling technique and b) through measurements in the field scenario shown in Fig. 3.25a. The scattering components are recreated very accurately by our channel modeling technique.

Figure 3.26 shows a comparison between the channel obtained applying the proposed channel modeling technique in the field scenario (Fig. 3.26a) and the measured channel (Fig. 3.26b). In both cases, the channel is composed mainly of two distinguishable components: the LoS component centered at $\tau = 3\,\mu s$ and $f_d = 0\,Hz$ and stretching in the delay and Doppler directions, and the scattering components arriving after $\tau = 5\,\mu s$. As discussed in Section 3.3.1, the LoS component should theoretically appear as a discrete point in the squared delay/Doppler-spread function, but the time-

and bandwidth-limited sampling of the channel leads to the observed spread in delay and Doppler domains. Figure 3.26a shows that the spread of the LoS component is also recreated accurately.

The scattering components arrive after a delay of approximately $\tau = 5\,\mu s$ and widen in the Doppler direction as the delay increases, forming the parabolic shape commonly seen in the literature. One can see that our technique recreates the scattering components very accurately, including their starting delay, the limiting frequencies setting the boundary of the scattering components, and their power distribution within those frequencies. In addition, it is important to notice that our model accurately predicts that the power of the scattering components concentrates on the limiting Doppler frequencies as the delay increases, leading to the well-known Jakes spectrum for high delays. It is to be noted that the scattering components are caused mainly by the field, i.e., the ground plane, given that the small hill located nearby is not elevated enough compared to the aircraft altitude.

Some additional components can be observed in the measurements (Fig. 3.26b) before the LoS component, i.e., before $\tau = 3\,\mu s$, mainly at the limiting Doppler frequencies ($f_d = \pm 100\,Hz$). These components are caused by the periodic correlation of the channel sounding signal during the measurements. In other words, the components appearing at low delays before the LoS component are actually the high-delay trail from the previous channel measurement. This can be seen more clearly in the measurements in the valley scenario (Fig. 3.27). Our technique does not recreate these measurement artifacts deliberately, as shown in Fig. 3.26a.

The valley scenario has been simulated for multiple positions of the aircraft within the valley. Figures 3.27 and 3.28 show the obtained results, compared with the channel measurements, for three different points within the valley. While Fig. 3.27 is obtained shortly after both aircraft enter the valley, Fig. 3.28a and Fig. 3.28b are obtained approximately 30 s later, for two consecutive 2-second blocks, with both aircraft roughly in the middle of the valley. In all results, one can recognize the strong LoS component centered at $\tau \approx 5\,\mu s$ and with a Doppler shift slightly above $f_d = 0\,Hz$. After the LoS component, one can identify the strong SR component from the ground. This component, which was not as strongly visible in the field scenario in Fig. 3.26 because of the irregularity of the terrain, is centered at $\tau \approx 6.5\,\mu s$ and has a Doppler shift slightly below the LoS Doppler shift, i.e., closer to $f_d = 0\,Hz$. This is understandable considering the geometry in this scenario given that the SR component is almost orthogonal to the velocity vectors of the aircraft, both at transmission and reception. Furthermore, the SR component spreads in delay and Doppler directions because of the time- and bandwidth-limited effect, as recreated by our model.

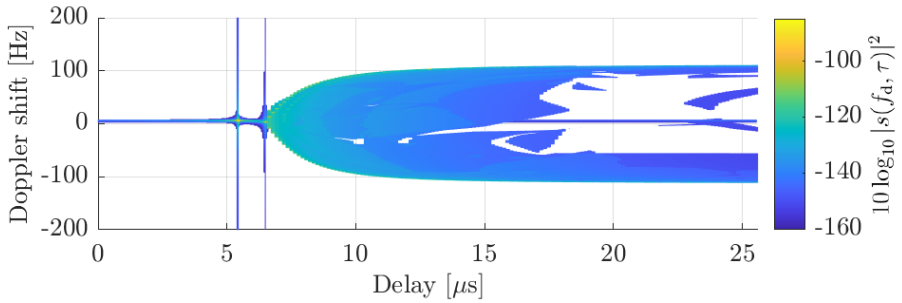

(a) Results of our model.

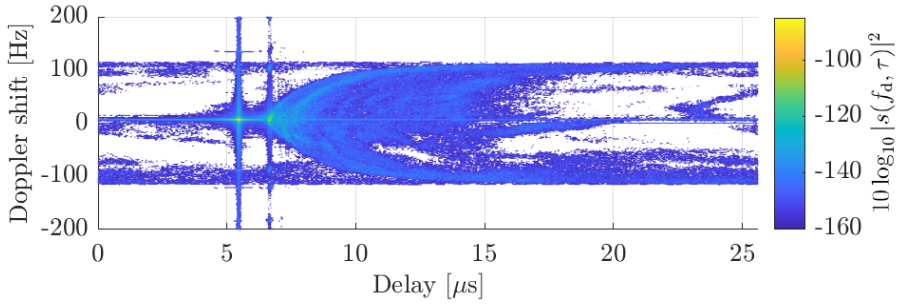

(b) Measurements.

Figure 3.27. Channel obtained using a) the proposed channel modeling technique and b) through measurements (14:19:00.00 to 14:19:02.10 UTC) in the valley scenario.

After the LoS and SR components, one can see the scattering components caused by the ground and by the mountains surrounding the aircraft. Overall, the scattering components determined by our channel modeling technique match the measured scattering components very accurately. Specifically, one can identify some interesting effects that are well recreated by our technique. First, the outer shape of the scattering components is practically identical to the one observed in the field scenario and is well recreated by our technique. Second, the scattering components are most powerful shortly after the specular reflection, i.e., between $\tau = 6.5\,\mu s$ and $\tau = 8\,\mu s$. This is actually caused by the geometry of the valley. The lowest parts of the mountains and the region around the SR point cause scattering components with very similar Doppler shifts and delays. This increases the power density in a narrow Doppler shift range immediately after the SR component. Third, one can see that the proposed model is capable of accurately predicting the Doppler and delay regions where no scattering components are expected, as well as the isolated clusters of scattering components present at higher delays. For example, the scattering components in Fig. 3.27 and Fig. 3.28 span most Doppler shifts within the limiting frequencies until a delay of $\tau \approx 15\,\mu s$. Afterwards, they are mainly concentrated around the limiting Doppler frequencies, i.e., $f_d \approx \pm 100\,Hz$, and only some isolated clusters can be seen, like the

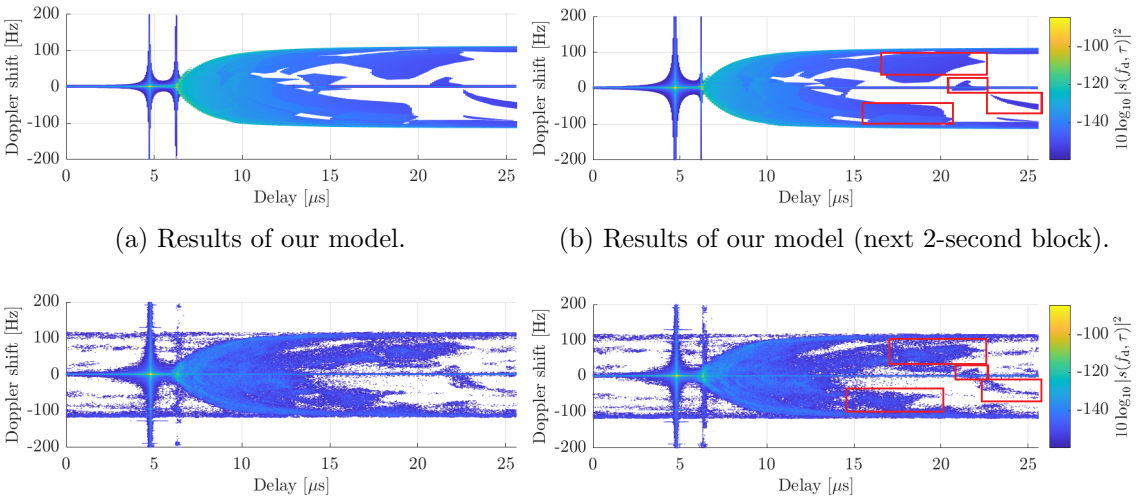

(a) Results of our model.

(b) Results of our model (next 2-second block).

(c) Measurements.

(d) Measurements (next 2-second block).

Figure 3.28. Channel obtained using the proposed channel modeling technique and through measurements in the valley scenario. Two consecutive 2-second blocks are considered: 14:19:29.36 to 14:19:31.46 UTC in a) and c), and 14:19:31.46 to 14:19:33.55 UTC (next 2 seconds) in b) and d). The red rectangles highlight some well-recreated clusters of scattering components. The channel changes between both blocks but slowly because of the slowly-changing geometry. Our technique can track these changes.

ones marked with red rectangles in Fig. 3.28. Our model is also capable of recreating these isolated clusters of scattering components, as well as the wider distribution of the scattering components at $f_\mathrm{d} = -100\,\mathrm{Hz}$, compared to its narrower distribution at $f_\mathrm{d} = 100\,\mathrm{Hz}$. Here it is important to understand that the presence of the scattering components at certain Doppler frequencies and delays, or the absence thereof, can be seen as a deterministic process mainly driven by the geometry between the aircraft and their surroundings. Thus, one can use our model not only to predict the channel response very accurately, but also to identify which parts of the channel response correspond to specific reflectors, e.g., a specific mountainside, which can be helpful for some applications.

Let us now briefly discuss the channel observed at different time instants. One can notice some differences and similarities in the channel between the aircraft when entering the valley (Fig. 3.27) and in the middle of the valley approximately 30 seconds afterwards (Fig. 3.28). On the one hand, the characteristics of the LoS and SR components remained generally stable, as the distance between both aircraft and the ground did not change substantially. Moreover, the overall shape of the scattering components and the limiting frequencies did not vary significantly between both positions. On the other hand, the distribution of the scattering components within the

limiting frequencies changed distinctly from the beginning (Fig. 3.27) to the middle of the valley (Fig. 3.28c and Fig. 3.28d). Comparing now Fig. 3.28c with Fig. 3.28d, the channel did not change noticeably. This is expected given that the results shown in Fig. 3.28c and Fig. 3.28d are taken within 2 seconds of each other, leading to practically no change in the geometry between both positions. Nonetheless, one may notice that the isolated clusters of scattering components shifted slightly in Doppler and delay directions. For example, the cluster located at around $f_\mathrm{d} = 0\,\mathrm{Hz}$ and $\tau = 22\,\mu\mathrm{s}$ shifted towards lower delays and frequencies from Fig. 3.28c to Fig. 3.28d. This movement of scattering components in the delay/Doppler domain, which can also be noticed for the other clusters, is to be expected because of the changing geometry between the aircraft and their surroundings as the aircraft move. Although this movement of the scattering components might be considered slow (Fig. 3.28c vs Fig. 3.28d), it leads to significant changes in the channel response (Fig. 3.27 vs Fig. 3.28c) as the geometry changes slowly but consistently. Importantly, we verified that our proposed model can recreate the channel response at any arbitrary time instant and, thus, track the changes in the channel response as the transmitter and receiver move.

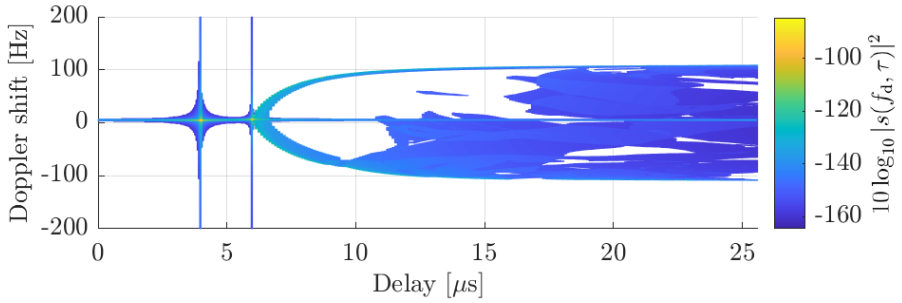

(a) Results of our model.

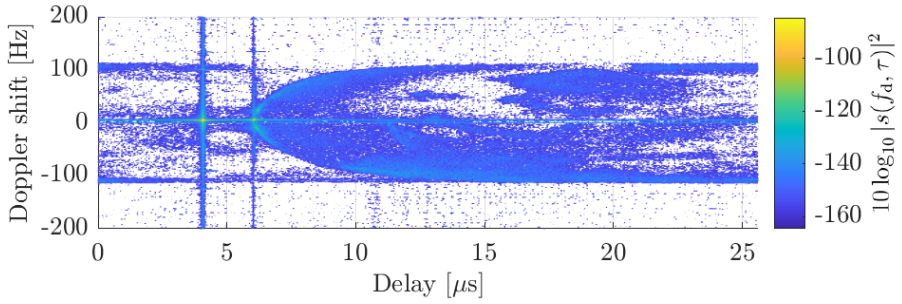

(b) Measurements.

Figure 3.29. Channel obtained shortly after arriving to the lake (14:24:26.79 to 14:24:28.89 UTC) in the A2A lake scenario (Fig. 3.25c) using a) the proposed M2M channel modeling technique and b) measurements.

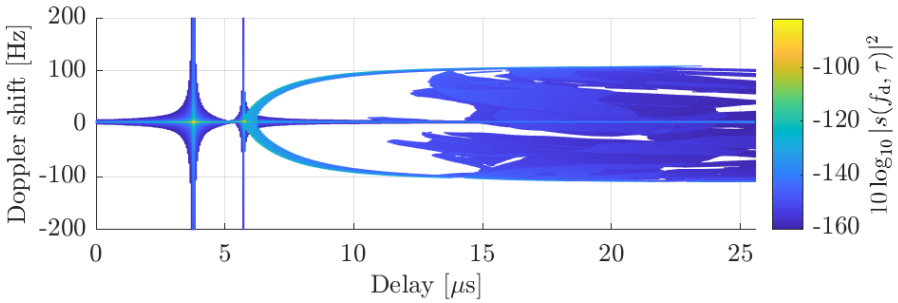

(a) Results of our model.

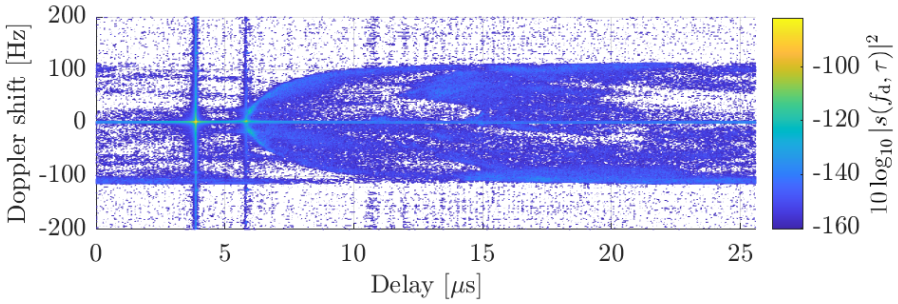

(b) Measurements.

Figure 3.30. Channel obtained at the middle of the lake (14:24:39.37 to 14:24:41.47 UTC) in the A2A lake scenario (Fig. 3.25c) using a) the proposed M2M channel modeling technique and b) measurements.

Figures 3.29–3.31 show the channel response obtained using the proposed technique and through measurements in the lake scenario for three different positions of the aircraft: shortly after arriving to the lake (Fig. 3.29), at the middle of it (Fig. 3.30), and just before leaving it (Fig. 3.31). In all positions, the channel presents strong LoS and SR components, which were reproduced faithfully. We do not discuss them in more detail as we analyzed them thoroughly in Section 3.2. The power of the scattering components is high immediately after the SR component but decreases very rapidly for higher delays. Afterwards, the scattering components caused by the lake are mainly concentrated around the limiting frequencies. The scattering components off the lake are concentrated around the SR component and on the limiting frequencies because the aircraft and the lake waves, caused by the wind, move in the same direction. Thanks to our way of modeling the lake surface (see Fig. 3.25c), the proposed technique was able to recreate this distribution accurately. After a certain delay, the scattering components increase in power and are more homogeneously distributed at intermediate frequencies, as they are now caused by the lake shore and the mountains surrounding the lake. This effect is more pronounced in the results of our model, and slightly less obvious in the channel measurements. However, it becomes clear when one notices that the

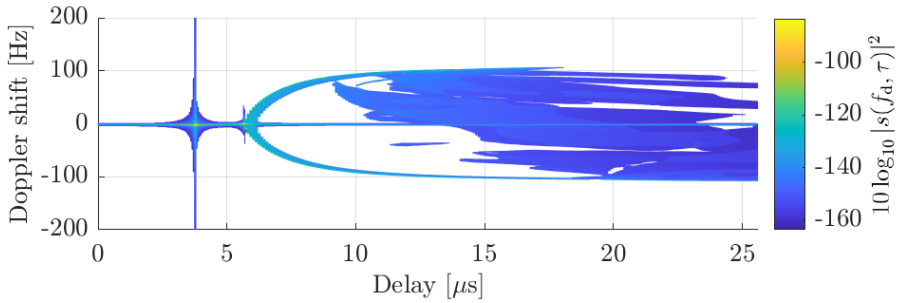

(a) Results of our model.

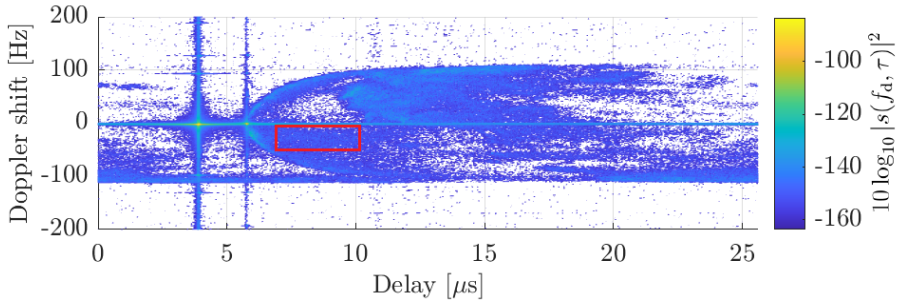

(b) Measurements.

Figure 3.31. Channel obtained just before leaving the lake (14:24:51.95 to 14:24:54.05 UTC) in the A2A lake scenario (Fig. 3.25c) using a) the proposed M2M channel modeling technique and b) measurements.

scattering components from the lake shore appear first at negative Doppler frequencies in Fig. 3.29, given that the aircraft just entered the lake and left the southern lake shore immediately behind them, leading to negative Doppler frequencies. The scattering components with positive Doppler frequencies, with a higher delay, arrive from the northern lake shore that the aircraft are flying toward. This is reversed in Fig. 3.31 when the aircraft are about to leave the lake. Now the northern shore is closer to the aircraft and the scattering components with positive Doppler frequencies arrive before those caused by the more distant southern shore left behind. Following the same reasoning, one can notice that the aircraft are halfway through the lake in Fig. 3.30, given that the scattering components off the terrain appear at negative and positive Doppler frequencies from the same delay approximately.

One can notice that the lake surface behaves neither as a perfect mirror nor as an ideal scatterer. For example, we highlight in Fig. 3.31b with a red rectangle some non-negligible scattering components caused by the lake surface. These components are caused by physical deviations of the lake surface from the idealized plane assumed in our model. Of course, such deviations could be recreated if they are sufficiently characterized, by for example introducing more, smaller planes to model the lake surface, or

by using other techniques such as the one investigated for the sea surface by the author and colleagues in [Rau+23]. However, we still advocate for the more general solution used in this work, where the lake surface is modeled as a single narrow plane stretching in the direction of the lake waves, given that it already recreates faithfully the main channel components caused by the lake surface. Without being too scenario-specific, this model of the lake surface is effective, simple, and only requires the knowledge of the direction of the waves.

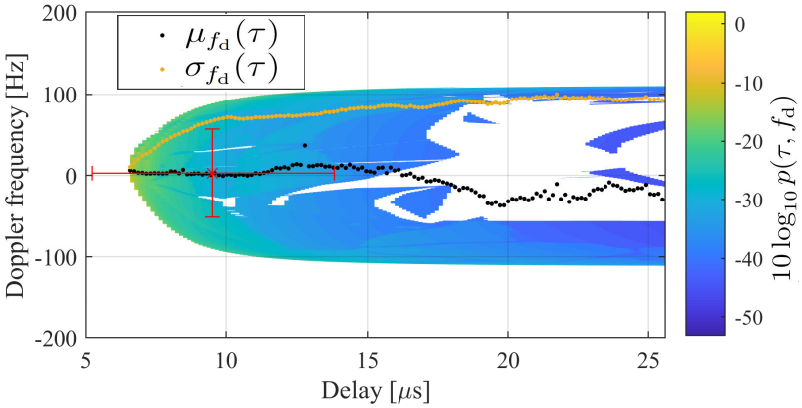

Figure 3.32. Computed joint delay Doppler pdf of the scattering components in the A2A valley scenario (Fig. 3.27). The joint delay Doppler pdf is used to obtain the delay-dependent Doppler mean $\mu_{f_\mathrm{d}}(\tau)$ and spread $\sigma_{f_\mathrm{d}}(\tau)$ shown here. The mean delay and mean Doppler for all delays and Doppler frequency shifts are shown as a red asterisk ($*$) with the bounds depicting the spread in the delay and Doppler directions. Adapted from [BMW24]. © 2024 IEEE.

So far, the computed pdfs have only been used to obtain the squared delay/Doppler-spread function of the channel. However, as discussed in Section 3.3.1, many additional characteristics of the channel can be derived from the pdfs obtained using the proposed technique. As an example, Fig. 3.32 shows one joint delay Doppler pdf of the scattering components obtained in the valley scenario, together with the delay-dependent Doppler mean $\mu_{f_\mathrm{d}}(\tau)$ and spread $\sigma_{f_\mathrm{d}}(\tau)$ derived from it. The pdf is also used to obtain the mean delay and mean Doppler shift of the scattering components, as well as their spreads. The result is shown in Fig. 3.32 as a red asterisk centered at the mean delay and Doppler shift, and with the bounds depicting the obtained delay and Doppler spreads. From the obtained results, one can conclude that the main scattering components are present at low delays with a moderate Doppler spread, which increases with the delay as the scattering components concentrate around the limiting frequencies. Note that the LoS and SR components are not considered here for simplicity, but could also be taken into account as in Fig. 3.27.

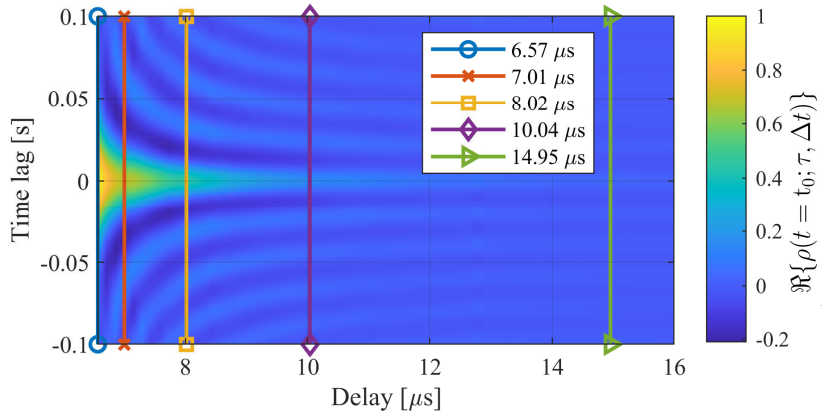

Figure 3.33. Hybrid time delay characteristic pdf (real part) computed from one joint delay Doppler pdf of the A2A valley scenario (Fig. 3.32). Adapted from [BMW24]. © 2024 IEEE.

One can also derive the time-variant hybrid time delay characteristic pdf[11] $\rho(t;\tau,\Delta t)$ by doing an inverse Fourier transform in the Doppler direction of the joint delay Doppler pdf shown in Fig. 3.32. The resulting function, shown in Fig. 3.33, provides information about the stability of the channel. For example, Fig. 3.34 depicts several cuts of the computed function at different delays. These cuts show that the channel becomes less stable as the delay increases. At high delays, they resemble the Bessel function, which is to be expected given that our results already showed (e.g., in Fig. 3.26) that the spectrum becomes practically identical to a Jakes Doppler spectrum at high delays.

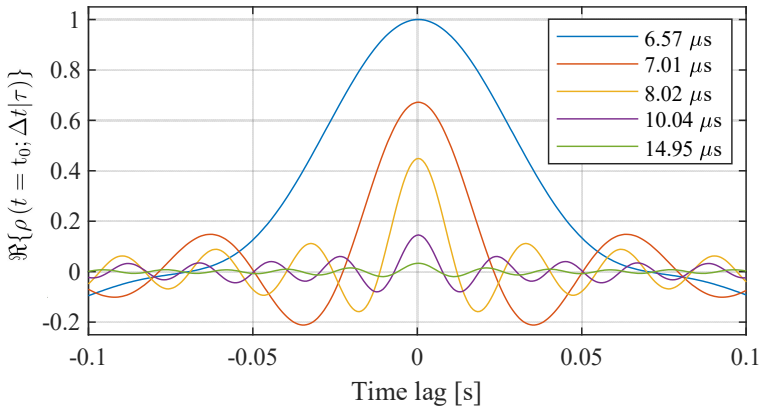

Figure 3.34. Hybrid time delay characteristic pdf (real part) for specific delays. Adapted from [BMW24]. © 2024 IEEE.

The proposed channel modeling technique was also verified in additional M2M scenarios, including D2D, V2V, and S2S scenarios. The results for these scenarios, as

[11] We follow the notation proposed by the author and colleagues in [Wal+25].

well as the measurements used to verify them, are discussed in detail in [BMW24]. Special emphasis has been placed on the scattering components and their distribution in the delay/Doppler domain, as it is the main objective of the proposed technique. In all scenarios, the scattering components were recreated very faithfully, validating the proposed methodology, mainly theoretical, with the real-wold channel measurements.

3.4 Geometry-Based Stochastic A2A Channel Model

After having identified and analyzed the main components of the A2A channel using channel measurements in Section 3.2 and having proposed and verified a technique to characterize the scattering components in terms of their delay/Doppler distribution in Section 3.3, we now propose and validate a geometry-based stochastic A2A channel model that can be used, among others, to optimally design A2A wireless links for communication, navigation, or surveillance. The A2A channel model proposed in this section is based on the geometry between the aircraft and on the statistics observed in the measurements. Our previous work showed that many parameters of the channel components can be derived from the geometry and can generally be considered deterministic, such as the delay and the Doppler frequency shift. Other parameters, such as the attenuation, fluctuate strongly based on numerous factors and must generally be represented in a stochastic manner. Of course, some of these parameters benefit from a dual geometrical and stochastic representation. For example, the analysis in Section 3.2 showed that the slow fading of the LoS and SR components can be generally computed based on the theoretical FSPL and reflection coefficients, while their fast fading must be modeled stochastically. Thus, we opt for a geometry-based stochastic characterization of the A2A channel in order to exploit the advantages of both.

Based on the measurements and in accordance with Bello [Bel73], our A2A channel model is composed of three components: the LoS component, the SR component, and the diffuse scattering components. The contribution of the three channel components to the total channel WF can be separated as [Bel73]

$$h(t,\tau) = h_{\mathrm{los}}(t,\tau) + h_{\mathrm{sr}}(t,\tau) + h_{\mathrm{sc}}(t,\tau)\,. \tag{3.60}$$

These components are recreated considering the geometry shown in Fig. 3.35, which is comprised by both aircraft and the Earth's surface. The transmitter is located at $\mathbf{p}_{\mathrm{t}} = [p_{\mathrm{t}x}, p_{\mathrm{t}y}, p_{\mathrm{t}z}]^{\mathrm{T}}$ and the receiver at $\mathbf{p}_{\mathrm{r}} = [p_{\mathrm{r}x}, p_{\mathrm{r}y}, p_{\mathrm{r}z}]^{\mathrm{T}}$, with velocity vectors $\mathbf{v}_{\mathrm{t}} = [v_{\mathrm{t}x}, v_{\mathrm{t}y}, v_{\mathrm{t}z}]^{\mathrm{T}}$ and $\mathbf{v}_{\mathrm{r}} = [v_{\mathrm{r}x}, v_{\mathrm{r}y}, v_{\mathrm{r}z}]^{\mathrm{T}}$, respectively. The Earth's surface comprises the XY-plane. Considering the depicted geometry, one can easily obtain the length of the LoS component path d_{los} and its delay τ_{los}, as well as the length of the SR component

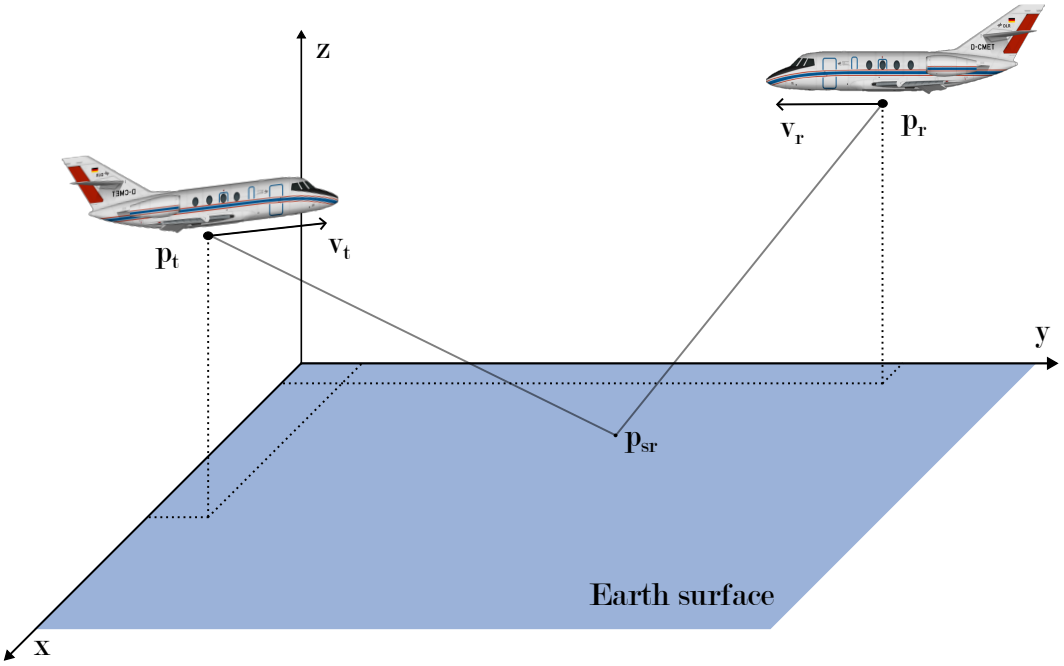

Figure 3.35. Geometry considered for the A2A channel model.

path d_{sr} and its delay τ_{sr}. The Doppler frequency shift of the LoS component $f_{\mathrm{d_{los}}}$ can be easily obtained as

$$f_{\mathrm{d_{los}}} = \frac{f_{\mathrm{c}}}{\mathrm{c}_0} \frac{< \Delta\mathbf{v}, \mathbf{p}_{\mathrm{t,r}} >}{||\mathbf{p}_{\mathrm{t,r}}||}, \tag{3.61}$$

where $\Delta\mathbf{v} = -(\mathbf{v}_{\mathrm{r}} - \mathbf{v}_{\mathrm{t}})$, $\mathbf{p}_{\mathrm{t,r}} = \mathbf{p}_{\mathrm{r}} - \mathbf{p}_{\mathrm{t}}$ are the opposite relative velocity and position vectors, respectively, and $< \Delta\mathbf{v}, \mathbf{p}_{\mathrm{t,r}} >$ represents the scalar product between $\Delta\mathbf{v}$ and $\mathbf{p}_{\mathrm{t,r}}$. Similarly, the Doppler shift of the SR component requires obtaining first the SR point $\mathbf{p}_{\mathrm{sr}}$ and then computing the Doppler frequency shift $f_{\mathrm{d_{sr}}}$ as [Wal16]

$$f_{\mathrm{d_{sr}}} = \frac{f_{\mathrm{c}}}{\mathrm{c}_0} \left(\frac{< \mathbf{v}_{\mathrm{t}}, \mathbf{p}_{\mathrm{t,sr}} >}{||\mathbf{p}_{\mathrm{t,sr}}||} + \frac{< \mathbf{v}_{\mathrm{r}}, \mathbf{p}_{\mathrm{r,sr}} >}{||\mathbf{p}_{\mathrm{r,sr}}||} \right), \tag{3.62}$$

where $\mathbf{p}_{\mathrm{t,sr}} = \mathbf{p}_{\mathrm{sr}} - \mathbf{p}_{\mathrm{t}}$ and $\mathbf{p}_{\mathrm{r,sr}} = \mathbf{p}_{\mathrm{sr}} - \mathbf{p}_{\mathrm{r}}$ are the relative position vectors between transmitter and reflection point, and reflection point and receiver, respectively. Note that (3.62) can be easily generalized for any reflector or scatterer by using its position instead of $\mathbf{p}_{\mathrm{sr}}$. Given that the position and velocity vectors of the aircraft are time-dependent, all the aforementioned parameters are also implicitly time-dependent. However, we do not indicate this time dependency explicitly for easier reading.

The amplitude of each component is affected by slow-changing and fast-changing parameters, which model the fading seen in the measurements. According to the results presented in Section 3.2, the slow fading of the LoS component is mainly driven by the FSPL between the stations and the gains of the antennas. Using the Friis trans-

mission equation [Fri46; Fri71] to reproduce the slow fading and including a shadowing parameter and a fast fading distribution, we model the LoS component as

$$h_{\text{los}}(t,\tau) = \overbrace{\frac{\text{c}_0}{4\pi f_\text{c} d_{\text{los}}(t)}\sqrt{G_{\text{t,los}}(t)G_{\text{r,los}}(t)}\chi_{\text{los}}(t)\alpha_{\text{f,los}}(t)\text{e}^{j\phi_{\text{los}}(t)}}^{\alpha_{\text{los}}(t)}\delta(\tau-\tau_{\text{los}}(t))\,, \quad (3.63)$$

where $\phi_{\text{los}}(t) = 2\pi(f_\text{c}\tau_{\text{los}}(t) + f_{\text{d}_{\text{los}}}(t)t)$ builds the phase and Doppler shift of the LoS component and $G_{\text{t,los}}(t)$ and $G_{\text{r,los}}(t)$ are the transmitter and receiver antenna gains that depend on the angles of departure $\varphi_{\text{t,los}}(t), \theta_{\text{t,los}}(t)$ and arrival $\varphi_{\text{r,los}}(t), \theta_{\text{r,los}}(t)$, respectively, i.e., $G_{\text{t,los}}(\varphi_{\text{t,los}}(t), \theta_{\text{t,los}}(t))$ and $G_{\text{r,los}}(\varphi_{\text{r,los}}(t), \theta_{\text{r,los}}(t))$. The parameter $\chi_{\text{los}}(t) \in [0,1]$ accounts for the possible shadowing, or blocking, of the LoS component, which can happen for example during banking maneuvers. The fast fading of the LoS component amplitude is recreated by the random variable $\alpha_{\text{f,los}}(t)$, which follows a Rician distribution with a K-factor defined in Table 3.3 for different cases.

The SR component is modeled similarly but also accounting for the ground reflection coefficient α_r obtained using (3.59)[12]. Thus, the SR component is given by

$$h_{\text{sr}}(t,\tau) = \overbrace{\frac{\text{c}_0}{4\pi f_\text{c} d_{\text{sr}}(t)}\sqrt{G_{\text{t,sr}}(t)G_{\text{r,sr}}(t)}\chi_{\text{sr}}(t)\alpha_\text{r}(t)\alpha_{\text{f,sr}}(t)\text{e}^{j\phi_{\text{sr}}(t)}}^{\alpha_{\text{sr}}(t)}\delta(\tau-\tau_{\text{sr}}(t))\,, \quad (3.64)$$

where $\phi_{\text{sr}}(t) = 2\pi(f_\text{c}\tau_{\text{sr}}(t) + f_{\text{d}_{\text{sr}}}(t)t)$ builds the phase and Doppler shift of the SR component and $G_{\text{t,sr}}(t)$ and $G_{\text{r,sr}}(t)$ are the transmitter and receiver antenna gains that depend on the angles of departure to the SR point $\varphi_{\text{t,sr}}(t), \theta_{\text{t,sr}}(t)$ and arrival from the SR point $\varphi_{\text{r,sr}}(t), \theta_{\text{r,sr}}(t)$, respectively, i.e., $G_{\text{t,sr}}(\varphi_{\text{t,sr}}(t), \theta_{\text{t,sr}}(t))$ and $G_{\text{r,sr}}(\varphi_{\text{r,sr}}(t), \theta_{\text{r,sr}}(t))$. The fast fading of the SR component amplitude is recreated by the random variable $\alpha_{\text{f,sr}}(t)$ that follows a Rician distribution with a K-factor defined in Table 3.3 for different cases. Note that the fast fading of the SR component could be modeled using either Rician or Nakagami distributions, as shown in Section 3.2. Given that both distributions provide a very good fit in all scenarios, we propose to solely use the Rician distribution for the SR component for multiple reasons. First, because it is probably the most widespread distribution to account for this type of fading and, thus, efficient implementations of it can be found easily. Second, the different scenarios can be easily considered by only changing the K-factor. Third, it is already proposed for the fading of the LoS component, allowing for an overall easier implementation of the A2A channel model. The parameters used to model the SR component are based on the analysis performed in Section 3.2 and can be found in Table 3.3. The parameter $\chi_{\text{sr}}(t) \in [0,1]$ models any additional effect reducing the amplitude of the SR component. For example, it can model the deviation between the ideal reflection coefficient α_r and the actual

[12]The complex relative permittivity can be found in the ITU Recommendation P.527-6.

one experienced because of the roughness of the surface or because of its continuously changing shape. This way, it could be used to recreate the intermittent appearance and disappearance of the SR component in the field scenario. Analyzing this phenomenon in the measurements proved very challenging and we leave its modeling as future work.

Let us now model the scattering components. Although these components are generally weaker than the LoS and SR components, their Doppler/delay distribution and ubiquity might lead to non-negligible effects for a data link. In addition, the measurements have shown that there are scenarios, e.g., the forest scenario, where no SR component is present and the scattering components are the main MPCs of the channel. Moreover, the total or partial blockage of the LoS component, e.g., because of banking maneuvers, leads to a significant decrease in its power and a much greater relevance of the scattering components.

The scattering components are distributed from the SR delay until a maximum delay $\tau_{\mathrm{sr}} + \tau_{\max}$. Considering L_{sc} delay taps to reproduce the scattering components, they can be described as

$$h_{\mathrm{sc}}(t,\tau) = \sum_{l=0}^{L_{\mathrm{sc}}-1} h_{\mathrm{sc}_l}(t)\delta(\tau - \tau_{\mathrm{sc}_l}(t))\,. \tag{3.65}$$

We exploit the results of the analysis conducted in Section 3.2 and the technique proposed in Section 3.3 to propose a simple, yet very effective way to model the amplitude of the scattering components. Based on the bistatic radar equation [Sko08; FD20] presented in (3.33), the weights of the scattering components are modeled as

$$h_{\mathrm{sc}_l}(t) = \overbrace{\sqrt{G_{\mathrm{t}}(t)G_{\mathrm{r}}(t)\frac{{\mathrm{c}_0}^2}{f_{\mathrm{c}}^2(4\pi)^3(d_{\mathrm{t,sr}}(t)d_{\mathrm{sr,r}}(t))^2}\sigma_{\mathrm{RCS}}}}^{\alpha_{\mathrm{RCS}}(t)} \sqrt{w_{\mathrm{sc}_l}(t)}\alpha_{\mathrm{f,sc}}(t)\,, \tag{3.66}$$

where $\alpha_{\mathrm{RCS}}(t)$ is based on (3.33) and considers the geometry between the transmitter, the SR point, and the receiver, to determine the power of the scattering components. Note that the SR point is used because it was the reference point used in Section 3.2 to measure the power of the scattering components and to estimate σ_{RCS}, now used in (3.66). The transmitter and receiver antenna gains $G_{\mathrm{t}}(t)$ and $G_{\mathrm{r}}(t)$ depend on the angles of departure (TX to SR point) and arrival (SR point to RX), respectively. These angles can be derived from the geometry presented in Fig. 3.35, as well as the TX-to-SR distance $d_{\mathrm{t,sr}}(t)$ and SR-to-RX distance $d_{\mathrm{sr,r}}(t)$. Note that $\alpha_{\mathrm{RCS}}(t)$ does not depend on l, i.e., remains the same for all $h_{\mathrm{sc}_l}(t)$ with equal t. However, as shown in Section 3.2, the power of the scattering components decreases with the delay. To account for this, one can obtain the delay-dependent weighting function $w_{\mathrm{sc}_l}(t,\tau)$, which can be interpreted

as the normalized PDP of the scattering components. Based on the model presented in Section 3.3, the delay-dependent scattering power decay is given by

$$w'_{\mathrm{sc}_l}(t,\tau_{\mathrm{sc}_l}) = \int_{\xi^*_{\min}}^{\xi^*_{\max}} \int_{\eta_{\min}}^{\eta_{\max}} \frac{d^2_{\mathrm{los}}\sqrt{A^2+B^2+C^2}\,\mathrm{d}\eta\mathrm{d}\xi}{2(\xi^2-\eta^2)\sqrt{(\xi^2-1)(1-\eta^2)(A^2+B^2)-(D-C\xi\eta)^2}}\,, \tag{3.67}$$

where $\xi^*_{\min} = \left(\tau_{\mathrm{sc}_l} - \frac{\Delta\tau}{2}\right)/\tau_{\mathrm{los}}$ and $\xi^*_{\max} = \left(\tau_{\mathrm{sc}_l} + \frac{\Delta\tau}{2}\right)/\tau_{\mathrm{los}}$ define the limits of the delay considered in each delay tap and, thus, depend on the delay resolution $\Delta\tau$ used to obtain realizations of the channel model. Note that a lower $\Delta\tau$ leads to a higher accuracy at recreating the power decay of the scattering components, reaching the exact solution for $\Delta\tau \to 0$ (infinite bandwidth). Then, the normalized PDP is computed as

$$w_{\mathrm{sc}_l}(t,\tau_{\mathrm{sc}_l}) = \frac{w'_{\mathrm{sc}_l}(t,\tau_{\mathrm{sc}_l})}{\sum_{l=0}^{L_{\mathrm{sc,n}}-1} w'_{\mathrm{sc}_l}(t,\tau_{\mathrm{sc}_l})}\,, \tag{3.68}$$

such that $\sum_{l=0}^{L_{\mathrm{sc,n}}-1} w_{\mathrm{sc}_l}(t,\tau_{\mathrm{sc}_l}) = 1$ for $L_{\mathrm{sc,n}} \leq L_{\mathrm{sc}}$. In other words, $w_{\mathrm{sc}_l}(t,\tau)$ assigns a lower power to the scattering components with higher delay, following the decay expected from the theory (Section 3.3) and seen in the measurements (Section 3.2). The total power, or attenuation, of the scattering components is then modeled using $\alpha_{\mathrm{RCS}}(t)$ (see (3.66)). For correctness, $L_{\mathrm{sc,n}}$ covers the delay window used to measure σ_{RCS}, e.g., 1 µs in our analysis, although it is defined generally here so that the proposed model can still be used with new measurements of σ_{RCS}. For example, if the delay step is 0.2 µs, and σ_{RCS} was measured with a delay window of 1 µs, then $L_{\mathrm{sc,n}}$ shall be 5. This way, the realizations of the scattering components will have the same power, on average, as the one measured, presenting additionally the expected power decay given by (3.67). Using $L_{\mathrm{sc,n}}$ equal to L_{sc} can be valid if the window used to measure σ_{RCS} covers the most powerful scattering components, but would lead to an underestimation of the scattering components otherwise.

Note that (3.67) is only valid if a single plane is used to recreate the Earth's surface. In Section 3.3, we proposed and verified a technique to model the channel by first defining a set of planes recreating the Earth's surface and by second applying the proposed methodology to obtain the joint delay Doppler pdf. However, until it can be fully automatized, the planes must be initially defined manually for each environment to be simulated. In addition, using multiple planes makes the derivation of the joint delay Doppler pdf computationally intensive and might not be adequate *yet* for the time-efficient simulations required for a thorough data link design and optimization. Thus, although it has been shown in this work that using multiple planes allows us to recreate the channel very accurately in each specific scenario, here we opt to use only the most relevant plane, i.e., the Earth's surface, in order to enable a more efficient

implementation of the A2A channel model and less computationally-intensive simulations. This assumption is more valid as the altitude of the aircraft increases, given that the irregularities of the specific terrain topography, such as hills or mountains, become less important. Nonetheless, once the technique proposed in Section 3.3 is fully automatized and efficiently implemented, it could be applied fully to recreate the channel more accurately, especially for low-flying aircraft.

Finally, $\alpha_{\mathrm{f,sc}_l}(t) = |\alpha_{\mathrm{f,sc}_l}(t)|\mathrm{e}^{\mathrm{j}\phi_{\mathrm{f,sc}_l}(t)}$ models the fast fading of the scattering components and their distribution in the delay/Doppler plane. For this, the analytical model proposed in Section 3.3 is first used to obtain the limiting frequencies of the scattering components. The closed-form expression required to obtain the limiting frequencies comprises a sixth-order polynomial with seven coefficients depending on a total of eleven parameters, yielding a polynomial with 2632 components. Thus, it is not included here but the reader is referred to the supplementary code from [Wal+20] published in Code Ocean, where the code to compute the limiting frequencies is available. The theory shows that up to two pairs of limiting frequencies, or poles of the delay/Doppler pdf, can be obtained per delay. Both pairs generally overlap partially and evolve as the delay increases. The first pair is termed $\mathbf{f}_{\mathrm{lim}}^{(1)}$ and the second pair $\mathbf{f}_{\mathrm{lim}}^{(2)}$. The spectrum created by each pair of limiting frequencies presents many similarities with a Jakes distribution, especially at high delays, and therefore it was decided to use a Jakes distribution to stochastically model the spectrum power within each pair of limiting frequencies and for each delay tap. This enables a very realistic distribution of the scattering components in the delay/Doppler plane as well as a very efficient implementation for fast simulations. The Jakes spectrum, originally derived by Clarke, is defined by its Doppler pdf as

$$p_{\mathrm{Jakes}}(f) = \frac{1}{\pi f_{\max}\sqrt{1-\left(\frac{f}{f_{\max}}\right)^2}}\,, \quad |f| \leq f_{\max}\,, \tag{3.69}$$

where $f_{\max}$ is the maximum frequency. The Jakes spectrum is symmetrical and centered at 0 Hz. Our limiting frequencies are, however, not centered at 0 Hz, so the Jakes spectrum must be adapted to use it. This is done for each pair of limiting frequencies by fixing the width of the Doppler spectrum to the distance between the maximum limiting frequency, $\max\{\mathbf{f}_{\mathrm{lim}}^{(i)}\}$, and the minimum one, $\underline{\min}\{\mathbf{f}_{\mathrm{lim}}^{(i)}\}$. Then, the spectrum is shifted to the mean between both limiting frequencies $\overline{f_{\mathrm{lim}}^{(i)}} = \frac{1}{2}(\max\{\mathbf{f}_{\mathrm{lim}}^{(i)}\} + \min\{\mathbf{f}_{\mathrm{lim}}^{(i)}\})$. The resulting Doppler pdf for both pairs of limiting frequencies is obtained as

$$p_{\mathrm{sc}}(f) = \frac{1}{N_{\mathrm{pairs}}}\sum_{i=1}^{N_{\mathrm{pairs}}} \frac{1}{\pi f_{\mathrm{hw}}^{(i)}\sqrt{1-\left(\frac{f-\overline{f_{\mathrm{lim}}^{(i)}}}{f_{\mathrm{hw}}^{(i)}}\right)^2}}\,, \quad |f-\overline{f_{\mathrm{lim}}^{(i)}}| \leq f_{\mathrm{hw}}^{(i)}\,, \tag{3.70}$$

where $N_{\text{pairs}} \leq 2$ and $f_{\text{hw}}^{(i)} = \max\{\mathbf{f}_{\text{lim}}^{(i)}\} - \overline{f_{\text{lim}}^{(i)}}$ represents half of the width of each spectrum. Note that all parameters used to obtain $p_{\text{sc}}(f)$ depend on t and τ, i.e., $N_{\text{pairs}}(t,\tau)$, $\mathbf{f}_{\text{lim}}^{(i)}(t,\tau)$, as well as $f_{\text{hw}}^{(i)}(t,\tau)$ and $\overline{f_{\text{lim}}^{(i)}}(t,\tau)$. Thus, $p_{\text{sc}}(f)$ also depends on t and τ. We drop these dependencies here to simplify the notation. The complex values of $\alpha_{\text{f,sc}_l}$, used to compute (3.66), are drawn from the distribution described in (3.70), i.e., $\alpha_{\text{f,sc}_l} \sim p_{\text{sc}}(f)$.

Table 3.3. Measurements-based stochastic parameters of the proposed A2A channel model.

Component	**Fast fading**			$10\log_{10}(\sigma_{\text{RCS}}[\text{m}^2])$
	Favorable conditions*	**Slightly adverse conditions†**	**Strongly adverse conditions‡**	
LoS	Rician K=32 dB	Rician K=24 dB	Rician K=13 dB	-
SR (over water)	Rician K=27 dB	Rician K=22 dB	Rician K=9 dB	-
Scattering	Delay-dependent Jakes spectrum within each pair of $\mathbf{f}_{\text{lim}}^{(i)}$ (see (3.70))			Forest: 45 dB Calm water: 38.8 dB Rough water: 43.7 dB

* For LoS component: clear propagation path with no obstacles and no reflectors near the antennas, e.g., propellers. For SR component: bottom antennas with ideal propagation (strong SR).

† For LoS component: either slightly affected propagation path, e.g., because of aircraft fuselage, or reflectors near one antenna, e.g., propellers. For SR component: either bottom antennas with weak SR, e.g., through bad antenna alignment, or one top antenna without reflectors near it, e.g., propellers.

‡ For LoS component: affected propagation path, e.g., because of aircraft fuselage, and reflectors near one antenna, e.g., propellers. For SR component: top antennas or one top antenna with reflectors near it, e.g., propellers.

Table 3.3 lists the parameters proposed for the stochastic part of the A2A channel model. For the fast fading of the LoS and SR components, it is proposed to use Rician distributions with K-factors depending on the propagation conditions, e.g., on the propagation path, on the strength of the reflection of the SR component, or on the presence of objects (such as propellers) near the antennas. Note that the K-factors are given in Table 3.3 for three different path conditions of the LoS and SR components: favorable, slightly adverse, and strongly adverse. The K-factors for these conditions

are based on the many scenarios analyzed in Section 3.2, where different geometries and antenna positions led to very contrasting results. Combining the different conditions defined for the LoS and SR components allows us to reproduce any arbitrary scenario, including the scenarios investigated in Section 3.2. The SR component's parameters are given for over-water scenarios, where they could be measured accurately. For the scattering components, different values of σ_{RCS} can be used in (3.66) depending on the scenario to be recreated, e.g., forests or calm or rough water surfaces. In Section 3.2, σ_{RCS} was estimated together with the best-fitting normal distribution parameters to model it in each scenario (see Fig. 3.20b and Fig. 3.21b). However, it has been decided to assign σ_{RCS} a constant value for each scenario in Table 3.3 to save the model from additional complexity without a significant impact. Given that no SR component is expected in the forest scenario and the scattering components become the main MPCs, it is proposed to use a σ_{RCS} slightly higher than the mean of the distribution shown in Fig. 3.20b. Note that all the values proposed in Table 3.3 are based on the analysis of the measurements showed in Section 3.2. Future measurement campaigns might consolidate these values or adjust them as necessary.

The proposed A2A channel model has been implemented in MATLAB in order to compare our model with the available measurements and to enable the optimal design of an A2A data link through simulations in Chapter 4. To validate the accurateness of the proposed A2A GBSCM, some realizations of the proposed channel model can be compared with the measurements. First, the time-variant squared WF of the channel is compared in some of the considered scenarios. For this, our channel model implementation is fed with the same time-variant aircraft geometry as the one of the flight campaign, and a realization of the channel is obtained every second. Figure 3.36 shows the comparison between the time-variant squared WF obtained in the lake scenario (in SR-D-D-600-600) using the proposed channel model (Fig. 3.36a) and measurements (Fig. 3.36b)[13]. One can see that the channel model recreates very accurately the LoS and SR components. Both, their power and stability, are reproduced with great precision. The scattering components can also be slightly seen in Fig. 3.36a. They are similarly weak to the ones observed in the measurements. However, the measurements also show the stronger scattering components caused by the terrain surrounding the lake and appearing after a short delay. For simplicity, our implementation of the proposed channel model does not include this change in the terrain after a certain delay, but it could be extended to do so as part of the future work.

[13]Favorable conditions are considered for the LoS and SR components and calm water for the scattering components (see Table 3.3).

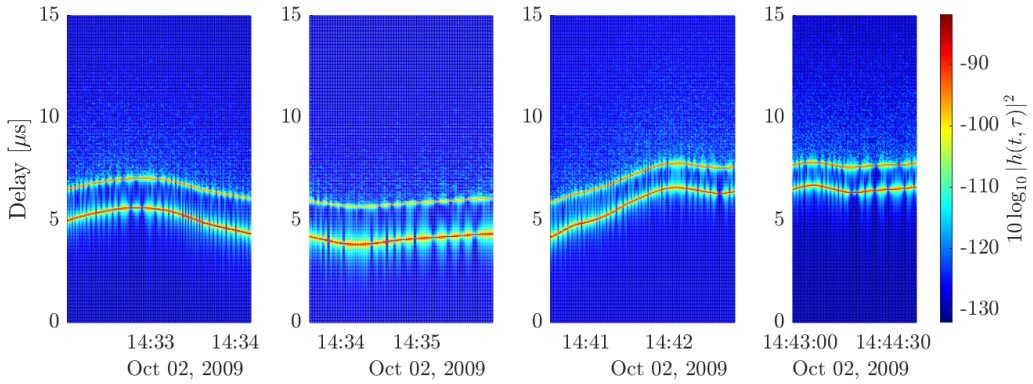

(a) Channel model realization.

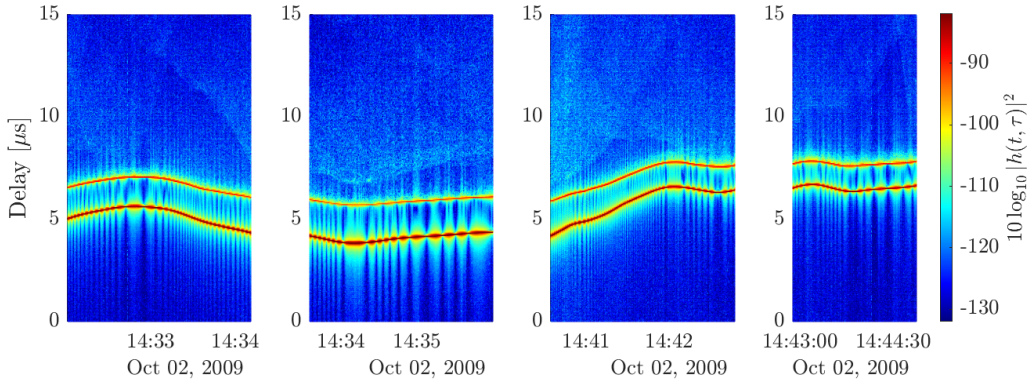

(b) Channel measurements.

Figure 3.36. Time-variant WF (squared magnitude) obtained in the lake scenario (in SR-D-D-600-600) using our channel model (Fig. 3.36a) and measurements (Fig. 3.36b).

The comparison is repeated for the lake scenario but in the SR-U-U-600-600 flight segments, where the top antennas were used instead of the bottom ones. The results, which can be found in Appendix A (Fig. A.7), consolidate the great match between the channel model and the channel measurements. Particularly, one can see that the channel model correctly recreates a much weaker and unstable SR component, compared to the one shown in Fig. 3.36. This is caused by the change in the antenna gains caused by the different placements of the antennas, and by the use of a much lower K-factor, given that the SR component is now considered to face strongly adverse conditions according to Table 3.3.

The last comparison of the time-variant squared WF is conducted in the forest scenario in the LOS-D-D-600-600 flight segment. The results can be found in Appendix A (Fig. A.8). One can see that the channel model recreates the scenario quite accurately, accounting for no SR component but for the relatively strong scattering components recreated following Table 3.3. The model generates a more homogeneous channel com-

pared to the one observed in the measurements, where the scattering coefficient changed continuously and a weak SR component might have been present intermittently for a short time. However, one can argue that the channel model realization provides a very good overall representation of the channel.

Let us assess now the accuracy of the spectrum obtained using our channel model. For this, Fig. 3.37 shows the squared SF obtained using our model and the one measured in the lake scenario (in SR-D-D-600-600). The comparison in the forest scenario (in LOS-D-D-600-600) can be found in Appendix A (Fig. A.9). Despite the different delay and Doppler resolution between the model realization and the measurements, the channel model recreates LoS and SR components (the latter only in the lake scenario) accurately, as well as the scattering components following a delay/Doppler distribution very similar to the one observed in the measurements. Here, one can notice the simplification made by our channel model, where the scattering components are distributed uniformly within the well-recreated limiting frequencies. This results in the power of the scattering components being more evenly distributed over the delay, whereas in the measurements they are slightly more concentrated immediately after the SR delay. As previously discussed, this assumption simplifies the channel model implementation enormously and enables quick simulations, while still delivering a very reasonable realization of the scattering components in both scenarios.

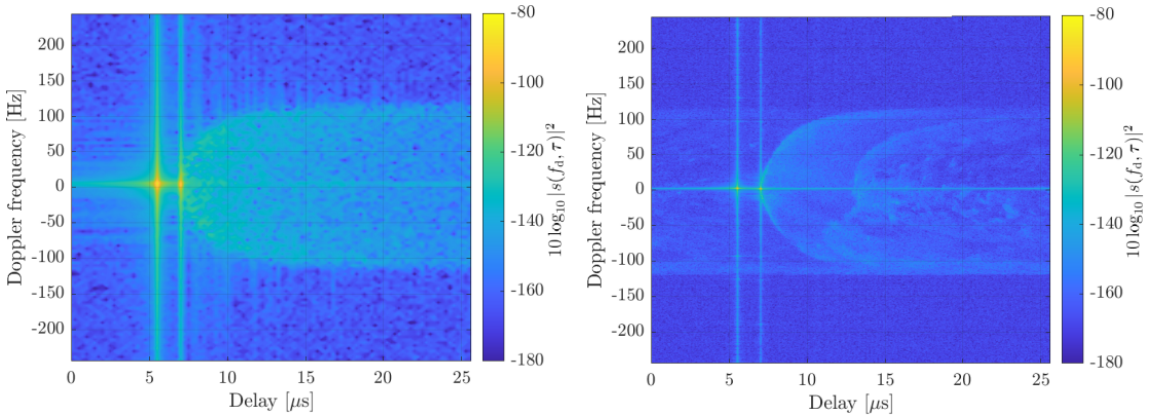

(a) Channel model realization.

(b) Channel measurements.

Figure 3.37. Local SF (squared magnitude) obtained in the lake scenario (in SR-D-D-600-600) using our channel model (Fig. 3.37a) and measurements (Fig. 3.37b).

Chapter 4

A2A Data Link Design

In this chapter, the A2A channel model proposed in Chapter 3 is used to design an A2A data link. Specifically, the LDACS A2A communications system, specifying the design according to its requirements, boundary conditions, and frequency band. The requirements and constraints are discussed first, together with the scenarios of interest and the channel characteristics that can be expected in them. This is followed by the definition of the main functional blocks of the physical layer of LDACS A2A and how they are implemented for the simulations. Finally, the simulation results are analyzed and the optimal physical-layer design is proposed. Note that both, our A2A channel model and the approach followed for the design of LDACS A2A, can be applied to the design of any arbitrary A2A data link, albeit particularizing it to its specific requirements and constraints.

4.1 System Requirements

Any A2A data link must fulfill some performance requirements mainly derived from the applications to be supported by it. In addition, the spectral compatibility with other systems must be taken into account. In order to enable a swift acceptance by the aviation community, it would be advisable to reuse technologies already employed by other well-established systems. Part of the work presented in this section has being published by the author and colleagues in [BM18; BM+22].

In aviation, performance requirements are generally divided into communication, navigation, and surveillance. Since the primary objective of LDACS A2A is to provide data communications and a means for surveillance, we focus on the communication and surveillance performance requirements. Although LDACS A2A might also be used to enhance the navigation capabilities of the aircraft, its requirements in this regard have not been fully investigated or defined and are therefore not considered in this work.

The required communications range of the system depends on the applications to be supported. Also, surveillance applications generally require a shorter range and a lower latency than pure point-to-point communications. In a joint effort [ER07], the FAA and Eurocontrol conducted an initial study on the modernization of the ATM and defined an A2A range of 100 nmi for surveillance services and 150 nmi for the largest fixed-range transmission volume for broadcast. ADS–B, however, defines multiple ranges and maximum update intervals depending on the service and type of equipment. The highest required range is 90 nmi but a range of 120 nmi is desired [RTC02]. As discussed in Section 2.1, a higher communications range is required to enhance aircraft connectivity in ORP regions. A minimum of 135 nmi is proposed in [HMG22], while a communications range of 162 nmi might be required to achieve an aircraft connectivity of 90%, and above 200 nmi to achieve a connectivity of 95% [MHL23]. Taking these values into account, one can conclude that a range of 120 nmi would suffice for surveillance applications such as ADS–B, while a higher range of up to 200 nmi would be ideal to maximize aircraft connectivity in the North Atlantic region and coincides with the maximum air-ground range supported by LDACS A/G. An intermediate value of 150 nmi was considered for A2A beaconing in [Fra15].

The surveillance performance of ADS–B is defined in terms of the maximum update interval for different communication ranges and domains [RTC02]. In the terminal, en-route, and ORP regions, the maximum update interval, in its 95-th percentile, increases from 3 s for distances shorter than 3 nmi, up to 12 s for distances between 40 and 90 nmi. In the 99-th percentile, these requirements are relaxed to 6 s and 24 s, respectively. The strictest requirements are observed in the approach and airport surface regions, where the aircraft are closer than 10 nmi or 5 nmi, respectively. In these cases, the update interval cannot exceed 1.5 s in the 95-th percentile and 3 s in the 99-th percentile, although a maximum update interval of 1 s is desired. These requirements directly impact the target message error rate of the surveillance broadcast. For example, the A2A beaconing analysis conducted in [Fra15] used a target update interval of 1 s with a tolerable probability of outdated information of 10^{-3}.

The number of information bits to be carried by the broadcast messages depends on the data to be transmitted and has not been specified yet. An ADS–B beacon transmitted using the 1090 MHz (Mode S) Extended Squitter comprises 14 information bytes containing basic surveillance data. However, LDACS A2A shall not only be used for basic surveillance but also for communications and more advanced surveillance applications, and thus longer messages might be necessary. For example, UAT uses 18 information bytes for the basic beacons and 34 bytes for the longer ones. This also goes in line with the recommendation from [ER07] to use 34 information bytes for broadcast

messages. The additional information bytes, compared to the 14 or 18 bytes required for basic surveillance, would also be required to exchange basic information enabling the establishment of an ad hoc communications network with other aircraft. For example, they can be used for medium access control, i.e., to organize the transmissions from the aircraft and to reserve resources to establish additional communication links.

The communication requirements in terms of message error rate or data throughput are significantly more difficult to define. For example, the required data throughput depends on the applications to be supported, the number of aircraft in each region, as well as the network topology when the data have to be relayed, e.g., in the North Atlantic region. Recent studies [HMG22; HMG23] have investigated the possible data communication demands for an A2A data link in the North Atlantic region and concluded that, in order to support ATS and AOC applications with a coverage of at least 120 nmi, the A2A data link should be able to support at least an average of 2 kbps of user data with peaks of up to 15 kbps.

Communication systems generally define a minimum bit error rate (BER) or packet error rate (PER) that shall not be exceeded. Surpassing the BER or PER might lead to a drastic decrease in the performance of the system, for example if too many retransmissions are triggered. In addition, some applications require a minimum BER or PER to perform correctly. Unfortunately, there are no clear communication requirements in this regard for LDACS A2A. As discussed above, the ADS–B requirements are defined in terms of update intervals and ranges for certain percentiles. Thus, depending on the used technology, a different PER would be acceptable. For example, the most stringent ADS–B requirement defines an update interval of 1 s for the 95-th percentile, relaxed down to 3 s for the 99-th percentile. In this case, if LDACS A2A transmits one ADS–B message per second, the message error rate should not exceed 5% and the probability of losing three consecutive beacons should be lower than 10^{-2}.

One of the main constraints in the design of LDACS A2A is that it shall reuse the main transmission characteristics of the LDACS reverse link, i.e., of the aircraft's transmissions, including the use of windowed OFDM with a channel bandwidth of 500 kHz. The reason for this is that LDACS A2A is expected to be rolled out as an extension to the current LDACS specification. This will facilitate its acceptance in the standardization activities and will enable the use of the same spectrum allocated by LDACS, without requiring new allocations. Sharing the same transmission characteristics with the LDACS airborne stations will allow reusing the compatibility criteria developed between LDACS and the legacy systems of the L-band, which will result in a much shorter standardization phase. In fact, we already verified in [BMS21] that LDACS A2A can operate in many LDACS frequency channels without affecting the legacy sys-

tems, as long as it shares the current transmission characteristics of the LDACS reverse link. In addition, using OFDM enables the application of the interference mitigation techniques developed for LDACS to cope with the pulsed interference from the legacy systems, e.g., from DME/TACAN [ES17].

4.2 Scenarios of Interest and Channel Parameters

As shown in Section 3.2, the channel characteristics depend strongly on the geometry between the aircraft and the Earth's surface. Thus, we define two scenarios of interest for the design of LDACS A2A and obtain the channel characteristics in both scenarios.

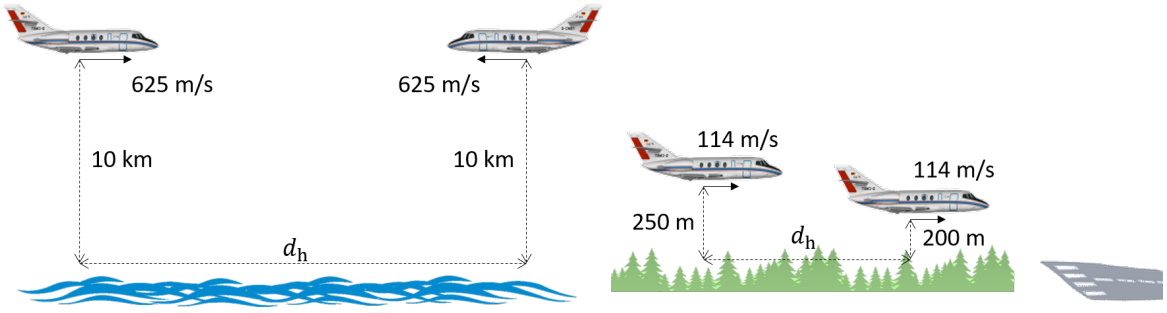

(a) Oceanic. (b) Airport joint approach.

Figure 4.1. Scenarios of interest for the LDACS A2A design.

Oceanic. In the oceanic scenario, both aircraft fly towards each other at the same altitude over the ocean separated by a distance d_h. This scenario, depicted in Fig. 4.1a, covers both, the long-range communications required in ORP regions, as well as the close-range communications required when two aircraft approach each other at the same altitude. To reproduce the real scenario as faithfully as possible, the aircraft fly at an altitude of 10 km above of sea surface. Note that a low altitude is not expected when flying over the ocean, whereas a higher one can be expected but would yield a less challenging channel. In [ER07], two different phases are envisaged in the modernization of the ATM. In the first phase, only subsonic aircraft speeds are considered, yielding a maximum relative airspeed of 617.33 m/s (1200 knots[1]) between two aircraft. In the second phase, supersonic aircraft speeds are also expected, and thus the maximum relative airspeed between two aircraft increases up to 1250.10 m/s (2430 knots). A higher relative speed yields a higher Doppler frequency shift and spread, which can degrade the performance of the datalink severely. In order to consider the most challenging case for the design, we use the highest aircraft airspeed, i.e., 625 m/s

[1]The requirements in [ER07] are defined in knots.

for each aircraft. In order to reflect the real scenario as faithfully as possible, the aircraft do not fly parallel to the Earth's surface but with a slight pitch-up of 4 degrees.

Airport joint approach. In the second scenario, depicted in Fig. 4.1b, both aircraft are approaching an airport following the same approach line. The aircraft are flying over dense forest, such that strong scattering components are present but no SR. A typical approaching airspeed of 114 m/s is assumed for each aircraft. Moreover, it is assumed that the tailing aircraft flies at 250 m above ground and the leading aircraft is already at a lower altitude, as it will land first, of 200 m above ground. This difference in altitude is extremely important for the channel characteristics, as it will lead to a significant attenuation of the LoS component caused by the aircraft fuselage and antenna radiation pattern. Thus, the channel MPCs become much more relevant.

The A2A channel model proposed in Section 3.4 is used to recreate the channel in both scenarios, considering an operating frequency of 1 GHz. One can notice that the proposed A2A channel model was verified with measurements at 250 MHz and some of its stochastic characteristics still have to be verified with measurements at 1 GHz. This was not possible as no actual A2A channel measurements at 1 GHz were either available or reported in the literature. Nonetheless, the SR component was identified as the main MPC present in the A2A channel and our channel model recreates it based on the geometry and on the reflection model provided by the International Telecommunication Union (ITU), which are also applicable to the L-band. The scattering components are also partly based on a geometrical model, which is also applicable to the L-band, but the actual RCS in the L-band may differ from the one measured at 250 MHz. However, the power of the scattering components, as well as the RCS, generally decreases as the frequency increases. Thus, we are confident that our A2A channel model can be applied to the L-band and that it will recreate the A2A channel realistically, albeit possibly overestimating the power of the scattering components and yielding a more conservative scenario for the design of LDACS A2A.

For link budget considerations and to estimate the signal-to-noise ratio (SNR), the characteristics of the LDACS airborne station are assumed, including a maximum equivalent isotropic radiated power (EIRP) of 41 dBm, a receiver loss of 4 dB, and a receiver noise figure of 6 dB [Grä+19]. In addition, we consider the common, blade-style vertically polarized L-band antennas used in aviation, with nominal omni-directional radiation in azimuth and cosinusoidal in elevation, achieving a maximum antenna gain of 4 dBi. The antennas are located below the aircraft and facing downwards.

Figure 4.2 shows some of the main channel characteristics derived from our A2A channel model in both scenarios. For long-range communications, the main parameter

of interest is the SNR influenced by the thermal noise at the receiver. The average, expected SNR is shown in Fig. 4.2 together with the SNR that would be obtained with a perfect antenna alignment, which can be seen as an upper bound. The difference between the average SNR, considered for the simulations, and the upper bound is roughly 6 dB, which means that the simulations are based on a realistic, yet conservative scenario in terms of the SNR. Comparing the oceanic and the approach scenarios, one can notice that the SNR mainly plays a role in the oceanic scenario, given that the short distances considered in the approach scenario yield an SNR higher than 40 dB in any case. In the oceanic case, the SNR is very high at short aircraft distances, e.g., more than 20 dB for separations below 40 km, and decreases slowly as the distance increases, reaching roughly 0 dB at a distance of 450 km. Taking into account these values, one can already expect that the physical layer will have to implement robust modulation and FEC schemes to achieve a long communications range. By contrast, higher modulation and coding rates yielding a higher data throughput could be used for short-distance communications to exploit the higher SNR.

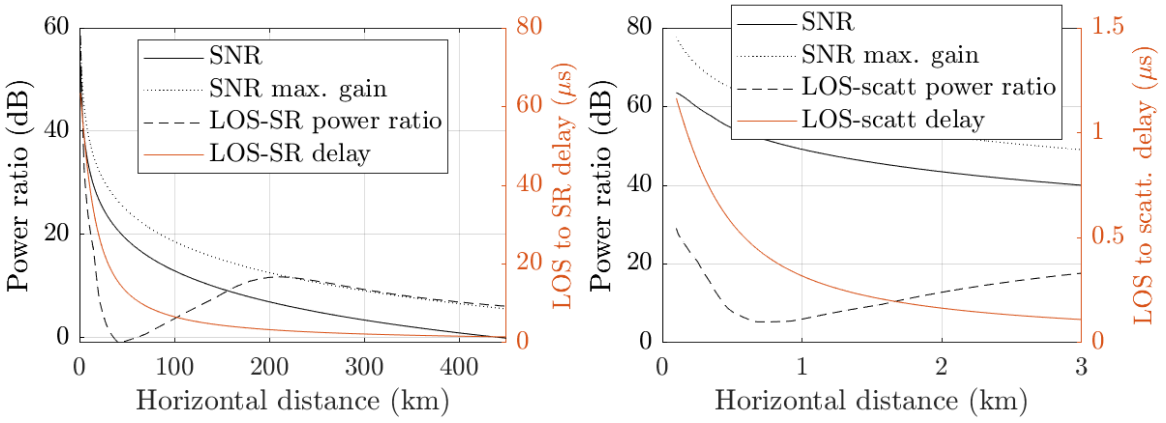

(a) Oceanic.

(b) Airport joint approach.

Figure 4.2. Average SNR and upper bound (for perfect antenna alignment). Relation between LoS and main MPC (SR or scattering) in power and in delay.

Figure 4.2 also depicts the relation in power and in delay between the LoS and the main MPC of each scenario, i.e., the SR component in the oceanic scenario and the scattering components in the approach scenario. For the scattering components, the relation is shown with respect to the scattering components with the lowest delay, i.e., arriving first, as they are generally the strongest. In both scenarios, the LoS component and the main MPC get closer in delay as the distance between both aircraft increases. In other words, both components arrive with a relatively large separation when the aircraft are close, but are received practically together when the aircraft

are far apart. However, although the difference in length between both propagation paths decreases monotonically with the distance, the LoS-to-MPC power ratio does not decrease monotonically but presents multiple inflection points. In both scenarios, although many factors contribute to the LoS-to-MPC power ratio, the main drivers of the non-monotonic behaviour are 1) the antenna gain experienced by the MPC and 2) the reflection coefficient of the Earth's surface. To better illustrate this, we focus on the oceanic scenario (Fig. 4.2a). When the aircraft are located very close to each other, the SR component experiences a much longer propagation path and a much lower antenna gain, because of the high misalignment with the main radiation lobe of the antennas, compared to the LoS component. When the distance increases, the angle of departure of the SR component changes very rapidly and the SR component reaches a better alignment with the main radiation lobe of the antennas, experiencing an antenna gain much higher than the one of the LoS component. The antenna gain, reflection coefficient, and some angles of interest are shown in Appendix C (Fig. C.1) for the sake of completeness. The much higher antenna gain experienced by the SR component leads to the minimum in the LoS-to-SR power ratio observed at a separation of roughly 45 km, where the SR component becomes more powerful than the LoS component. After that, the antenna gain experienced by the SR component starts decreasing and the LoS-to-SR power ratio increases again. However, the LoS-to-SR power ratio reaches a maximum at a separation of roughly 200 km, where the sea reflection coefficient reaches a minimum and the reflected wave is attenuated the most by the sea. For higher aircraft separations, the LoS-to-SR power ratio decreases monotonically.

In the oceanic scenario, the SR component becomes slightly stronger than the LoS component when the aircraft are roughly 45 km apart. In the approach scenario, the scattering components are only 5 dB below the LoS component for separations of approximately 800 m. This means that the most challenging channel for the physical layer does not necessarily have to be the point with the lowest SNR, but it will depend on many parameters, including the SNR, the excess delay of the main MPC, and its power relative to the one of the LoS component. It is difficult to assess which combinations of these parameters are more challenging for the physical layer. On the one hand, a higher excess delay will lead to inter-symbol interference (ISI) unless compensated with a longer cyclic prefix. On the other hand, the highest excess delay occurs when the LoS component is significantly stronger than the main MPC. However, both parameters decrease as the distance increases, yielding new combinations of them that can have a different impact on the performance of the physical layer. On top of that, the SNR also decreases with the distance, becoming increasingly important and yielding new combinations of the channel parameters with an unforeseeable impact

on the performance. Without computer simulations, it would be unfeasible to find the optimum physical layer design as there is no theoretical framework relating these combinations of the channel parameters with the expected performance.

Let us look into two interesting parameters of the channel: the RMS delay spread and the RMS Doppler spread. After obtaining realizations of the channel using the proposed A2A channel model, both parameters are estimated using (3.16) and (3.19), respectively. Both spreads, depicted in Fig. 4.3 for the scenarios of interest, present a similar behaviour. They increase initially with the distance and reach the maxima at a separation of roughly 30 km in the oceanic case and of 800 m in the approach case. One can notice that the spreads are closely related to the results shown in Fig. 4.2, as in general the maximum spreads are obtained when the LoS-to-MPC power ratio are low. Nonetheless, it is also interesting to see that the extremes do not happen for exactly the same distances, e.g., in the oceanic scenario the spreads are maximum at a distance of roughly 30 km while the LoS-to-MPC power ratio is minimum for a distance of roughly 45 km. This clearly shows that not only the power ratio is important when designing a system, but also how the MPCs are spread in the delay and Doppler domains. The delay and Doppler spreads can be used to estimate the coherence bandwidth and coherence time of the channel by using (3.22) and (3.24), respectively. As discussed in Section 3.1, (3.22) and (3.24) only provide estimations or bounds to the actual coherence parameters, but can still be used to get a rough idea of how quickly the channel changes in frequency and time, respectively. As expected, the computed coherence time and coherence bandwidth of the channel, shown in Fig. 4.4, are inversely proportional to the Doppler and delay spreads, respectively.

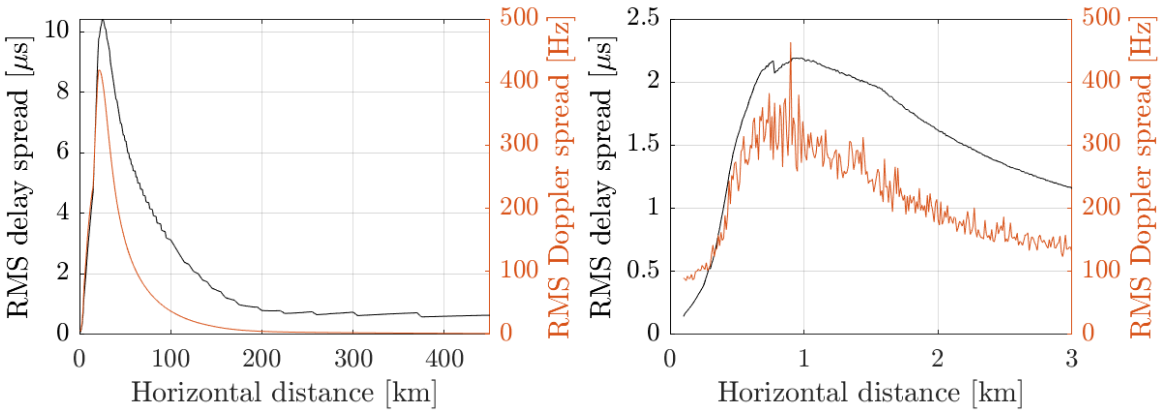

(a) Oceanic.

(b) Airport joint approach.

Figure 4.3. RMS delay and Doppler spreads estimated using the A2A channel model.

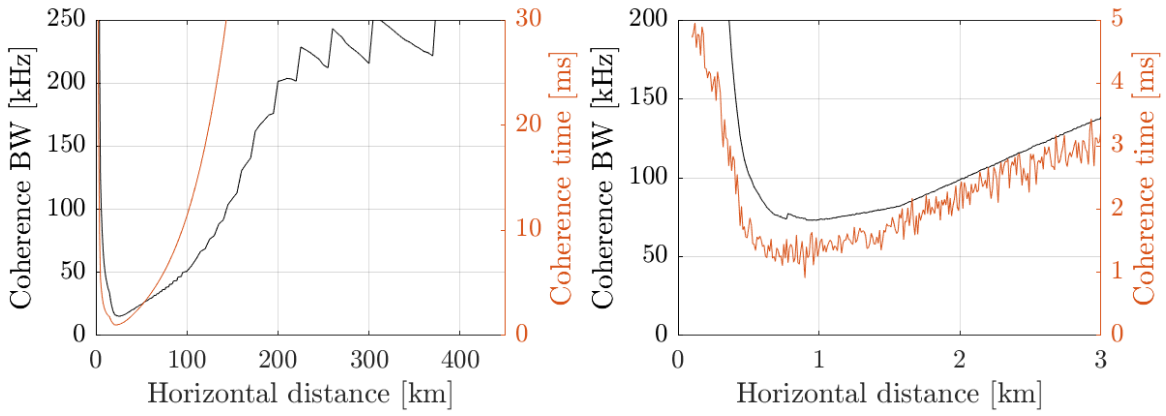

(a) Oceanic.

(b) Airport joint approach.

Figure 4.4. Approximation to the coherence time and coherence bandwidth.

4.3 Physical Layer Design

We dive into the design of the physical layer of LDACS A2A. First, we discuss the transmitter and receiver chains and the main design options and parameters. Second, we perform simulations in the scenarios of interest to obtain the performance of the different designs and to assess which of them are most suitable. Based on this analysis, we finally propose a physical layer design.

4.3.1 Transmitter

The transmitter chain shown in Fig. 4.5 is considered for the design of the physical layer of LDACS A2A. The main operations in this layer are first described to later dive into each block separately to discuss the different options and design criteria. The input data bits $\mathbf{b} = [b_0, b_1, ..., b_{N_\mathrm{B}-1}]^\mathrm{T}$ from the upper layers are encoded using a suitable FEC and then bit-interleaved to randomly spread them over the time and frequency domain. The encoded and interleaved bits $\mathbf{b}^\mathrm{e} = [b_0^\mathrm{e}, b_1^\mathrm{e}, ..., b_{N_\mathrm{e}-1}^\mathrm{e}]^\mathrm{T}$ are then mapped to modulation symbols from a given constellation. Following the required serial to parallel (S/P) conversion of the data symbols, these are then assigned to different subcarriers of the available OFDM symbols following a predefined pattern. Each OFDM symbol comprises N_FFT subcarriers spaced Δf_sc apart, being each subcarrier capable of transmitting one symbol. Other symbols with multiple purposes can also be assigned to some subcarriers in this step, such as pilot, synchronization, automatic gain control (AGC), and peak-to-average power ratio (PAPR) reduction symbols. By applying an inverse fast Fourier transform (IFFT) to each OFDM symbol, the frequency-domain symbols are transformed to a time-domain OFDM symbol of length $T_\mathrm{os} = 1/\Delta f_\mathrm{sc}$. Then, a

prefix with a duration of T_{cp} is appended to each OFDM symbol, such that the length of the total OFDM symbol increases to $T_{\mathrm{s}} = T_{\mathrm{os}} + T_{\mathrm{cp}}$. This prefix is a copy of the last part of the OFDM symbol, creating a sort of cyclical repetition of the signal whose benefits will be explained later. Then, windowing is applied to improve the spectral characteristics of the transmit waveform. In this work, baseband digital models of the transmitter, receiver, and channel are employed, such that computer simulations can be conducted to assess the performance of each design option. The transmit vector $\mathbf{s} = [s_0, s_1, ..., s_{N_{\mathrm{sa}}-1}]^{\mathrm{T}}$ is generated with a sampling period $T_{\mathrm{sa}} = 0.4\,\mu\mathrm{s}$. The number of samples N_{sa} per message depends on the message length and, consequently, on the physical-layer design under test.

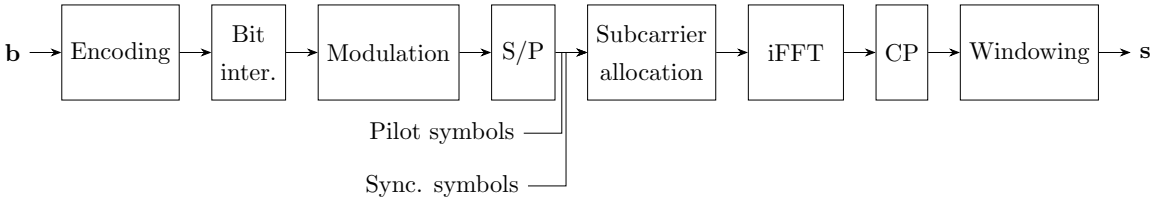

Figure 4.5. Physical layer (transmitter side) of the LDACS A2A.

Forward Error Correction

There are many FEC schemes that can be used to protect the data bits by adding redundancy to them and allowing the receiver to detect and correct a certain amount of bit errors. For our analysis, five different schemes already employed by other systems are compared. We consider the two encoding schemes used by LDACS A/G, i.e., convolutional code (CC) and concatenated Reed-Solomon and convolutional code (CRSCC), the turbo code (TC) used in 4G (Long Term Evolution (LTE)) mobile communications, as well as the LDPC and the polar codes used in 5G mobile communications.

For all considered FEC schemes, a coding rate of 1/3 is used. LDACS A/G employs a rate-1/3 zero-termination convolutional code with a constraint length equal to 7 for cell access and dedicated control data. For user data, LDACS A/G uses a CRSCC code with block interleaving between the outer Reed-Solomon (RS) code and the inner CC code. The inner CC code has a coding rate 1/2 by default. For a fair comparison between all codes, the rate-1/2 CC is applied and a RS coding rate is used such that the total coding rate of the CRSCC is 1/3. The details of the CC and CRSCC codes used by LDACS can be found in its specification [Grä+19]. The TC considered for our analysis and used in the LTE standard is composed of two parallel recursive systematic convolutional encoders. The details of the specific TC, as well as the interleaving pattern used between both sub-codes, are comprehensively described in [Alt11]. The

increase in computational power and the great performance of the LDPC and polar codes [Ari09], which have shown to be close to the Shannon limit, have led to their adoption by many new systems and to supersede CC and TC in the 5G mobile communications standard. We consider the cyclic redundancy check (CRC)-aided polar code[2] and the LDPC code defined for the up-link in 5G. The reader is referred to the 5G standard [ETS24] for more information on both FEC schemes.

Note that a coding rate of roughly 1/3 is considered for all FEC schemes since it provides a good trade-off between robustness and net throughput. However, LDACS A2A shall use adaptive coding and modulation (ACM) to achieve a higher net data throughput when the channel conditions are more favorable. The coding rate can be changed by applying puncturing to the output bits. We focus on the basic operation of the physical layer and leave the less-important definition of ACM as future work.

Bit Interleaving

After the FEC, which in some cases already includes some sort of interleaving, helical bit interleaving is applied as in LDACS A/G to evenly spread the encoded bits in the frequency (subcarriers) and time (OFDM symbols) plane. The helical interleaving has two parameters, a_{bi} and b_{bi}, whose multiplication results in the number of coded bits. For completeness, the achievable performance is compared with and without bit interleaving, in order to assess its effectiveness.

Modulation

Although multiple modulation schemes could be considered, the focus is placed on quadrature amplitude modulation (QAM) because of its wide adoption in most communication systems, such as LTE, and to facilitate the backwards compatibility between LDACS A2A and LDACS A/G. As done by these systems, 4-QAM is employed as the baseline providing most robustness and enabling the highest communications range. A higher modulation can be used when the channel conditions allow it. In all cases, Gray mapping is applied to minimize the number of bit errors.

CP-OFDM Waveform

One of the main constraints in the LDACS A2A design is that the waveform should be as similar as possible to the one of the reverse link of LDACS A/G, in order to facilitate a later standardization of the system. Thus, many parameters are reused from the LDACS A/G specification, including the subcarrier spacing $\Delta f_{\mathrm{sc}} = 9.765625\,\mathrm{kHz}$

[2] 11 bits are used for the CRC.

and the number of subcarriers per OFDM symbol $N_{\mathrm{FFT}} = 64$. To comply with the LDACS A/G spectral mask, only $N_{\mathrm{u}} = 50$ subcarriers are actively used and nothing is transmitted at the 7 lowest and 6 highest subcarriers, left as guard bands, and at the DC subcarrier[3]. The effective bandwidth of the system remains the same as for LDACS A/G, i.e., $(N_{\mathrm{u}} + 1) \cdot \Delta f_{\mathrm{sc}} = 498.05\,\mathrm{kHz}$, taking into account the N_{u} active subcarriers and the DC subcarrier.

Ideally, the subcarrier spacing Δf_{sc} would be designed carefully taking into account the channel characteristics and the system requirements. It must be high enough to cope with the Doppler spread of the channel, so that the orthogonality between the subcarriers is maintained and the inter-carrier interference (ICI) is minimized. A high subcarrier spacing also increases the tolerance of the system against clock frequency inaccuracies. In addition, the frequency-domain one-tap equalization performs best if the channel remains constant for the entire duration of the OFDM symbol (T_{s}). A higher Δf_{sc} yields a lower T_{s}, and thus a more valid assumption of the channel remaining constant. Nonetheless, the subcarrier spacing cannot be increased indefinitely. Importantly, increasing Δf_{sc} eventually leads to a decrease in the spectrum efficiency. Given that the overall bandwidth of the system is limited, increasing Δf_{sc} leads to a lower number of subcarriers usable to carry symbols. This could be compensated by transmitting more, shorter OFDM symbols because of the inversely-proportional decrease in T_{os}. However, transmitting more OFDM symbols also leads to more CPs, whose length does not change with Δf_{sc}, therefore increasing the overall overhead. Thus, Δf_{sc} is a parameter that should be chosen, ideally, as a careful trade-off between multiple effects. Assessing whether the subcarrier spacing $\Delta f_{\mathrm{sc}} = 9.765625\,\mathrm{kHz}$ can be used to cope with the A2A channel is not straightforward. There are some text-book approximations that provide upper and lower bounds for the subcarrier spacing based mainly on the channel spread and coherence parameters. Although these approximations are useful for a preliminary design when no realistic channel model is available for simulations, they do not account for all channel effects and ignore that some of these effects can be better coped with by other parts of the physical layer, e.g., by the FEC. Thus, simulations are required for a reliable and optimal design of the physical layer.

In the most widespread version of OFDM, which is the one used in LDACS and LTE, a CP with a duration of T_{cp} is appended in time domain before each OFDM symbol to protect it, increasing the total duration of the OFDM symbol to $T_{\mathrm{s}} = T_{\mathrm{os}} + T_{\mathrm{cp}}$. This prefix is a copy of the last part of the OFDM symbol, T_{cp}. The CP does not contain useful information and is removed at reception. Although it helps to alleviate the effect

[3]The DC subcarrier, i.e., the subcarrier with no shift to the carrier frequency, is commonly left unused in most systems to prevent the performance loss caused by the leakage from the local oscillator.

of synchronization inaccuracies, the CP is mainly aimed at mitigating the effect of the propagation channel on the signal. Its most crucial benefit is that it enables the use of one-tap channel equalization in the frequency domain, as the effect of the channel on the signal can then be seen as a cyclic convolution, and therefore its effect on the signal can be compensated in the frequency domain through a simple division at the receiver. For this, however, the CP should be theoretically longer than the longest echo of the channel, such that consecutive OFDM symbols do not overlap at reception because of the multi-path propagation in the channel, which leads to ISI and to a decrease in the performance. However, increasing the length of the CP also leads to an increase in the overhead and a decrease in the spectrum efficiency, as well as to a larger change in the channel experienced by consecutive OFDM symbols and a less effective pilot-aided channel estimation and equalization. Thus, in reality, the CP must be designed to cover only the relevant channel MPCs and to accept the ICI and ISI introduced by the longer echoes. Given the geometry-dependent nature of the A2A channel, illustrated in Fig. 4.2, it becomes clear that the CP length yielding the maximum performance cannot be estimated analytically but must be computed through simulations.

Time/Frequency Symbol Distribution

Each packet, or frame, is comprised of N_{os} OFDM symbols with N_{u} usable subcarriers each. Out of the $N_{\mathrm{u}} \cdot N_{\mathrm{os}}$ subcarriers available per packet, only some are used to transmit data symbols. Other symbols with multiple purposes are carried by the remaining subcarriers, including pilot, synchronization, AGC, and PAPR reduction symbols[4]. Synchronization symbols are used to allow the receiver to synchronize in time and frequency to the signal in order to decode it. They are commonly transmitted in a synchronization preamble immediately before the N_{os} OFDM symbols of the packet. This synchronization preamble can be composed of one or multiple OFDM symbols. For example, LDACS A/G uses two OFDM symbols for synchronization before the transmission of a forward link frame, and under some conditions in the reverse link. The synchronization symbols in the preamble compose the so-called CAZAC (constant amplitude, zero autocorrelation) sequences, which present good correlation properties in time domain. In this work, we assume perfect time and frequency synchronization with the LoS signal and thus do not recreate the initial synchronization procedure. However, it is recommended to use the same synchronization preamble used by LDACS A/G, as it has proven effective in flight trials [BM+22]. AGC symbols are used in the reverse link of LDACS A/G but are not considered to be needed for LDACS A2A.

[4]Formally, the DC subcarrier and the subcarriers left unused at the sides of the spectrum also carry symbols with zero amplitude, which are commonly referred to as null symbols.

The impact of the PAPR reduction symbols used in the reverse link of LDACS A/G are unclear, and thus are not considered here. Pilot symbols are used to estimate the channel at the receiver and to later equalize it, improving the decoding capabilities significantly. An optimum distribution of pilots over the frequency and time plane is crucial to exploit the advantages of pilot-aided channel estimation while minimizing the loss in net throughput. In order to be able to faithfully recreate the channel, the distance between the pilot symbols in time and frequency must not be too high compared to the coherence time and coherence bandwidth of the channel, respectively.

Distribution of Pilot Symbols Different pilot patterns are tested for the design. Changing the spacing of pilots in frequency and/or time, it can be assessed which patterns provide the lowest overhead while fulfilling the required performance. All considered pilot patterns follow one basic rule: in order to avoid having to extrapolate the channel at any subcarrier, the lowest and highest active subcarriers of the first and last OFDM symbols always carry pilot symbols. The remaining pilot symbols are then distributed over the time/frequency plane uniformly maintaining a maximum frequency separation of $(\Delta f_\mathrm{p})_\mathrm{max}$ subcarriers and a maximum time separation of $(\Delta t_\mathrm{p})_\mathrm{max}$ OFDM symbols. This is illustrated with two exemplary patterns in Fig. 4.6, where $N_\mathrm{os} = 10$ OFDM symbols are used per packet to transmit $L_\mathrm{B} = 34$ data bytes. In Fig. 4.6a, pilots are placed every 4 subcarriers in frequency and 3 OFDM symbols in time. In Fig. 4.6b, the maximum spacing between pilots is reduced to 3 subcarriers in frequency and increased to 5 OFDM symbols in time. One could think here of sending an additional OFDM symbol in Fig. 4.6b for a more uniform pilot spacing in the time domain. However, the rule of making transmissions as short as necessary to transmit the required L_B data bytes prevails over the uniformity or optimization of the distribution of pilots.

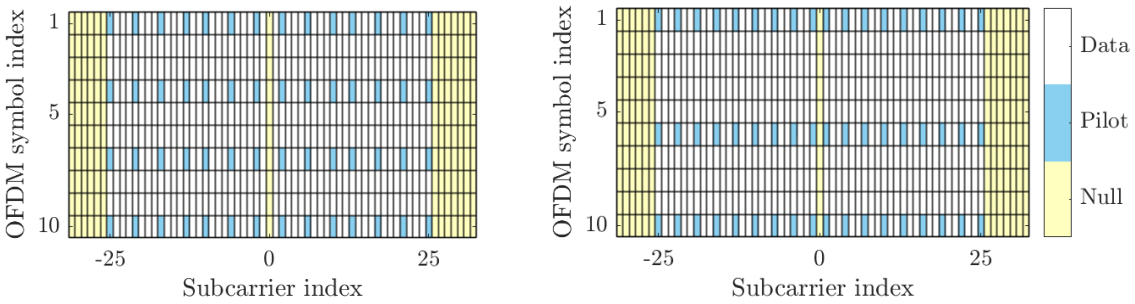

(a) $(\Delta f_\mathrm{p})_\mathrm{max} = 4$ and $(\Delta t_\mathrm{p})_\mathrm{max} = 3$.

(b) $(\Delta f_\mathrm{p})_\mathrm{max} = 3$ and $(\Delta t_\mathrm{p})_\mathrm{max} = 5$.

Figure 4.6. Distribution of pilot symbols over the OFDM time-frequency plane for two exemplary configurations.

Windowing

Transmit windowing might have to be applied to the transmit signal after CP-OFDM to achieve the spectrum characteristics of LDACS A/G. It aims at smoothing the sharp transitions between OFDM symbols to reduce out-of-band radiation. The transmit windowing defined in LDACS A/G is also applied here, which consist of a raised cosine function with a roll-off factor of 0.107. For it to be applied, a cyclic postfix of duration T_{w} is appended to each OFDM symbol after it. It is a cyclical repetition of the beginning of the OFDM symbol. However, it does not increase the overall duration of the OFDM symbol as the cyclic postfix overlaps with the beginning of the CP of the following OFDM symbol. The raised cosine function is applied to the beginning of each CP during T_{w} and to its postfix of T_{w} duration. Since windowing is not the focus of this work, the reader is referred to [Grä+19] for further details on it. In order to comply with the LDACS spectral mask, a minimum CP length of 12.8 µs is required.

4.3.2 Receiver

The propagation of the signal through the channel can be reproduced as a convolution of the transmit signal with the weight function of the channel. In our simulation chain, baseband digital models of the transmitter, receiver, and channel are employed. The received vector $\mathbf{r} = [r_0, r_1, ..., r_{N_{\mathrm{sa}}-1}]^{\mathrm{T}}$ is obtained as

$$r_{n_{\mathrm{sa}}} = \sum_{k=0}^{L_{\mathrm{h}}-1} s_{n_{\mathrm{sa}}-k} \cdot h_{n_{\mathrm{sa}},k} + w_{\mathrm{n}_{n_{\mathrm{sa}}}} \,, \tag{4.1}$$

where $n_{\mathrm{sa}} = 0, 1, ..., N_{\mathrm{sa}} - 1$ is the sample index, $h_{n_{\mathrm{sa}},k}$ is the channel weight function for the n_{sa}-th sample with $k = 0, 1, ..., L_{\mathrm{h}} - 1$ as the delay index and L_{h} the channel length, and $w_{\mathrm{n}_{n_{\mathrm{sa}}}}$ is white Gaussian noise. Note that $s_{n_{\mathrm{sa}}-k} = 0$ for $n_{\mathrm{sa}} - k < 0$. The received signal $\mathbf{r}$ is processed following the receiver chain shown in Fig. 4.7. After the initial synchronization, which is assumed perfect in our work, the different OFDM symbols of the received signal can be delimited, such that $\mathbf{r}_{l_{\mathrm{os}}} = [r_{l_{\mathrm{os}},0}, r_{l_{\mathrm{os}},1}, ..., r_{l_{\mathrm{os}},N_{\mathrm{sa,os}}-1}]^{\mathrm{T}}$ contains the $N_{\mathrm{sa,os}} = \frac{T_{\mathrm{s}}}{T_{\mathrm{sa}}}$ samples of the l_{os}-th OFDM symbol, for $l_{\mathrm{os}} = 0, 1, ..., N_{\mathrm{os}} - 1$. The CP of each OFDM symbol is removed and a fast Fourier transform (FFT) is then applied to the remaining samples of the OFDM symbol to obtain the N_{u} data and pilot symbols of interest. After doing this process for the N_{os} OFDM symbols transmitted per message, the $N_{\mathrm{os}} \cdot N_{\mathrm{u}}$ data and pilot symbols contained in the message are obtained. The pilot symbols, $\mathbf{R}_{\mathrm{pil}}$, are used to estimate the channel at each subcarrier and OFDM symbol. Although there are many different channel estimation schemes, we apply 2D linear interpolation [ES10] as it performs reasonably well without requiring previous knowledge on the channel, e.g., its correlation. The obtained performance can then

be seen as the baseline, given that better-performing alternatives can be applied in the future to further improve it. The data symbols, $\mathbf{R}_{\text{data}}$, are then equalized using the estimation of the channel. Two linear equalization schemes, based on the zero-forcing (ZF) and minimum mean square error (MMSE) criteria, have been tested. The initial tests showed that the linear equalization based on ZF performs significantly worse than the one based on MMSE because of the enhancement of the noise when the channel presents very deep fades. This is actually the case in the A2A channel because of the presence of two signal components, i.e., the LoS and the SR components, with similar power. Thus, only MMSE linear equalization is considered in the presented results. Using the equalized data symbols, log-likelihood ratios (LLRs) are computed to enable soft decoding. After de-interleaving the LLRs, decoding is performed to recover the original data symbols. For this, the standard decoding approach for each FEC scheme is used, i.e., soft Viterbi decoding for CC, parallel concatenated convolutional decoding for TC [Ben+96; Vit98] using up to 10 iterations, the sum-product message-passing algorithm for LDPC, and CRC-aided successive-cancellation list decoding of size 8 for the polar code.

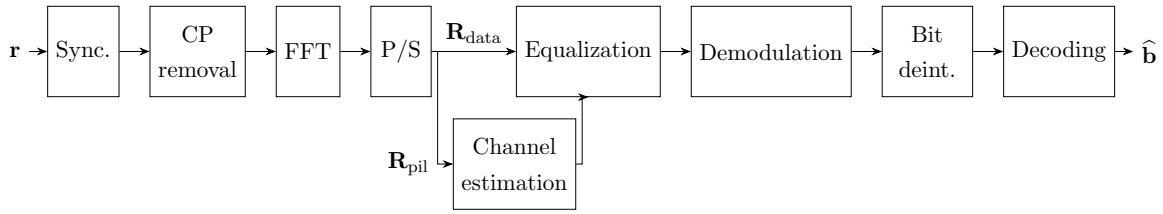

Figure 4.7. Physical layer (receiver side) of LDACS A2A.

4.3.3 Simulation Results

The design of the physical layer is based on the performance obtained through computer simulations for the different design options. At each position of interest in each scenario, multiple packets are transmitted to obtain the performance, based on the PER, following the Monte Carlo method. The airplanes exchange messages of $L_{\text{B}} = 34$ bytes. The data bits are generated randomly with equal probability between zeros and ones. Each generated message is fed to the transmitter, which processes it and produces the transmit packet $\mathbf{s}$. The transmission of the signal through the A2A channel is reproduced as in (4.1). The statistics of the channel depend on the specific scenario and geometry under test, as defined in Section 3.4. The channel is recreated up to a delay of 30 µs after the SR delay, i.e., $L_{\text{h}} = \left\lceil \frac{\tau_{\text{sr}} + 30\,\mu\text{s}}{T_{\text{sa}}} \right\rceil$, covering the SR component and the most significant scattering components of the channel. A new realization of the time-variant channel weight function $h_{n_{\text{sa}},k}$ is obtained for each new message $\mathbf{s}$ using

our A2A channel model. Note that, unlike other analysis such as [Haa02], $h_{n_{\mathrm{sa}},k}$ does not remain constant within a packet, but changes from sample to sample, i.e., with n_{sa}. The received signal $\mathbf{r}$ is processed by the receiver, which is able, or not, to recover the original message. Following the Monte Carlo approach, this process is repeated until enough packets have been transmitted for each design option and position in the scenario, such that a solid estimation of the PER is attained.

First, the performance in the oceanic scenario is obtained, assuming initially a perfect channel estimation. Note that, even with perfect knowledge of the channel, one can never achieve a perfect channel equalization if one-tap frequency-domain equalization is used, given that the channel changes continuously, i.e., from sample to sample, and thus the different samples of one OFDM symbols are affected by slightly different channels. In our simulations, when perfect channel estimation is assumed, we use the snapshot of the channel in the middle of the OFDM symbol to perform the one-tap frequency-domain equalization. Figure 4.8 shows the PER obtained in the oceanic scenario for the five FECs schemes considered and using the CP length of LDACS ($T_{\mathrm{cp}} = 17.6\,\mu\mathrm{s}$). To assess the effectiveness of bit interleaving, the results are shown with helical bit interleaving (Fig. 4.8a) and without it (Fig. 4.8b). One can see that a perfect channel estimation helps maintaining a PER below 10^{-4} for all FEC schemes until the aircraft are separated by a long distance, where the SNR gets critically low and the PER increases. There are significant differences in the achievable performance between the FEC schemes. The worst-performing coding schemes are CRSCC and CC, which can only achieve a communications range of roughly 350 km with a PER of 10^{-3}. Note that CRSCC can be used with or without interleaving between the inner and outer codes. The CRSCC scheme employed to obtain the simulations results shown here uses no interleaving between both codes. However, the results for CRSCC with random byte interleaving between the outer and inner codes were also obtained and no differences in the PER performance was noticed. Using LDPC or TC increases the achievable communications range, but all coding schemes are clearly outperformed by the polar coding, which shines at low SNR regimes and is capable of achieving a communications range of almost 450 km with a PER of 10^{-3}. This is significantly better than the desired communications range of roughly 370 km in the oceanic scenario. Comparing Fig. 4.8a with Fig. 4.8b, it is verified that helical bit interleaving proves its effectiveness and helps reducing the PER in all cases. The difference is minimal for the CRSCC, LDPC, and polar codes, but significant for TC and specially CC. From now on, only the two best-performing FEC schemes are considered, i.e., TC and polar coding, and always with helical bit interleaving.

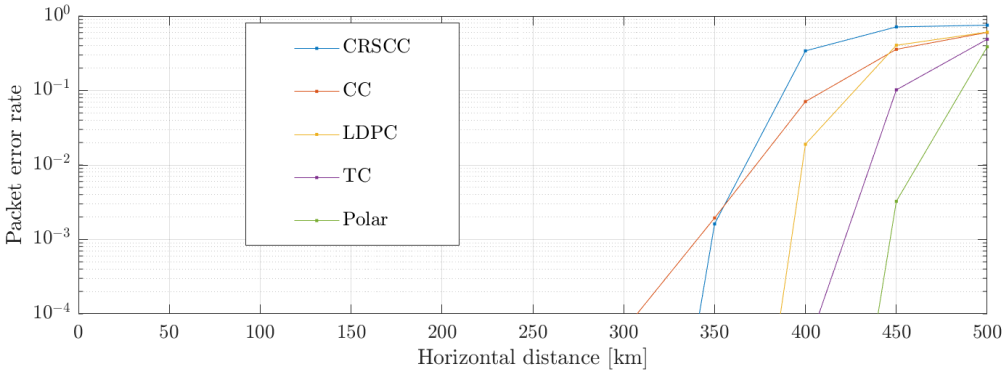

(a) With helical bit interleaving.

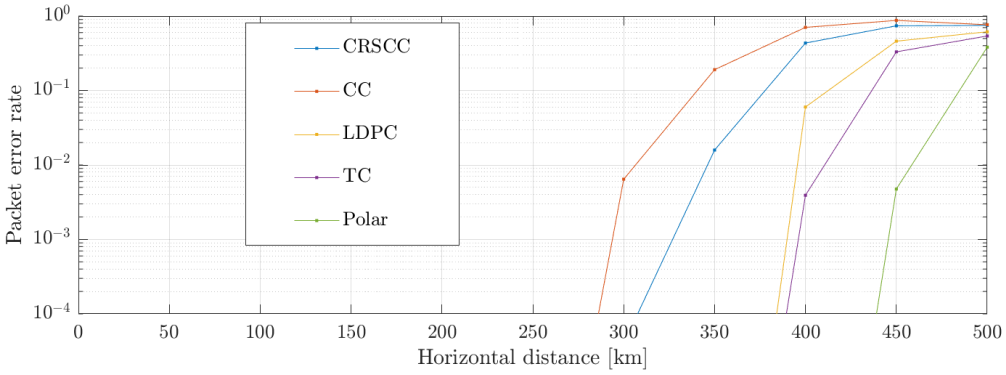

(b) Without bit interleaving.

Figure 4.8. PER in the oceanic scenario using different FEC schemes. Perfect channel estimation with MMSE linear equalization. $T_{\mathrm{cp}} = 17.6\,\mu\mathrm{s}$.

Next, the assumption of a perfect channel estimation is dropped and the receiver performs pilot-aided channel estimation based on 2D linear interpolation. Figure 4.9 presents the obtained PER for multiple $(\Delta f_{\mathrm{p}})_{\mathrm{max}}$ and $(\Delta t_{\mathrm{p}})_{\mathrm{max}}$ configurations, i.e., maximum allowed separation in time (OFDM symbols) and frequency (subcarriers), respectively, between pilots. Note that varying the pilot spacing yields a different number of OFDM symbols, N_{os}, required to transmit the 34-bytes packet. The required N_{os} is displayed in the legend. As expected, the communications range shrinks when no perfect channel estimation is possible, given that the low SNR reduces the accuracy of the channel estimation and, consequently, of the equalization. One can notice that TC and polar coding perform now very similarly. Also, the use of imperfect channel estimation leads to the PER spiking for a separation between the aircraft of 34 km. This goes in line with the channel characteristics shown previously in Fig. 4.3a and Fig. 4.4a, which already indicated that a challenging channel would be expected around this point. For this challenging region, the effect of using different pilot patterns becomes clear, as some of them are able to keep a PER below 10^{-4}, while others yield a very high

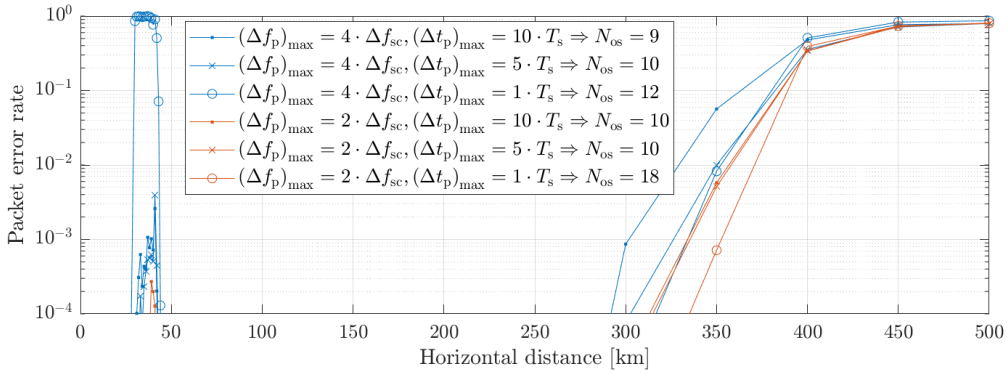

(a) TC FEC.

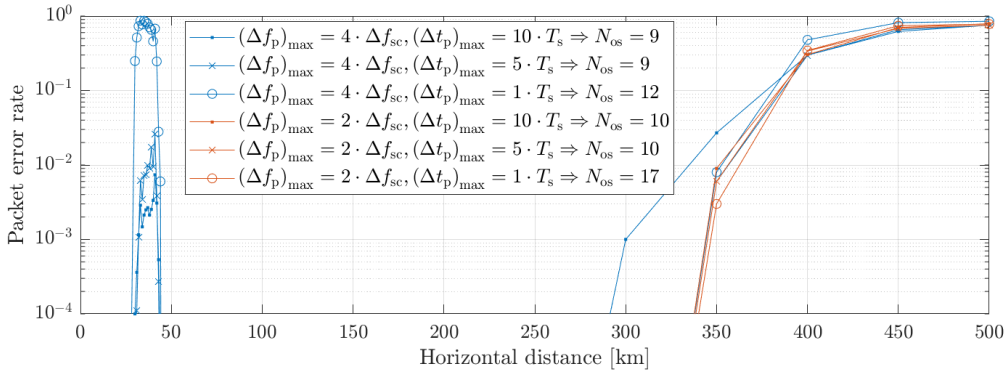

(b) Polar FEC.

Figure 4.9. PER in the oceanic scenario for multiple pilot patterns. 2D linear interpolation channel estimation with MMSE linear equalization. $T_{cp} = 17.6\,\mu s$.

PER. The separation of pilots in frequency seems more critical than in time, given that spacing the pilots every 4 subcarriers is not sufficient to attain the desired performance, but having a separation of 10 OFDM symbols between pilots might suffice as long as the pilots are separated by 2 subcarriers. In some cases, this would mean that only the first and the last OFDM symbol would transmit pilots, which reduces significantly the overhead and the duration of transmissions, being both features highly desired for the design of the physical layer.

The performance in the approach scenario is now discussed. When perfect channel estimation is assumed, all FEC schemes are able to maintain a PER below 10^{-4}, thanks to the short distances and high SNR values of this scenario compared to the oceanic one. Figure 4.10 shows the results for realistic pilot-aided channel estimation using 2D linear interpolation, considering TC and polar coding. Same as for the oceanic scenario, there are certain distances where the PER spikes if the pilots are too separated either in time or in frequency. Again, they coincide with the most challenging channel conditions observed in Fig. 4.3b and Fig. 4.4b. In this case, however, the separation in time

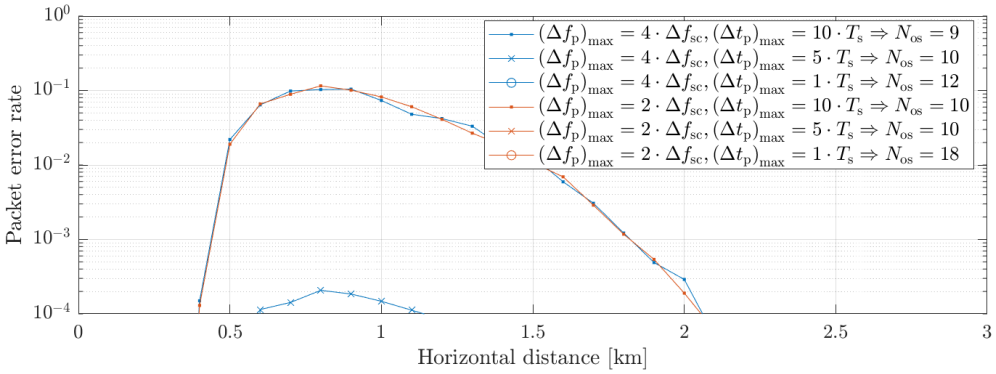

(a) TC FEC.

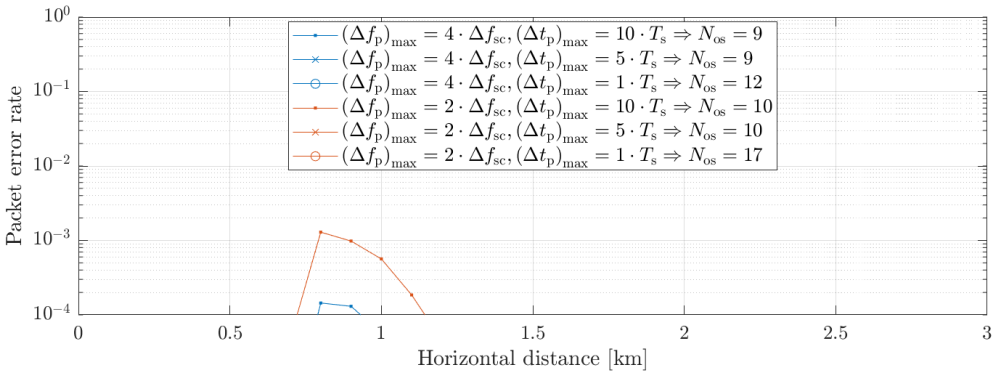

(b) Polar FEC.

Figure 4.10. PER in the approach scenario for multiple pilot patterns. 2D linear interpolation channel estimation and MMSE linear equalization. $T_{cp} = 17.6\,\mu s$.

between pilots becomes more critical than in the oceanic scenario, while their separation in frequency is less constraining. In any case, there are pilot patterns yielding a PER below 10^{-4} for both, TC and polar coding schemes. However, one can notice that polar coding significantly outperforms TC when the same pilot patterns are employed.

The results have shown that a fine tuning of the pilot spacing in time and frequency is required in both scenarios of interest. Thus, a search over the pilot distances in time and frequency is now conducted. Different CP lengths are also tested to assess its impact on the performance. To simplify the analysis, the distance between the aircraft is fixed to 34 km in the oceanic scenario and to 800 m in the approach scenario, which are the most challenging points observed so far at intermediate distances. The PER obtained for a distance of 34 km between aircraft in the oceanic scenario is shown in Fig. 4.11 for polar coding. The different subfigures depict the results for a different pilot spacing in frequency, i.e., placing a pilot every subcarrier (Fig. 4.11a) and up to every 4 subcarriers (Fig. 4.11d). The horizontal axis indicates the number of OFDM symbols carrying pilots and the total number of OFDM symbols required to transmit

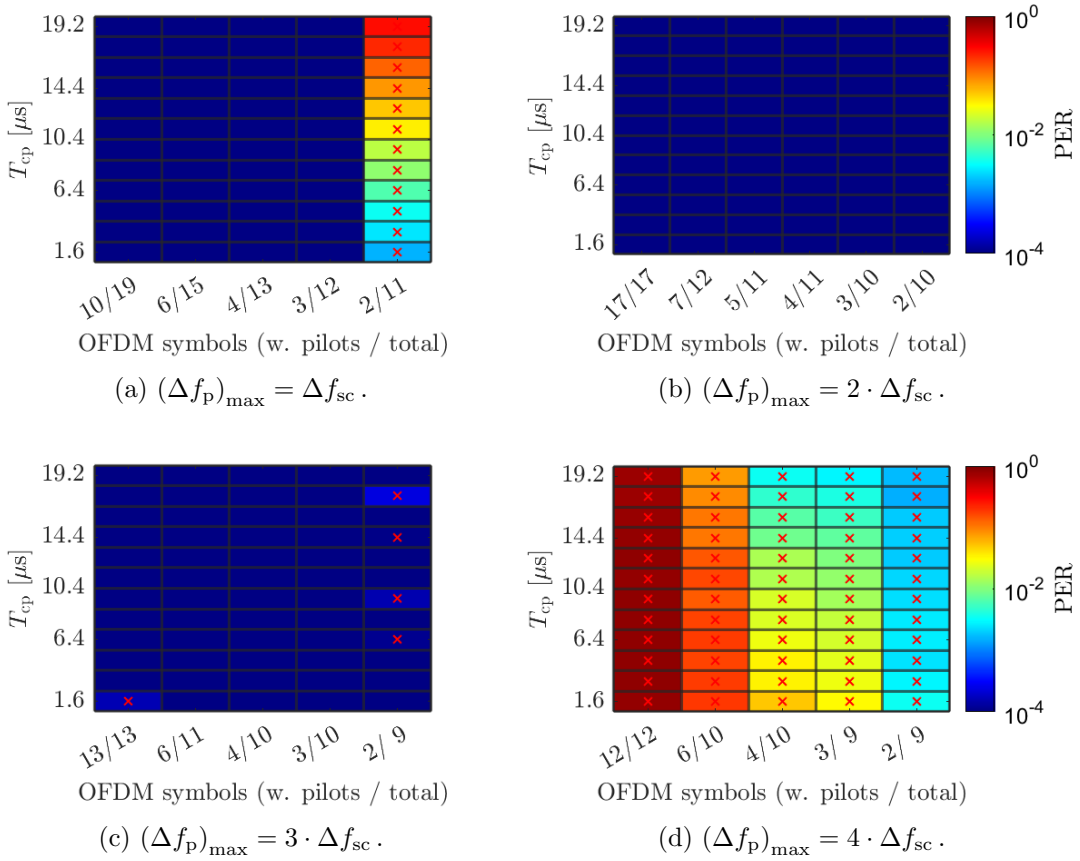

(a) $(\Delta f_{\mathrm{p}})_{\max} = \Delta f_{\mathrm{sc}}$.

(b) $(\Delta f_{\mathrm{p}})_{\max} = 2 \cdot \Delta f_{\mathrm{sc}}$.

(c) $(\Delta f_{\mathrm{p}})_{\max} = 3 \cdot \Delta f_{\mathrm{sc}}$.

(d) $(\Delta f_{\mathrm{p}})_{\max} = 4 \cdot \Delta f_{\mathrm{sc}}$.

Figure 4.11. PER in the oceanic scenario with $d_{\mathrm{h}} = 34$ km for different CP lengths and pilot patterns in time and frequency. The horizontal axis indicates the number of OFDM symbols carrying pilots and the total number of OFDM symbols required to transmit the packet. Polar FEC. 2D linear interpolation channel estimation with MMSE linear equalization.

the packet. For example, '3/10' means that pilots are transmitted every 3 OFDM symbols and that a total of 10 OFDM symbols are required to transmit the desired 34 data bytes. Naturally, a denser distribution of pilots in either time or frequency leads to more OFDM symbols being required to transmit the data. Many interesting conclusions can be derived from Fig. 4.11. First, pilots cannot be farther than 3 subcarriers apart to attain the required performance. Second, a longer CP reduces the PER in some cases (see Fig. 4.11d) but becomes detrimental when the pilot spacing in time is increased (see the '2/11' configuration in Fig. 4.11a), given that the absolute time between pilots increases because of the longer CP and the channel estimation and equalization becomes less accurate. Third, the CP might not be needed in A2A channels, as the required performance is already achieved for some configurations even if a minimum CP length of 1 sample is considered. This can be understood from the

nature of the A2A channel. In contrast to other channels such as the air-ground one, the A2A channel is mainly composed of two strong components that interfere with each either constructively and destructively. This leads to very deep fades in the spectrum, which might make symbols unrecoverable even if the CP covers the main MPCs and the channel estimation and equalization are very accurate, given that the deep fades might bring the symbols below the noise floor. The deep fades, however, are not very numerous and only few symbols are lost because of them, making a robust FEC scheme a more suitable solution to cope with them. If a less-capable FEC scheme is employed, such as CC, the CP becomes more relevant, as we show in Appendix C with the results for CC FEC (Fig. C.3). The results for TC FEC can also be found in Appendix C (Fig. C.2) and are similar to the ones obtained for polar coding in the oceanic scenario.

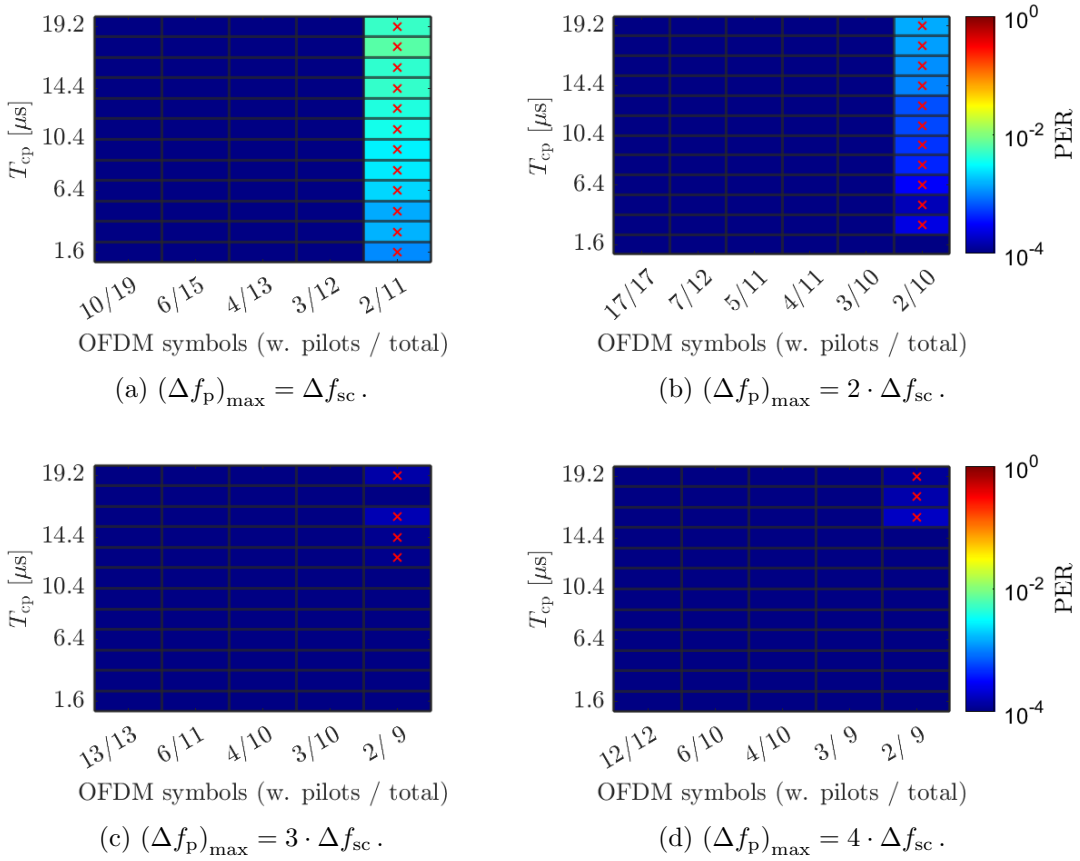

(a) $(\Delta f_{\mathrm{p}})_{\max} = \Delta f_{\mathrm{sc}}$.

(b) $(\Delta f_{\mathrm{p}})_{\max} = 2 \cdot \Delta f_{\mathrm{sc}}$.

(c) $(\Delta f_{\mathrm{p}})_{\max} = 3 \cdot \Delta f_{\mathrm{sc}}$.

(d) $(\Delta f_{\mathrm{p}})_{\max} = 4 \cdot \Delta f_{\mathrm{sc}}$.

Figure 4.12. PER in the approach scenario with $d_{\mathrm{h}} = 800$ m using different CP lengths and pilot patterns in time and frequency. The horizontal axis indicates the number of OFDM symbols carrying pilots and the total number of OFDM symbols required to transmit the packet. Polar FEC. 2D linear interpolation channel estimation with MMSE linear equalization.

Figure 4.12 shows the results in the approach scenario for a distance of 800 m between the aircraft. In general, one can see that a less challenging channel is experienced in this scenario compared to the oceanic one. The approach scenario would allow for a sparser distribution of pilots in the frequency domain, i.e., even every 4 subcarriers, compared to the oceanic case. This pilot spacing relaxation is, however, not possible in the time domain, as the pilot distance in time seems to be again a critical factor and, in fact, the '2/10' pilot pattern acceptable in the oceanic scenario (see Fig. 4.11b) yields an unacceptable PER in the approach one (see Fig. 4.12b).

4.3.4 Proposed Design

The conducted analysis focuses on the periodic broadcasts, or beacons, since they are considered the backbone of the A2A network. Any additional communication capabilities, such as point-to-point (P2P) communications, will be built upon the initial establishment of the network through the periodic broadcasts. Based on the obtained results, it is recommended to use the rate-1/3 polar code employed in 5G communications to protect these broadcasts. This FEC scheme provides, in all considered scenarios, a significantly better performance, i.e., lower PER, than the other candidates. Although the TC FEC presents a similar performance in some cases, it is clearly outperformed by the polar code in other scenarios, such as in the approach one. The other candidates, including CC, CRSCC, and LDPC, provide a significantly worse performance in any case.

Shorter periodic broadcasts are beneficial for the medium access control of LDACS A2A, since they lead to less message collisions as we show in [BMS19]. Depending on the pilot distribution, more or fewer OFDM symbols are required for each beacon. Based on the obtained results, pilots must be located every either 2 or 3 subcarriers to be able to estimate the channel accurately while still minimizing the number of OFDM symbols required per beacon. Using a '2/9' pilot pattern with a pilot spacing of 3 subcarriers would be possible if a very short CP is used. However, that would be in the limit of the desired performance and, in fact, a CP duration of at least 12.8 µs might be required for compatibility with LDACS. Thus, we propose to use the '3/10' pilot pattern with a pilot subcarrier spacing of 3. In other words, each periodic broadcast comprises the synchronization preamble[5] and 10 OFDM symbols, transmitting pilots every 3 subcarriers in the first, central, and last OFDM symbols. A CP duration of 12.8 µs is proposed to enable the same windowing applied by LDACS and, thus, to guarantee spectrum compliance with LDACS. Note that a lower CP, or even the absence

[5]The same synchronization preamble used by LDACS is proposed, which comprises 2 OFDM symbols carrying CAZAC sequences.

Table 4.1. Parameters of the physical layer of LDACS A2A. Parameters not specified here, e.g., EIRP and windowing characteristics, follow the LDACS A/G specification.

Subcarrier spacing: Δf_{sc}	9.765625 kHz
FFT size: N_{FFT}	64
Active subcarriers per OFDM symbol (see Fig. 4.6b): N_{u}	50
Effective bandwidth	498.05 kHz
Cyclic prefix duration: T_{cp}	12.8 µs
OFDM symbol duration: T_{s}	115.2 µs
Modulation	Adaptive-order QAM
FEC	Adaptive-rate CRC-aided polar
Bit interleaving	Helical

thereof, would be recommended if allowed based on the obtained results. The proposed design entails a message duration of 1.3824 ms, including the synchronization preamble. It allows to transmit up to 297 data bits, comprising the required 34 data bytes and 25 spare bits, yielding a data throughput of 212.14 kbps if all bits carry data. If the spare bits are not used to carry additional data, they can carry more pilot symbols to enhance the performance. In fact, the pilot subcarrier spacing could be reduced to 2 and still 9 spare bits would be available. Other parameters of the proposed design are the helical interleaving parameters $a_{\text{bi}} = 223$ and $b_{\text{bi}} = 4$. The OFDM parameters are the same as the ones used by LDACS: 64 subcarriers spaced 625/64 kHz = 9.765625 kHz apart with the center subcarrier left unused and 25 active subcarriers on each side. Overall, the proposed design fulfills the LDACS A2A requirements: 34 data bytes can be transmitted with a sufficiently low PER up to a distance of 350–450 km, even in the challenging conditions considered in our analysis. The proposed design for the physical layer of LDACS A2A is summarized in Table 4.1 and the one for the short broadcasts (beacons) in Table 4.2.

The periodic broadcasts can be used to organize other data transmissions or P2P communications. These might comprise packets of different lengths but generally larger than the 34 bytes considered for the broadcasts. Given that the performance of the FEC schemes generally improves with larger packets, one could use a higher coding rate with longer packets and still attain the same PER performance of the shorter packets considered here. Thus, in order to maximize the data throughput of the variable-size data transmissions, it is advisable to use an adaptive coding and modulation scheme to dynamically employ a different configuration matching the experienced channel con-

Table 4.2. Short broadcast (beacon) frame of LDACS A2A.

OFDM symbols	12 (2 for sync. and 10 for data & pilots)
synchronization	2 (CAZAC sequences defined in [Grä+19])
data & pilots	10 (following Fig. 4.6b pattern)
Data bits capacity	297 bits
Message duration	1.3824 ms
Throughput	212.14 kbps
Modulation	4-QAM
FEC	Rate-1/3 CRC-aided polar
Helical bit interleaving	$a_{\text{bi}} = 223$, $b_{\text{bi}} = 4$

ditions and desired packet length. This way, the beacons are protected with the most robust coding and modulation scheme, i.e., the proposed rate-1/3 polar code with 4-QAM modulation, and other transmissions can be protected with either the same scheme or using a higher-throughput alternative if the channel conditions and packet length allow it. New coding and modulation schemes can be defined by puncturing the base rate-1/3 polar code to achieve higher coding rates and/or by using higher-order QAM modulations.

Chapter 5

Summary and Outlook

Direct aircraft-to-aircraft (A2A) communications will play a significant role in the future of air traffic. However, no A2A communications link operating at the moment is capable of supporting the data demands foreseen for the air traffic in the future and, thus, a new A2A data link has to be designed. Recognizing the importance of an optimum design of the A2A data link, we identified the critical need for a realistic channel model and detailed channel information, a gap that has been largely overlooked in the existing literature. To fill this void, we embarked on a comprehensive study of A2A channels, analyzing a wealth of channel measurements and deriving numerous statistics for various configurations. These configurations encompassed different ground surfaces, including forest, fields, and lakes, different geometries between aircraft and the Earth's surface, and diverse antenna configurations. It has been shown how the line-of-sight (LoS) component can be affected significantly by the alignment between the antennas and by the shadowing caused by the aircraft fuselage, for example during banking maneuvers. The position of the antennas on the aircraft also plays an important role, as positioning them close to other parts of the aircraft, such as propellers, causes large short-term fluctuations in the amplitude of the LoS component. This is also observed in the specular reflection (SR) component from the Earth's surface, although its absolute amplitude is mainly driven by the characteristics of the terrain below the aircraft. This way, the SR component becomes very powerful and stable when flying over water, intermittent over fields, and mainly absent when overflying forests. The scattering components are present in all cases but are generally weaker than the SR component, when present. Their importance lies in their apparent omnipresence in A2A channels and in their peculiar distribution in the delay/Doppler plane. Analyzing the measured amplitude of the channel components in the different scenarios allowed us to provide very valuable statistics not yet measured in A2A channels in such detail. In addition, in our quest for a more accurate model and for a deeper understanding of the scattering

components, we developed a novel theoretical technique to model the scattering components with a particular emphasis on their delay/Doppler distribution, an aspect that has been largely disregarded in the literature. The technique was validated through measurements in multiple A2A scenarios, providing a valuable tool for recreating the propagation channel in any arbitrary scenario more accurately. Building upon this foundation, we proposed a geometry-based stochastic A2A channel model. This model not only merges the information acquired from the measurements and the novel technique to model the scattering components, but also offers a significant advancement in the field by providing a practical tool for simulating the propagation channels in any arbitrary A2A scenario. In order to consolidate the channel model and identify which parts of it require further research, future work includes conducting flight trials to verify the proposed geometry-based stochastic A2A channel model in multiple frequency bands and scenarios of interest. This would provide valuable insights into the accuracy of the model under real-world conditions. To demonstrate the practicality of our model, we applied it to the design of the physical layer of the LDACS extension towards A2A communications. By doing so, we were able to determine the optimal design, a feat previously hindered by the lack of a realistic A2A channel model usable for simulations. In addition, it allowed us to fill the gap in the literature by assessing the performance of CP-OFDM and different forward error correction coding schemes, including LDPC and polar codes used in 5G communications, in A2A channels.

As future work, the physical layer proposed for LDACS A2A could be implemented in prototypes, which can later be used to verify the performance of the physical layer through flight trials. This would offer a comprehensive evaluation of the proposed design and its practical implementation. In conclusion, this research has significantly advanced our understanding of A2A channels and provided very valuable statistics and models that can be employed by the fellow researchers to further advance in the field. Illustrated by the design of the physical layer of LDACS A2A, the proposed geometry-based stochastic A2A channel model offers a valuable resource for the design of A2A communication systems, paving the way for a more efficient and reliable air traffic management in the future.

Appendix A

Additional A2A Measurements and Results

This appendix contains additional information on the A2A channel measurements and on the conducted analysis. Table A.1 lists the main information on the flights. Table A.2 and Table A.3 describe the scenarios considered for the analysis of the LoS and SR components, respectively. The flight tracks of these scenarios are shown in Fig. A.1.

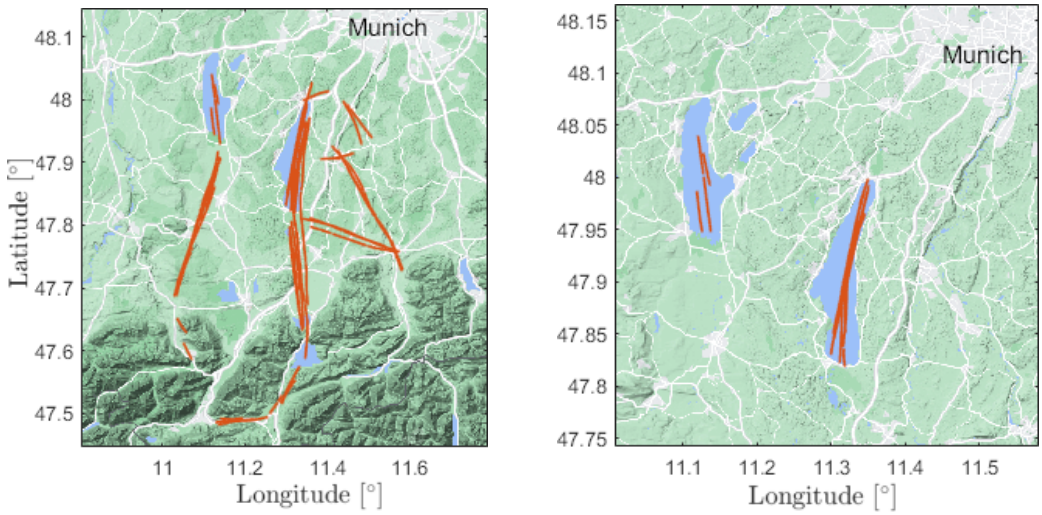

(a) For the LoS component.

(b) For the lake-reflected SR component.

Figure A.1. Flight tracks (TX) considered for the analysis of the LoS and SR components. From [BMFW22].

The measured relative power of the LoS component in different scenarios is shown in Fig. A.2 and Fig. A.3, and the one of the SR component in Fig. A.4. An exemplary

Table A.1. Flights conducted to measure the A2A channel (AGL = above ground level).

Flight identifier	**Route**	**Antenna configuration TX → RX**	**TX height AGL (m)**	**RX height AGL (m)**
R1-D-D-600-600	1	down → down	600	600
R2-D-D-600-600	2	down → down	600	600
R1-D-D-1600-1600	1	down → down	1600	1600
R2-D-D-1600-1600	2	down → down	1600	1600
R1-D-D-2600-2600	1	down → down	2600	2600
R2-D-D-2600-2600	2	down → down	2600	2600
R1-D-U-600-600	1	down → up	600	600
R1-D-U-1600-600	1	down → up	1600	600
R1-D-U-2600-600	1	down → up	2600	600
R1-U-U-600-600	1	up → up	600	600
R1-U-U-1600-600	1	up → up	1600	600
R1-U-D-1600-600	1	up → down	1600	600
R1-U-D-600-600	1	up → down	600	600
R2-U-D-600-600	2	up → down	600	600
R1-U-D-1600-600	1	up → down	1600	600
R2-U-D-1600-600	2	up → down	1600	600
R1-D-D-1600-600	1	down → down	1600	600

Table A.2. Scenarios for the LoS component (AGL = above ground level) [BMFW22].

Scenario identifier	**Antenna configuration TX → RX**	**TX height AGL (m)**	**RX height AGL (m)**
LOS-D-D-600-600	down → down	600	600
LOS-D-D-1600-1600	down → down	1600	1600
LOS-D-D-2600-2600	down → down	2600	2600
LOS-D-U-600-600	down → up	600	600
LOS-U-D-600-600	up → down	600	600
LOS-U-U-600-600	up → up	600	600
LOS-D-D-1600-600	down → down	1600	600
LOS-D-U-1600-600	down → up	1600	600
LOS-U-D-1600-600	up → down	1600	600
LOS-U-U-1600-600	up → up	1600	600

Table A.3. Scenarios for the SR component (AGL = above ground level) [BMFW22].

Scenario identifier	**Antenna configuration TX → RX**	**TX height AGL (m)**	**RX height AGL (m)**
SR-D-D-600-600	down → down	600	600
SR-D-D-1600-1600	down → down	1600	1600
SR-D-U-600-600	down → up	600	600
SR-U-D-600-600	up → down	600	600
SR-U-U-600-600	up → up	600	600

SF measured within 1 second is shown in Fig. A.5 in two scenarios of interest. Figure A.6 indicates the parts of the flight used to measure the power and the RCS of the scattering components.

The Rician distribution yields the best fit for the fast fading observed in many scenarios. Its pdf is given by

$$p_{\mathrm{ric}}(x) = 2\tfrac{(K+1)x}{\Omega}\mathrm{e}^{-\left(K+\frac{(K+1)x^2}{\Omega}\right)}\mathrm{I}_0\left(2\sqrt{\tfrac{K(K+1)}{\Omega}}x\right), \tag{A.1}$$

where K is the Rician K-factor and represents the power ratio between the dominant component and all other MPCs causing the fast fading, $\Omega = \mathbb{E}\{x^2\}$ is the average power, and $\mathrm{I}_0(\cdot)$ is the zero-order modified Bessel function of the first kind. As commonly done in the literature, e.g., see [Unt+21; WRJ19], the K-factor can be obtained using the method of moments [GME99; Abd+01] as

$$K = \frac{\sqrt{1-\gamma}}{1-\sqrt{1-\gamma}}, \tag{A.2}$$

where $\gamma = \frac{\mathrm{Var}\{x^2\}}{(\mathbb{E}\{x^2\})^2}$ with $\mathrm{Var}\{\cdot\}$ denoting the variance operator.

Other distribution providing a great match in some scenarios is the Nakagami distribution, whose pdf is given by

$$p_{\mathrm{nak}}(x) = 2\left(\frac{\mu}{\omega}\right)^{\mu}\frac{1}{\Gamma(\mu)}x^{(2\mu-1)}\mathrm{e}^{-\frac{\mu}{\omega}x^2}, \tag{A.3}$$

where $\omega > 0$ models the spread and $\mu \geq 1/2$ is the shape parameter.

Several comparisons between the channel predicted by our model and the measured one are shown in Fig. A.7, Fig. A.8, and Fig. A.9.

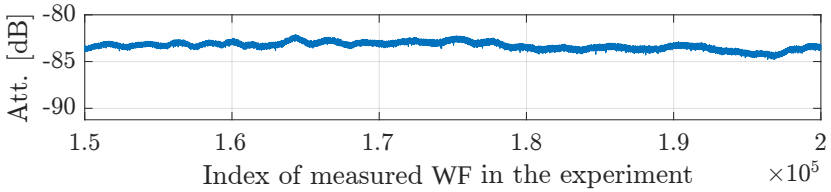

(a) LOS-D-D-600-600 scenario.

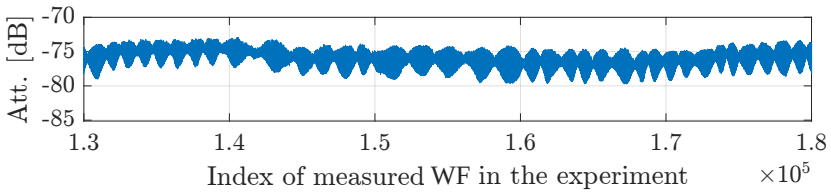

(b) LOS-D-U-600-600 scenario.

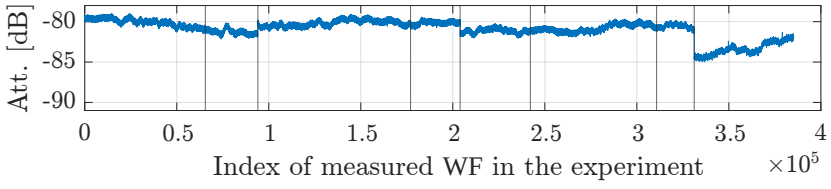

(c) LOS-D-D-1600-1600 scenario.

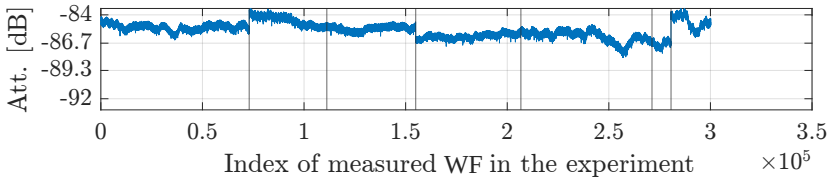

(d) LOS-D-D-2600-2600 scenario.

Figure A.2. Measured LoS component attenuation (or relative power) in multiple scenarios with both aircraft at the same altitude and using the bottom antennas. Note that not all WFs are measured consecutively, but multiple flight segments are considered. These are graphically divided using vertical black lines.

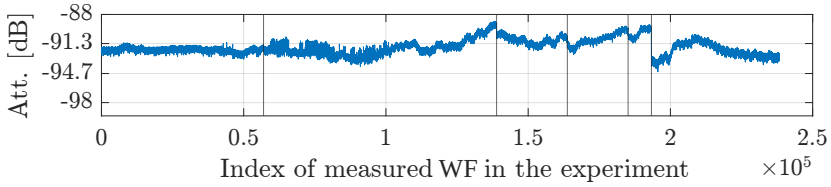

(a) LOS-D-D-1600-600 scenario.

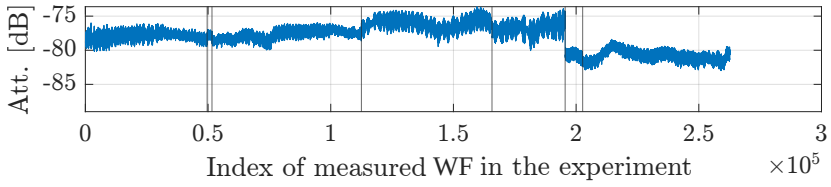

(b) LOS-D-U-1600-600 scenario.

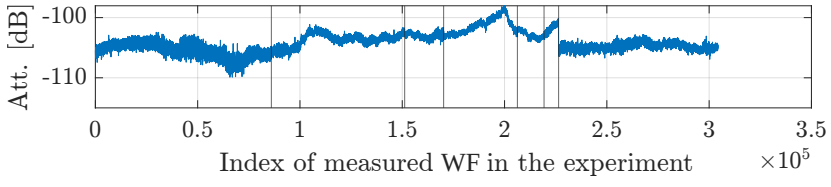

(c) LOS-U-D-1600-600 scenario.

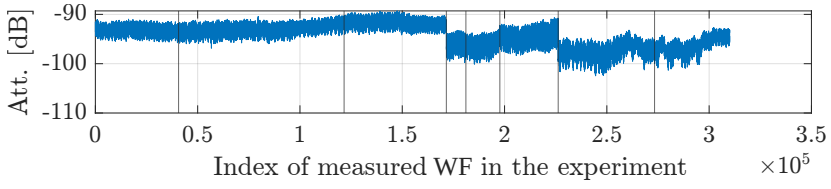

(d) LOS-U-U-1600-600 scenario.

Figure A.3. Measured LoS component attenuation (or relative power) in multiple scenarios with the aircraft at different altitudes and using different antenna configurations. Note that not all WFs are measured consecutively, but multiple flight segments are considered. These are graphically divided using vertical black lines.

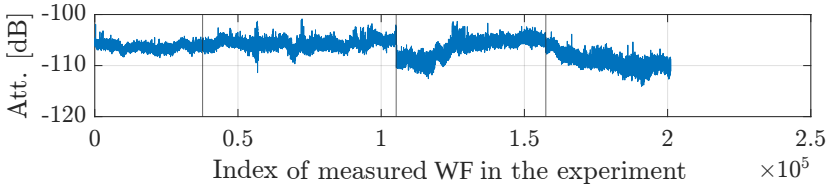

(a) SR-D-D-1600-1600 scenario.

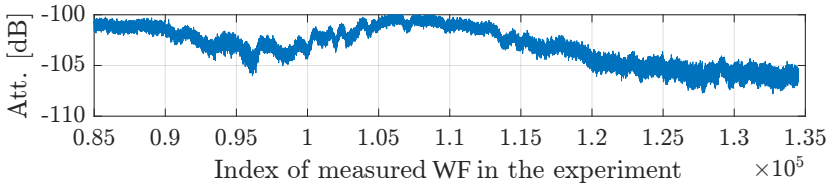

(b) SR-U-D-600-600 scenario.

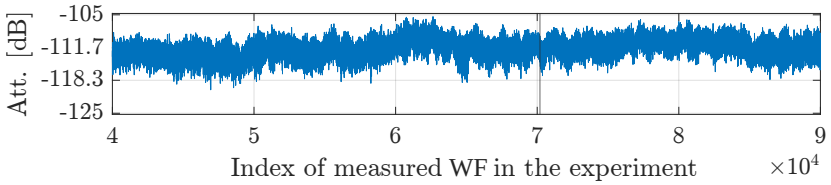

(c) SR-U-U-600-600 scenario.

Figure A.4. Measured SR component attenuation (or relative power) in multiple scenarios with both aircraft at 600 m above ground. Note that not all WFs are measured consecutively, but multiple flight segments are considered. These are graphically divided using vertical black lines.

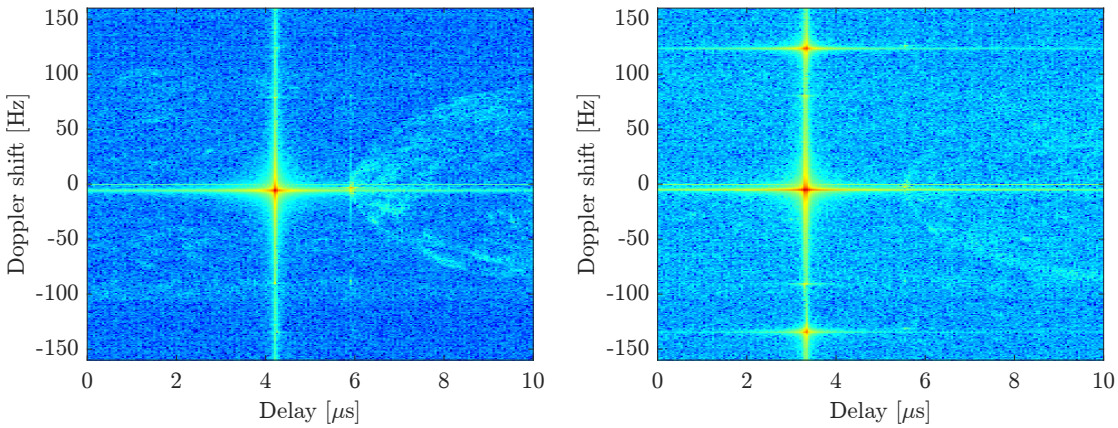

(a) LOS-U-D-600-600 scenario.

(b) LOS-U-U-600-600 scenario.

Figure A.5. Measured SF (1 second) in different scenarios of interest with the aircraft at the same altitude. One can see the significant MPCs, at the LoS delay with ±120 Hz Doppler shifts, caused by the propeller blades of the Dornier (receiver) when its top antenna is used (Fig. A.5b). The MPCs caused by the propellers of the Cessna are weaker but also visible at ±90 Hz Doppler shifts.

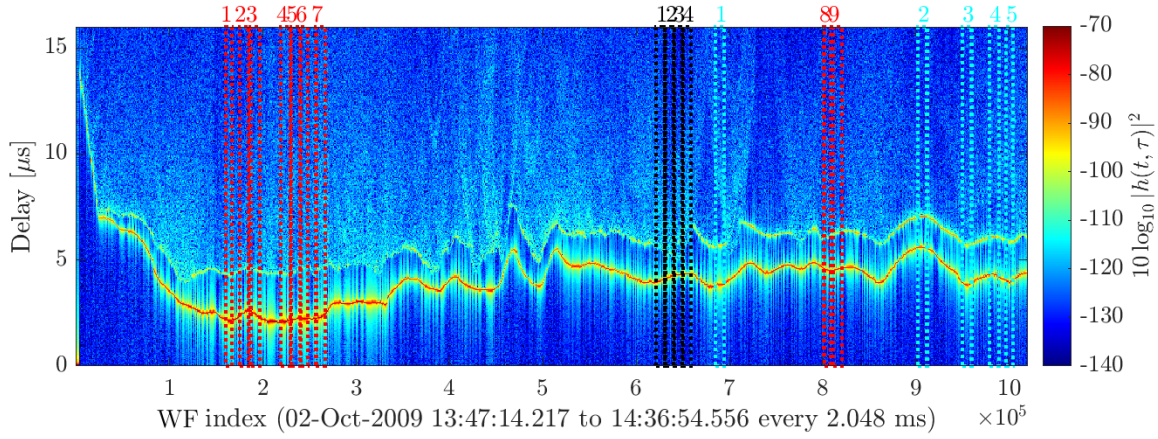

(a) First flight, first flight route.

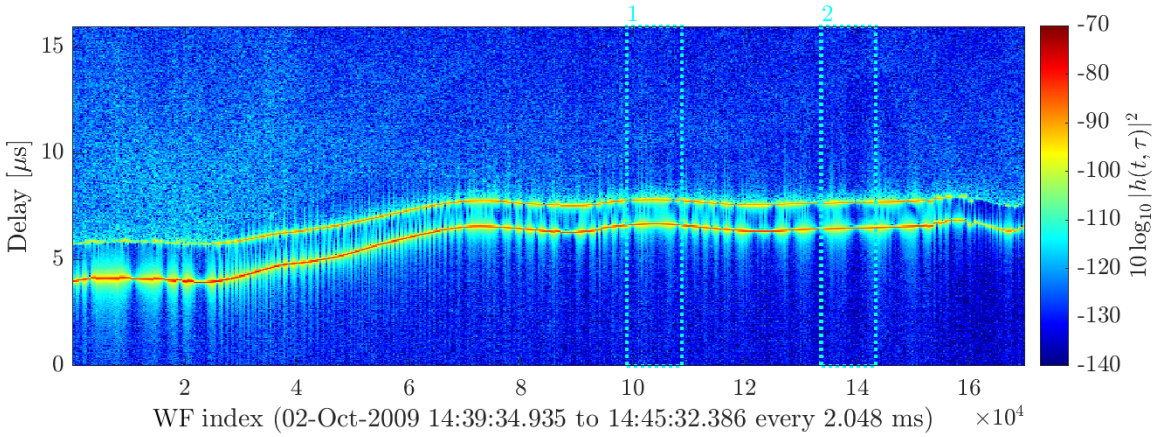

(b) Second flight, second flight route.

Figure A.6. Time-variant WF (squared amplitude) of the first and second flights, covering respectively the first and second flight routes, with the sections highlighted where the scattering components power and radar cross section are measured for forest (black rectangles), field (red rectangles), and lake (cyan rectangles) scenarios.

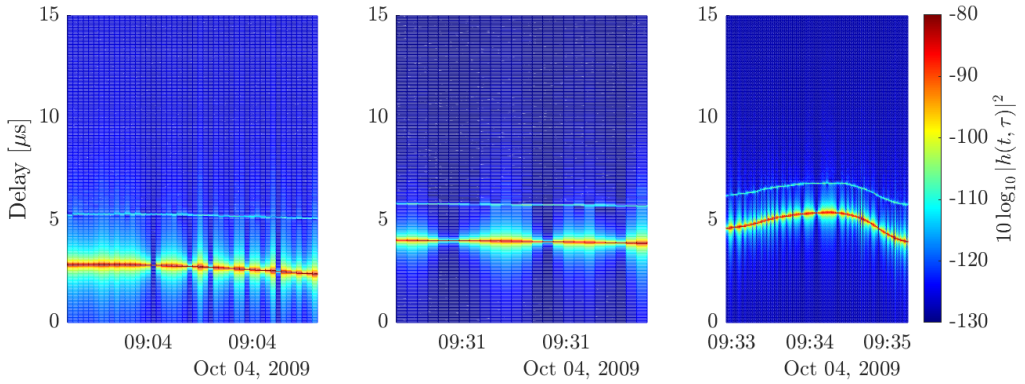

(a) Channel model realization.

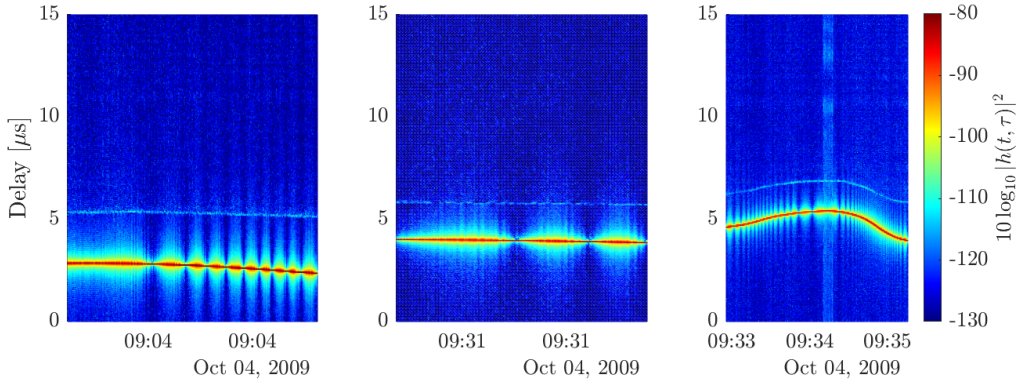

(b) Channel measurements.

Figure A.7. Time-variant WF (squared amplitude) obtained in the lake scenario (in SR-U-U-600-600) using the proposed channel model (Fig. A.7a) and measurements (Fig. A.7b). External interference can be observed at approximately 09:34. The channel model deliberately does not recreate this interference, as it is not part of the physical propagation channel.

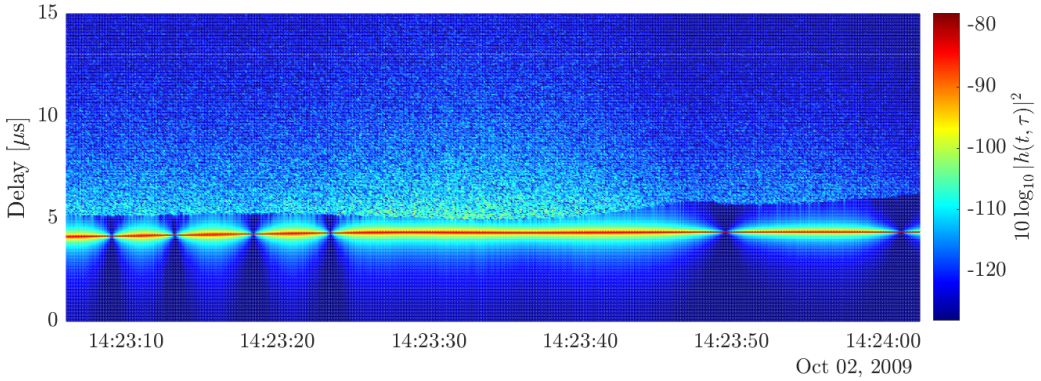

(a) Channel model realization.

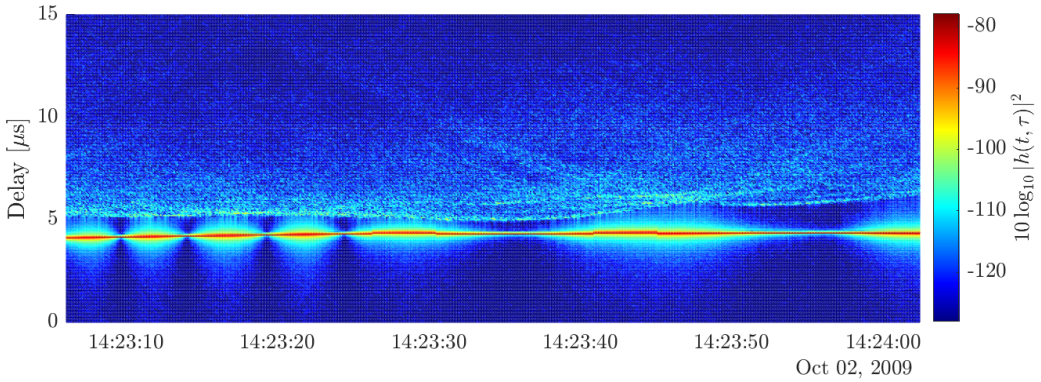

(b) Channel measurements.

Figure A.8. Time-variant WF (squared amplitude) obtained in the forest scenario (in LOS-D-D-600-600) using the proposed channel model (Fig. A.8a) and measurements (Fig. A.8b).

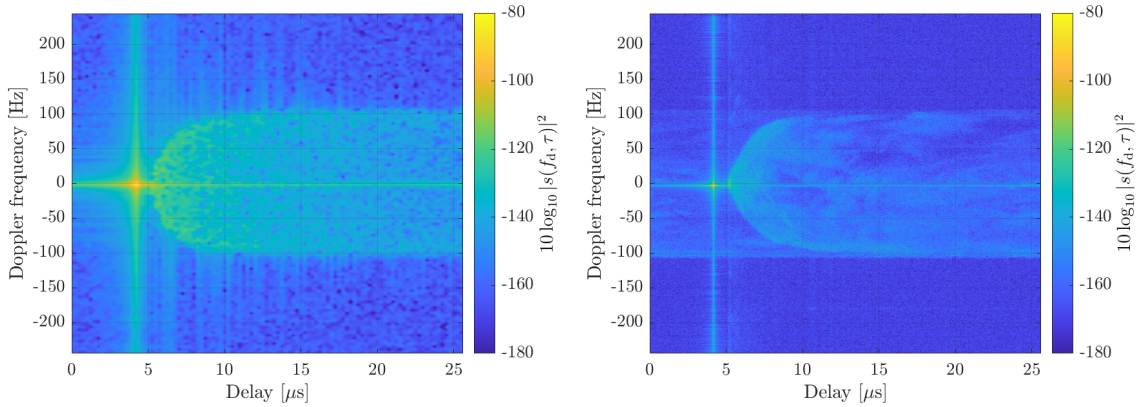

(a) Channel model realization.

(b) Channel measurements.

Figure A.9. Local SF (squared amplitude) obtained in the forest scenario (in LOS-D-D-600-600) using the proposed channel model (Fig. A.9a) and measurements (Fig. A.9b).

Appendix B

Equivalent Low-Pass Channel Model

The time-variant equivalent low-pass channel transfer function for L multi-path components is given by

$$H(t,f) = \sum_{l=0}^{L(t)-1} \alpha_{\mathrm{r}_l}(t)\alpha_{\mathrm{p}_l}(t)\mathrm{e}^{-\mathrm{j}2\pi f_\mathrm{c}\tau_l(t)}\mathrm{e}^{-\mathrm{j}2\pi f\tau_l(t)}\,, \tag{B.1}$$

where $\alpha_{\mathrm{p}_l}(t)$ represents the path loss of the l-th component, $\alpha_{\mathrm{r}_l}(t)$ models its complex reflection coefficient, and $\tau_l(t)$ its delay.

One can consider the Taylor series expansion of the delay

$$\tau_l(t) = \sum_{n=0}^{\infty} \frac{\tau_l^{(n)}(t_0)}{n!}\,(t-t_0)^n = \tau_l(t)|_{t=t_0} + \left.\frac{\partial\tau_l(t)}{\partial t}\right|_{t=t_0}(t-t_0) + \ldots\,, \tag{B.2}$$

and approximate it until the linear term in the first exponential and until the constant term in the second exponential in (B.1), such that the variables t and τ can be separated. Then, by considering that $\partial\tau_l(t)/\partial t|_{t=t_0}\, f_\mathrm{c} = -f_{\mathrm{d},l}$, and using $t_0 = 0$ without loss of generality, one can approximate (B.1) as

$$H(t,f) = \sum_{l=0}^{L(t)-1} \tilde{\alpha}_l(t)\mathrm{e}^{\mathrm{j}2\pi f_{\mathrm{d},l}t}\mathrm{e}^{-\mathrm{j}2\pi f\tau_l(0)}\,, \tag{B.3}$$

where the notation is simplified by defining

$$\tilde{\alpha}_l(t) = \alpha_{\mathrm{r}_l}(t)\alpha_{\mathrm{p}_l}(t)\mathrm{e}^{-\mathrm{j}2\pi f_\mathrm{c}\tau_l(0)}\,.$$

For a clearer notation, the time dependency is not indicated explicitly, e.g, for $\tilde{\alpha}_l$ and L, hereinafter. When measuring the channel, its transfer function is actually sampled in time domain at $t = m\Delta t$ with $m = 0, 1, ..., M-1$ for an observation window

$T_\mathrm{o} = M\Delta t$. It is also sampled in frequency domain at N points within a bandwidth B_s such that $\Delta f = B_\mathrm{s}/N$ and $f = n\Delta f$. The sampled transfer function is then given by

$$H(m,n) = \sum_{l=0}^{L-1} \tilde{\alpha}_l \mathrm{e}^{\mathrm{j}2\pi f_{\mathrm{d},l} m\Delta t} \mathrm{e}^{-\mathrm{j}2\pi n\Delta f \tau_l} = \sum_{l=0}^{L-1} \tilde{\alpha}_l \mathrm{e}^{\mathrm{j}\frac{2\pi m}{M} f_{\mathrm{d},l} T_\mathrm{o}} \mathrm{e}^{-\mathrm{j}\frac{2\pi n}{N} B_\mathrm{s}\tau_l} . \tag{B.4}$$

The weight function $h(m,k)$, where $k = 0, 1, ..., K-1$ is the delay index with a delay resolution $\Delta\tau = 1/B_\mathrm{s}$, is obtained as

$$\begin{aligned} h(m,k) &= \frac{1}{N}\sum_n H(m,n)\mathrm{e}^{\mathrm{j}\frac{2\pi}{N}nk} = \frac{1}{N}\sum_n \sum_{l=0}^{L-1} \left(\tilde{\alpha}_l \mathrm{e}^{\mathrm{j}\frac{2\pi m}{M} f_{\mathrm{d},l} T_\mathrm{o}} \mathrm{e}^{-\mathrm{j}\frac{2\pi n}{N} B_\mathrm{s}\tau_l}\right) \mathrm{e}^{\mathrm{j}\frac{2\pi n}{N}k} \\ &= \sum_{l=0}^{L-1} \tilde{\alpha}_l \mathrm{e}^{\mathrm{j}\frac{2\pi m}{M} f_{\mathrm{d},l} T_\mathrm{o}} \frac{1}{N}\sum_n \mathrm{e}^{\mathrm{j}\frac{2\pi n}{N}(k - B_\mathrm{s}\tau_l)} . \end{aligned} \tag{B.5}$$

Now, considering frequencies on both sides of the carrier frequency f_c, one can simplify (B.5) for an odd number of frequencies, i.e., $n = -\frac{N-1}{2}, ..., 0, ..., \frac{N-1}{2}$., to

$$\begin{aligned} h(m,k) &= \sum_{l=0}^{L-1} \tilde{\alpha}_l \mathrm{e}^{\mathrm{j}\frac{2\pi m}{M} f_{\mathrm{d},l} T_\mathrm{o}} \frac{1}{N} \sum_{n=-\frac{N-1}{2}}^{\frac{N-1}{2}} \mathrm{e}^{\mathrm{j}\frac{2\pi n}{N}(k - B_\mathrm{s}\tau_l)} \\ &= \sum_{l=0}^{L-1} \tilde{\alpha}_l \mathrm{e}^{\mathrm{j}\frac{2\pi m}{M} f_{\mathrm{d},l} T_\mathrm{o}} \frac{1}{N} \mathrm{e}^{-\mathrm{j}\frac{\pi(N-1)}{N}(k - B_\mathrm{s}\tau_l)} \frac{1 - \mathrm{e}^{\mathrm{j}\frac{2\pi N}{N}(k - B_\mathrm{s}\tau_l)}}{1 - \mathrm{e}^{\mathrm{j}\frac{2\pi}{N}(k - B_\mathrm{s}\tau_l)}} \\ &= \sum_{l=0}^{L-1} \tilde{\alpha}_l \mathrm{e}^{\mathrm{j}\frac{2\pi m}{M} f_{\mathrm{d},l} T_\mathrm{o}} \frac{1}{N} \frac{\mathrm{e}^{-\mathrm{j}\pi(k - B_\mathrm{s}\tau_l)} - \mathrm{e}^{\mathrm{j}\pi(k - B_\mathrm{s}\tau_l)}}{\mathrm{e}^{-\mathrm{j}\frac{\pi}{N}(k - B_\mathrm{s}\tau_l)} - \mathrm{e}^{\mathrm{j}\frac{\pi}{N}(k - B_\mathrm{s}\tau_l)}} \\ &= \sum_{l=0}^{L-1} \tilde{\alpha}_l \mathrm{e}^{\mathrm{j}\frac{2\pi m}{M} f_{\mathrm{d},l} T_\mathrm{o}} \frac{1}{N} \frac{\sin\left(\pi\left(k - B_\mathrm{s}\tau_l\right)\right)}{\sin\left(\frac{\pi}{N}\left(k - B_\mathrm{s}\tau_l\right)\right)} \\ &= \sum_{l=0}^{L-1} \tilde{\alpha}_l \mathrm{e}^{\mathrm{j}\frac{2\pi m}{M} f_{\mathrm{d},l} T_\mathrm{o}} \frac{\mathrm{sinc}\left(k - B_\mathrm{s}\tau_l\right)}{\mathrm{sinc}\left(\frac{1}{N}\left(k - B_\mathrm{s}\tau_l\right)\right)} \end{aligned} \tag{B.6}$$

and similarly for an even number of frequencies, i.e., $n = -\frac{N}{2}, ..., 0, ..., \frac{N}{2} - 1$, to

$$\begin{aligned} h(m,k) &= \sum_{l=0}^{L-1} \tilde{\alpha}_l \mathrm{e}^{\mathrm{j}\frac{2\pi m}{M} f_{\mathrm{d},l} T_\mathrm{o}} \frac{1}{N} \sum_{n=-\frac{N}{2}}^{\frac{N}{2}-1} \mathrm{e}^{\mathrm{j}\frac{2\pi n}{N}(k - B_\mathrm{s}\tau_l)} \\ &= \sum_{l=0}^{L-1} \tilde{\alpha}_l \mathrm{e}^{\mathrm{j}\frac{2\pi m}{M} f_{\mathrm{d},l} T_\mathrm{o}} \frac{\mathrm{e}^{-\mathrm{j}\frac{2\pi}{N}\frac{N}{2}(k - B_\mathrm{s}\tau_l)}}{N} \frac{1 - \mathrm{e}^{\mathrm{j}\frac{2\pi N}{N}(k - B_\mathrm{s}\tau_l)}}{1 - \mathrm{e}^{\mathrm{j}\frac{2\pi}{N}(k - B_\mathrm{s}\tau_l)}} \\ &= \sum_{l=0}^{L-1} \tilde{\alpha}_l \mathrm{e}^{\mathrm{j}\frac{2\pi m}{M} f_{\mathrm{d},l} T_\mathrm{o}} \frac{\mathrm{e}^{-\mathrm{j}\frac{\pi}{N}(k - B_\mathrm{s}\tau_l)}}{N} \frac{\mathrm{e}^{-\mathrm{j}\pi(k - B_\mathrm{s}\tau_l)} - \mathrm{e}^{\mathrm{j}\pi(k - B_\mathrm{s}\tau_l)}}{\mathrm{e}^{-\mathrm{j}\frac{\pi}{N}(k - B_\mathrm{s}\tau_l)} - \mathrm{e}^{\mathrm{j}\frac{\pi}{N}(k - B_\mathrm{s}\tau_l)}} \\ &= \sum_{l=0}^{L-1} \tilde{\alpha}_l \mathrm{e}^{\mathrm{j}\frac{2\pi m}{M} f_{\mathrm{d},l} T_\mathrm{o}} \frac{\mathrm{e}^{-\mathrm{j}\frac{\pi}{N}(k - B_\mathrm{s}\tau_l)}}{N} \frac{\sin\left(\pi\left(k - B_\mathrm{s}\tau_l\right)\right)}{\sin\left(\frac{\pi}{N}\left(k - B_\mathrm{s}\tau_l\right)\right)} \\ &= \sum_{l=0}^{L-1} \tilde{\alpha}_l \mathrm{e}^{\mathrm{j}\frac{2\pi m}{M} f_{\mathrm{d},l} T_\mathrm{o}} \mathrm{e}^{-\mathrm{j}\frac{\pi}{N}(k - B_\mathrm{s}\tau_l)} \frac{\mathrm{sinc}\left(k - B_\mathrm{s}\tau_l\right)}{\mathrm{sinc}\left(\frac{1}{N}\left(k - B_\mathrm{s}\tau_l\right)\right)} \end{aligned} \tag{B.7}$$

with $\mathrm{sinc}(x) = \frac{\sin(\pi x)}{\pi x}$. In both cases, i.e., for even and odd N, the weight function is affected by sinc functions that depend on $k - B_\mathrm{s}\tau_l$, i.e., on the difference between the sampling instant and the time-variant delay of each multi-path component. In practice, this leads to a time-variant widening of the multi-path components in the delay direction, as observed in the measurements in Section 3.2, e.g., in Fig. 3.4.

This effect can also be seen in the delay/Doppler-spread function, although not only in the delay direction but also in the Doppler one. The delay/Doppler-spread function can be obtained as the Fourier transform of $h(m,k)$ with respect to m, such that

$$\begin{aligned} s(q,k) &= \sum_m h(m,k)\mathrm{e}^{-\mathrm{j}\frac{2\pi m}{M}q} = \sum_m \sum_l \left(\tilde{\alpha}_l \mathrm{e}^{\mathrm{j}\frac{2\pi m}{M} f_{\mathrm{d},l} T_\mathrm{o}} \frac{1}{N} \sum_n \mathrm{e}^{\mathrm{j}\frac{2\pi n}{N}(k - B_\mathrm{s}\tau_l)} \right) \mathrm{e}^{-\mathrm{j}\frac{2\pi m}{M}q} \\ &= \sum_m \sum_l \left(\tilde{\alpha}_l \mathrm{e}^{\mathrm{j}\frac{2\pi m}{M}(f_{\mathrm{d},l} T_\mathrm{o} - q)} \frac{1}{N} \sum_n \mathrm{e}^{\mathrm{j}\frac{2\pi n}{N}(k - B_\mathrm{s}\tau_l)} \right), \end{aligned} \tag{B.8}$$

where q represents the Doppler frequency shift index.

One can easily see the effect of the time- and bandwidth-limited sampling of the channel if it is assumed that $\tilde{\alpha}_l$ and τ_l are constant within the observation window T_o. Although the effect caused by the time- and bandwidth-limited sampling of the channel would appear even if this assumption does not stand, it allows us to derive a closed-form expression where the effect can be shown analytically. Considering $m = 0, 1, ..., M-1$ and assuming that $\tilde{\alpha}_l$ and τ_l are constant, (B.8) simplifies to

$$\begin{aligned} s(q,k) &= \sum_l \tilde{\alpha}_l \sum_{m=0}^{M-1} \mathrm{e}^{\mathrm{j}\frac{2\pi m}{M}(f_{\mathrm{d},l} T_\mathrm{o} - q)} \frac{1}{N} \sum_n \mathrm{e}^{\mathrm{j}\frac{2\pi n}{N}(k - B_\mathrm{s}\tau_l)} \\ &= \sum_l \tilde{\alpha}_l \frac{1 - \mathrm{e}^{\mathrm{j}2\pi\left(f_{\mathrm{d},l} T_\mathrm{o} - q\right)}}{1 - \mathrm{e}^{\mathrm{j}\frac{2\pi}{M}\left(f_{\mathrm{d},l} T_\mathrm{o} - q\right)}} \frac{1}{N} \sum_n \mathrm{e}^{\mathrm{j}\frac{2\pi n}{N}(k - B_\mathrm{s}\tau_l)} \\ &= \sum_l \tilde{\alpha}_l \mathrm{e}^{\mathrm{j}\pi\frac{M-1}{M}\left(f_{\mathrm{d},l} T_\mathrm{o} - q\right)} \frac{\mathrm{e}^{-\mathrm{j}\pi\left(f_{\mathrm{d},l} T_\mathrm{o} - q\right)} - \mathrm{e}^{\mathrm{j}\pi\left(f_{\mathrm{d},l} T_\mathrm{o} - q\right)}}{\mathrm{e}^{-\mathrm{j}\frac{\pi}{M}\left(f_{\mathrm{d},l} T_\mathrm{o} - q\right)} - \mathrm{e}^{\mathrm{j}\frac{\pi}{M}\left(f_{\mathrm{d},l} T_\mathrm{o} - q\right)}} \frac{1}{N} \sum_n \mathrm{e}^{\mathrm{j}\frac{2\pi n}{N}(k - B_\mathrm{s}\tau_l)} \\ &= M \sum_l \tilde{\alpha}_l \mathrm{e}^{\mathrm{j}\pi\frac{M-1}{M}\left(f_{\mathrm{d},l} T_\mathrm{o} - q\right)} \frac{\mathrm{sinc}\left(f_{\mathrm{d},l} T_\mathrm{o} - q\right)}{\mathrm{sinc}\left(\frac{1}{M}\left(f_{\mathrm{d},l} T_\mathrm{o} - q\right)\right)} \frac{1}{N} \sum_n \mathrm{e}^{\mathrm{j}\frac{2\pi n}{N}(k - B_\mathrm{s}\tau_l)}, \end{aligned} \tag{B.9}$$

following the same steps as in (B.6).

The sampled delay/Doppler-spread function can be further simplified by considering either an odd or even number of frequencies, as done for the weight function in (B.6) and (B.7), respectively. For an odd number of frequencies, i.e., $n = -\frac{N-1}{2}, ..., 0, ..., \frac{N-1}{2}$, and following the same steps as in (B.6), one can express (B.9) as

$$\begin{aligned} s(q,k) &= M \sum_l \tilde{\alpha}_l \mathrm{e}^{\mathrm{j}\pi\frac{M-1}{M}\left(f_{\mathrm{d},l} T_\mathrm{o} - q\right)} \frac{\mathrm{sinc}\left(f_{\mathrm{d},l} T_\mathrm{o} - q\right)}{\mathrm{sinc}\left(\frac{1}{M}\left(f_{\mathrm{d},l} T_\mathrm{o} - q\right)\right)} \frac{1}{N} \mathrm{e}^{-\mathrm{j}\frac{\pi(N-1)}{N}(k - B_\mathrm{s}\tau_l)} \frac{1 - \mathrm{e}^{\mathrm{j}\frac{2\pi N}{N}(k - B_\mathrm{s}\tau_l)}}{1 - \mathrm{e}^{\mathrm{j}\frac{2\pi}{N}(k - B_\mathrm{s}\tau_l)}} \\ &= M \sum_l \tilde{\alpha}_l \mathrm{e}^{\mathrm{j}\pi\frac{M-1}{M}\left(f_{\mathrm{d},l} T_\mathrm{o} - q\right)} \frac{\mathrm{sinc}\left(f_{\mathrm{d},l} T_\mathrm{o} - q\right)}{\mathrm{sinc}\left(\frac{1}{M}\left(f_{\mathrm{d},l} T_\mathrm{o} - q\right)\right)} \frac{\mathrm{sinc}\left(k - B_\mathrm{s}\tau_l\right)}{\mathrm{sinc}\left(\frac{1}{N}\left(k - B_\mathrm{s}\tau_l\right)\right)}. \end{aligned} \tag{B.10}$$

Otherwise, for an even number of frequencies with $n = -\frac{N}{2}, ..., 0, ..., \frac{N}{2} - 1$ and following the same steps as in (B.7), (B.9) is given by

$$s(q,k) = M \sum_l \tilde{\alpha}_l \frac{\operatorname{sinc}\left(f_{\mathrm{d},l} T_\mathrm{o} - q\right)}{\operatorname{sinc}\left(\frac{1}{M}\left(f_{\mathrm{d},l} T_\mathrm{o} - q\right)\right)} \frac{\operatorname{sinc}\left(k - B_\mathrm{s}\tau_l\right)}{\operatorname{sinc}\left(\frac{1}{N}\left(k - B_\mathrm{s}\tau_l\right)\right)} \times \mathrm{e}^{\mathrm{j}\pi\frac{M-1}{M}\left(f_{\mathrm{d},l} T_\mathrm{o} - q\right)} \mathrm{e}^{-\mathrm{j}\frac{\pi}{N}\left(k - B_\mathrm{s}\tau_l\right)}. \tag{B.11}$$

One can notice in (B.10) and (B.11) the sinc functions affecting the delay/Doppler-spread function in both k (delay) and q (Doppler) directions. The widening of the multipath components in the delay and Doppler directions can be seen in the measurements in Section 3.2, e.g., in Fig. 3.7b. For easier visualization, we depict in Fig. B.1 an exemplary delay/Doppler-spread function obtained using (B.10).

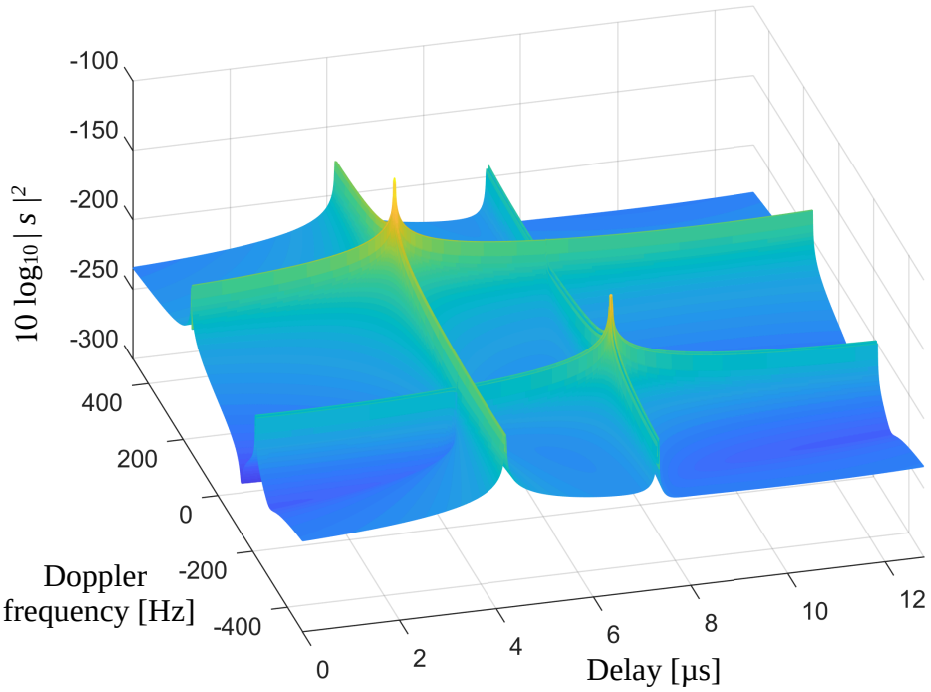

Figure B.1. Example of the effect of the time- and bandwidth-limited channel sampling in the spreading function. Two MPCs are considered: the LoS component with a delay of 4.2 µs and a Doppler frequency shift of 150 Hz, and the SR component with a delay of 7.3 µs, a Doppler frequency shift of −220 Hz, and a reflection coefficient with value 0.2. One can see the spread in delay and Doppler frequency directions around the nominal delay and Doppler frequency shifts of each component.

Appendix C

Additional Simulation Results

This chapter shows additional results complementary to those shown in Chapter 4, including some channel characteristics and the PER performance of LDACS A2A, obtained through simulations, with different design options for its physical layer.

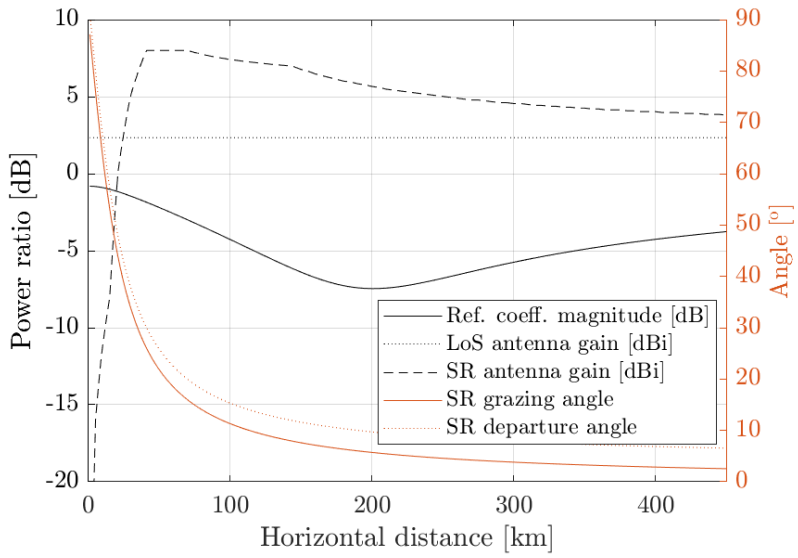

Figure C.1. Geometry and channel characteristics in the oceanic scenario: squared magnitude of the sea reflection coefficient, combined antenna gain (transmitting and receiving) for the LoS and SR components, grazing angle of the sea reflection, and angle of departure of the SR component.

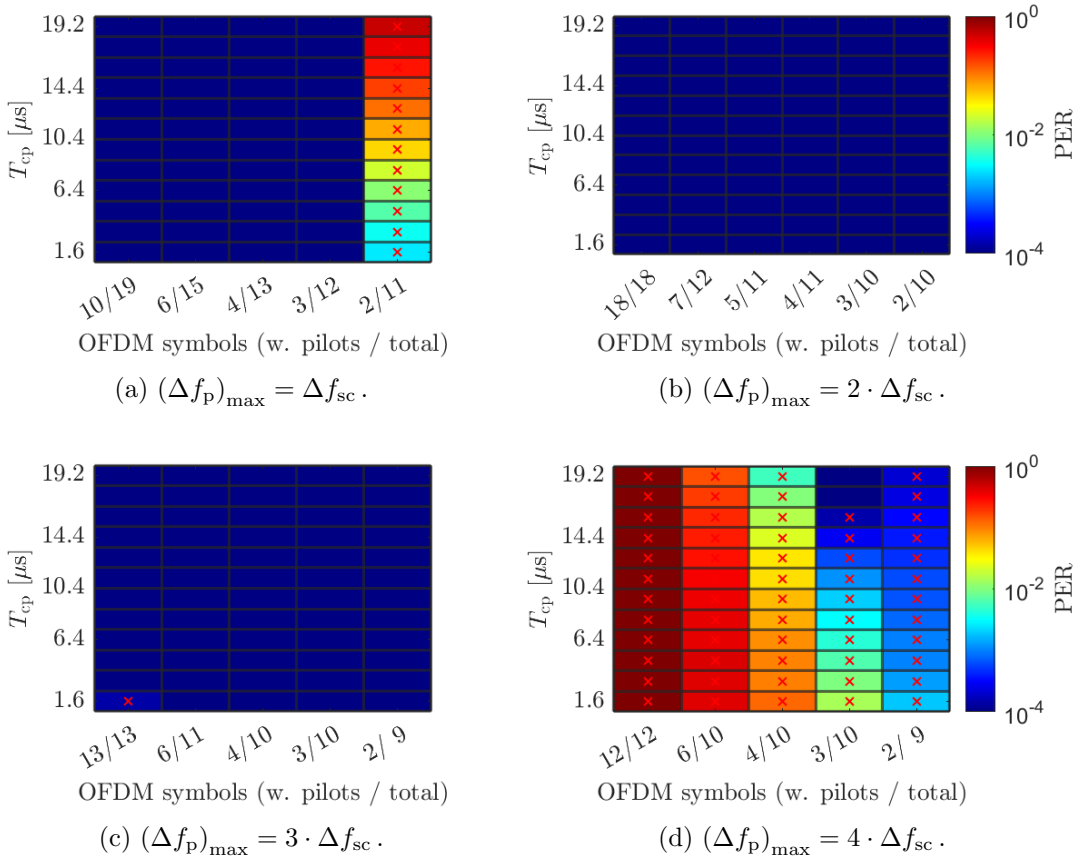

(a) $(\Delta f_{\mathrm{p}})_{\max} = \Delta f_{\mathrm{sc}}$.

(b) $(\Delta f_{\mathrm{p}})_{\max} = 2 \cdot \Delta f_{\mathrm{sc}}$.

(c) $(\Delta f_{\mathrm{p}})_{\max} = 3 \cdot \Delta f_{\mathrm{sc}}$.

(d) $(\Delta f_{\mathrm{p}})_{\max} = 4 \cdot \Delta f_{\mathrm{sc}}$.

Figure C.2. PER in the oceanic scenario with $d_{\mathrm{h}} = 34\,\mathrm{km}$ using different CP lengths and pilot distributions in time and frequency. TC FEC. 2D linear interpolation channel estimation with MMSE linear equalization.

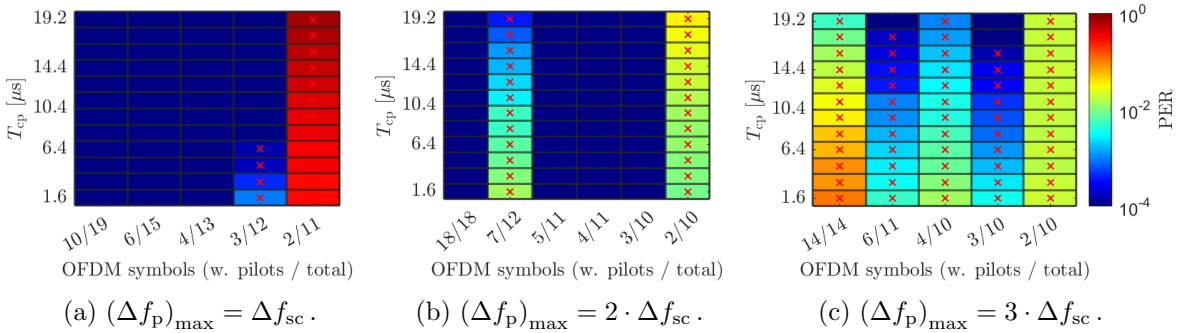

(a) $(\Delta f_{\mathrm{p}})_{\max} = \Delta f_{\mathrm{sc}}$.

(b) $(\Delta f_{\mathrm{p}})_{\max} = 2 \cdot \Delta f_{\mathrm{sc}}$.

(c) $(\Delta f_{\mathrm{p}})_{\max} = 3 \cdot \Delta f_{\mathrm{sc}}$.

Figure C.3. PER in the oceanic scenario with $d_{\mathrm{h}} = 34\,\mathrm{km}$ using different CP lengths and pilot distributions in time and frequency. CC FEC. 2D linear interpolation channel estimation with MMSE linear equalization.

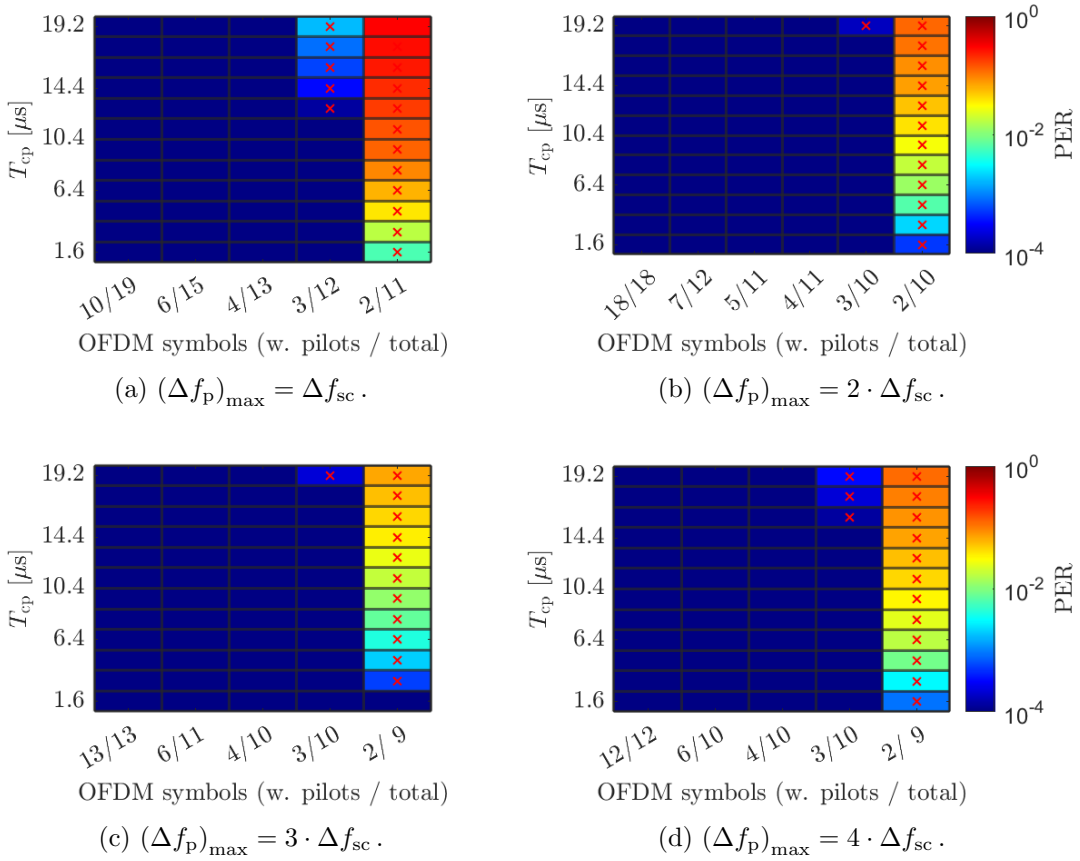

(a) $(\Delta f_{\mathrm{p}})_{\mathrm{max}} = \Delta f_{\mathrm{sc}}$.

(b) $(\Delta f_{\mathrm{p}})_{\mathrm{max}} = 2 \cdot \Delta f_{\mathrm{sc}}$.

(c) $(\Delta f_{\mathrm{p}})_{\mathrm{max}} = 3 \cdot \Delta f_{\mathrm{sc}}$.

(d) $(\Delta f_{\mathrm{p}})_{\mathrm{max}} = 4 \cdot \Delta f_{\mathrm{sc}}$.

Figure C.4. PER in the approach scenario with $d_{\mathrm{h}} = 800\,\mathrm{m}$ using different CP lengths and pilot distributions in time and frequency. The horizontal axis indicates the number of OFDM symbols carrying pilots and the total number of OFDM symbols required to transmit the packet. TC FEC. 2D linear interpolation channel estimation with MMSE linear equalization.

List of Abbreviations

1090ES	1090 extended squitter	2
A2A	aircraft-to-aircraft	2
A/G	air-ground	3
ACM	adaptive coding and modulation	107
ADS–B	automatic dependent surveillance – broadcast	2
AeroMACS	aeronautical mobile airport communications system	13
AGC	automatic gain control	105
AM(R)S	aeronautical mobile (route) service	13
AOC	airline operational control	2
ARNS	aeronautical radio navigation service	15
AS	airborne station	14
ATM	air traffic management	1
ATN	Aeronautical Telecommunication Network	2
ATS	air traffic service	2
BER	bit error rate	99
C2C	car-to-car	36
CC	convolutional code	106
CCS	Cartesian coordinate system	65
cdf	cumulative distribution function	48
CNS	communication, navigation, and surveillance	10
CP	cyclic prefix	4
CRC	cyclic redundancy check	107
CRSCC	concatenated Reed-Solomon and convolutional code	106

CSMA carrier-sense multiple access . . . 12
CTAF common traffic advisory frequency . . . 2
D2D drone-to-drone . . . 36
DFS Deutsche Flugsicherung . . . 6
DME distance measuring equipment . . . 16
ECEF Earth-centered, Earth-fixed . . . 66
EIRP equivalent isotropic radiated power . . . 101
FAA Federal Aviation Administration . . . 1
FCI Future Communications Infrastructure . . . 2
FEC forward error correction . . . 4
FFT fast Fourier transform . . . 111
FL forward link . . . 14
FSPL free-space path loss . . . 23
GBSCM geometry-based stochastic channel model . . . 21
GNSS global navigation satellite system . . . 16
GS ground station . . . 2
IATA International Air Transport Association . . . 9
ICAO International Civil Aviation Organization . . . 1
ICI inter-carrier interference . . . 108
IFFT inverse fast Fourier transform . . . 105
IO interacting object . . . 23
ISI inter-symbol interference . . . 103
ITU International Telecommunication Union . . . 101
JTIDS joint tactical information distribution system . . . 18
LDACS L-band Digital Aeronautical Communications System . . . 2
LDPC low-density parity-check . . . 4
LEO low earth orbit . . . 11
LLR log-likelihood ratio . . . 112
LoS line-of-sight . . . 7
LTI linear time-invariant . . . 24

LTV linear time-variant 24
LTE Long Term Evolution 106
MAC medium access control 6
M2M mobile-to-mobile 21
MIDS multifunctional information distribution system 18
MIMO multiple-input/multiple-output 12
MMSE minimum mean square error 112
MPC multi-path component 22
NAC North Atlantic Corridor 5
nmi nautical miles 6
OFDM orthogonal frequency-division multiplexing 4
ORP oceanic, remote, and polar 2
P2P point-to-point 119
PAPR peak-to-average power ratio 105
PDP power delay profile 28
pdf probability density function 26
PER packet error rate 99
PSC prolate spheroidal coordinate 66
PSCS prolate spheroidal coordinate system 65
PSK phase-shift keying 12
QAM quadrature amplitude modulation 107
QoS quality-of-service 11
RCS radar cross section 49
RL reverse link 14
RMS root mean square 28
rpm revolutions per minute 52
RS Reed-Solomon 106
RX receiver 36
S2S ship-to-ship 36
SF spreading function 39

SISO single-input/single-output 37
SNR signal-to-noise ratio 101
S/P serial to parallel 105
SR specular reflection 32
SSR secondary surveillance radar 19
TACAN tactical air navigation system 16
TC turbo code 106
TCAS traffic alert and collision avoidance system 2
TF transfer function 25
TX transmitter 36
UAT universal access transceiver 3
US uncorrelated scattering 26
VDL VHF data link 2
VDL-m2 VDL mode 2 2
VDL-m4 VDL mode 4 2
V2V vehicle-to-vehicle 33
WF weight function 25
WRC World Radiocommunication Conference 13
WSS wide-sense stationary 26
WSSUS wide-sense stationary uncorrelated scattering 26
ZF zero-forcing 112

List of Symbols

α	complex amplitude 23
α_{p}	amplitude path loss 46
α_{los}	complex amplitude of the line-of-sight component 74
α_{sr}	complex amplitude of the specular reflection component . 74
A	A-component of the scattering plane 65
B_{s}	bandwidth 36
B_{coh}	coherence bandwidth 29
B	B-component of the scattering plane 65
c_0	speed of light in vacuum 23
C	C-component of the scattering plane 65
d_{h}	ground distance between aircraft 102
d_{los}	length of the line-of-sight path 47
D	D-component of the scattering plane 65
d_{sr}	length of the specular reflection path 47
$\mathbb{E}\{\cdot\}$	expectation operator 26
η	η-coordinate of the prolate spheroidal coordinate system (Fig. 3.23) 66
f	frequency 25
f_{c}	carrier frequency 24
f_{d}	Doppler frequency shift 24
Δf	frequency difference or resolution 27
$(\Delta f_{\mathrm{p}})_{\mathrm{max}}$	maximum allowed frequecy separation, in subcarriers, between pilot symbols 112
$f_{\mathrm{d_{los}}}$	Doppler frequency shift of the line-of-sight component ... 74
$f_{\mathrm{d_{sr}}}$	Doppler frequency shift of the specular reflection component 74
f_{lim}	limiting frequencies of the delay/Doppler probability density function 71

Δf_{sc}	OFDM subcarrier spacing ... 107
GoF	goodness-of-fit indicator ... 48
G_{r}	receive antenna gain ... 49
G_{t}	transmit antenna gain ... 49
$H(\cdot,\cdot)$	time-variant transfer function of the channel ... 25
$h(\cdot,\cdot)$	time-variant weight function of the channel ... 24
L	number of multi-path components of the channel ... 137
$\mu_{f_{\mathrm{d}}}$	mean Doppler shift ... 28
μ_{τ}	mean delay ... 28
N_{FFT}	number of OFDM subcarriers ... 107
N_{os}	number of OFDM symbols per packet ... 111
N_{u}	number of active OFDM subcarriers ... 110
$p(t, f_{\mathrm{d}}\|\xi)$	time-variant delay-dependent Doppler probability density function of the channel ... 69
$\rho(t;\tau,\Delta t)$	time-variant hybrid time delay characteristic probability density function ... 86
$p(t,\xi,f_{\mathrm{d}})$	time-variant joint delay/Doppler probability density function of the channel ... 71
$P_{\mathrm{h}}(\tau)$	power delay profile ... 28
$P_{\mathrm{hh}}(\Delta t,\tau)$	delay cross power spectral density ... 27
P_{los}	relative power of the line-of-sight component ... 46
$\mathbf{p}_{\mathrm{r}}$	position vector of the receiver (CCS in Fig. 3.35) ... 89
$p_{\mathrm{r}x}$	x-component of the position vector of the receiver (CCS in Fig. 3.35) ... 89
$p_{\mathrm{r}y}$	y-component of the position vector of the receiver (CCS in Fig. 3.35) ... 89
$p_{\mathrm{r}z}$	z-component of the position vector of the receiver (CCS in Fig. 3.35) ... 89
$P_{\mathrm{s}}(f_{\mathrm{d}},\tau)$	scattering function ... 27
P_{scatt}	relative power of the scattering components ... 49
P_{sr}	relative power of the specular reflection component ... 46
$P_{\mathrm{T}}(f_{\mathrm{d}})$	Doppler power spectral density ... 28
$P_{\mathrm{TT}}(f_{\mathrm{d}},\Delta f)$	Doppler cross power spectral density ... 27
$\mathbf{p}_{\mathrm{t}}$	position vector of the receiver (CCS in Fig. 3.35) ... 89
$p_{\mathrm{t}x}$	x-component of the position vector of the transmitter (CCS in Fig. 3.35) ... 89

p_{ty}	y-component of the position vector of the transmitter (CCS in Fig. 3.35) ... 89
p_{tz}	z-component of the position vector of the transmitter (CCS in Fig. 3.35) ... 89
σ_{RCS}	radar cross section ... 49
$r_{\mathrm{HH}}(t, t', f, f')$	frequency time autocorrelation function ... 26
$r_{\mathrm{hh}}(t, t', \tau, \tau')$	delay time autocorrelation function ... 26
$r_{\mathrm{rx}}(\cdot)$	received signal ... 24
$r_{\mathrm{ss}}(f_{\mathrm{d}}, f'_{\mathrm{d}}, \tau, \tau')$	delay Doppler autocorrelation function ... 26
$r_{\mathrm{TT}}(f_{\mathrm{d}}, f'_{\mathrm{d}}, f, f')$	frequency Doppler autocorrelation function ... 26
$s(\cdot, \cdot)$	delay/Doppler-spread function of the channel ... 25
$\sigma_{f_{\mathrm{d}}}$	root mean square Doppler spread ... 29
σ_τ	root mean square delay spread ... 28
$\mathrm{sinc}(\cdot)$	sinc function, defined as $\mathrm{sinc}(x) = \frac{\sin(\pi x)}{\pi x}$ ... 45
$s_{\mathrm{tx}}(\cdot)$	transmitted signal ... 24
$\sup\{\cdot\}$	supremum operator ... 48
$T(f_{\mathrm{d}}, f)$	Doppler-variant transfer function of the channel ... 25
t	time ... 24
τ	delay ... 23
$\Delta\tau$	delay difference or resolution ... 36
τ_{los}	delay of the line-of-sight component ... 43
τ_{sr}	delay of the specular reflection component ... 45
T_{coh}	coherence time ... 29
T_{cp}	cyclic prefix duration ... 108
Δt	time difference or resolution ... 26
$(\Delta t_{\mathrm{p}})_{\mathrm{max}}$	maximum allowed time separation, in OFDM symbols, between pilot symbols ... 112
ϑ	ϑ-coordinate of the prolate spheroidal coordinate system (Fig. 3.23) ... 66
T_{os}	OFDM symbol duration (without cyclic prefix) ... 108
T_{s}	OFDM symbol duration including cyclic prefix ... 108
T_{w}	windowing duration ... 112
$\mathbf{v}_{\mathrm{r}}$	velocity vector of the receiver (CCS in Fig. 3.35) ... 89
$\mathbf{v}'_{\mathrm{r}}$	velocity vector of the receiver (local CCS in Fig. 3.23) ... 67
$v_{\mathrm{r}x}$	x-component of the velocity vector of the receiver (CCS in Fig. 3.35) ... 89

$v_{\mathrm{r}x'}$ x'-component of the velocity vector of the receiver (local CCS in Fig. 3.23) 67

$v_{\mathrm{r}y}$ y-component of the velocity vector of the receiver (CCS in Fig. 3.35) 89

$v_{\mathrm{r}y'}$ y'-component of the velocity vector of the receiver (local CCS in Fig. 3.23) 67

$v_{\mathrm{r}z}$ z-component of the velocity vector of the receiver (CCS in Fig. 3.35) 89

$v_{\mathrm{r}z'}$ z'-component of the velocity vector of the receiver (local CCS in Fig. 3.23) 67

$\mathbf{v}_{\mathrm{t}}$ velocity vector of the transmitter (CCS in Fig. 3.35) 89

$\mathbf{v'}_{\mathrm{t}}$ velocity vector of the transmitter (local CCS in Fig. 3.23) 67

$v_{\mathrm{t}x}$ x-component of the velocity vector of the transmitter (CCS in Fig. 3.35) 89

$v_{\mathrm{t}x'}$ x'-component of the velocity vector of the transmitter (local CCS in Fig. 3.23) 67

$v_{\mathrm{t}y}$ y-component of the velocity vector of the transmitter (CCS in Fig. 3.35) 89

$v_{\mathrm{t}y'}$ y'-component of the velocity vector of the transmitter (local CCS in Fig. 3.23) 67

$v_{\mathrm{t}z}$ z-component of the velocity vector of the transmitter (CCS in Fig. 3.35) 89

$v_{\mathrm{t}z'}$ z'-component of the velocity vector of the transmitter (local CCS in Fig. 3.23) 67

ξ ξ-coordinate of the prolate spheroidal coordinate system (Fig. 3.23) 66

x' x'-coordinate of the local Cartesian coordinate system (Fig. 3.23) 65

y' y'-coordinate of the local Cartesian coordinate system (Fig. 3.23) 65

z' z'-coordinate of the local Cartesian coordinate system (Fig. 3.23) 65

$(\cdot)^*$ complex conjugate 26

List of Author's Publications

As First Author

- M. A. Bellido-Manganell and M. Walter. "Non-stationary 3D M2M Channel Modeling and Verification With Aircraft-to-Aircraft, Drone-to-Drone, Vehicle-to-Vehicle, and Ship-to-Ship Measurements". *IEEE Transactions on Vehicular Technology*, 73 (5), pp. 6045–6060, May 2024. DOI: 10.1109/TVT.2023.3339299
- M. A. Bellido-Manganell, U.-C. Fiebig, and M. Walter. "Aircraft-to-Aircraft Channel Measurements in the VHF/UHF Band: Analysis of the Line-of-Sight and Lake-Reflected Channel Components". In *Proceedings IEEE 96th Vehicular Technology Conference (VTC Fall)*, London, UK, Sept. 2022. DOI: 10.1109/VTC2022-Fall57202.2022.10012832
- M. A. Bellido-Manganell and M. Schnell. "Feasibility of the Frequency Planning for LDACS Air-to-Air Communications in the L-Band". In *Proceedings Integrated Communications Navigation and Surveillance Conference (ICNS)*, Dulles, VA, USA, Apr. 2021. DOI: 10.1109/ICNS52807.2021.9441623
- M. A. Bellido-Manganell et al. "LDACS Flight Trials: Demonstration and Performance Analysis of the Future Aeronautical Communications System". *IEEE Transactions on Aerospace and Electronic Systems*, 58 (1), pp. 615–634, Feb. 2022. DOI: 10.1109/TAES.2021.3111722
- M. A. Bellido-Manganell, T. Gräupl, and M. Schnell. "Impact Assessment of the L-Band Digital Aeronautical Communications System on the Joint Tactical Information Distribution System". *IEEE Transactions on Vehicular Technology*, 68 (4), pp. 3629–3641, Apr. 2019. DOI: 10.1109/TVT.2019.2898524
- M. A. Bellido-Manganell and M. Schnell. "Towards Modern Air-to-Air Communications: the LDACS A2A Mode". In *Proceedings IEEE/AIAA 38th Digital Avionics Systems Conference (DASC)*, San Diego, CA, USA, Sept. 2019. DOI: 10.1109/DASC43569.2019.9081678

- M. A. Bellido-Manganell. "Design Approach of a Future Air-to-Air Data Link". In *Proceedings IEEE/AIAA 37th Digital Avionics Systems Conference (DASC)*, London, UK, Sept. 2018. DOI: 10.1109/DASC.2018.8569594

As Co-Author

- M. Walter et al. "Mobile-to-Mobile Uncorrelated Scatter Channels". *IEEE Transactions on Wireless Communications (Early Access)*, Feb. 2025. DOI: 10.1109/TWC.2025.3542478
- R. Raulefs et al. "Propagation Channel for Communications and Navigation Between Moving Ships". In *Proceedings OCEANS Conference*, Halifax, NS, Canada, Sept. 2024. DOI: 10.1109/OCEANS55160.2024.10754252
- T. Marks, A. Hillebrecht, and M. A. Bellido-Manganell. "Applications and Challenges for Airborne Ad-Hoc Communication Networks in ORP Airspaces Using the L-Band". In *Proceedings 34th Congress of the International Council of the Aeronautical Sciences (ICAS)*, Florence, Italy, Sept. 2024
- R. Raulefs et al. "Verification and Modeling of the Maritime Channel for Maritime Communications and Navigation Networks". *Frontiers in Marine Science*, 10, Nov. 2023. DOI: 10.3389/fmars.2023.1158524
- D. M. Mielke et al. "Application of Path-Based Multipath Component Tracking on Air-Ground Channel Measurement Data". *IEEE Transactions on Vehicular Technology*, 72 (5), pp. 5546–5559, May 2023. DOI: 10.1109/TVT.2022.3230357
- M. Walter and M. A. Bellido-Manganell. "Differential Geometric Description of Future Mobile-to-Mobile Channels". In *Proceedings 17th European Conference on Antennas and Propagation (EuCAP)*, Florence, Italy, Mar. 2023. DOI: 10.23919/EuCAP57121.2023.10133585
- T. Gräupl et al. "LDACS Flight Trials: Demonstration of ATS-B2, IPS, and Seamless Mobility". In *Proceedings Integrated Communication, Navigation and Surveillance Conference (ICNS)*, Herndon, VA, USA, Apr. 2023. DOI: 10.1109/ICNS58246.2023.10124329
- A. Gürbüz, D. M. Mielke, and M. A. Bellido-Manganell. "On the Application of Beamforming in LDACS". In *Proceedings Integrated Communication, Navigation and Surveillance Conference (ICNS)*, Dulles, VA, USA, Apr. 2022. DOI: 10.1109/ICNS54818.2022.9771514
- A. Filip-Dhaubhadel et al. "Feasibility Assessment of LDACS-Based Wide Area Multilateration". In *Proceedings IEEE/AIAA 41st Digital Avionics Systems*

Conference (DASC), Portsmouth, VA, USA, Sept. 2022. DOI: 10.1109/DASC55683.2022.9925808

- D. M. Mielke et al. "Analysis of the Dominant Signal Component of the Air-Ground Channel Based on Measurement Data at C-Band". *IEEE Transactions on Vehicular Technology*, 70 (4), pp. 2955–2968, Apr. 2021. DOI: 10.1109/TVT.2021.3065143
- N. Mäurer et al. "Flight Trial Demonstration of Secure GBAS via the L-band Digital Aeronautical Communications System (LDACS)". *IEEE Aerospace and Electronic Systems Magazine*, 36 (4), pp. 8–17, Apr. 2021. DOI: 10.1109/MAES.2021.3052318
- M. Mostafa, M. A. Bellido-Manganell, and T. Gräupl. "Feasibility of Cell Planning for the L-Band Digital Aeronautical Communications System Under the Constraint of Secondary Spectrum Usage". *IEEE Transactions on Vehicular Technology*, 67 (10), pp. 9721–9733, Oct. 2018. DOI: 10.1109/TVT.2018.2862829
- T. Gräupl et al. "L-band Digital Aeronautical Communications System (LDACS) Flight Trials in the National German Project MICONAV". In *Proceedings Integrated Communications, Navigation, Surveillance Conference (ICNS)*, 4A2–1–4A2–7, Herndon, VA, USA, Apr. 2018. DOI: 10.1109/ICNSURV.2018.8384881

Patents

- Sebastian Lindner, M. A. Bellido-Manganell et al., "Multi-Channel Self-Organized Time Division Multiple Access (MCSOTDMA) Protokoll für verteilten Kanalzugriff in Funknetzen" - submitted to the German patent office (*Deutsche Patentanmeldung* Nr. 102022212008.6), 2023.

References

[Abd+01] A. Abdi et al. "On the Estimation of the K Parameter for the Rice Fading Distribution". *IEEE Communications Letters*, 5 (3), pp. 92–94, Mar. 2001. DOI: 10.1109/4234.913150.

[AH86] A. S. Akki and F. Haber. "A Statistical Model of Mobile-to-Mobile Land Communication Channel". *IEEE Transactions on Vehicular Technology*, 35 (1), pp. 2–7, Feb. 1986. DOI: 10.1109/T-VT.1986.24062.

[AK02] A. Abdi and M. Kaveh. "A Space-Time Correlation Model for Multielement Antenna Systems in Mobile Fading Channels". *IEEE Journal on Selected Areas in Communications*, 20 (3), pp. 550–560, Apr. 2002. DOI: 10.1109/49.995514.

[Alt11] Altera Corporation. *3GPP LTE Turbo Reference Design*. San Jose, CA, USA, Jan. 2011. URL: https://cdrdv2-public.intel.com/654042/an505.pdf.

[Ari09] E. Arikan. "Channel Polarization: A Method for Constructing Capacity-Achieving Codes for Symmetric Binary-Input Memoryless Channels". *IEEE Transactions on Information Theory*, 55 (7), pp. 3051–3073, July 2009. DOI: 10.1109/TIT.2009.2021379.

[Bel63] P. Bello. "Characterization of Randomly Time-Variant Linear Channels". *IEEE Transactions on Communications Systems*, 11 (4), pp. 360–393, Dec. 1963. DOI: 10.1109/TCOM.1963.1088793.

[Bel73] P. Bello. "Aeronautical Channel Characterization". *IEEE Transactions on Communications*, 21 (5), pp. 548–563, May 1973. DOI: 10.1109/TCOM.1973.1091707.

[Ben+96] S. Benedetto et al. *A Soft-Input Soft-Output Maximum A Posteriori (MAP) Module to Decode Parallel and Serial Concatenated Codes*. TDA Progress Report 42-127. Nov. 1996. URL: https://ipnpr.jpl.nasa.gov/progress_report/42-127/127H.pdf.

[Ber12] L. Bernadó. “Non-Stationarity in Vehicular Wireless Channels”. PhD thesis. Vienna, Austria: Technische Universität Wien, Apr. 2012.

[Ber+15] L. Bernadó et al. “Time- and Frequency-Varying K-Factor of Non-Stationary Vehicular Channels for Safety-Relevant Scenarios”. *IEEE Transactions on Intelligent Transportation Systems*, 16 (2), pp. 1007–1017, Apr. 2015. DOI: 10.1109/TITS.2014.2349364.

[BM18] M. A. Bellido-Manganell. “Design Approach of a Future Air-to-Air Data Link”. In *Proceedings IEEE/AIAA 37th Digital Avionics Systems Conference (DASC)*, London, UK, Sept. 2018. DOI: 10.1109/DASC.2018.8569594.

[BM+22] M. A. Bellido-Manganell et al. “LDACS Flight Trials: Demonstration and Performance Analysis of the Future Aeronautical Communications System”. *IEEE Transactions on Aerospace and Electronic Systems*, 58 (1), pp. 615–634, Feb. 2022. DOI: 10.1109/TAES.2021.3111722.

[BMFW22] M. A. Bellido-Manganell, U.-C. Fiebig, and M. Walter. “Aircraft-to-Aircraft Channel Measurements in the VHF/UHF Band: Analysis of the Line-of-Sight and Lake-Reflected Channel Components”. In *Proceedings IEEE 96th Vehicular Technology Conference (VTC Fall)*, London, UK, Sept. 2022. DOI: 10.1109/VTC2022-Fall57202.2022.10012832.

[BMGS19] M. A. Bellido-Manganell, T. Gräupl, and M. Schnell. “Impact Assessment of the L-Band Digital Aeronautical Communications System on the Joint Tactical Information Distribution System”. *IEEE Transactions on Vehicular Technology*, 68 (4), pp. 3629–3641, Apr. 2019. DOI: 10.1109/TVT.2019.2898524.

[BMS19] M. A. Bellido-Manganell and M. Schnell. “Towards Modern Air-to-Air Communications: the LDACS A2A Mode”. In *Proceedings IEEE/AIAA 38th Digital Avionics Systems Conference (DASC)*, San Diego, CA, USA, Sept. 2019. DOI: 10.1109/DASC43569.2019.9081678.

[BMS21] M. A. Bellido-Manganell and M. Schnell. “Feasibility of the Frequency Planning for LDACS Air-to-Air Communications in the L-Band”. In *Proceedings Integrated Communications Navigation and Surveillance Conference (ICNS)*, Dulles, VA, USA, Apr. 2021. DOI: 10.1109/ICNS52807.2021.9441623.

[BMW24] M. A. Bellido-Manganell and M. Walter. "Non-stationary 3D M2M Channel Modeling and Verification With Aircraft-to-Aircraft, Drone-to-Drone, Vehicle-to-Vehicle, and Ship-to-Ship Measurements". *IEEE Transactions on Vehicular Technology*, 73 (5), pp. 6045–6060, May 2024. DOI: 10.1109/TVT.2023.3339299.

[Cla68] R. H. Clarke. "A Statistical Theory of Mobile-Radio Reception". *The Bell System Technical Journal*, 47 (6), pp. 957–1000, 1968. DOI: 10.1002/j.1538-7305.1968.tb00069.x.

[ER07] EUROCONTROL/FAA Future Communications Study Operational Concepts and Requirements Team. *Communications Operating Concept and Requirements for the Future Radio System (COCR), Ver. 2*. 2007.

[ES10] U. Epple and M. Schnell. "Channel Estimation in OFDM Systems With Strong Interference". In *Proceedings 15th International OFDM Workshop*, Hamburg, Germany, Sept. 2010.

[ES17] U. Epple and M. Schnell. "Advanced Blanking Nonlinearity for Mitigating Impulsive Interference in OFDM Systems". *IEEE Transactions on Vehicular Technology*, 66 (1), pp. 146–158, Jan. 2017. DOI: 10.1109/TVT.2016.2535374.

[ETS24] ETSI. *5G NR Multiplexing and Channel Coding*. 3GPP TS 38.212 Version 18.2.0 Release 18. May 2024.

[EUR07] EUROCONTROL/FAA. *Action Plan 17 — Future Communications Study: Final Conclusions and Recommendations Report*. EUROCONTROL/FAA Memorandum of Cooperation, 2007.

[EUR21] EUROCONTROL. *Radio Frequency Function 2020 Report*. First edition. Mar. 2021.

[FD20] A. Filip-Dhaubhadel. "L-Band Digital Aeronautical Communication System (LDACS)-Based Non-Cooperative Passive Multistatic Radar for Civil Aviation Surveillance". PhD thesis. Technische Universität Chemnitz, 2020. ISBN: 978-3843948135.

[FD+22] A. Filip-Dhaubhadel et al. "Feasibility Assessment of LDACS-Based Wide Area Multilateration". In *Proceedings IEEE/AIAA 41st Digital Avionics Systems Conference (DASC)*, Portsmouth, VA, USA, Sept. 2022. DOI: 10.1109/DASC55683.2022.9925808.

[Fla57] C. Flammer. *Spheroidal Wave Functions*. Stanford, CA: Stanford University Press, 1957. ISBN: 978-0486446394.

[Fle96] B. Fleury. “An Uncertainty Relation for WSS Processes and its Application to WSSUS Systems”. *IEEE Transactions on Communications*, 44 (12), pp. 1632–1634, Dec. 1996. DOI: 10.1109/26.545890.

[Fle+99] B. Fleury et al. “Channel Parameter Estimation in Mobile Radio Environments Using the SAGE Algorithm”. *IEEE Journal on Selected Areas in Communications*, 17 (3), pp. 434–450, Mar. 1999. DOI: 10.1109/49.753729.

[Fra15] N. Franzen. “Spectrally Efficient Beaconing for Aeronautical Applications”. PhD thesis. Technical University Darmstadt, 2015.

[Fri46] H. T. Friis. “A Note on a Simple Transmission Formula”. *Proceedings of the IRE*, 34 (5), pp. 254–256, May 1946. DOI: 10.1109/JRPROC.1946.234568.

[Fri71] H. T. Friis. “Introduction to Radio and Radio Antennas”. *IEEE Spectrum*, 8 (4), pp. 55–61, Apr. 1971. DOI: 10.1109/MSPEC.1971.5218045.

[Ge+22] C. Ge et al. “A 3-D Dynamic Non-WSS Cluster Geometrical-Based Stochastic Model for UAV MIMO Channels”. *IEEE Transactions on Vehicular Technology*, July 2022. DOI: 10.1109/TVT.2022.3168193.

[GMBM22] A. Gürbüz, D. M. Mielke, and M. A. Bellido-Manganell. “On the Application of Beamforming in LDACS”. In *Proceedings Integrated Communication, Navigation and Surveillance Conference (ICNS)*, Dulles, VA, USA, Apr. 2022. DOI: 10.1109/ICNS54818.2022.9771514.

[GME99] L. J. Greenstein, D. G. Michelson, and V. Erceg. “Moment-Method Estimation of the Ricean K-Factor”. *IEEE Communications Letters*, 3 (6), pp. 175–176, June 1999. DOI: 10.1109/4234.769521.

[Grä16] T. Gräupl. “FACTS2: A Service Oriented Simulation Framework for Aeronautical Communication System Evaluation”. In *Proceedings IEEE/AIAA 35th Digital Avionics Systems Conference (DASC)*, Sacramento, CA, USA, Sept. 2016. DOI: 10.1109/DASC.2016.7777988.

[Grä17a] T. Gräupl. “FACTS2: Extended Simulation Framework for ATM Communication Demand Analysis of Europe”. In *Proceedings IEEE/AIAA 36th Digital Avionics Systems Conference (DASC)*, St. Petersburg, FL, USA, Sept. 2017. DOI: 10.1109/DASC.2017.8102053.

[Grä17b] T. Gräupl. "Validating the FACTS2 Air Traffic Simulation Framework". In *Proceedings Integrated Communications, Navigation and Surveillance Conference (ICNS)*, pp. 1D4–1–1D4–8, Herndon, VA, USA, Apr. 2017. DOI: 10.1109/ICNSURV.2017.8011893.

[Grä+18] T. Gräupl et al. "L-band Digital Aeronautical Communications System (LDACS) Flight Trials in the National German Project MICONAV". In *Proceedings Integrated Communications, Navigation, Surveillance Conference (ICNS)*, 4A2–1–4A2–7, Herndon, VA, USA, Apr. 2018. DOI: 10.1109/ICNSURV.2018.8384881.

[Grä+19] T. Gräupl et al. *LDACS A/G Specification*. Tech. rep. PJ14-02-01 D3.3.030. SESAR2020, Aug. 2019.

[Grä+23] T. Gräupl et al. "LDACS Flight Trials: Demonstration of ATS-B2, IPS, and Seamless Mobility". In *Proceedings Integrated Communication, Navigation and Surveillance Conference (ICNS)*, Herndon, VA, USA, Apr. 2023. DOI: 10.1109/ICNS58246.2023.10124329.

[Haa02] E. Haas. "Aeronautical Channel Modeling". *IEEE Transactions on Vehicular Technology*, 51 (2), pp. 254–264, Mar. 2002. DOI: 10.1109/25.994803.

[HH99] P. Hoeher and E. Haas. "Aeronautical Channel Modeling at VHF-Band". In *Proceedings IEEE 50th Vehicular Technology Conference (VTC Fall)*, pp. 1961–1966, Amsterdam, Netherlands, Sept. 1999. DOI: 10.1109/VETECF.1999.797280.

[HMG22] A. Hillebrecht, T. Marks, and V. Gollnick. "Assessment of Real-Time Data Transmission via Ad-Hoc Communication Networks in the North Atlantic Oceanic Airspace". In *Proceedings 33rd Congress of the International Council of the Aeronautical Sciences (ICAS)*, Stockholm, Sweden, Sept. 2022.

[HMG23] A. Hillebrecht, T. Marks, and V. Gollnick. "An Aeronautical Data Communication Demand Model for the North Atlantic Oceanic Airspace". *CEAS Aeronautical Journal*, 14 (2), pp. 553–567, Mar. 2023. DOI: 10.1007/s13272-023-00651-4.

[Hoy+23] J. Hoydis et al. "Sionna RT: Differentiable Ray Tracing for Radio Propagation Modeling". *arXiv e-prints*, arXiv:2303.11103, Mar. 2023. DOI: 10.48550/arXiv.2303.11103.

[Ind19] Industry High Level Group (IHLG). *Aviation Benefits Report*. 2019. URL: https://www.icao.int/sustainability/Documents/AVIATION-BENEFITS-2019-web.pdf.

[Int01] International Civil Aviation Organization. *Doc 9776: Manual on VHF Digital Link (VDL) Mode 2*. First edition. 2001.

[Int04] International Civil Aviation Organization. *Manual on VHF Digital Link (VDL) Mode 4*. First edition. 2004.

[Int07] International Telecommunication Union. *Final Acts WRC-07*. 2007.

[Int09] International Civil Aviation Organization. *Manual on the Universal Access Transceiver (UAT)*. 2009.

[Int18a] International Civil Aviation Organization. *Doc 9718: Handbook on Radio Frequency Spectrum Requirements for Civil Aviation, Volume I, ICAO Spectrum Strategy, Policy Statements and Related Information*. Second edition. 2018.

[Int18b] International Civil Aviation Organization. *Finalization of LDACS Draft SARPs*. Second meeting of DCIWG (Data Communication Infrastructure Working Group), Montreal, Oct. 2018.

[Int19] International Civil Aviation Organization. *Doc 9750 – Global Air Navigation Plan*. 2019.

[Int21] International Telecommunication Union. *Electrical Characteristics of the Surface of the Earth*. Recommendation P. 527-6. Geneva: ITU-R, 2021.

[Int22] International Air Transport Association (IATA). *Global Outlook for Air Transport*. June 2022. URL: https://www.iata.org/en/iata-repository/publications/economic-reports/airline-industry-economic-performance---june-2022---report/.

[Int24] International Civil Aviation Organization. *Air Transport Monthly Monitor March 2024*. 2024. URL: https://www.icao.int/sustainability/Documents/MonthlyMonitor-2024/ICAO%20Monthly%20Monitor_March%202024.pdf.

[Int90] International Telecommunication Union. *Reflection from the Surface of the Earth*. Report 1008-1. Geneva: ITU-R, 1990.

[Jak94] W. C. Jakes. *Microwave Mobile Communications*. IEEE Press Classic Reissue. New York, USA: Wiley, May 1994. ISBN: 0780310691.

[Kam18] B. Kamali. *AeroMACS: An IEEE 802.16 Standard-based Technology for the Next Generation of Air Transportation Systems*. John Wiley & Sons, Oct. 2018. ISBN: 978-1119281108.

[M̈+21] N. Mäurer et al. "Flight Trial Demonstration of Secure GBAS via the L-band Digital Aeronautical Communications System (LDACS)". *IEEE Aerospace and Electronic Systems Magazine*, 36 (4), pp. 8–17, Apr. 2021. DOI: 10.1109/MAES.2021.3052318.

[Mat05] G. Matz. "On Non-WSSUS Wireless Fading Channels". *IEEE Transactions on Wireless Communications*, 4 (5), pp. 2465–2478, Sept. 2005. DOI: 10.1109/TWC.2005.853905.

[MBMG18] M. Mostafa, M. A. Bellido-Manganell, and T. Gräupl. "Feasibility of Cell Planning for the L-Band Digital Aeronautical Communications System Under the Constraint of Secondary Spectrum Usage". *IEEE Transactions on Vehicular Technology*, 67 (10), pp. 9721–9733, Oct. 2018. DOI: 10.1109/TVT.2018.2862829.

[Med+08] D. Medina et al. "Feasibility of an Aeronautical Mobile Ad Hoc Network Over the North Atlantic Corridor". In *Proceedings 5th Annual IEEE Communications Society Conference on Sensor, Mesh and Ad Hoc Communications and Networks*, pp. 109–116, San Francisco, CA, USA, June 2008. DOI: 10.1109/SAHCN.2008.23.

[MHBM24] T. Marks, A. Hillebrecht, and M. A. Bellido-Manganell. "Applications and Challenges for Airborne Ad-Hoc Communication Networks in ORP Airspaces Using the L-Band". In *Proceedings 34th Congress of the International Council of the Aeronautical Sciences (ICAS)*, Florence, Italy, Sept. 2024.

[MHL23] T. Marks, A. Hillebrecht, and F. Linke. "Modeling Air-to-Air Communication Networks in the North Atlantic Region". *CEAS Aeronautical Journal*, pp. 1–21, May 2023. DOI: 10.1007/s13272-023-00656-z.

[Mie+21] D. M. Mielke et al. "Analysis of the Dominant Signal Component of the Air-Ground Channel Based on Measurement Data at C-Band". *IEEE Transactions on Vehicular Technology*, 70 (4), pp. 2955–2968, Apr. 2021. DOI: 10.1109/TVT.2021.3065143.

[Mie+23] D. M. Mielke et al. "Application of Path-Based Multipath Component Tracking on Air-Ground Channel Measurement Data". *IEEE Transac-*

tions on Vehicular Technology, 72 (5), pp. 5546–5559, May 2023. DOI: 10.1109/TVT.2022.3230357.

[MJ51] F. J. Massey Jr. "The Kolmogorov-Smirnov Test for Goodness of Fit". *Journal of the American Statistical Association*, 46 (253), pp. 68–78, Mar. 1951. DOI: 10.1080/01621459.1951.10500769.

[Mol11] A. F. Molisch. *Wireless Communications*. 2nd ed. John Wiley & Sons, 2011. ISBN: 978-0470741863.

[Nex] *NextGen homepage:* https://www.faa.gov/nextgen/. Accessed: 2024-11-08.

[Ono+17] F. Ono et al. "Measurements on C-band Air-to-Air Channel for Coexistence Among Multiple Unmanned Aircraft Systems". In *Proceedings International Conference on Unmanned Aircraft Systems (ICUAS)*, pp. 1160–1164, Miami, FL, USA, June 2017. DOI: 10.1109/ICUAS.2017.7991486.

[Pai+08] A. Paier et al. "Non-WSSUS Vehicular Channel Characterization in Highway and Urban Scenarios at 5.2 GHz Using the Local Scattering Function". In *International ITG Workshop on Smart Antennas (WSA)*, pp. 9–15, Darmstadt, Germany, Feb. 2008. DOI: 10.1109/WSA.2008.4475530.

[Pät02] M. Pätzold. *Mobile Fading Channels*. John Wiley & Sons, 2002. ISBN: 978-0471495499.

[Pät+05] M. Pätzold et al. "A MIMO Mobile-To-Mobile Channel Model: Part I – The Reference Model". In *Proceedings IEEE 16th International Symposium on Personal, Indoor and Mobile Radio Communications (PIMRC)*, pp. 573–578, Berlin, Germany, Sept. 2005. DOI: 10.1109/PIMRC.2005.1651501.

[PB82] J. D. Parsons and A. S. Bajwa. "Wideband Characterisation of Fading Mobile Radio Channels". In *IEE Proceedings F (Communications, Radar and Signal Processing)*, pp. 95–101, Apr. 1982. DOI: 10.1049/ip-f-1.1982.0016.

[PHY08] M. Pätzold, B. O. Hogstad, and N. Youssef. "Modeling, Analysis, and Simulation of MIMO Mobile-to-Mobile Fading Channels". *IEEE Transactions on Wireless Communications*, 7 (2), pp. 510–520, Feb. 2008. DOI: 10.1109/TWC.2008.05913.

[PSP05] C. S. Patel, G. L. Stüber, and T. G. Pratt. "Simulation of Rayleigh-Faded Mobile-to-Mobile Communication Channels". *IEEE Transactions on Communications*, 53 (11), pp. 1876–1884, Nov. 2005. DOI: 10.1109/TCOMM.2005.858678.

[PW03] P. Potocki and E. Walter. *AIRBUS Views on Datalinks and VDL Mode 4*. Working paper 11 presented in the CP/WG-M. Montreal, Canada: International Civil Aviation Organization, Apr. 2003.

[Rap01] T. S. Rappaport. *Wireless Communications: Principles and Practice*. 2nd ed. Prentice Hall, Dec. 2001. ISBN: 978-0130422323.

[Rau+23] R. Raulefs et al. "Verification and Modeling of the Maritime Channel for Maritime Communications and Navigation Networks". *Frontiers in Marine Science*, 10, Nov. 2023. DOI: 10.3389/fmars.2023.1158524.

[Rau+24] R. Raulefs et al. "Propagation Channel for Communications and Navigation Between Moving Ships". In *Proceedings OCEANS Conference*, Halifax, NS, Canada, Sept. 2024. DOI: 10.1109/OCEANS55160.2024.10754252.

[Roy15] A. Roy. *VDL Systems: Current Status in the USA and Spectrum Considerations for Potential Future VDL Systems*. Thirty-third meeting of the Frequency Spectrum Management Panel (FSMP) Working Group F (Frequency). Montreal, Canada: International Civil Aviation Organization, Aug. 2015.

[RTC02] RTCA. *Minimum Aviation System Performance Standards for Automatic Dependent Surveillance Broadcast (ADS-B)*. RTCA DO-242A. 2002.

[RTC09] RTCA. *Minimum Operational Performance Standards for 1090 MHz Extended Squitter Automatic Dependent Surveillance – Broadcast (ADS-B) and Traffic Information Services – Broadcast (TIS-B)*. RTCA DO-260B. Dec. 2009.

[RTC14] RTCA. *Minimum Operational Performance Standards (MOPS) for the Aeronautical Mobile Airport Communication System (AeroMACS)*. RTCA DO-346. 2014.

[Ses] *SESAR homepage:* http://www.sesarju.eu/. Accessed: 2024-11-08.

[Sko08] M. I. Skolnik. *Radar Handbook*. 3rd ed. New York, NY: McGraw-Hill, 2008. ISBN: 978-0071485470.

[Som+19] G. Sommerkorn et al. “Experimental and Analytical Characterization of Time-Variant V2V Channels in a Highway Scenario”. In *Proceedings 13th European Conference on Antennas and Propagation (EuCAP)*, Krakow, Poland, Apr. 2019.

[STA18] STATFOR. *European Aviation in 2040. Challenges of Growth. Annex 1: Flight Forecast to 2040*. EUROCONTROL, 2018.

[Tak+14] K. Takizawa et al. “Measurement on S-band Radio Propagation Characteristics for Unmanned Aircraft Systems”. In *Proceedings 8th European Conference on Antennas and Propagation (EuCAP)*, pp. 3068–3072, The Hague, Netherlands, Apr. 2014. DOI: 10.1109/EuCAP.2014.6902475.

[TM03] Z. Tang and A. S. Mohan. “A Correlated Indoor MIMO Channel Model”. In *Proceedings Canadian Conference on Electrical and Computer Engineering*, pp. 1889–1892, Montreal, QC, Canada, May 2003. DOI: 10.1109/CCECE.2003.1226281.

[Unt+16] P. Unterhuber et al. “A Survey of Channel Measurements and Models for Current and Future Railway Communication Systems”. *Mobile Information Systems*, 2016 (7308604), July 2016. DOI: https://doi.org/10.1155/2016/7308604.

[Unt+21] P. Unterhuber et al. “Stochastic Channel Parameters for Train-to-Train Communications”. *IEEE Open Journal of Antennas and Propagation*, 2, pp. 778–792, July 2021. DOI: 10.1109/OJAP.2021.3094672.

[VF97] F. Vatalaro and A. Forcella. “Doppler Spectrum in Mobile-to-Mobile Communications in the Presence of Three-Dimensional Multipath Scattering”. *IEEE Transactions on Vehicular Technology*, 46 (1), pp. 213–219, Feb. 1997. DOI: 10.1109/25.554754.

[Vit98] A. J. Viterbi. “An Intuitive Justification and a Simplified Implementation of the MAP Decoder for Convolutional Codes”. *IEEE Journal on Selected Areas in Communications*, 16 (2), pp. 260–264, Feb. 1998. DOI: 10.1109/49.661114.

[Wal+10] M. Walter et al. “UHF/VHF Air-to-Air Propagation Measurements”. In *Proceedings 4th European Conference on Antennas and Propagation (EuCAP)*, Barcelona, Spain, Apr. 2010.

[Wal16] M. Walter. “Scattering in Non-Stationary Mobile-to-Mobile Communications Channels”. PhD thesis. Universität Ulm, 2016. ISBN: 978-3831645510.

[Wal+19] M. Walter et al. “Analysis of Non-Stationary 3D Air-to-Air Channels Using the Theory of Algebraic Curves”. *IEEE Transactions on Wireless Communications*, 18 (8), pp. 3767–3780, Aug. 2019. DOI: 10.1109/TWC.2019.2908863.

[Wal+20] M. Walter et al. “Geometric Analysis of the Doppler Frequency for General Non-Stationary 3D Mobile-to-Mobile Channels Based on Prolate Spheroidal Coordinates”. *IEEE Transactions on Vehicular Technology*, 69 (10), pp. 10419–10434, Oct. 2020. DOI: 10.1109/TVT.2020.3011408.

[Wal+25] M. Walter et al. “Mobile-to-Mobile Uncorrelated Scatter Channels”. *IEEE Transactions on Wireless Communications (Early Access)*, Feb. 2025. DOI: 10.1109/TWC.2025.3542478.

[WBM23] M. Walter and M. A. Bellido-Manganell. “Differential Geometric Description of Future Mobile-to-Mobile Channels”. In *Proceedings 17th European Conference on Antennas and Propagation (EuCAP)*, Florence, Italy, Mar. 2023. DOI: 10.23919/EuCAP57121.2023.10133585.

[WFZ14] M. Walter, U.-C. Fiebig, and A. Zajić. “Experimental Verification of the Non-Stationary Statistical Model for V2V Scatter Channels”. In *Proceedings IEEE 80th Vehicular Technology Conference (VTC Fall)*, Vancouver, BC, Canada, Sept. 2014. DOI: 10.1109/VTCFall.2014.6965981.

[WM15] J. M. Wichgers and J. P. Mitchell. *Identification and Analysis of Future Aeronautical Communications Candidates*. NASA, 2015.

[WRJ19] W. Wang, R. Raulefs, and T. Jost. “Fading Characteristics of Maritime Propagation Channel for Beyond Geometrical Horizon Communications in C-Band”. *CEAS Space Journal*, 11 (1), pp. 95–104, Mar. 2019. DOI: 10.1007/s12567-017-0185-1.

[WS11a] M. Walter and M. Schnell. “Statistical Distribution of Line-of-Sight and Reflected Path in the Aeronautical Channel”. In *Proceedings IEEE/AIAA 30th Digital Avionics Systems Conference (DASC)*, pp. 4D1–1–4D1–9, Seattle, WA, USA, Oct. 2011. DOI: 10.1109/DASC.2011.6095909.

[WS11b] M. Walter and M. Schnell. “The Doppler-Delay Characteristic of the Aeronautical Scatter Channel”. In *Proceedings IEEE 74th Vehicular Technology Conference (VTC Fall)*, pp. 1–5, San Francisco, CA, USA, Sept. 2011. DOI: 10.1109/VETECF.2011.6093064.

[WSD17] M. Walter, D. Shutin, and A. Dammann. "Time-Variant Doppler PDFs and Characteristic Functions for the Vehicle-to-Vehicle Channel". *IEEE Transactions on Vehicular Technology*, 66 (12), pp. 10748–10763, Dec. 2017. DOI: 10.1109/TVT.2017.2722229.

[WSF14a] M. Walter, D. Shutin, and U.-C. Fiebig. "Delay-Dependent Doppler Probability Density Functions for Vehicle-to-Vehicle Scatter Channels". *IEEE Transactions on Antennas and Propagation*, 62 (4), pp. 2238–2249, Apr. 2014. DOI: 10.1109/TAP.2014.2301432.

[WSF14b] M. Walter, D. Shutin, and U.-C. Fiebig. "Joint Delay Doppler Probability Density Functions for Air-to-Air Channels". *International Journal of Antennas and Propagation*, 2014 (814218), Apr. 2014. DOI: 10.1155/2014/814218.

[WSF15] M. Walter, D. Shutin, and U.-C. Fiebig. "Prolate Spheroidal Coordinates for Modeling Mobile-to-Mobile Channels". *IEEE Antennas and Wireless Propagation Letters*, 14, pp. 155–158, Feb. 2015. DOI: 10.1109/LAWP.2014.2358265.

[WZS15] M. Walter, T. Zemen, and D. Shutin. "Empirical Relationship Between Local Scattering Function and Joint Probability Density Function". In *Proceedings IEEE 26th International Symposium on Personal, Indoor, and Mobile Radio Communications (PIMRC)*, Hong Kong, China, Aug. 2015. DOI: 10.1109/PIMRC.2015.7343359.

[Zaj+09] A. G. Zajić et al. "Wideband MIMO Mobile-to-Mobile Channels: Geometry-Based Statistical Modeling With Experimental Verification". *IEEE Transactions on Vehicular Technology*, 58 (2), pp. 517–534, Feb. 2009. DOI: 10.1109/TVT.2008.928001.

[ZS08] A. G. Zajić and G. L. Stüber. "Three-Dimensional Modeling, Simulation, and Capacity Analysis of Space-Time Correlated Mobile-to-Mobile Channels". *IEEE Transactions on Vehicular Technology*, 57 (4), pp. 2042–2054, July 2008. DOI: 10.1109/TVT.2007.912150.

[ZS09] A. G. Zajić and G. L. Stüber. "Three-Dimensional Modeling and Simulation of Wideband MIMO Mobile-to-Mobile Channels". *IEEE Transactions on Wireless Communications*, 8 (3), pp. 1260–1275, Mar. 2009. DOI: 10.1109/TWC.2009.070379.